SURFACE MODIFICATION OF ZINC OXIDE-BASED THIN FILMS FOR GAS SENSING APPLICATIONS

BY

Qasem Ahmed Qasem Drmosh

A Dissertation Presented to the
DEANSHIP OF GRADUATE STUDIES

KING FAHD UNIVERSITY OF PETROLEUM & MINERALS
DHAHRAN, SAUDI ARABIA

In Partial Fulfillment of the
Requirements for the Degree of

DOCTOR OF PHILOSOPHY

In

PHYSICS

January 2016

KING FAHD UNIVERSITY OF PETROLEUM & MINERALS

DHAHRAN- 31261, SAUDI ARABIA

DEANSHIP OF GRADUATE STUDIES

This thesis, written by **Qasem Ahmed Qasem Drmosh** under the direction of his thesis advisor and approved by his thesis committee, has been presented and accepted by the Dean of Graduate Studies, in partial fulfillment of the requirements for the degree of **DOCTOR OF PHILOSOPHY IN PHYSICS**.

Dr. Zain Hassan Yamani
(Advisor)

Dr. Abdullah A. Al-Sunaidi
Department Chairman

Dr. Salam A. Zummo
Dean of Graduate Studies

5/5/16

Date

Dr. Abdel-Naseer Aly Kawde
(Member)

Dr. Khalil Ali Ziq
(Member)

Dr. Mohammed Sardar Ayub

(Member)

Dr. Ayman Sharif El-Said

(Member)

DEDICATION

To my beloved parents

To the apples of my eyes..Basma, Husam and Houssain

To my brothers and sisters

To my lovely wife Om Husam

God Bless them all

ACKNOWLEDGMENTS

Praise to Allah for giving me the strength and perseverance to carry out this research. I acknowledge my advisor, Dr. Zain Yamani, Director of the Center of Excellence in Nanotechnology (CENT), for giving me the time and for keeping me focused on my research. I cannot thank him enough for all his patience, guidance, assistance and constructive criticism.

I also would like to acknowledge and express my deep thanks for my thesis committee members, Prof. Khalil Ziq, Prof. Mohammed Sardar Ayub, Dr. Abdel-Naseer Aly Kawde and Dr. Ayman Sherif El-Said, for their attention and constructive feedback.

My deep appreciation goes to Prof. Abdul-Majeed Azad for his constant support keeping his door always open for me. I am most indebted to him for his encouragement, cooperation, and helpful comments.

I also would like to express my appreciation to CENT, and the Physics Department for their assistance and support to conduct this research work.

I express my deep thanks to the Chairman of Physics department, Dr. Abdullah A. Al-Sunaidi and to all faculty members of the Physics Department, especially who taught and helped me during my PhD study.

Particular thanks go to Dr. Nouar Tabet, Dr. Abbas Hakeem, Dr. M. Kamal, Dr. M. Faiz and Mr. Abdul Majeed Hendi for their help, support, and encouragement.

I would like to acknowledge the support provided by King Abdulaziz City for Science and Technology (KACST) through the Science & Technology Unit at King Fahd University of Petroleum & Minerals (KFUPM) for funding this work through project No. 09-NAN772-04 as part of the National Science, Technology and Innovation Plan.

I owe a debt of gratitude to my dear parents, the gift of Allah to me. May Allah (S.W.T.) give them good health and give me ample opportunity to be of service to them. I am also greatly indebted to my brothers Ali and Omer and my sisters for their prayers and patience.

TABLE OF CONTENTS

LIST OF TABLES

LIST OF FIGURES

LIST OF ABBREVIATIONS

DC	:	Direct Current
RF	:	Radio Frequency
XRD	:	X-ray Diffraction
XPS	:	X-ray Photoelectron Spectroscopy
FE-SEM	:	Field Emission Scanning Electron Microscope
AFM	:	Atomic Force Microscope
PO_2	:	Partial pressure of Oxygen
IDE	:	Interdigitated Electrodes
SDA	**:**	Semiconductor Device Analyzer
ppm	**:**	Part Per Million

ABSTRACT

Full Name : [QASEM AHMED QASEM DRMOSH]
Thesis Title : [SURFACE MODIFICATION OF ZINC OXIDE-BASED THIN FILMS FOR GAS SENSING APPLICATIONS]
Major Field : [PHYSICS]
Date of Degree : [JANUARY, 2016]

The work reported in this dissertation focuses on:(a) modifying the surface of ZnO-based thin films, and (b) assessing the effect of modification on their gas sensing applications. The films were made by a sputtering process. For this, two appraoches were employed. In the first method, the sputtered films were modified by incorporating noble metals, such as, Ag, Au or Pt, in the following three sequential steps. First, ZnO thin films were fabricated by DC reactive sputtering. Then, an ultra-thin layer of the noble metal M (M = Ag, Au or Pt) was deposited on the ZnO surface. Finally, M/ZnO films were annealed at different temperatures to obtain nanostructured morphology of M on the thin films. This strategy also resulted in uniformly dispersed metal nanoparticles on the metal oxide surface. The size and interparticle distance was controlled by parameters such as deposition time and annealing conditions (temperature-time). A number of techniques such as X-ray diffraction (XRD), Field Emission Scanning Electron Microscope (FE-SEM) Atomic Force Microscopic (AFM), X-ray Photoelectron Spectroscopy (XPS), and UV-Vis were employed for the characterization of these films.

The XRD data of the as-synthesized and annealed ZnO thin films revealed a preferential orientation along its c axis (002) and a peak-shift to higher diffraction angle after heat treatment. The grain size was calculated using Scherrer equation. It showed a systematic increase with increasing annealing temperature. The FE-SEM images showed that the size and density of the metal nanoparticles on the surface of ZnO thin films can be controlled by deposition time and annealing treatment. In each case, the growth of a thin layer of the noble metal and its continuity on the ZnO surface was confirmed from the FE-SEM images and XPS depth profiling. The optical properties were measured by UV–Vis spectrophotometry which showed reduction in the optical band gap in the post-annealed samples. For comparison, the sputtered Zn thin films were oxidized at very low oxygen partial pressure (PO_2), created experimentally by different H_2/H_2O mixtures at different temperatures. The microstructural features of ZnO in this case were notably influenced by H_2/H_2O ratio and the annealing temperature.

The gas sensing behavior of the M/ZnO films toward H_2 was studied. The results showed that the films exhibited good response towards H_2 even at very low concentration (close to ppb level). Among them, the performance of Pt/ZnO film was the most promising with the highest response and shortest response time. The optimum temperature of operation of the Pt/ZnO sensor was 300 ºC while for those with Ag or Au was 400 ºC.

In the case of the ZnO thin films prepared by DC reactive sputtering of Zn film, oxidized in H_2/H_2O mixture, there was no significant change in their response toward H_2 gas detection. However, this response time was shorter.

ملخص الرسالة

الاسم الكامل: قاسم أحمد قاسم درموش

عنوان الرسالة: تعديل أسطح أغشية رقيقة معتمدة على أكسيد الخارصين لاستخدامها كمتحسسات غازية

التخصص: فيزياء

تاريخ الدرجة العلمية: يناير 2016 م

إنّ الهدف الأساس من هذه الدراسة هو تصميم متحسسات لديه القدرة على كشف وتحسس غاز الهيدروجين وذلك بتعديل سطح مادة أكسيد الخارصين بطريقتين جديدتين . الطريقة الأولى تمثلت بإضافة تراكيب نانوية البنية على أسطح أغشية رقيقة من مادة أكسيد الخارصين ، وهذه المعادن تشمل الفضة والذهب والبلاتين. تمت عملية إضافة المواد المعدنية نانوية البنية إلى أسطح رقائق أكسيد الخارصين من خلال ثلاث مراحل. في المرحلة الأولى تم ترسيب طبقة رقيقة من مادة أكسيد الخارصين على زجاج باستخدام جهاز الترسيب بالرش المهبطي ،وفي الخطوة الثانية تم ترسيب طبقة رقيقة من أحد المعادن (فضة أو ذهب أو بلاتين) على سطح أكسيد الخارصين أيضاً باستخدام جهاز الترسيب بالرش المهبطي ، وفي الخطوة الأخيرة تم تحويل طبقة المعدن الرقيقة إلى تراكيب نانوية من خلال تسخين طبقة المعدن الرقيقة المترسبة على سطح أكسيد الخارصين عند درجات حرارة مختلفة ولفترات زمنية مختلفة.

بعد عملية إنتاج الأغشية الرقيقة في كلتا الطريقتين تم فحصها باستخدام العديد من الأجهزة ، حيث تم استخدام جهاز حيود الأشعة السينية لدراسة الخصائص البلورية للمواد المنتجة ، كما تم استخدام المجهر الماسح الإلكتروني مجهر القوى الذرية لمعرفة شكل وأبعاد مادة أكسيد الخارصين و المواد النانوية المتكونة عليه. أما جهاز مطياف - الإلكترون الضوئي - فقد تم استخدامه لدراسة معرفة مكونات المواد المنتجة ، وتم أيضاً استخدام جهاز الامتصاص في الضوء المرئي وفوق البنفسجي لدراسة الخصائص البصرية للأغشية الرقيقة .

أظهرت نتائج جهاز حيود الأشعة السينية للرقائق المنتجة بهذه الطريقة انتظام بلورات مادة أكسيد الخارصين في الاتجاه البلوري(002) كما تم ملاحظة وجود زيادة في حجم بلورات أكسيد الخارصين وزيادة في انحراف زاوية الحيود بزيادة درجة حرارة تسخين الرقائق . كما أظهرت صور المجهر الماسح الالكتروني تكون تراكيب نانوية من المعادن على أسطح جسيمات أكسيد الخارصين ووجدت الدراسة أن كثافة وحجم هذه التراكيب يتغير بتغير درجات

الحرارة وزمن الترسيب أما جهاز مجهر القوة الذرية فقد أوضحت أن كلا من أكسيد الزنك والتراكيب النانوية على سطحه تكونت بشكل أعمدة نانوية أما جهاز الامتصاص في الضوء المرئي وفوق البنفسجي فقد وضح تغير في قيمة طاقة الفجوة بتغير درجة الحرارة.

الطريقة الثانية التي استخدمت في تعديل سطح أكسيد الخارصين تمثلت في تغيير طبيعة سطح أكسيد الخارصين من خلال أكسدة مادة الخارصين المحضر بجهاز الرش المهبطي عند تراكيز منخفضة جدا للأكسجين ، تم حساب قيمها بناء على قوانين الديناميكا الحرارية. إنّ عملية التحكم بتركيز الأكسجين تمت من خلال التحكم بكمية الهيدروجين وبخار الماء التي يتم إدخالها إلى فرن التسخين. أظهرت نتائج جهاز حيود الأشعة السينية تحول رقائق الخارصين إلى أكسيد الخارصين وذلك بتسخين هذه الرقائق عند درجة حرارة أعلى من 200 درجة مئوية عند تراكيز منخفضة من الأكسجين أما جهاز الماسح الإلكتروني فقد بين وجود فروقات واضحة في الطبيعة الشكلية لأسطح الرقائق التي تم تسخينها.

تم في هذه الدراسة أيضاً استخدام الأغشية الرقيقة المنتجة بالطريقتين أعلاه لصناعة متحسسات غازية ، وتم التركيز في هذه الدراسة على غاز الهيدروجين وغاز ثاني أكسيد النيتروجين وغاز الأمونيا.

نتائج هذه الدراسة أوضحت أن جميع الأغشية الرقيقة المنتجة قادرة على الكشف على غاز الهيدروجين ؛ إلا أن الأغشية الرقيقة لأكسيد الخارصين المعدل سطحه بتراكيب نانوية من مادة البلاتين أظهرت استجابة عالية حتى عند التراكيز المنخفضة جداً (حوالي جزء من بليون جزء) مقارنة بغيرها من الأغشية الرقيقة .

تم في هذه الدراسة أيضاً دراسة تأثير درجة الحرارة في كفاءة تحسس غاز الهيدروجين ، وقد بينت الدراسة وجود علاقة قوية بين كفاءة التحسس ودرجة الحرارة ؛ ففي حين كانت درجة الحرارة الملائمة للكشف عن غاز الهيدروجين لأكسيد الخارصين المعدل سطحه بمادة الفضة و مادة الذهب 400 ° م كانت الحرارة المناسبة لتحسس نفس الغاز لأكسيد الخارصين المعدل بالبلاتين عند 300 ° م.

تم في هذه الدراسة أيضاً دراسة تأثير زمن ترسيب البلاتين على سطح أكسيد الخارصين (سمك طبقة البلاتين على سطح مادة أكسيد الخارصين) ؛ و وجدت الدراسة أن فاعلية الكشف تزداد كلما قل زمن الترسيب تم أيضاً مقارنة تحسس أكسيد الخارصين النقي المحضر بالطريقة الأولى مع أكسيد الخارصين المحضر بالطريقة الثانية ؛ و وجد أن زمن الاستجابة في الحالة الثانية (أكسيد الخارصين المحضر بأكسدة الخارصين في كميات قليلة من الأكسجين) أسرع.

CHAPTER 1

INTRODUCTION

1.1 BACKGROUND

When atoms of any solid material interact to form an element or compound, their energy levels combine to form bands of energy. The band of energy occupied by electrons at absolute zero temperature is called the valence band (VB). On the other hand, the lowest empty energy band is called the conduction band (CB). The energy difference between the bottom of the conduction band (E_c) and the top of the valence band (E_v) is called band gap (E_g). Materials can be classified based on the band gap into three categories (Fig. 1.1): (i) insulators (large gap), (ii) semiconductors (small gap) and (iii) conductors (no gap).

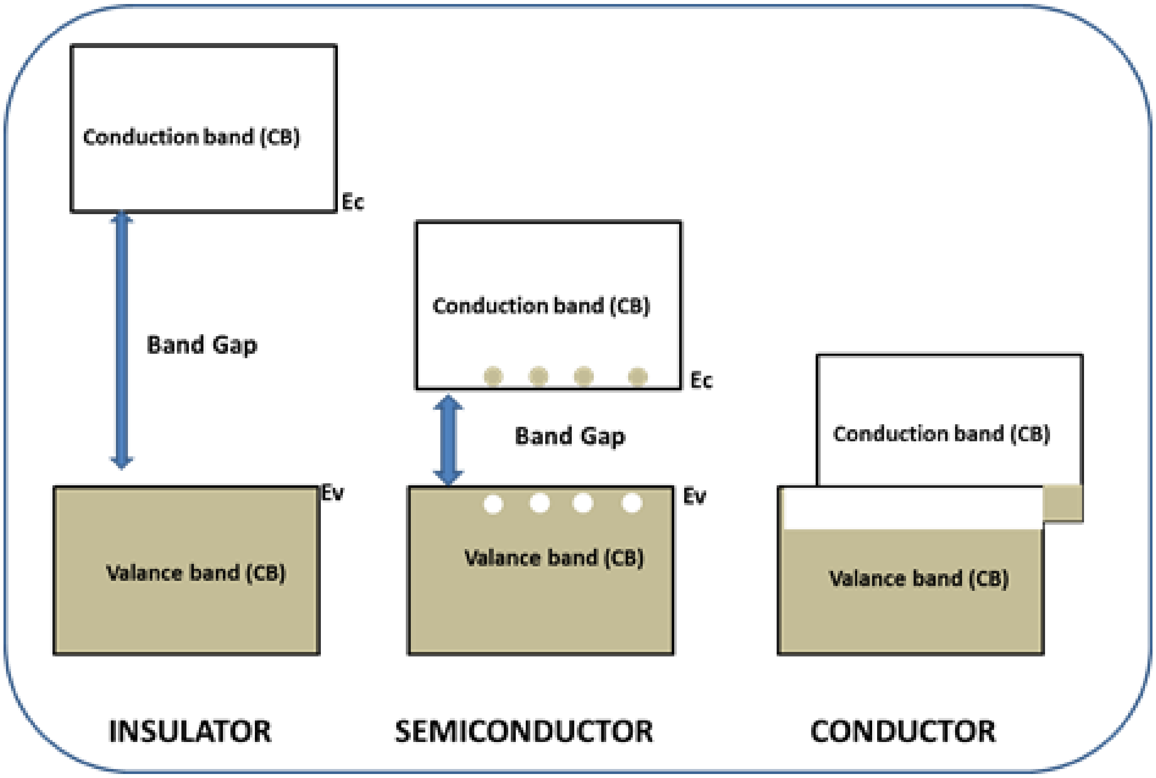

Figure 1.1. Schematic band diagrams for (i) an insulator, (ii) a semiconductor, and (iii) a conductor

Semiconductors are materials having electrical conductivities between those of conductors and insulators. They can be classified into two general groups: elemental semiconductor materials such as Si and Ge and compound semiconductor materials such as GaAs, ZnO and InP. Semiconductors are also classified into two categories: Intrinsic and Extrinsic. Intrinsic semiconductors, sometimes called undoped semiconductors, have equal numbers of negative charge carriers (electrons) and positive charge carriers (holes). Most intrinsic semiconductors are chemically very pure and show poor conductivity [1].

Extrinsic semiconductors, on the other side, are semiconductors with small amounts of impurities added by a process, known as doping, which alters the electrical and optical properties of the semiconductor. Doping semiconductors can be divided into: n-type and p-type. In n-type semiconductors, there are many occupied electron energy levels that can be excited into the conduction band. On the other hand, p-type semiconductors have unoccupied electron levels above the valance band that allow excitation of valence band electrons leaving conducting holes behind [2].

The Fermi energy level for the intrinsic semiconductor is called intrinsic Fermi energy (E_{Fi}) and it is related to the concentration of electrons (n_i) and holes (p_i) in the conduction and valence band respectively by the following formulas:

$$\left.\begin{aligned} n_i &= N_c\, e^{\frac{-(E_c - E_{Fi})}{kT}} \\ p_i &= N_v\, e^{\frac{-(E_{Fi} - E_v)}{kT}} \end{aligned}\right\} \qquad 1.1$$

Where N_c and N_v represent the effective density of states in the conduction and valance band respectively, and given by:

$$\left.\begin{aligned} N_c &= 2\left(\frac{2\pi m_n kT}{h^2}\right)^{3/2} \\ N_v &= 2\left(\frac{2\pi m_p kT}{h^2}\right)^{3/2} \end{aligned}\right\} \qquad 1.2$$

where m_n and m_p are the effective mass of electron and hole respectively. From the above two equations, it can be seen that the E_{Fi} would be exactly in the center of the band gap if $m_n = m_p$ [3]. However, the Fermi energy level of n-type and p-type semiconductors are shifted as presented in Fig. 1.2.

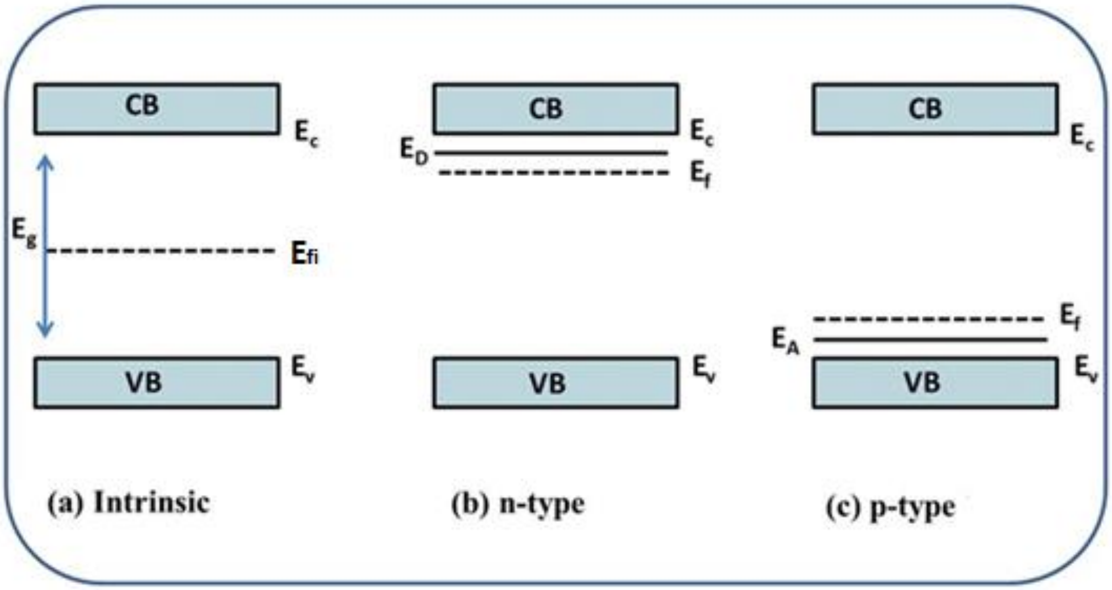

Figure 1.2. Energy band diagram of a) intrinsic b) n-type c) p-type semiconductors

(E_C - E_D) represents the energy necessary to release the electron from the atom (donor) to the conduction band and (E_A – E_V) denotes the energy required to release an electron from the valence band to the atom (acceptor).

It is worth mentioning that the position of the Fermi level also depends on the temperature. The temperature dependence of the Fermi level is given by the following equations:

Intrinsic semiconductor ($n_0 = p_0$)

$$E_F = E_{Fi} = \frac{E_c + E_v}{2} + \frac{3\,k\,T}{4}\ln\left(\frac{m_p}{m_n}\right)$$

n-type semiconductor ($N_D >> N_A$)

$$E_F - E_{Fi} = k\,T\ln\left(\frac{N_D}{n_i}\right)$$

p-type semiconductor ($N_A >> N_D$)

$$E_{Fi} - E_F = k\,T\ln\left(\frac{N_A}{n_i}\right)$$

1.3

The variation of the band gaps of semiconductors with temperature is given by Varshni empirical expression [4]:

$$E_g(T) = E_g(0) - \frac{AT^2}{(T+B)} \qquad 1.4$$

Where $E_g(0)$ is the band gap at zero Kelvin; A and B are constants for a given material. For ZnO, A and B are 3.386 eV, 6 $*10^{-4}$ eV/K, respectively [5].

1.2 ZINC OXIDE (ZnO)

ZnO is an n-type semiconductor with energy band gap (3.17-3.37 eV) [6]. It exists in any of three main crystallographic forms: wurtzite, zincblende and rocksalt. Rocksalt structure is usually obtained at relatively high pressure while zincblende can be stabilized only on cubic substrates. Wurtzite is the stable at near ambient conditions. It crystallizes in hexagonal form with a = 3.249 Å, c = 5.205 Å (Fig. 1.3) [7]. More information about ZnO is also listed in Table 1.1. The binary oxygen-zinc phase diagram is shown in Fig. 1.4. Zinc melts at 420 °C and boils at 1974°C. Sublimation of ZnO is appeared by breakdown:

$$\mathrm{ZnO} \longleftrightarrow \mathrm{Zn\ (gas)} + 0.5\ \mathrm{O_2\ (gas)}$$

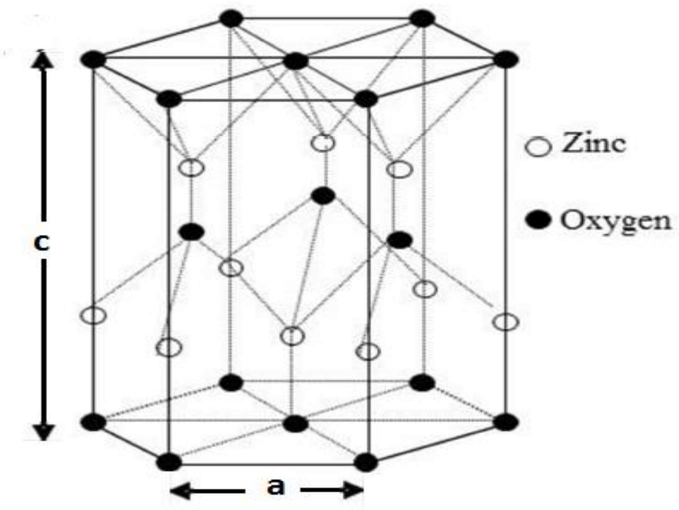

Figure 1.3. Crystal structure of wurtzite ZnO

Table 1.1 Physical properties of ZnO [8].

Properties	**Value**
Density	**5.60 g/cm^3**
Melting point	**2247 K**
Band gap at room temperature	**3.37 eV**
Thermal conductivity	**25 W/m.K at 20 ^{o}C**
Electron effective mass	**0.24 m_e**
Hole effective mass	**0.59 m_e**

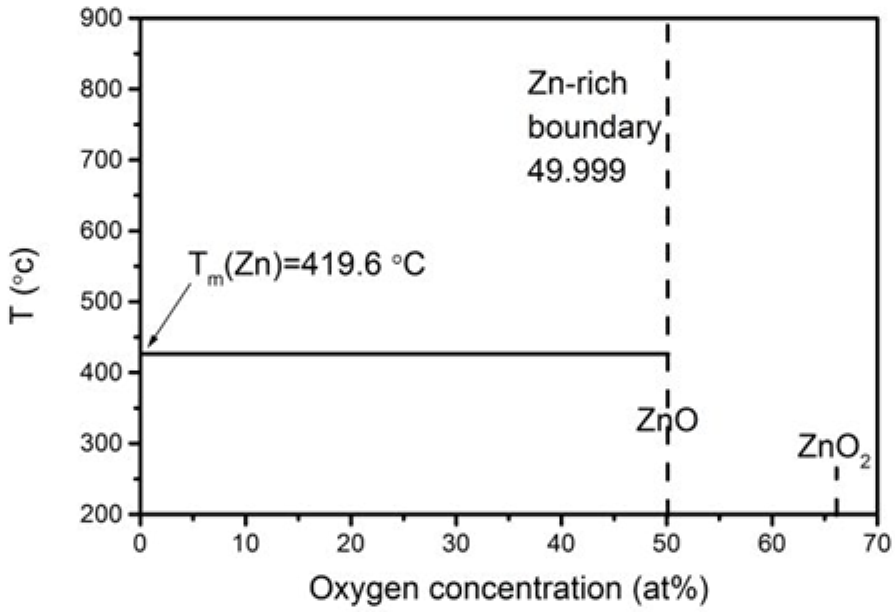

Figure 1.4. Zn-O binary phase diagram (P = 1atm.) [9]

Depending on different parameters such as method of the preparation, doping, and annealing, the conductivity of ZnO ranges from 10^{-17} ohm^{-1} (insulator) to 10^{3} ohm^{-1} (semiconductor) [9].

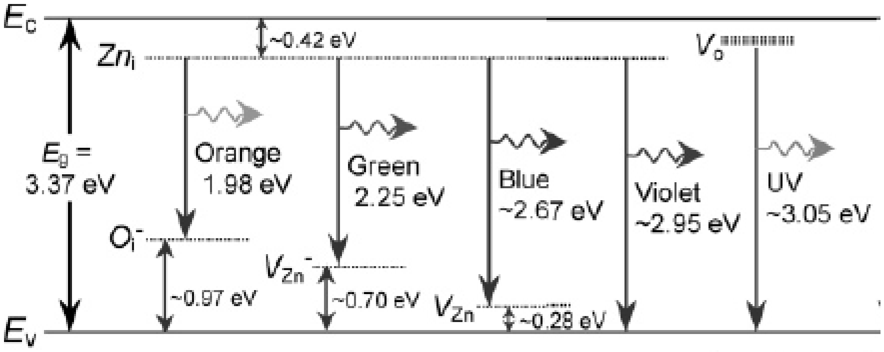

Figure 1.5. Energy level diagram of intrinsic defects in ZnO [8]

It is reported that defects play an important role in the optical properties of ZnO. For instance, Vanheusden et al. [10] found that oxygen vacancies are responsible for the blue/green luminescence in the ZnO. The visible luminescence of ZnO can also be due to certain defects in the ZnO matrix which can trap electrons and radiate photons [11]. Figure 1.5 shows the energy levels created by different native defects. Those energy levels can have different effects on the optical properties of ZnO. Visible photoluminescence in regions of orange, green, blue, and violet is caused by radiative transition emission from deep donor levels of neutral zinc interstitials (Zn_i) to acceptor levels of singly ionized oxygen interstitials (O_i-), singly ionized zinc vacancies (V_{Zn}-), neutral zinc vacancies (V_{Zn}), and valence band, respectively [8].

1.3 ZnO THIN FILMS

Thin films are a thin layers of solid material deposited on a solid support called substrate by controlled condensation of the individual atomic or molecular species [13]. On the other hand, films fabricated by allowing paste or dispersion of the material to dry on a substrate are called thick films [13]. In general, there are three main steps in any thin film fabrication:(i) separation of atomic, molecular and ionic species from target either by heat, electric potential field or laser energy, (ii) transportation of particles to substrate, and (iii) condensation of particles on substrate. The nucleation of thin films can be described by three nucleation modes [13]: (i) island growth (Volmer – Weber), ii) layer-by-layer growth (Frank – van der Merwe), and (iii) Stranski – Krastanov (mixed growth). For the case of Volmer-Weber modes (Fig. 1.6 (a)), condensed atoms are more strongly bound to each other than to the substrate leading to the growth of islands of particles on the surface of the substrate. In the Frank–van der Merwe modes (Fig. 1.6 (b)), condensed atoms are more strongly bound to the substrate than to each other resulting in growth of layers of particles on the surface of the substrate. In the Stranski-Krastanov mode (fig 1.6 (c)), condensed atoms start to grow as a layer by layer up to certain thickness followed by the formation of islands.

Different methods are used to synthesize ZnO thin films; this includes pulsed laser deposition (PLD) [14 -17], chemical vapor deposition (CVD) [18-21] and sputtering [22-34].

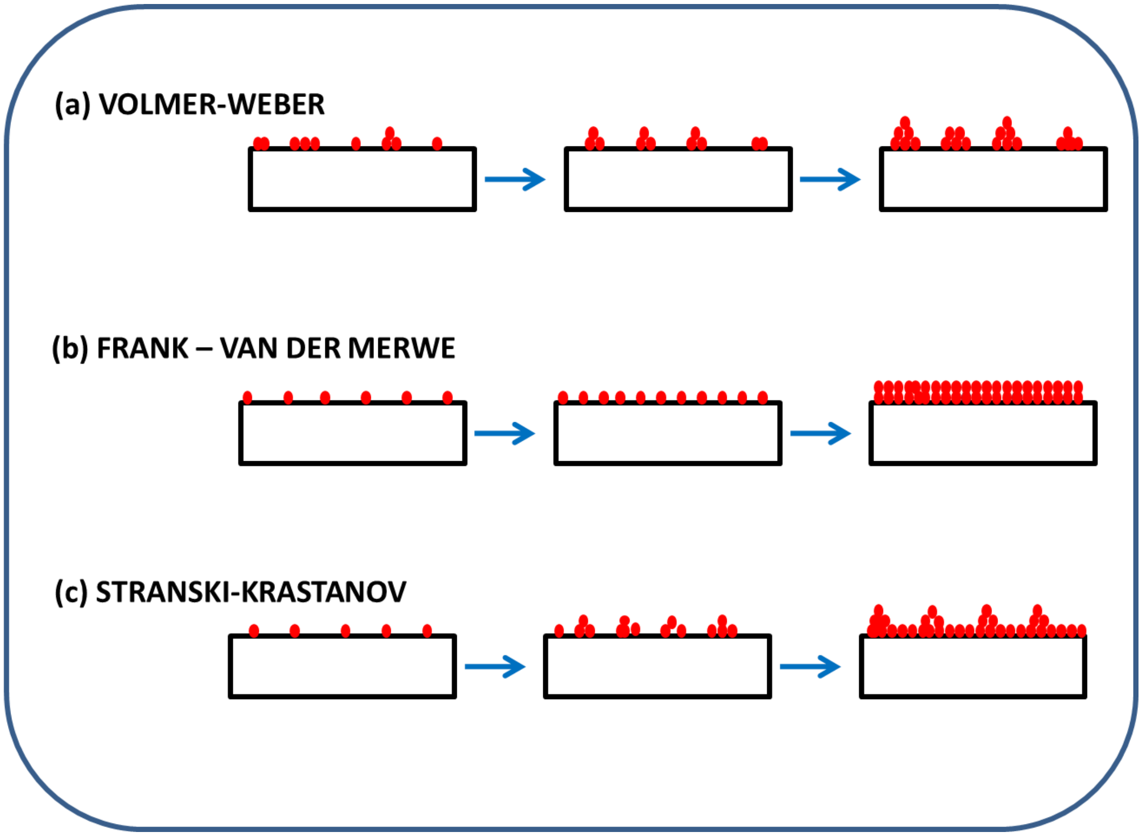

Figure 1.6. A schematic depiction of the nucleation of thin film (a) Volmer-Weber, (b) Frank-Van der Merwe and (c) Stranski-Krastanov

1.4 ZnO THIN FILMS THROUGH SPUTTERING TECHNIQUE

Sputtering is a high vacuum process in which target atoms are ejected from the surface of the target due to bombardment of the surface by energetic particles, and then deposited on a substrate. In sputtering, there are two mains operation modes: DC (direct current) and RF (radio frequency).

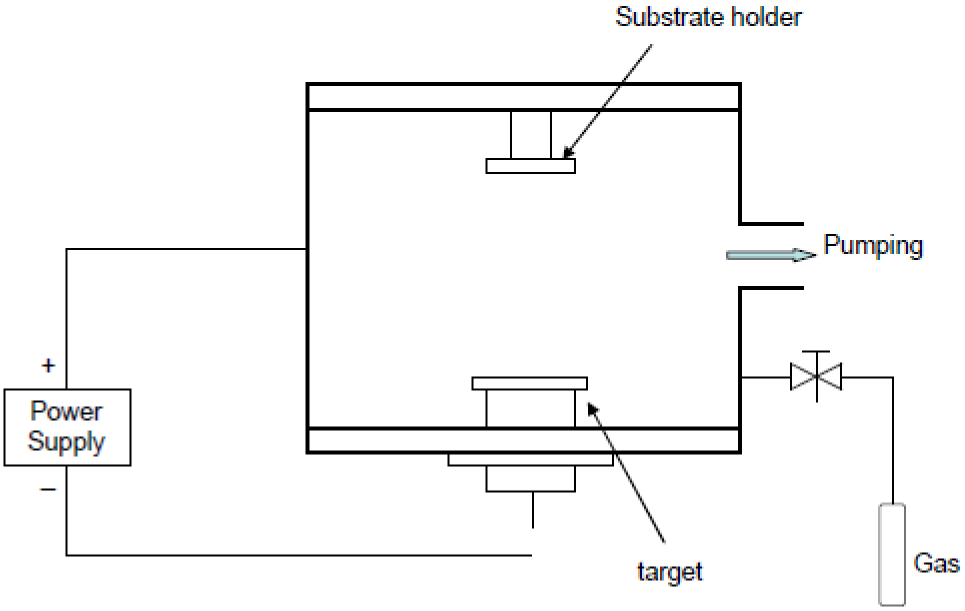

Figure 1.7. A schematic of DC sputtering system

In DC mode, an inert gas such as Ar is used as a working gas. By applying the electrical potential between the cathode (conducting target) and the anode (substrate) in a high vacuum chamber (Fig. 1.7), a few electrons present in the chamber from the background of the chamber are accelerated towards the substrate (anode). The kinetic energy is supplied by the difference in potential between the electrodes. If the accelerated electrons have sufficient energy, they can ionize neutral gas particles (e.g. Ar) through inelastic collisions via the following reaction [35]:

$$e^- + Ar \rightarrow 2e^- + Ar^+$$

The process results in two electrons that can be used to further ionize the gas atoms. The resulting gas ions (Ar+) are accelerated towards the cathode (target) and the energy of the accelerated ions are transferred to the target atoms to break the bonds that hold the atoms in the solid target. These ejected atoms can travel toward the substrate and deposit to form a film [36]. Fig. 1.8 shows the sputtering system (Model: NSC 4000 manufactured by Nanomaster, USA) used for preparing Zn, ZnO and M/ZnO (M= Ag, Au and Pt) thin films that used for gas detection.

Figure 1.8 The DC and RF sputtering machine at CENT- KFUPM

1.5 ZINC OXIDE GAS SENSORS

Gas sensors are devices that detect the presence of gases in the ambient. Gas sensors often act as safety alarms or as process control parameters in industrial applications. Metal oxide-based gas sensors translate the concentration of gaseous chemical species into electrical signals [37]. The variation in the resistance (increase or decrease) of the ZnO sensor depends on the nature of the sensing materials (n-type or p-type) and the type of the gas (oxidizing or reducing). There are many qualities that are used to evaluate the quality of any sensor. These include: selectivity, response, speed of response (response and recovery time), detection limit and stability. Stability of the sensor is the ability to keep its performance steady for a period of time. Response (many references named it sensitivity) of gas sensing, on the other hand, can be defined as [38,39]:

$$\left.\begin{array}{ll} \text{Response (\%)} = \left(\dfrac{R_{air} - R_{gas}}{R_{air}}\right) \times 100 & \text{for reducing gas} \\[2em] \text{Response (\%)} = \left(\dfrac{R_{gas} - R_{air}}{R_{gas}}\right) \times 100 & \text{for oxdizing gas} \end{array}\right\} \qquad 1.5$$

where R_{air} stands for the resistance of gas sensors in air and R_{gas} stands for the resistance of the sensor in target gases. Selectivity is the ability of a sensor to measure a concentration of a gas in presence of other gases. Response time is the time required for reaching 90% of the total resistance change.

Even though the films made with ZnO were one of the earliest materials that showed sensing ability toward oxidizing and reducing gases [40], they suffer from long response recovery time and exhibit low response and prominent cross-selectivity. Several strategies have been employed to enhance their performance including annealing [41-42], doping [43-45], or compositing [46,47]. Recently [48-50], it has been reported that addition of uniformly dispersed metal (such as gold, platinum or palladium) nanoparticles on the ZnO surface was beneficial in enhancing the interaction between the gas of interest and the film surface with adsorbed oxygen.

1.6 IMPORTANCE OF HYDROGEN DETECTION

Hydrogen is colorless, odorless and tasteless. Moreover, H_2 is the lightest gas used extensively in a large number of industrial processes. It is also the fuel of choice for the low temperature proton exchange membrane (PEM) and the solid oxide fuel cells (SOFCs) towards future technology with lower carbon footprints. H_2-based PEMFCs are projected to be used in automobiles for higher efficiency, better mileage and practically no exhaust pollution. In addition, there are already hydrogen filling stations in the US, Europe and Japan for the fuel cell-based buses and cars. However, hydrogen when present in concentrations to 4 vol. % (40, 000 ppm) forms an explosive mixture with air. Thus, it's pronounced volatility and the prospect of easy escape due to leaks lead to the build-up of an explosive mixture with air in confined spaces, such as in automobiles. Thus, there is a genuine need for sensing H_2 at extremely low (~ 1500th of the lower explosive limit) concentrations.

1.7 LITERATURE REVIEW

The first ZnO-based gas sensor was reported in 1962 by Seiyama et al. for the detection of ethanol [40]. This work was based on the variation of electrical properties of the ZnO exposed to reducing gas. This phenomena was reported for the first time by Wanger et al. in 1950 [51]. After that, many kinds of semiconductor oxides were used as gas sensing materials for different gases. For H_2 detection, several types of semiconductors oxides were investigated, including WO_3 [52,53], SnO_2 [54-60], MoO_3 [61,62], Nb_2O_5 [63,64], ZrO_2 [65], In_2O_3 [66,67], TiO_2 [68-69], FeO [70], NiO [71,72], Sb_2O_5 [73]. ZnO in different formats, such as, thick and thin films [74,75], nanowires [76,80], nanorods [81,87], and nanotubes [88,89] were used as hydrogen gas sensor. ZnO thin films were one of the earliest materials that showed sensing ability toward reducing gases such as H_2. Yet they suffer from long response recovery time, and exhibit low response compared with ZnO nanorods and nanowires. In the last few years, scientists have been focusing on improving high performance gas sensors by modifying the surface of ZnO thin films by different methods, including doping or compositing. In the following section, the results of recent published papers related to improving the gas sensing performance toward H_2 by modifying the surface of ZnO thin films will be discussed.

Impurity doping is one of the most efficient methods used for enhanced H_2 sensing. Galstyan et al. [90] doped ZnO with aluminum using high frequency magnetron sputtering and succeeded to produce good response time for hydrogen concentration between 1000 ppm and 5000 ppm (about 200 seconds at 5000 ppm).

K. Vijayalashmi et. al. [91] investigated the effect of magnesium (Mg) doped ZnO thin films. They used spray pyrolysis method to prepare ZnO thin films doped by 1%, 2%, 3%

and 4% of Mg and they measured the resistance change under hydrogen atmosphere at concentration of 100, 200, 300 and 400 ppm. Their results showed that the response and recovery times are improved at 3% Mg concentration.

Y. Liu et al. [92] also prepared Mg doped ZnO thin films fabricated using PLD technique for hydrogen gas detection. Based on their work, Mg doped ZnO thin films showed much higher hydrogen sensing performance compared with the undoped ZnO thin film. For instance, the gas response of doped ZnO thin films was 98 % for 5000 ppm of hydrogen at 300 °C while the response of undoped ZnO thin films at the same conditions was about 60% .

K. Vijayalashmi et al. [4-93] studied the influence of annealing temperature on the properties of ZnO thin films for hydrogen sensing. According to their work, by annealing ZnO thin films at 400 °C properties such as the morphology and crystalline quality improved. In addition, they found that the magnitude of sensor response increased as the crystal size increased which was explained due to the mesoporous size of annealed ZnO thin films. However, increasing saturated at 500 ppm and this saturation was explained by the fact that the gas molecules covered the whole surface of the sample.

The effect of annealing, temperature and electrode structure of ZnO nanorods fabricated by using thermal methods was investigated by Torun and his group [94]. In their work, they showed that annealing ZnO nanorods in air at 200 °C lead to short hydrogen sensor response time compared with as deposited ZnO nanorods. They justified this decreases due to the decreasing oxygen vacancies of the ZnO nanorods by heating in air.

B. Mondal et al. [95] recently prepared ZnO-SnO_2 composite material using a chemical route to be used as hydrogen gas sensor. They used a solution of zinc acetate dehydrate and stannic chloride pentahydrate in polyvinylalcohol to prepare ZnO-SnO_2 composite. Then they studied the effect of annealing on the sensing characteristics. According to their results, ZnO-SnO_2 composite showed higher response compared with pure ZnO and pure SnO_2 due to the formation of ZnO-SnO_2 hetero-junctions.

The effect of the substrate of the sputtered ZnO thin films on the detection of hydrogen gas at room temperature has been reported in the literature [96]. ZnO thin films were deposited by RF-sputtering on two different substrates: polyethylene telephthalate (PET) and quartz. ZnO thin film deposited on the PET substrate showed better sensitively at low temperatures compared with ZnO thin films on quartz that showed no response toward H_2 gas at operation temperatures less than 100 °C.

J. Eriksson and his group [97] compared between the effect of ZnO nanoparticles and polycrystalline ZnO thin films on gas sensing. Based on their work, ZnO nanoparticles show higher response for oxygen gas detection compared with polycrystalline ZnO thin films.

P. Mitra and H.S. Maiti published an article about ZnO thin films sensors [98]. In their work, ZnO thin films were synthesized using dip-coating technique and used as a gas sensor for 3 vol% hydrogen. One of the major results in this work was that the hydrogen has poor recovery time when it was mixed with air comparing with hydrogen mixed in nitrogen.

1.8 THESIS OBJECTIVES

There are four main objectives to this dissertation:

1) Modify the surface of sputtered ZnO thin film via incorporating nanostructures of (Ag, Pt, Au).
2) Control the oxidation of Zn thin films in H_2/H_2O mixture.
3) Investigate the optical, electrical, morphological and compositional properties using different techniques.
4) Test the prepared thin films for hydrogen sensing.

These objectives were achieved by carrying out the following tasks:

Task 1 Modify the surface of sputtered ZnO thin film by incorporating nanostructures of (Ag, Pt, Au).

- Synthesis of pure ZnO thin films using DC reactive sputtering.
- Synthesis of thin layer of metals using DC sputtering on the ZnO thin films (M/ZnO) M= Ag, Au and Pt.
- Transform the metal layer to nanostructures by post annealing of (M/ZnO) thin films at different temperatures in different atmospheres.
- Control the density and the size of the metal nanostructures by varying the deposition time and the temperature.

Task 2 Controlled oxidation of Zn thin films in H_2/H_2O mixture.

- Synthesis of pure Zn thin films using DC sputtering.

- Built a set-up for establishing the desired partial pressure of oxygen (PO_2).
- Investigate the effect of changingP_{O2}on the properties of ZnO thin film that oxidized in H_2/H_2O mixture.
- Investigate the effect of annealing temperature on the properties of ZnO thin film oxidized by annealing Zn thin film in H_2/H_2O mixture.

Task 3 Investigate the optical, electrical, morphological and compositional properties using different techniques.

The films fabricated in task 1 and 2 will be characterized by:

- X-ray diffraction (XRD).
- X-ray Photoelectron Spectroscopy (XPS).
- Field Emission Scanning Electron Microscope (FE-SEM).
- Atomic Force Microscope (AFM).
- UV-Vis Spectroscopy.

Task 4 Test the prepared thin films for hydrogen sensing.

- Evaluate the gas response and response time performance for the detection of hydrogen for different modified sensors.
- Test the selectivity of the prepared sensors by comparing the response of the sensor toward H_2 with the response toward another reducing gas such as ammonia (NH_3) and oxidizing gas such as nitrogen dioxide (NO_2).

- Explain the gas sensor behavior through a proposed physical mechanism.

1.9 THESIS ORGANIZATION

This thesis is organized as follows. In chapter one, the background to the thesis has been introduced. This background includes general information about semiconductors, thin films, zinc oxide, sputtering technique and gas sensing. In addition, a review in the scientific literature of the ZnO-based thin films for detecting hydrogen is reported. In chapter two, the techniques used to conduct the fabricated thin films are described. In chapter three, we introduce a simple method for modifying the surface of sputtered ZnO by three different metals (Ag, Au, Pt). We also present results which show the optical, compositional and structural properties of the prepared films. In chapter four, we investigate the effect of changing PO_2 and annealing temperature on the properties of ZnO thin film oxidized in H_2/H_2O mixture. In chapter five, the performance of pure ZnO and M/ZnO (M = Ag, Au or Pt) thin films fabricated by DC reactive sputtering and oxidized in air or H_2/H_2O mixtures toward H_2, NH_3 and NO_2 gas sensing is studied. In chapter six, we conclude the thesis.

CHAPTER 2

THIN FILM CHARACTERIZATION TECHNIQUES

This chapter will describe the characterization techniques used to conduct the research presented in this dissertation. A variety of analysis techniques were applied for the characterization of thin films including XRD, FE-SEM, XPS, AFM and UV-Vis.

2.1 X-RAY DIFFRACTION (XRD)

XRD is a technique used for investigating crystalline structure of solids including determination of crystallinity, crystallite size (grain size), and orientation of single crystals. It is also commonly used for the determination of the lattice constants of the crystal. The basic principle of XRD depends on the interaction between the incident monochromatic X-rays with the electrons in the atoms of the material being tested. If the incident X-ray waves (with wavelength λ) diffracted from the sample are in phase, they interfere in a constructively and the X-ray detector registers large counts. This happens when the Bragg condition is satisfied, namely,

$$n\lambda = 2d\sin\theta \qquad 2.1$$

where θ is Bragg's angle, n is the order of diffracted beam and d is the atomic plane spacing (Fig. 2.1).

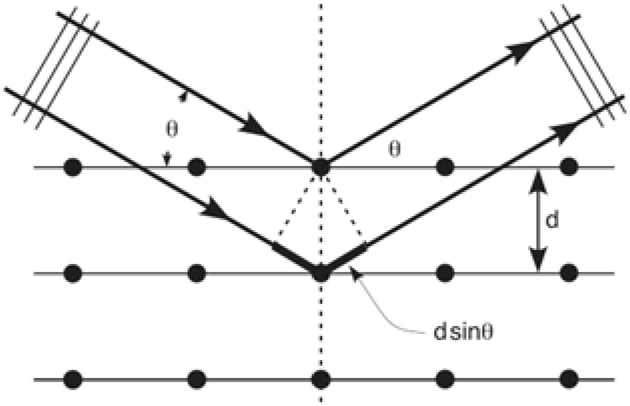

Figure 2.1. A schematic of diffraction of x-rays by a crystal

XRD peaks are often sharp. Yet, broadening of these peaks is caused due to different reasons. These include [99]:

1. The size of the crystallites.
2. Instrumental factors.
3. Variation in sample strain.

The theory and the information that can be extracted from the X-ray diffraction peak broadening will be discussed in details in the following sections.

The crystal size can be calculated using the well-known equation called Scherrer equation. This formula can be derived as follows: Starting with Bragg's law in equation 2.1 and by multiplying both sides of the equation by an integer m such that m×d = t, the thickness of the crystal. At n=1, this leads to:

$$m\lambda = 2t\ \sin\theta \qquad 2.2$$

By differentiating both sides of equation (2.2):

$$0 = 2\Delta t \sin\theta + 2t\cos\theta\ \Delta\theta \qquad 2.3$$

Since we are only interested in positive $\Delta\theta$ so.

$$t = \frac{\Delta t \sin\theta}{\cos\theta\,\Delta\theta} \qquad 2.4$$

Since d is the smallest increment in t, we can write ∆t = d, and substituting λ\2 for sinθ (from Bragg’s law):

$$t = \frac{\lambda}{2\cos\theta\,\Delta\theta} \qquad 2.5$$

Substituting β for, the angular width2∆θ, equation 2.5 becomes:

$$t = \frac{\lambda}{\beta\cos\theta} \qquad 2.6$$

Which is the Scherrer’s equation.

A more sophisticated analysis [100] adds a factor (0.9) to the right hand side of equation (2.6) which leads to the corrected Scherrer’s equation:

$$t = \frac{0.9\lambda}{\beta\cos\theta} \qquad 2.7$$

Due to the simplicity of this technique to estimate the average grain size, there are many references that use this formula in metals, metal oxides and composites. It is important to realize, however, that the Scherrer formula provides only an approximate value of the average grain size of the crystalline materials.

XRD spectra are used to analyze strain in the crystallites. Basically, there are two types of stress in materials: compressive and tensile stress, and if the crystallite is strained then the “d spacing” changes according to the type of the stress. A compressive stress would make the “d spacing” smaller whereas a tensile stress would make the “d spacing” larger. The strain (ε) in materials can be estimated by differentiating Bragg's Law and relating the strain to the differential δd/d. It turns out that the angular width is related to the strain by [101]:

$$\beta = 4\ \varepsilon \tan\theta$$

Since the crystallites constituting the sample usually do not have the same shape and size, Williamson and Hall [101,102] combined the Scherrer equation with the strain effect through the following relation:

$$\beta = \frac{k\lambda}{t\cos\theta} + 4\varepsilon\tan\theta \qquad 2.8$$

By rearranging equation (2.8):

$$\beta\ \cos\ \theta = \frac{k\,\lambda}{t} + 4\,\varepsilon\ \sin\theta \qquad 2.9$$

A plot of $\beta \cos \theta$ along the y-axis vs. $\sin \theta$ along x-axis, one can estimate the grain size from the y-intercept and the strain ε from the slope.

In this work, an XRD (Shimadzu 6000) with Cu K_α irradiation at $\lambda = 1.5406\ A^0$ located in the KFUPM Physics department was used to determine crystalline phase, average crystallites size, and strain.

2.2 X-RAY PHOTOELECTRON SPECTROSCOPY (XPS)

XPS is an analytical technique that provides the elemental composition and chemical state of the sample elements that exist beyond H and He. A typical XPS system consists of the following (see Fig. 2.2): a monochromatic X-ray source, an electron energy analyzer and an ultra-high vacuum chamber. XPS is based on the ejection of an electron from a core level by the X-ray photon of energy hv. The electron energy is then analyzed by the electron spectrometer, and the results are shown usually as a graph of electron intensity against the binding energy BE of the ejected electrons. The kinetic energy E_K of the electron is the experimental property measured by the spectrometer but it is related to binding energy BE, which has characteristic values for each atom through the Einstein equation:

$$BE = hv + E_k \qquad 2.10$$

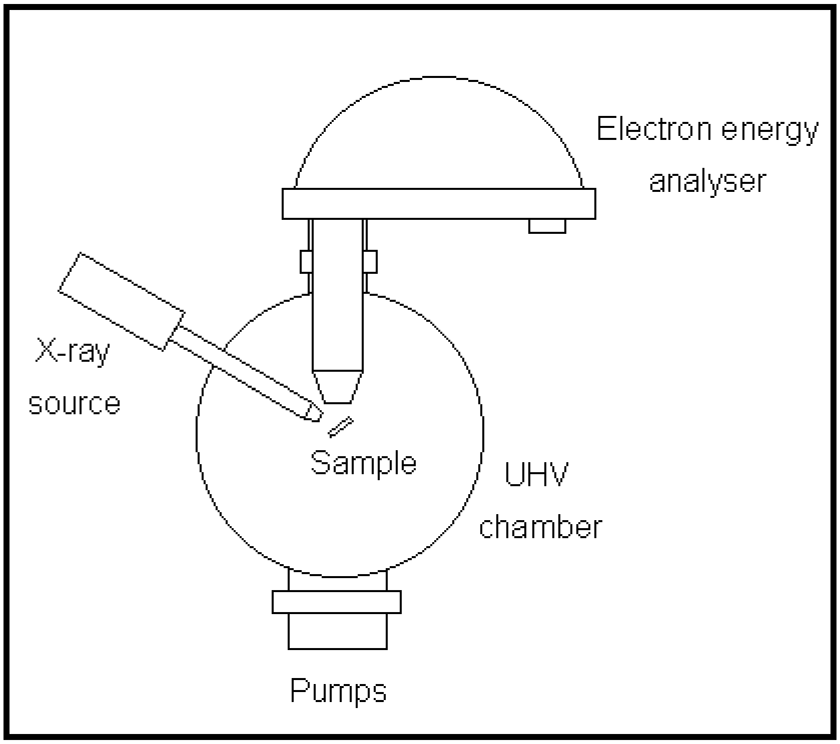

Figure 2.2. Schematic illustration of XPS main components

An XPS spectrum can have five types of peaks [103]:

1- Photo-emission from the core electron levels: this kind of peak appears when the sample is exposed to an X ray leading to removed electrons (called photoelectron) from the core levels. The energies of the emitted photoelectrons are characteristic of their original electronic states. The intensities of these peaks are proportional to the number of atoms exposed to the X-rays.

2-Auger emission can be considered as a result of involving three basic steps: in the first step electron remove electron from the core level (inner shell) of atoms leading the atom to become ionized. In the second step, the atom will quickly return to its normal state after refilling the inner electron vacancy with an outer shell electron. In the last step, Auger electron, or X-ray, will be emitted with an energy equal to the difference between the outer shell electron and the inner shell.

3-Shake-up satellite is a ghost peak that occurs from interaction between a photoelectron and a valence electron and no useful information can be obtained from this kind of peaks.

4-Multiplet splitting peaks occur in a compound that have unfilled atomic shells containing unpaired electrons. These kinds of peaks are useful for chemical analysis to distinguish between compounds. For example, one can differentiate between $Ni(OH)_2$ and NiO where $2P_{3/2}$ in NiO has multiplet splitting peak whereas $Ni(OH)_2$ does not.

5- Plasmon loss occurs when some of the energy of a photoelectron is lost due to the collective oscillations of conduction electrons in the metal sample. No useful information can be obtained from this kind of peak.

In our work, an XPS Model ESCALAB 250 Xi from Thermo Scientific having energy resolution of ±0.1 eV equipped with Al-Kα monochromatic X-ray radiation located in Physics department was used to study the elemental composition and the composition variation of the surface layer with thickness of the prepared thin films.

2.3 UV-VIS SPECTROSCOPY

UV-Vis absorption spectroscopy is a technique that is used to measure the optical properties (absorption, transmission, reflection) of different solid and liquid materials in the near infra-red, visible and near ultra violet region. Typically, an UV-Vis spectrometer consists of a source of light, sample holder, reference cell and detector.

The optical absorption for direct band gap semiconductor thin films is given by [104,106]:

$$\alpha hv = (hv - Eg)^{1/2} \qquad 2.11$$

Where α = absorption coefficient and E_g = optical band gap energy in eV.

The absorption coefficient (α) is calculated by [107,108]

$$\alpha = -\ln T/d \qquad 2.12$$

Where T and d are the transmittance and the film thickness respectively.

Band gap of the films can be calculated using equation 2.11 and 2.12 by the linear extrapolation of the plot of $(\alpha hv)^2$ versus hv to the energy axis.

In the present work, UV-Vis spectra were obtained using a double beam scanning spectrometer (Model JASCO V-570).

2.4 FIELD EMISSION SCANNING ELECTRON MICROSCOPE (FE-SEM)

FE-SEM is one of the advanced techniques that can be utilized for inspecting tiny structures on the surface of a solid and provides an idea about the local composition on the surface of the sample. The main idea of FE-SEM technique is that electrons are liberated from a filament placed in a high electrical potential gradient and then these electrons applied to scan the sample of interest. Compared to scanning electron microscopy (SEM) in which the electrons are thermally emitted by applying an electrical current, the electrons are generated in FE-SEM by exploiting a field emission gun. This most increases the density of generated electrons and provides better resolution image than SEM.

The main components of the FE-SEM including an electron emission source, condenser lens, scan coils, objective lens, sharp tungsten tip, an appropriate detector (scintillator) and photomultiplier tube. The electrons are ejected by applying a potential to an anode. The electrons are ejected and accelerated to higher energy by applying a high potential to the second anode. Better resolution is achieved by controlling the diameter of the released electrons using a condenser lens that generate narrow beams. The narrow beam of electrons is then focused over the sample by scan coils and objective lenses. As the electron beam bombards the surface of the sample, electrons are emitted off the sample and are directed to a scintillator. Then, the scintillator generates photons in response to these incident electrons. These photons are then amplified and detected by a photomultiplier to give signals. Various signals such as secondary electrons (SE), backscattered electrons (BSE) and X-ray are generated during the interaction between the incident electron beam and the sample surface. SEs are generated when the primary electrons collide with atoms in the sample inelastically, causing the specimen atom to ionize [109]. In BSE, the primary electrons hit the specimen atom and then directly backscattered to the detector. If there is more than one element in the sample, the element that have larger nucleus (high Z number) will appear brighter than those have lighter nucleus (small Z number).

Energy dispersive X-ray (EDX) scan are conducted with FE-SEM to identify and quantify the elemental composition of materials. Usually, the energy of the primary beam used for EDX analysis is in the range of 10- 20 keV. This energy causes characteristic X-ray to be emitted from the material. An energy dispersive detector is to separate the generated X-rays of different elements into an energy spectrum. FE-SEM (Tescan Lyra 3, Czech Republic) located in the KFUPM Imaging Lab CENT was used to examine the morphological features of the films while EDX was used to study the elemental composition of the films.

2.5 ATOMIC FORCE MICROSCOPE (AFM)

Atomic Force Microscopy (AFM) is one of the family of scanning probe microscopes (SPM) that provides information about the topography of the surface of thin films at the nanometeric scale. The basic laboratory setup for an AFM (Fig. 2.3) includes: a sharp tip, cantilever, laser, photodiode, electronics feedback and a piezoelectric motor.

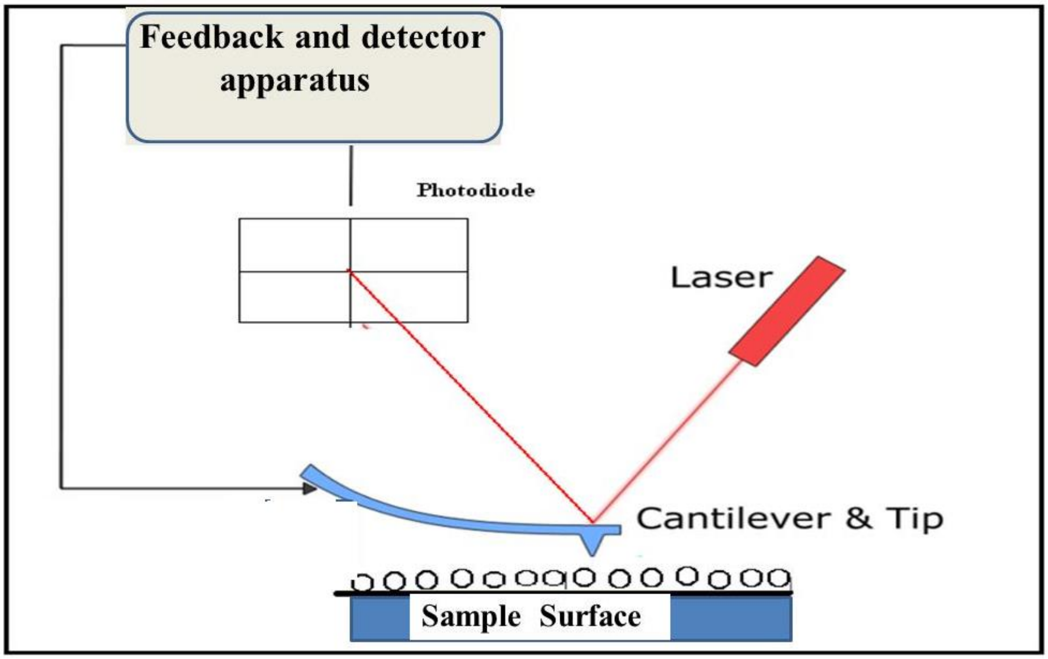

Figure 2.3. Basic principle of AFM technique

The basic principle of AFM depends on the interatomic force between a tip and surface. As the tip scans the surface of the sample, moving up and down due to surface morphology, the force between the tip and sample causes the cantilever to twist. A laser beam, which focuses onto the back side of the reflective cantilever, reflects off the cantilever surface to a photodiode screen. The photodiodes are position-sensitive and can discern, from the reflected laser beam, up-and-down motion confirming the topographic sample variations that are recorded on a computer as a function of x-y on a tip location on the sample. In one configuration, a feedback circuit is used to adjust the tip-to-sample distance to maintain a constant force between the tip and the sample.

Depending on the application of the AFM, it can be operated in a number of modes. Three modes are common: contact modes, non-contact mode and tapping mode. In contact mode, or sometimes called static mode, the tip of the cantilever is kept in constant contact with the sample surface. As the sample is scanned, the contact force bends the cantilever responding to the changes in the topography of the surface [110]. This mode is usually used for imaging a hard and relatively flat surface with high resolution and high scan speed. There are two main disadvantages for this mode. First, due to the direct contact between the sample and the tip, the sample may damage the tip or the tip may damage the sample [110]. Second, there is interaction of the cantilever tip with a layer of water vapour and other contaminants that might generate unwanted adhesive force [111].

In non-contact modes the tip does not touch the surface. Instead, it oscillates above the sample surface. The topographic image is constructed according to the van der Waals forces acting between the tip and the surface of the sample. However, this force is extremely small. To overcome this difficulty, a small oscillation is given to the cantilever tip to sense the small forces between the tip and the sample surface by measuring the change in amplitude of the oscillation [112]. An advantage of non-contact mode is that the surfaces of very soft samples can be measured without damage. The drawback of this mode is that the scan speed is usually relatively slow.

In tapping mode, the cantilever with attached tip is oscillated at its resonant frequency and scanned across the sample surface. In this mode, the tip hits the surface of the sample in a short time to minimize unwanted forces. This mode is also less destructive than contact mode. However, the scan speed of this mode is slightly slower than contact mode. In this study, the surface roughness and morphology were evaluated by KFUPM Mechanical Engineering department AFM (Bruker Dimension icon Scan Asyst, USA).

CHAPTER 3

SYNTHESIS AND CHARACTERIZATION OF ZnO THIN FILMS MODIFIED BY (Ag, Au and Pt) NANOSTRUCTURES

Researches around the world try to modify surfaces of thin films by dispersing small quantities of noble metals on cheaper materials (like metal oxide) to enhance the materials properties [113-116]. In this chapter, we introduce a new method for modifying the surface of sputtered ZnO thin films by metal nanostructures; namely, Ag, Pt and Au. This method is shown to provide pure, carbon contamination-free and inexpensive that have potential to improve material characteristics in applications like gas sensing, solar cells and possibly catalysis or otherwise. We find that thin layer of Ag, Pt and Au deposited on the ZnO layer can be converted to nanostructures by post annealing at appropriate temperatures. In addition, we show that the size and density of the metal nanostructures (number of particles per unit area) can be controlled by means of deposition power, deposition time and post annealing parameters.

3.1 SYNTHESIS AND CHARACTERIZATION OF Ag NANOSTRUCTURES MODIFIED SPUTTERED ZnO THIN FILMS

Metal nanoparticles exhibit exciting properties strongly dependent on their size, shape and inherent electrons distribution with reference to those of their macro-scaled counterparts [117]. Amongst them Ag nanoparticles have attracted huge interest because of their unique physical, chemical and biological properties [118-121]. Many synthesis methods are reported using chemical, physical and photochemical routes. Every route carries some pros and cons costs, uniformity, scalability, purity, etc [122-130].

In the following sections, we will explain the experimental work used to synthesize thin layer of silver on ZnO thin films (AgatZnO) using DC sputtering. Then, we will show the effect of post annealing, deposition time and annealing atmosphere on the physical properties of AgatZnO thin films.

3.1.1 EXPERIMENTAL WORK

For the synthesis of (AgatZnO) thin films using DC sputtering, high purity zinc (99.999 %) and silver (99.99%) targets (from Semiconductor wafer Inc) were used. The substrates were sonicated in acetone or methanol for 15 min. prior to sputtering. The zinc and silver targets were cleaned by pre-sputtering a blank for 3 and 1 min., respectively. The base pressure in the sputtering chamber was less than 4×10^{-6} Torr and the working pressure was set to 7×10^{-3} Torr by adjusting the O_2 and Ar gas flow. The target-substrate distance was fixed at 10 cm. The deposition of AgatZnO thin films was carried out in two steps. First, ZnO thin films were deposited on glass substrates for 40 minutes at 100 watt power using DC reactive sputtering. In the second step, Ag was sputtered using Ar plasma for 25 seconds at 20 watt. Identical samples were annealed at 200ºC, 400ºC and 600 ºC. This yielded films with different nanostructured morphology of the deposited Ag particles on ZnO thin films (AgNPsatZnO). The sequential film fabrication stages are shown in Fig. 3.1.

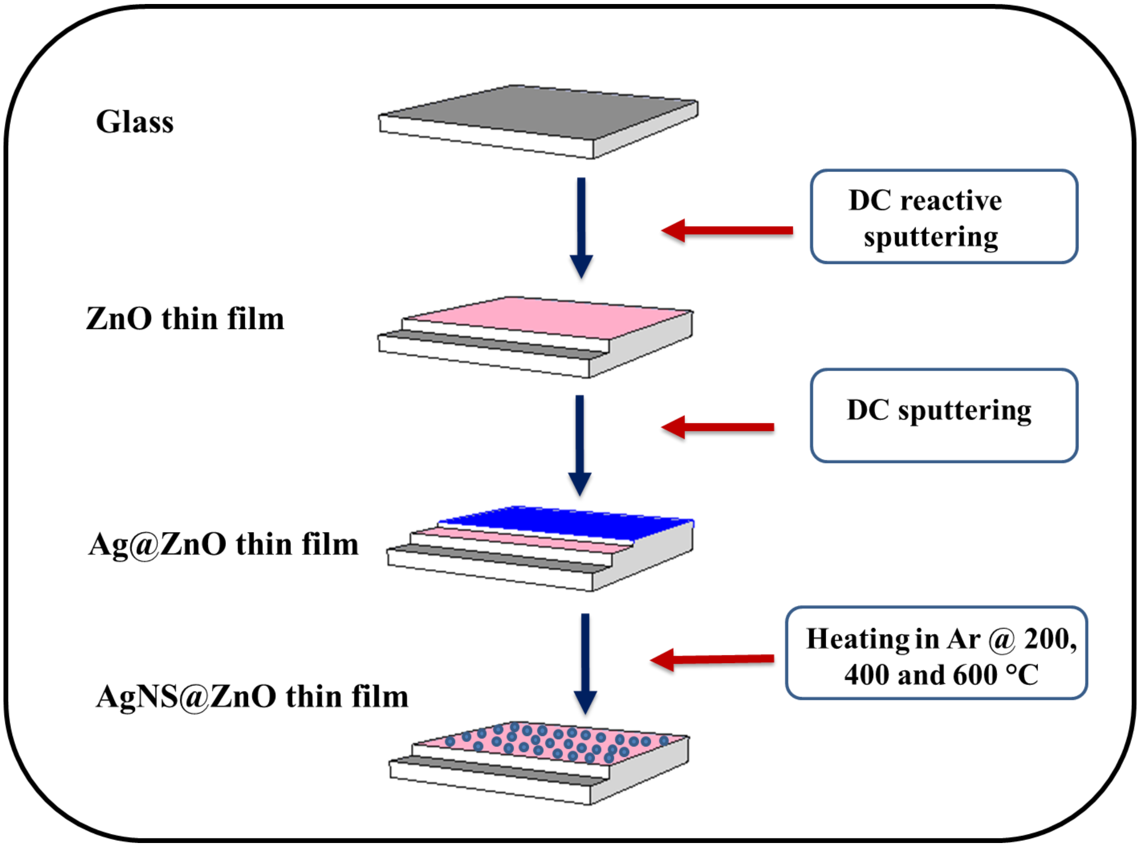

Figure 3.1. A schematic of the steps involved in the fabrication of AgNPs/ZnO films

3.1.2 XPS DEPTH PROFILING OF THE AS DEPOSITED Ag at ZnO

The XPS depth profiling of as deposited Ag at ZnO was used to discern the compositional uniformity across the exposed surface of the film. The surface was systematically and sequentially etched by a low energy (~2 keV) Ar ion gun for 8s, prior to collecting the XPS spectra at that depth. Figure 3.2 shows the variation of the as deposited Ag at ZnO thin films at twelve depths from the exposed film surface. All measurements with XPS were done under ~1x10^{-9} Torr pressure and the scales of all peaks positions were calibrated by fixing the binding energy of the C1s at 284.60 eV. The variation of the Ag3d concentration versus etching time for twelve levels of etching showed that the Ag concentration declined with depth and becoming negligible after 24 s etching indicating the formation of thin layer of silver. However, the silver almost vanishes after 32 s etching time. It can be seen that the silver diffuses up to 56 s which might be leading to the doping of the top layer in ZnO thin film. In contrast, the Zn and O concentrations increased steadily and became steady beyond the depth corresponding to 30s of etching. In addition, we found that the photoelectron binding energy peak position of Ag shifted (fig 3.3) after the first etching. This might be due to the effect of ion sputtering on the lattice.

(a) Ag3d Scan

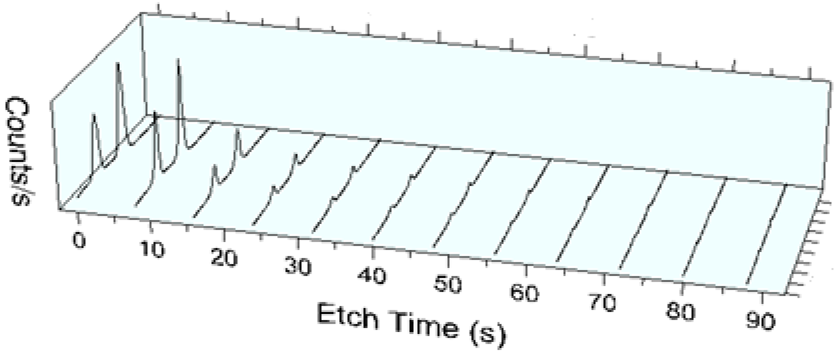

(b) O1s Scan

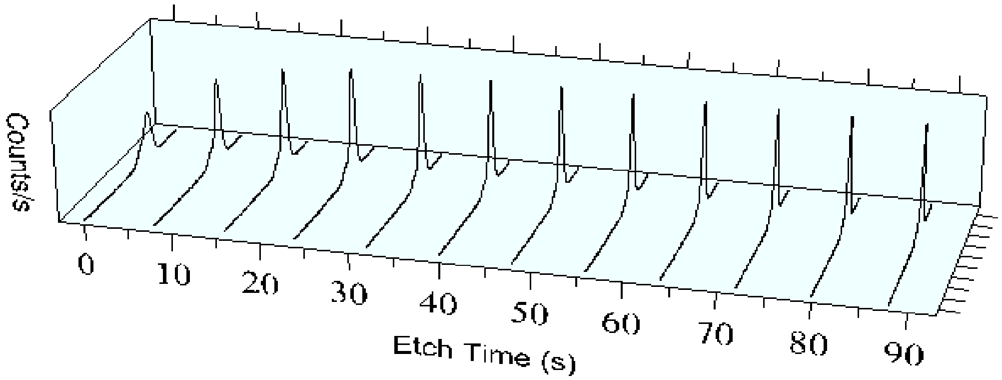

(c) Zn2p Scan

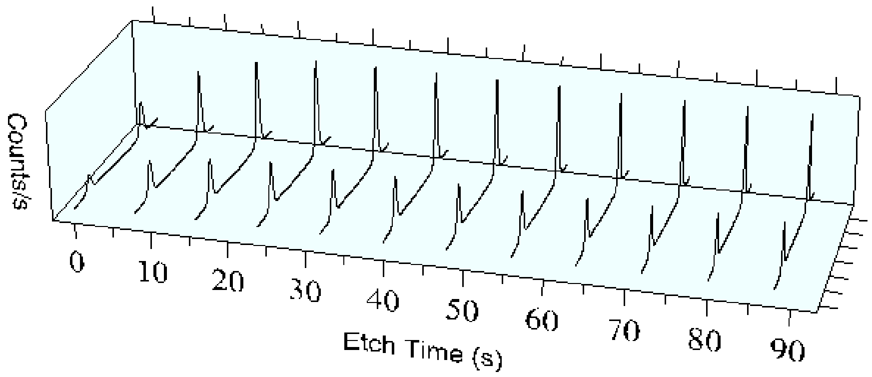

Figure 3.2. XPS depth profiling of (a) Ag3d, (b) O1s, and (c) Zn2p of the Ag at ZnO thin film

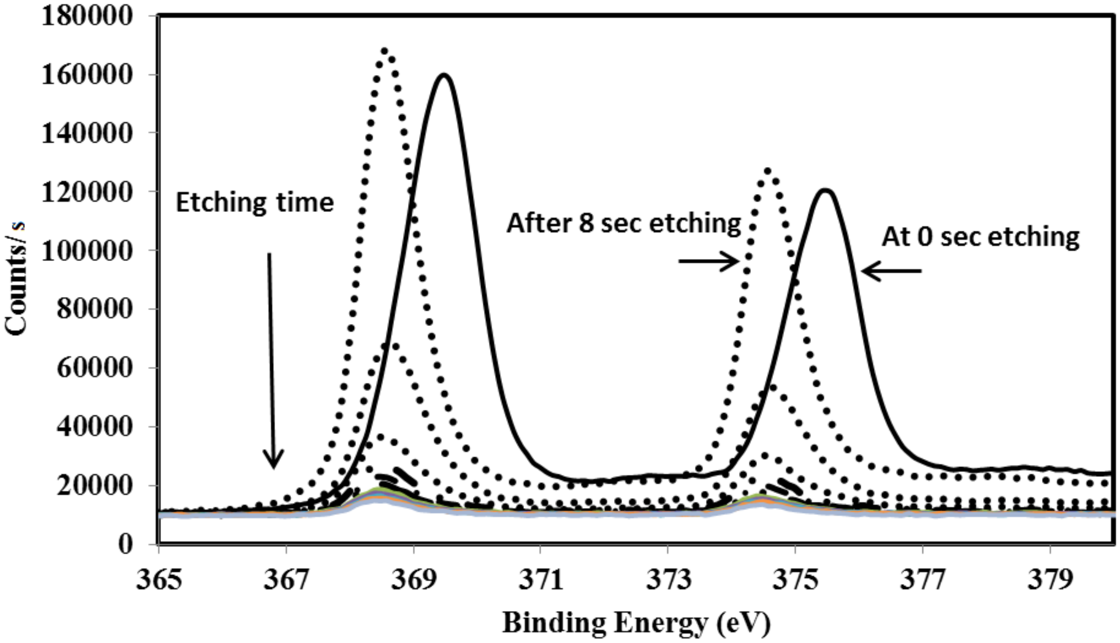

Figure 3.3. XPS depth profiling of Ag3d of the as prepared Ag/ZnO thin film

Figure 3.4 shows the concentration profiles (at.%) for Ag 3d, C1s, O1s and Zn2p at twelve depths from the exposed film surface. The variation of O1s and Zn2p core levels with the etching time shows more oxygen and less zinc at the surface and this is due to the adsorbed oxygen at the surface. After cleaning the surface, the Zn and O in the film are uniformly distributed. The XPS depth profile of C1s showed the vanishing of the carbon peak after the first 8 s. In addition, at the surface of the Ag at ZnO thin film an amount of about 25% of carbon is recorded. This presence of carbon is due to the occasional carbon contamination which we cannot avoid.

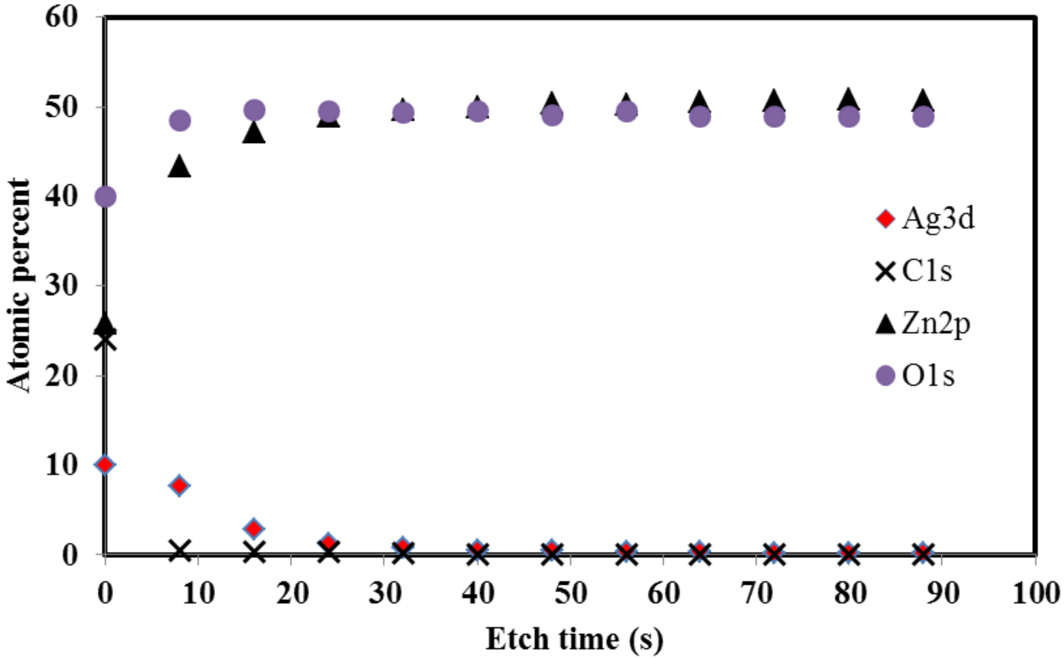

Figure 3.4. XPS depth profile of the Ag at ZnO thin film as a function of etching time

3.1.3 EFFECT OF POST ANNEALING ON THE PROPERTIES OF Ag/ZnO THIN FILM

The effect of the post annealing of the Ag at ZnO thin films on the structural, morphological and optical properties was investigated. Morphological observations were carried out using FE-SEM before and after annealing. Figure 3.5 shows FE-SEM images before and after thermal treatment at T = 200, 400 and 600 ^{o}C. The surface of as prepared sample (RT=27 °C) was smooth and uniform and showed no aggregation of silver particles (Fig. 3.5 (a)). Samples annealed at 200 °C showed similar smooth surfaces (Fig. 3.5 (b)). After 4 hours of annealing at 400 °C, silver islands of about 50 to 100 nm sizes were observed (Fig.3.5 (c)). As the annealing temperature was increased to 600 °C a random distribution of bright, round shape silver particles separated by an average distance of few hundreds nanometers were observed.

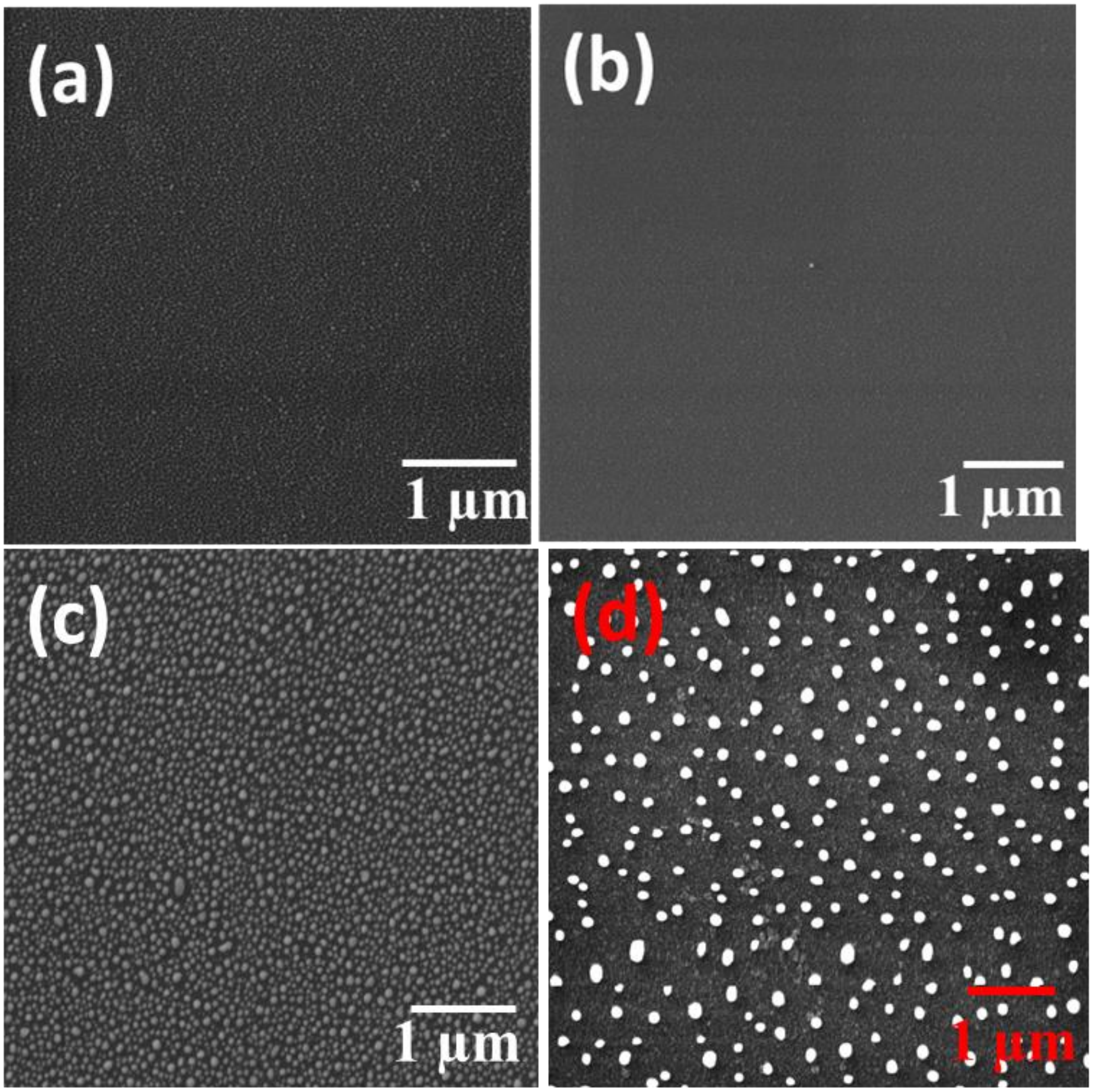

Figure 3.5. FE-SEM images of Ag/ZnO thin films annealed at (a) RT, (b) 200 °C, (c) 400 °C and (d) 600 °C

By further increasing of the annealing temperature to 700 ºC, one can see (Fig. 3.6 (a and b)) that the particle size increases and the density of the particles decrease. We observed the presence of a smaller density of larger spherical particles of about 350 nm diameter separated by an average distance of about 1.5 micron surrounded by much smaller nanostructures of about 50 nm diameter or less. These observations suggest the growth of the nanoparticles through Ostwald ripening mechanism [19] which explains the increase of the large islands at the expense of the small ones. Fig. 3.7 shows a uniform dispersion of Ag NPs over a large surface area . This is an interesting result as it shows that we have at hand a simple technique to grow uniform Ag nanostructures of controlled dimensions and separation on ZnO substrates which can find applications not only in chemical gas sensors but also in solar cells (plasmonic cells), catalysis, etc.

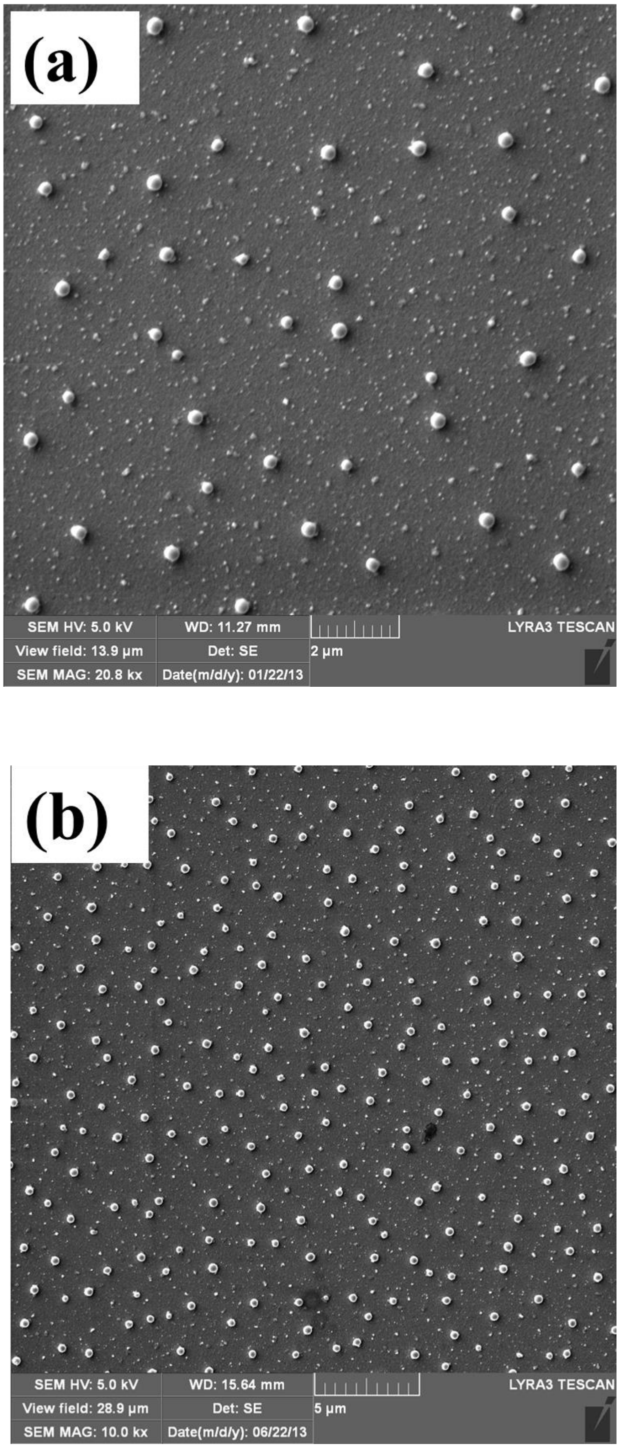

Figure 3.6. FE-SEM micrographs of Ag nanostructures on ZnO prepared by post annealing at 700 °C in Ar atmosphere (a) 20.8 kx magnification, (b) 10 kx magnification

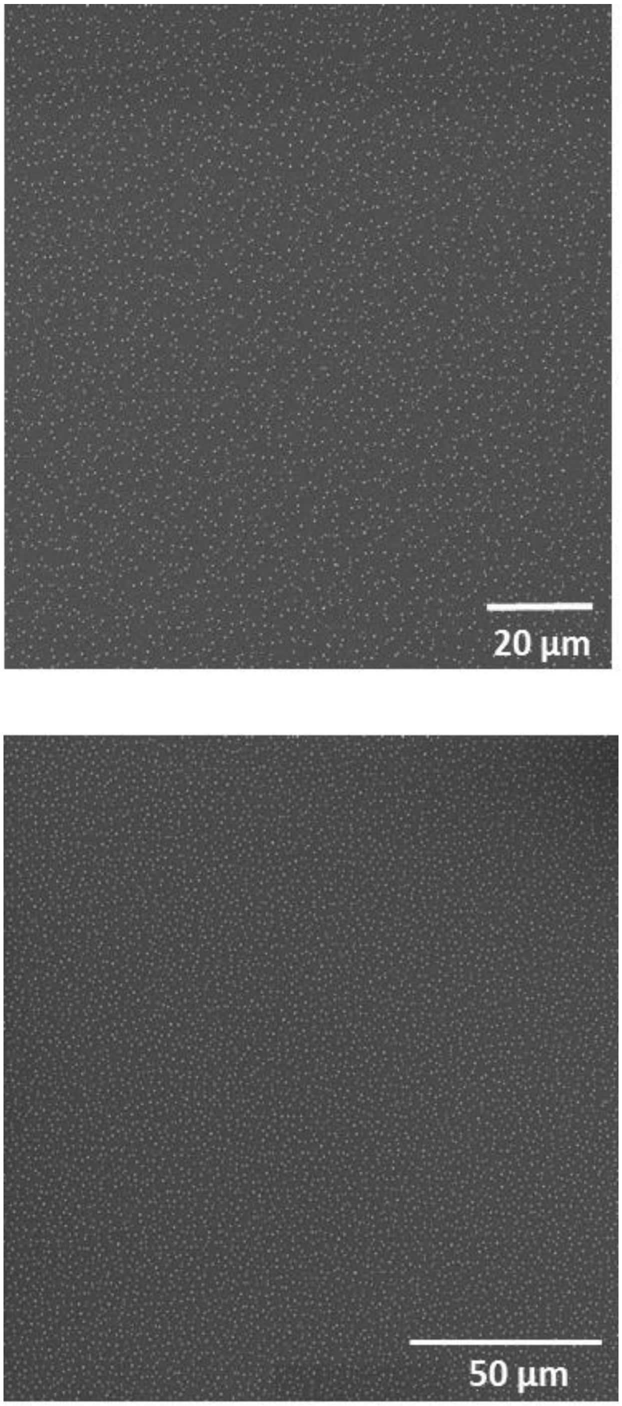

Figure 3.7. Uniformly dispersed silver nanostructures on ZnO thin films obtained after 4 hour annealing at 700 °C under Ar at different magnifications

The surface roughness of the ZnO (as-prepared) and AgNPs at ZnO (heat-treated at 700 °C) films was assessed by 5µm × 5µm AFM scan area, as shown in Fig.3.8. Root mean square (RMS) surface roughness values calculated by AFM were 2.6 nm and 9.4 nm for pure ZnO and AgNPs at ZnO thin film respectively. The 3D image of the ZnO film (Fig.3.8a) revealed the presence of a smooth and continuous surface with uniform columnar structure while that of the AgNPs at ZnO film (Fig.3.8b) shows the existence of rough surface texture with of Ag columnar structures.

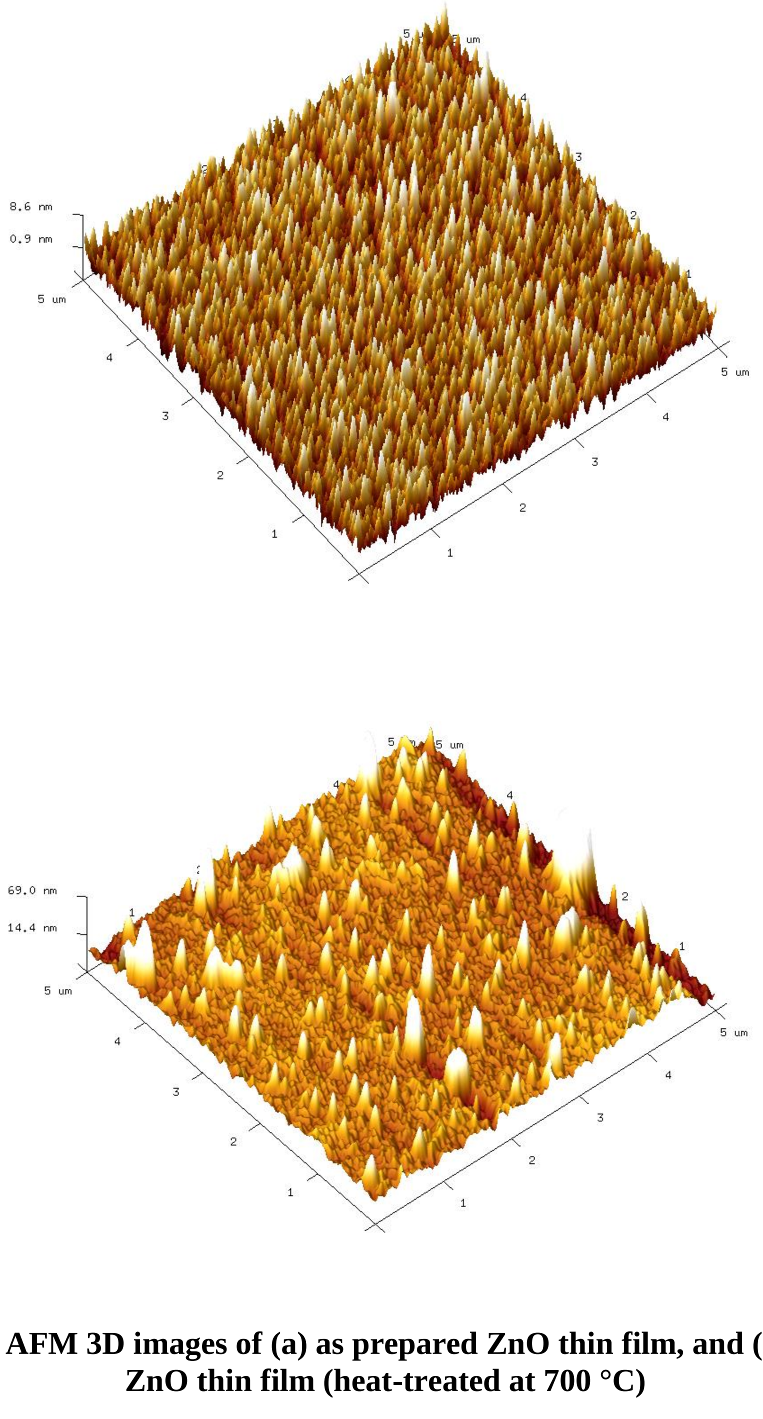

Figure 3.8. AFM 3D images of (a) as prepared ZnO thin film, and (b) AgNPs at ZnO thin film (heat-treated at 700 °C)

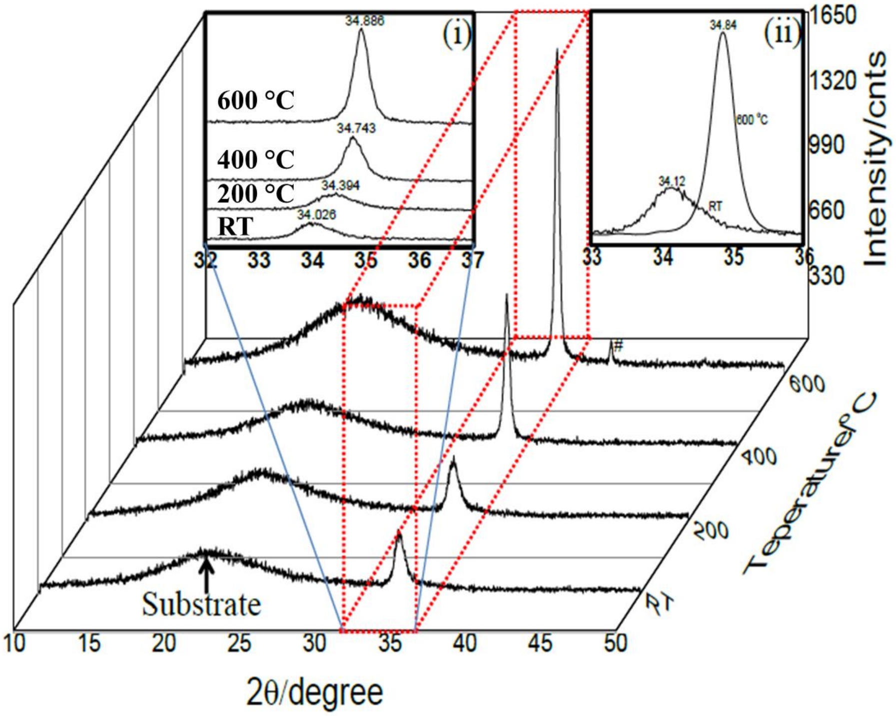

Figure 3.9 The 2D view of XRD patterns of Ag/ZnO film at different annealing temperatures. Inset (i): zoomed area to clearly show the shift of (002) peak. Inset (ii): pure ZnO films without silver annealed at RT and 600 °C

XRD pattern of the as-grown and the post-annealed Ag/ZnO and ZnO thin film shown in Fig. 3.9 was used to identify the crystalline phases present in the as-deposited films and measure the structural properties. Diffraction patterns were recorded in the 2θ range from 10° to 50°. The results showed the presence of the (002) diffraction peak only at 2θ = 34.0°-34.8° for different annealing conditions highlighting a preferential orientation of the films along the *c*-axis of the wurtzite structure of ZnO. After annealing, significant structural changes occurred. The (002) peak was shifted to higher 2θ values with increasing annealing temperatures. Inset (i) represents the magnified (002) peak position as marked by dotted box in Fig. 3.9 It is noteworthy that the peak shifted from 34.0° to 34.4°, 34.7° and 34.9° at annealing temperature of RT (27 °C), 200 °C, 400 °C and 600 °C respectively. Similar shifts were observed in the ZnO films without Ag deposition as shown in inset (ii) of Fig. 3.9 excluding any possible role of silver diffusion in the change of lattice parameter. An unknown peak marked '#' in Fig. 3.9 was observed for Ag-ZnO and ZnO thin film annealed at 600 °C. The shift of (002) peak may be related to stress relaxation resulting from the annealing. The level of stresses observed in sputtered ZnO films varies as a result of the different sputtering parameters [131-133]. The positive value represents tensile stress whereas the negative value represents compressive stress. The residual stress of the as-grown ZnO thin films has been shown to be tensile [134]. It was reported that the residual stresses in ZnO film contain a thermal stress component and an intrinsic stress component [135]. The thermal stress (i.e. tensile) is due to the difference in the thermal expansion coefficient between ZnO and substrate. On the other hand, the intrinsic stress is caused by imperfections in the crystallites during growth. In general, the magnitude of the compressive stress component is larger than that of the thermal (tensile) stress component, so the as-grown ZnO films exhibit an overall compressive residual stress [136]. Also, during the annealing process, the residual stress of the ZnO is effectively relaxed. With increasing annealing time and temperature, the tensile stress becomes stronger, and eventually exceeds the built-in compressive stress and leads to a change in the direction of stress [137]. Taking as a reference the lattice parameter of unstressed ZnO powder c =5.207 Ǻ as stated by American Society for Testing Materials (ASTM), we have estimated the stresses in our samples using an analysis suggested by [138-139]. The values are reported in Table 3.1. A transition from compressive stress to tensile stress was observed beyond 200 °C in agreement with those observations reported by Gupta et al. [138]. As an estimate, the Ag-ZnO films were stress free at annealing condition of ~ 217 °C as shown in Fig. 3.10 (c). The generation of tensile stresses can be related to the grain growth that results from the coalescence of individually nucleated islands with reference to substrate [140]. It is noteworthy that a drastic sharpening and an intensity increase of the (002) diffraction peak occurs as observed in the XRD patterns. The sharpening of the diffraction peak was a result of the grain growth. The grain size was estimated using Scherrer formula and is shown in Fig. 3.10 (a). As the annealing temperature increased the grain growth was found to rise monotonically until 600 °C. The results indicate a 140% increase of the average grain size after 4h annealing at 400 °C. Similar sharpening of the diffraction peaks of polycrystalline films prepared via MOCVD technique was observed while the glass substrate temperature increased from 150 °C to 250 °C [141]. In addition to the sharpening of the (002) peak, a significant enhancement of its intensity was also noted. Such intensity enhancement indeed indicates an increase of the diffracting volume in the film. The increase of the area under (002) peak with increasing annealing temperature is shown in Fig. 3.10 d suggesting that the as-grown films are not well crystallized. The area under (002) peak was observed to increase 63 % at 400 °C and 287% at 600 °C compared to the as grown.

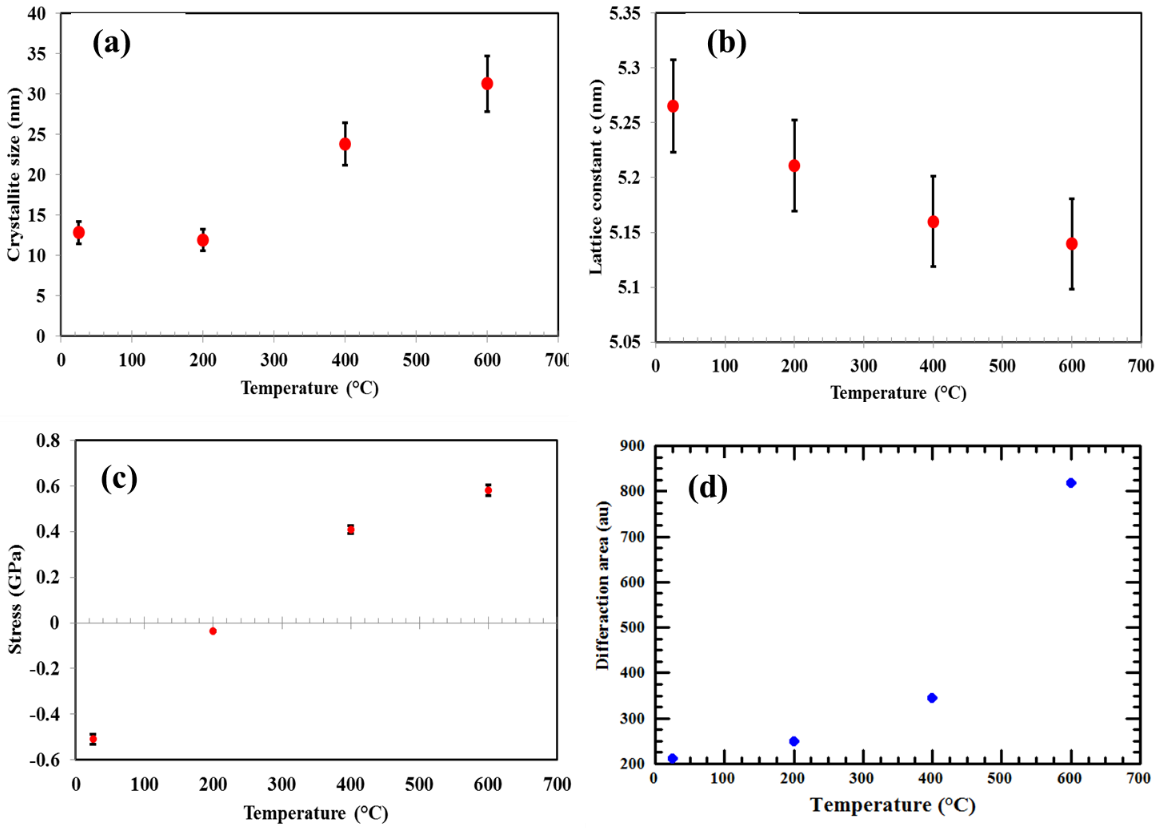

Figure 3.10. (a) Crystallite size, (b) lattice constant (c), stress and (d) diffraction area of Ag/ZnO thin films at different annealing temperatures

Table 3.1. Lattice parameters, grain size, energy gap and stresses, of Ag/ZnO thin film at different annealing temperatures

Temp. (°C)	2 θ (degree)	FWHM (degree)	Area (arb. unit)	Grain size (nm)	Lattice parameter (c) (Å)	Stress (GPa)	Eg (eV)
RT	34.02	0.79	211.0	13	5.26	- 0.51	3.31
200	34.39	0.85	250.0	12	5.21	- 0.037	3.26
400	34.74	0.43	344.5	24	5.16	0.41	3.24
600	34.89	0.33	818.5	31	5.14	0.58	3.25

The UV-Vis absorption spectra of the as-deposited and the post annealed Ag/ZnO films are shown in Fig. 3.11. From the figure, one can note a clear shift of the absorption edge towards longer wavelengths and a sharper increase of the absorption at the edge as the annealing temperature increases. The optical band gap is obtained by fitting the data using Tauc relation and are listed in Table 3.1. It was found that the optical band gap decreases from 3.31 eV for the as grown sample to 3.25 eV after annealing as shown in Fig 3.11 (b).

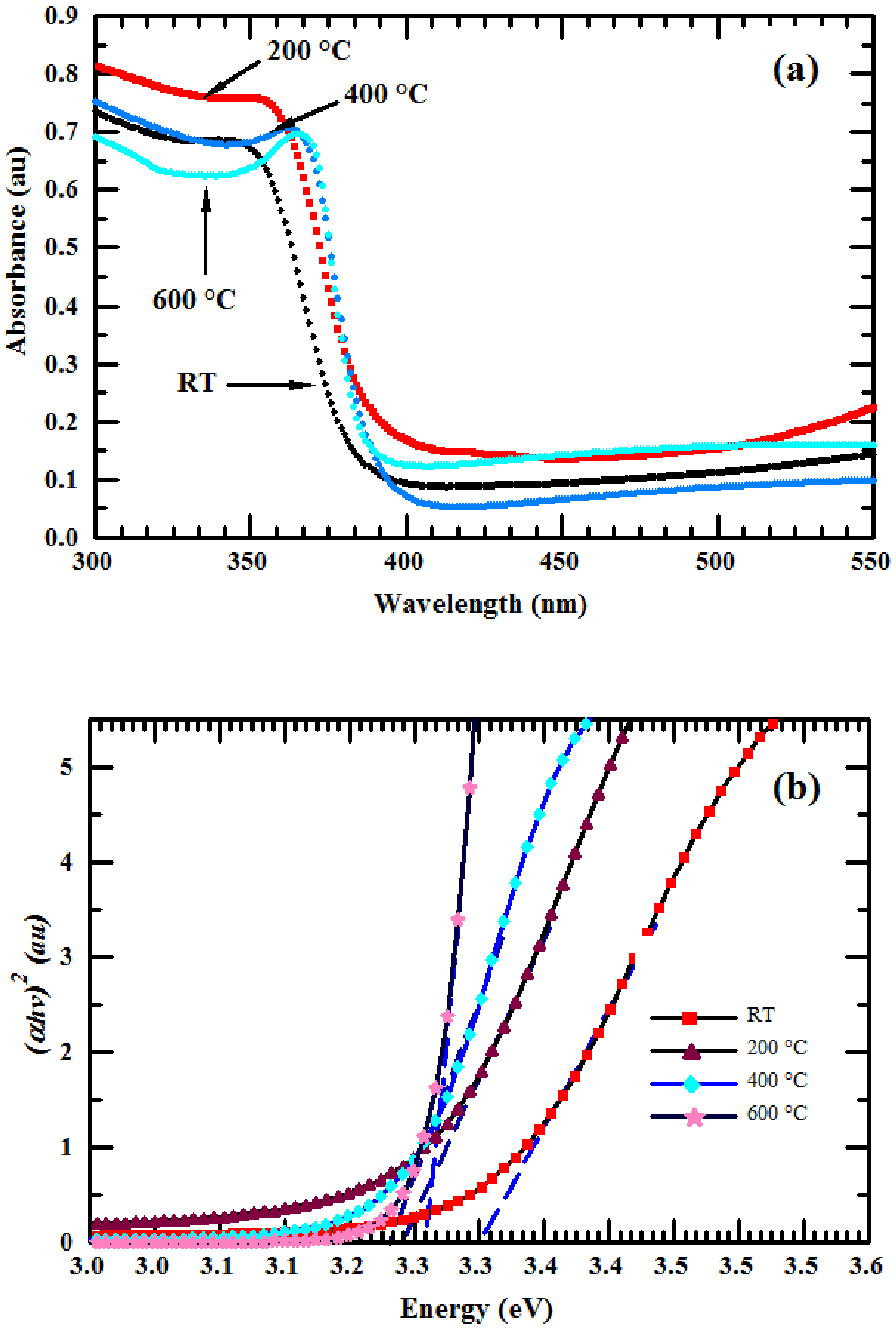

Figure 3.11. Absorption spectra of Ag/ZnO films (a) as-grown and post annealed films (b) Tauc curves of as grown and post annealed films

The surface chemistry of the as deposited ZnO and heat-treated AgNPs at ZnO thin films were investigated using XPS technique. The data obtained were fitted using Gaussain/Lorenzain mixed with smart background corrections. Figure 3.12 represents the wide scan of as fabricated ZnO thin film. The binding energies, full width at half maximum (FWHM) and atomic percent of the thin films were calculated and are listed in Table 3.2. From Table 3.2, the Zn2p showed doublet binding energies at around 1021.13 and1044.18 eV which correspond to Zn2p$_{3/2}$ and Zn2p$_{1/2}$ respectively [142-143]. The energy difference between doublet binding energies is 23.05 eV which is consistent with the standard value of 23.00 eV [144]. The splitting of the Zn2p peak is due to strong spin-orbit coupling as reported in [145].

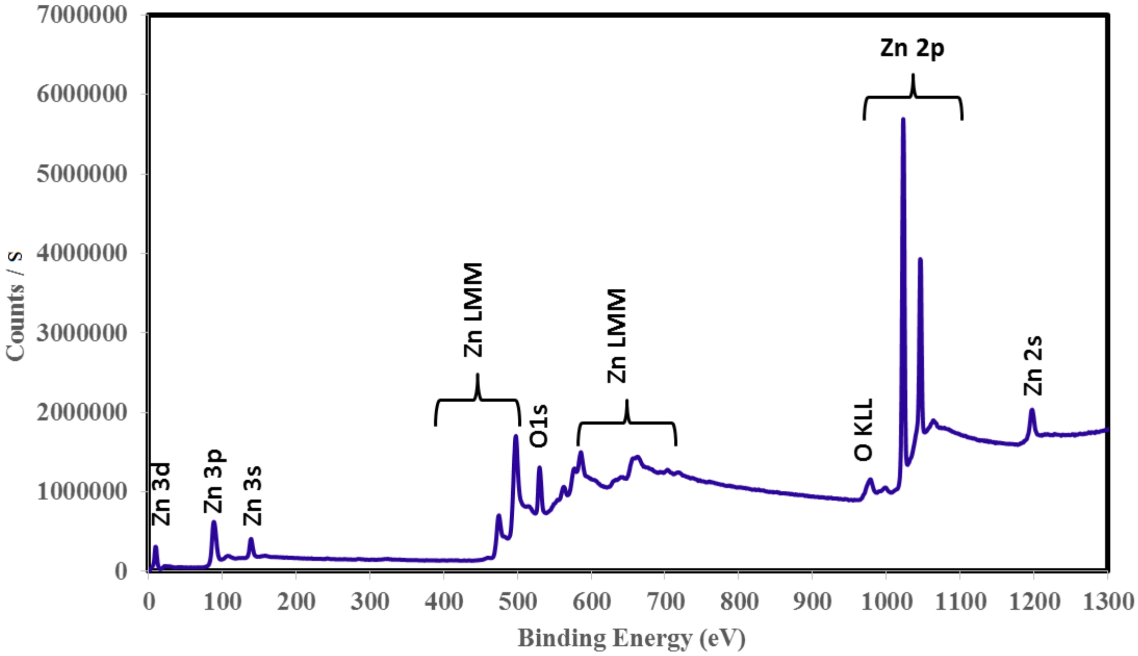

Figure 3.12. XPS wide scan of as prepared ZnO thin film

The fitted results of O1s of pure ZnO showed three components centered at 529.53 eV, 531.38 eV and 532.18 eV. The lowest binding energy (O_A) component of the O1s spectra is attributed to O^{2-} ions on the wurtzite structure of hexagonal Zn^{2+} ion array [146] while the highest binding energy (O_C) is attributed either due to a water vapour component or adsorbed oxygen [147]. The medium binding energy (O_B) is attributed to the presence of partially reduced ZnO (ZnO_x) [148,149]. The stoichiometric composition of the pure ZnO thin film prepared by DC reactive sputtering (Zn/O) is equal to 0.99.

The XPS data of the as-deposited Ag/ZnO thin film is also fitted and the results are included in Table 3.2. It is observed that the binding energy of $Zn2p_{3/2}$ spectrum is slightly higher than that of pure ZnO. The O1s in Ag/ZnO thin film also shows a slight difference; e.g. the binding energy of O_B is reduced in Ag/ZnO thin film. This might be due to the effect of the bombardment of pure ZnO thin film by energetic Ar ion during the growth of Ag thin film in the sputtering chamber. This assumption is supported by our observation that, during the depth profile experiments, we found that the medium binding energy of O1s (O_B) in the Ag/ZnO thin film decreased sharply after 8 sec etching via Ar ions. The high resolution XPS of the Ag3d peak in the as prepared Ag/ZnO sample showed doublet peaks corresponding to $Ag3d_{5/2}$ and $Ag3d_{3/2}$ separated by 5.93 eV. The spectrum of $Ag3d_{5/2}$ can be deconvoluted into two peaks centered at 368.59 eV and 369.62 eV with an amount of 7.24% and 0.30 % respectively. It has been reported [150] that the binding energy at around 368.59 eV is due to the Ag+ in the Ag_2O indicating the formation of silver oxide on the top layer of the as prepared Ag/ZnO thin film (see also Fig. 3.3). It has also been reported that Ag can be easily oxidized to Ag_2O even at room temperature [151]. The peak centered at 369.62 eV might be associated with Ag alloy such as Ag-ZnO or ZnO-Ag_2O.

The effect of the post annealing on the compositional properties and the chemical states of Ag/ZnO thin films were investigated (Fig. 3.13). Our observations (Table 3.2) show that the binding energies of Zn2p spectra of the Ag/ZnO films annealed at 400 °C are located at the same position of the as prepared Ag/ZnO films. In comparison with as deposited Ag/ZnO thin film, the Ag3d and O1s XPS spectra of the sample annealed at 400 °C showed slight differences. The middle binding energy of O1s showed higher atomic percent (13.42 %) comparing with 5.08% in as deposited Ag/ZnO thin film. This increase might be attributed to the formation of different silver oxides compounds. In addition, the sample annealed at 400 °C and 700 °C also showed an increase in the amount of the highest binding energy of O1s spectra. It has been reported that ZnO thin films prepared by DC reactive sputtering have columnar structure with different sizes of pores [152]. In addition, we reported in our previous work [153] that post annealing of sputtered ZnO films prepared by DC sputtering in inert gas environment increases the porosity of the film. This porosity could fill with water during exposure of the film to the air resulting to an increase of the concentration of O_C compound samples.

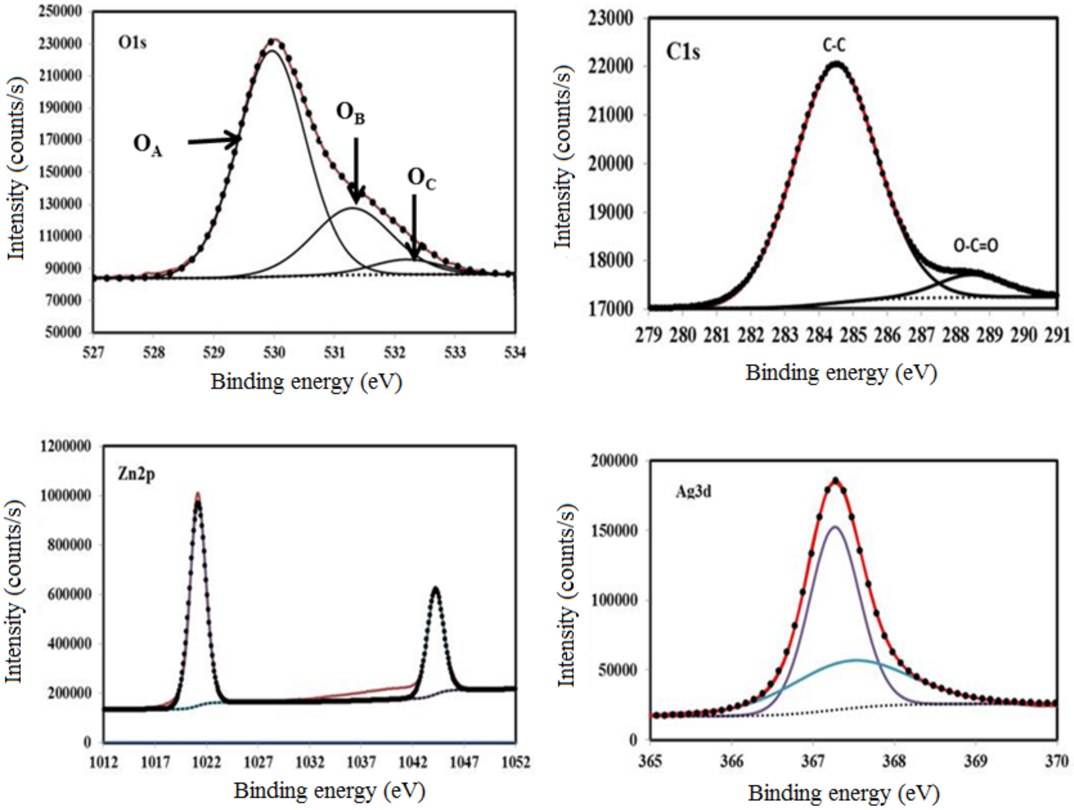

Figure 3.13. High resolution scan XPS spectra of O1s, C1s, Zn2p and Ag3d for Ag/ZnO thin films annealed at 600 °C in pure Ar

Table 3.2. XPS analysis of pure ZnO, as deposited Ag/ZnO and Ag/ZnO thin films annealed at 400 °C and 700 °C

	Name	Peak BE (eV)	FWHM (eV)	Atomic %	Zn2p/O1s
Pure ZnO (RT)	Zn2p	1021.13	1.92	45.68	0.99
	O1s A	529.53	1.66	46.08	
	O1s B	531.38	1.42	7.50	
	O1s C	532.18	0.73	0.74	
Ag/ZnO RT	Zn2p	1021.36	1.76	43.52	1.02
	O1s A	529.45	1.49	42.54	
	O1s B	531.28	1.41	5.08	
	O1s C	532.06	1.52	1.32	
	Ag3d	368.59	1.04	7.24	
	Ag3d Scan A	369.62	0.74	0.30	
Ag/ZnO 400 °C	Zn2p	1021.39	1.82	39.61	1.00
	O1sA	529.96	1.34	39.23	
	O1s B	531.3	1.54	13.42	
	O1s C	532.2	1.35	2.66	
	Ag3d	367.26	0.74	3.16	
	Ag3d Scan A	367.45	1.73	1.93	
Ag/ZnO 700 °C	Zn2p	1021.14	1.37	44.27	1.13
	O1sA	529.77	1.85	39.02	
	O1s B	531.1	1.47	12.21	
	O1s C	532.05	1.37	3.38	
	Ag3d	367.19	1.12	1.10	
	Ag3d Scan A	368.08	1.17	0.02	

3.1.4 EFFECT OF DEPOSITION TIME ON THE PROPERTIES OF Ag at ZnO THIN FILMS

For the study of the effect of deposition time on the morphology properties, silver thin films were deposited on ZnO thin films for 5, 10, 20 and 60 s using DC sputtering followed by annealing the Ag at ZnO samples at 600 ºC in a tube furnace for four hours in argon atmosphere. FE-SEM images (Fig. 3.14) show that the density and the size of the silver nanostructures increase with increasing sputtering time. Also, most of the particles are semi-cubical. The Ag nanorings are not clear enough; rather individual such particles are making ring like circles.

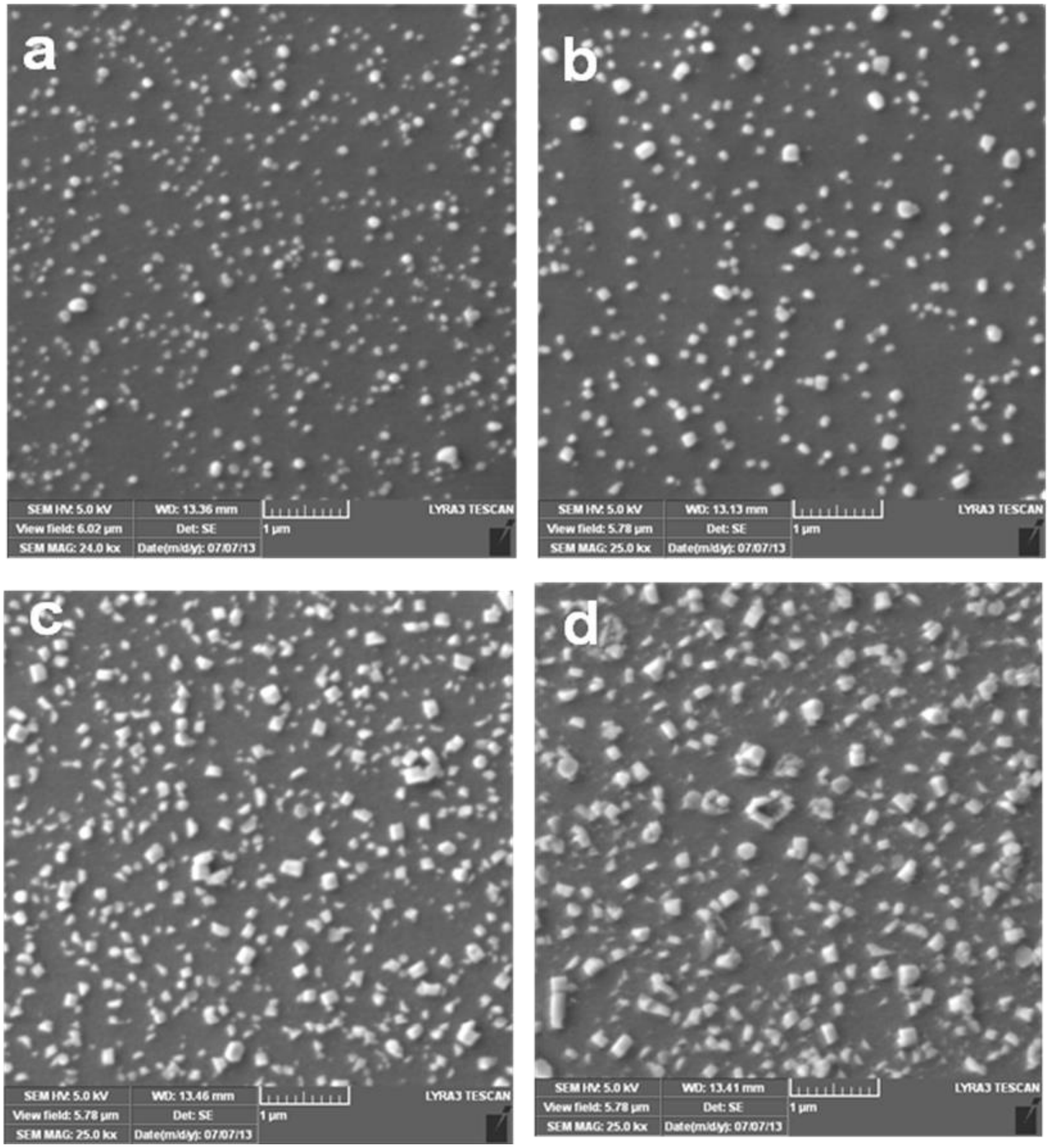

Figure 3.14. SEM images of Ag/Zno thin films grown at deposition time of (a) 5 s (b) 10 s (c) 20 s, and (d) 60 s

3.1.5 EFFECT OF THE DURATION OF THE POST ANNEALING TIME ON THE PROPERTIES OF Ag/ZnO THIN FILMS

The effect of the annealing duration on the silver nanostructures size by carrying out successive treatments on the same sample at 600°C was investigated under a constant flow of Ar. Figure 3.15 shows the despersion of silver nanostructures after 3h, 9h (3+6) and 24 (3+6+15) total annealing durations. The FE-SEM images showed that after 3h and 9h treatments nanostructures of various sizes were present Fig 3.15 a and b). They can be classified roughly in three main categories: A – particles of size less than 50 nm, B- particles of size between 50 and 150 nm, and C particles of size between 150 nm and 250 nm. After 24 hour treatment, particles of small size (A) are almost non-existead and the size distribution is bimodal, made of particles B and C as seen in Fig.3.15c.

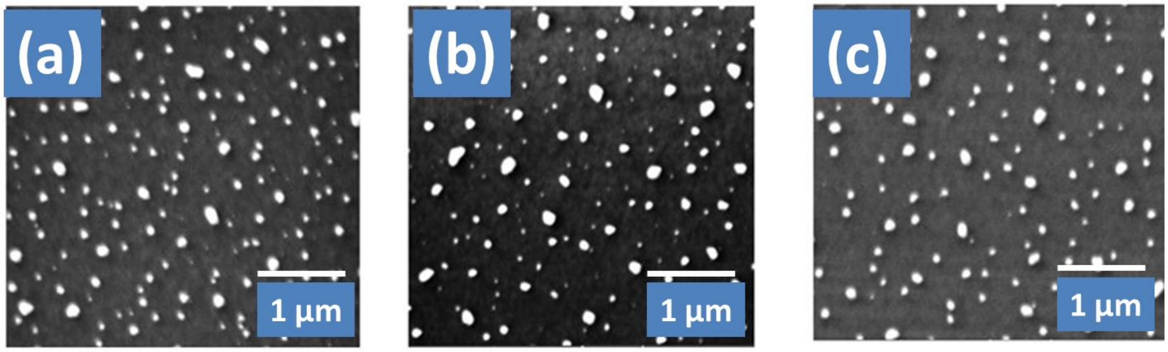

Figure 3.15. Distributions of silver nanostructures after (a) 3h, (b) 9h and (c) 24h total annealing durations at 600 °C

3.1.6 SYNTHESIS AND CHARACTERIZATION OF Ag NANORINGS ON ZnO THIN FILMS

Ag/ZnO samples were annealed at different temperatures from 200 to 700 °C in pure N_2 atmosphere. We found no significant change in the size and shape of the silver nanostructures in most of the cases. However, the samples annealed at 600 °C showed a striking result: the formation of silver nanorings. Figure 3.16 showed that the rings have an inner diameter of about 600 nm diameter and an outer diameter exceeding 1 micron. It can be observed also that the rings do not have smooth circular contours but seem to be made of "nanoparticles" as shown in Fig. 3.16 (c and d).

In order to confirm the crystalline phases and measure the structural properties of the Ag nanoring decorated on ZnO thin film, XRD was used (Fig. 3.17). Diffraction pattern in Fig. 3.17 shows the presence only of the (002) diffraction peak at $2\theta = 34.76°$ which indicates a preferential orientation of the film along the c-axis of the wurtzite structure of ZnO. We found no significant difference between the XRD diffraction in this case and the diffraction of Ag nanostructures on ZnO thin films or even in pure ZnO annealed at the same temperature in argon atmosphere. The Ag nanorings sample was also analyzed by EDX. Figure 3.18 shows the EDX analysis of single nanoring located on the surface of ZnO thin film. As can be seen, silver was only recorded inside the wall of the ring and no silver in or outside the ring was detected.

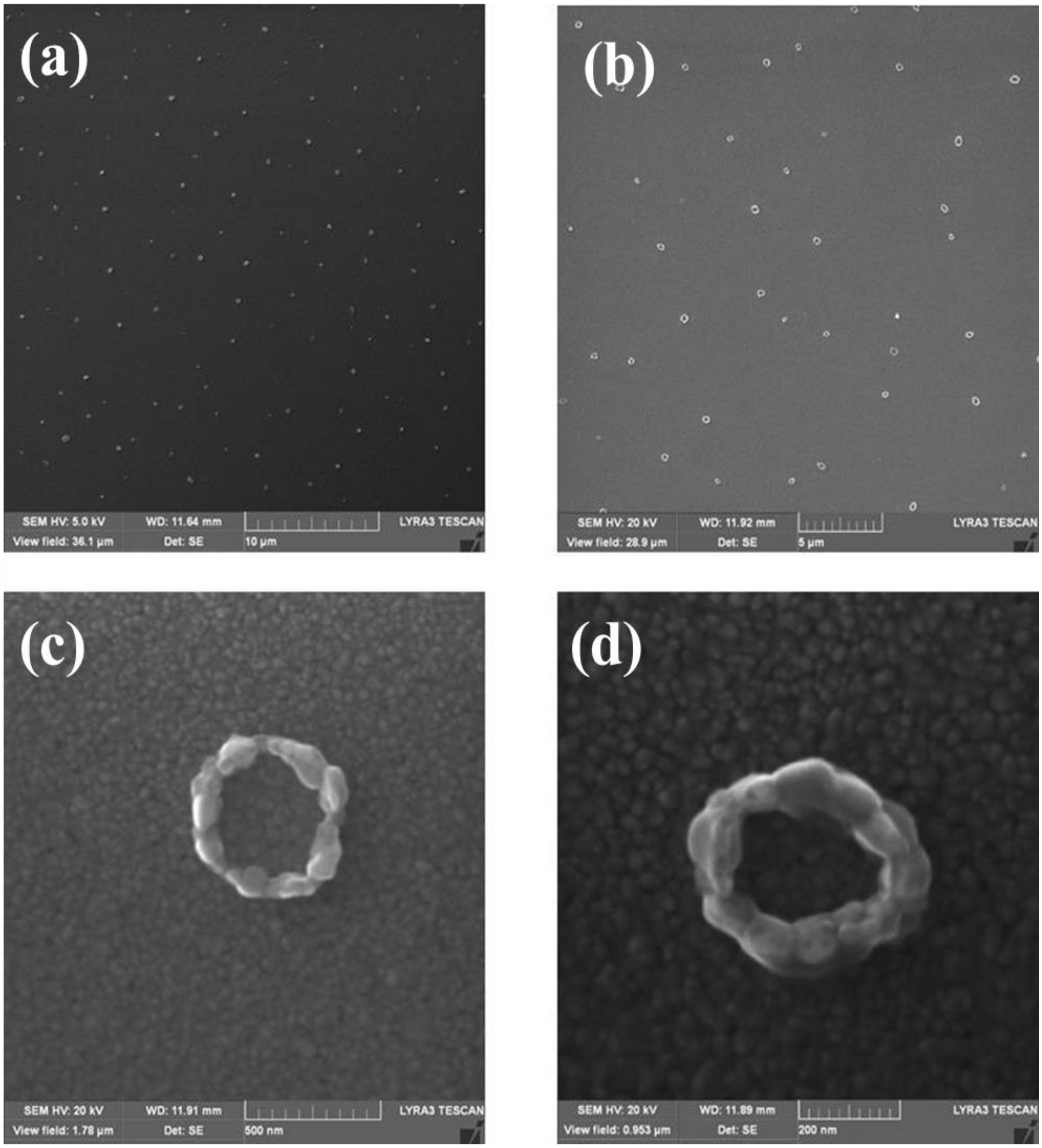

Figure 3.16. Ag Nanoring on ZnO thin film prepared by post annealing at 4 hours under nitrogen in tube furnace at (a,b) low magnifications and (c,d) high magnifications

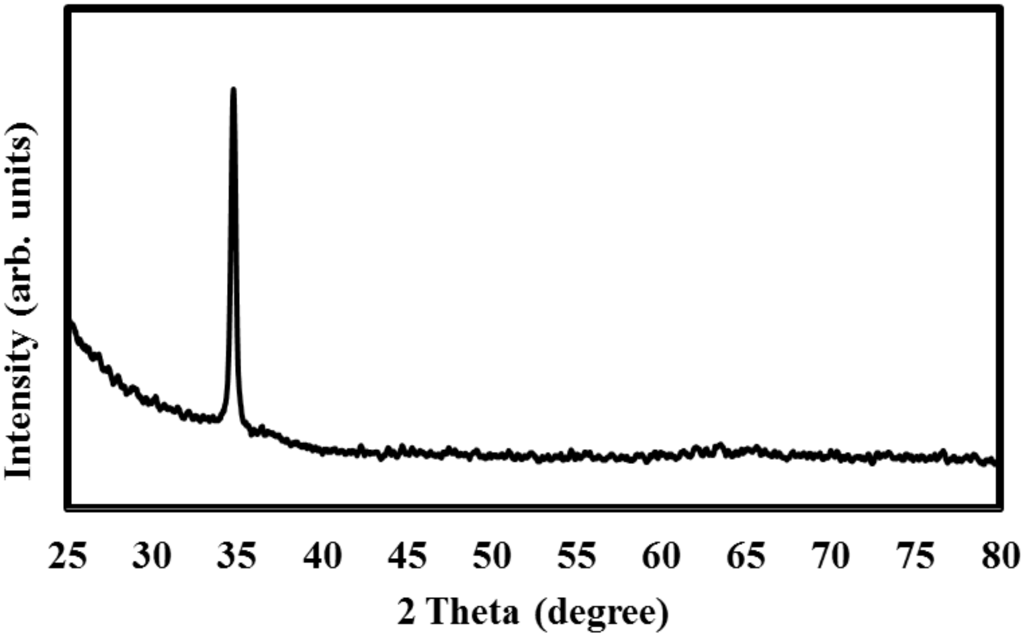

Figure 3.17. XRD pattern of Ag nanorings on ZnO thin film fabricated by sputtering technique

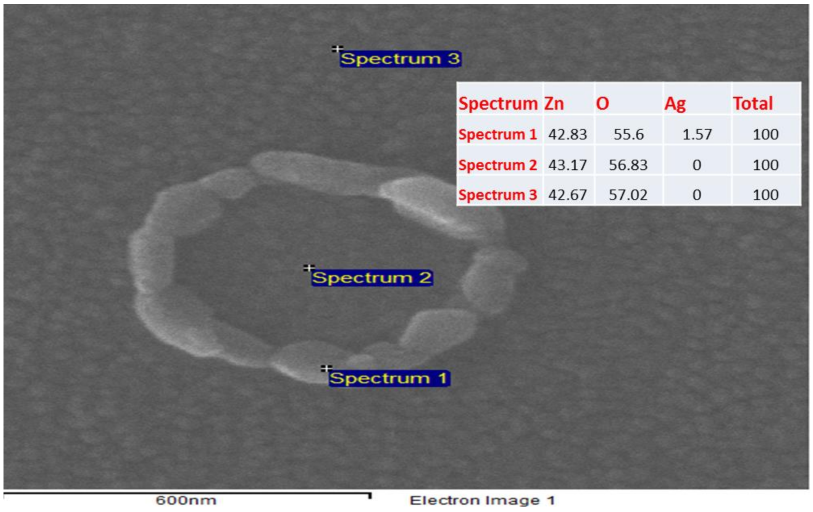

Spectrum	Zn	O	Ag	Total
Spectrum 1	42.83	55.6	1.57	100
Spectrum 2	43.17	56.83	0	100
Spectrum 3	42.67	57.02	0	100

Figure 3.18. EDX analysis of Ag nanoring on ZnO thin film

3.2 SYNTHESIS AND CHARACTERIZATION OF Au NANOSTRUCTURES MODIFIED ZnO THIN FILMS

Gold (Au) in the form of nanoparticles has been used in different applications such as plasmonic photovoltaic applications [154], sensors [155], photocatalysis [156], surface-enhanced Raman scattering [157]. Rai et al. [158], for example, developed a method for preparing and depositing 4 nm gold nanoparticles onto single crystalline ZnO synthesized by hydrothermal method for gas sensing applications. According to their work, Au/ZnO showed significantly enhanced sensing for CO gas. Au NPs on different thin film substrateس including semiconductor, insulator and metals have been investigated by different groups [159-161].

3.2.1 EXPERIMENTAL WORK

For the synthesis of Au nanostructures on the surface of ZnO thin films (AuNPsatZnO), an automated sputter coater was used to prepare pure as well as Au-decorated ZnO thin films. The glass substrates were sonicated in acetone for 15 min. prior to sputtering. The Zn and Au targets received from Semiconductor Wafer Inc., were cleaned by pre-sputtering a blank for 3 and 1 min., respectively. The base pressure in the chamber was kept below 5×10^{-6} Torr while the working pressure was set at 7×10^{-3} Torr. ZnO films were fabricated by DC reactive sputtering of metallic zinc at 100 W in oxygen for for 40 min. on glass substrates. An ultrathin layer of Au was deposited on the sputtered ZnO surface (Au at ZnO) at 30 W for 30s. The Au at ZnO thin film and pure ZnO thin films were heated at 600 °C for 3h in argon. This yielded films with nanostructured morphology of the deposited Au nanostructures on ZnO (AuNPs at ZnO). The film making sequence is illustrated in Fig. 3.19.

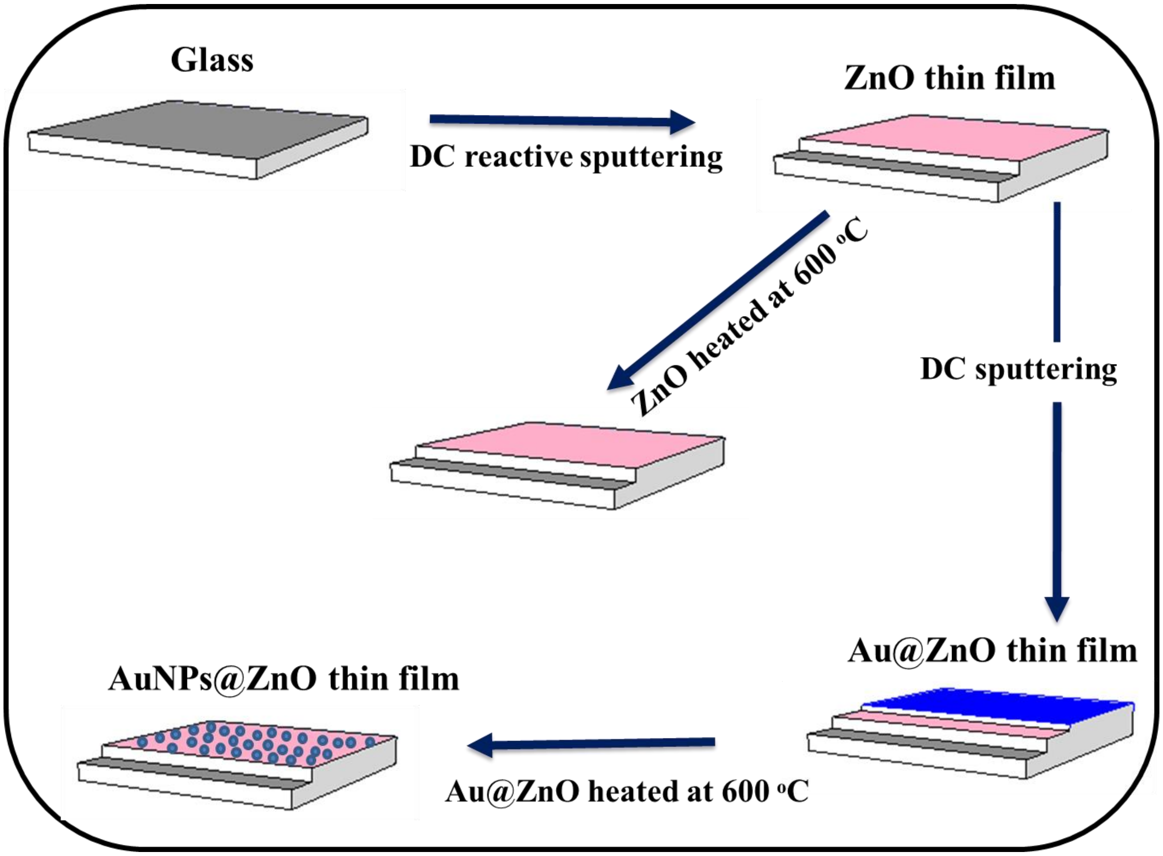

Figure 3.19. Schematic of the steps involved in the fabrication of AuNPs at ZnO films

3.2.2 XPS DEPTH PROFILING OF THE AS DEPOSITED AuatZnO

The XPS depth profiling of as deposited Au at ZnO was used to investigate the compositional uniformity across the exposed surface of the film. The surface was sequentially etched by a low energy (~2 keV) ion gun for 10s at time, prior to collecting the XPS spectra at that depth. Figure 3.20 shows the variation of the as deposited Au at ZnO thin films at twelve depths from the exposed film surface. The variation of the Au4f concentration displayed that the Au concentration decreased sharply after 30 s etching indicating the formation of very thin layer of Au (Fig. 3.20 (a)). Zn and O concentrations in opposition to that increased steadily for the first 30 s (Fig. 3. 20 (b,c)).

Figure 3.21 shows the concentration profiles (at.%) for Au4f, C1s, O1s and Zn2p at twelve depths from the exposed film surface. As can be seen, the Au concentration declined (ca. ~ 27 at. % at the surface to ~ 10 at. %) within 30s of etching indicating the formation of a very thin layer of gold. The variation of O1s and Zn2p core levels with the etching time shows more oxygen and less zinc at the surface. This is due to adsorbed oxygen at the surface. After cleaning the surface, the Zn and O in the film are equally distributed by XPS, However, depth profile of C1s showed the vanishing of the carbon peak after the first 10s. At the surface of the Au at ZnO thin film an amount of about 35% of carbon was recorded.

(a) Au4f Scan

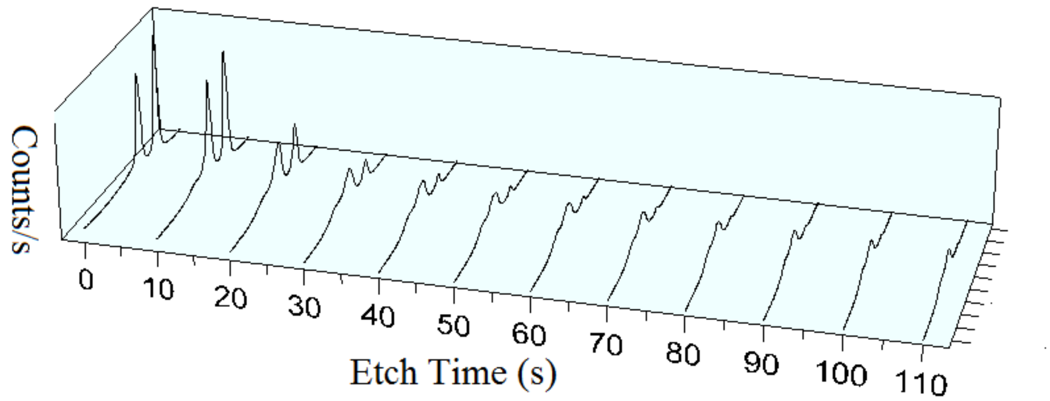

(b) O1s Scan

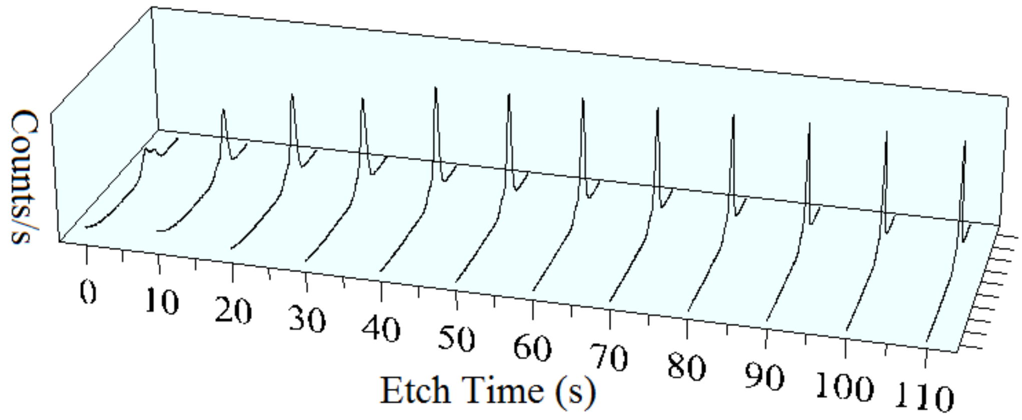

(c) Zn2p Scan

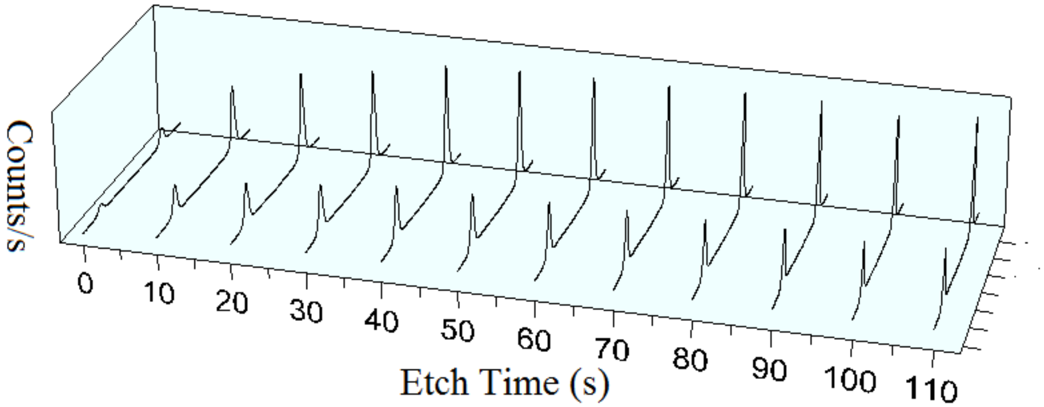

Figure 3.20**.** DPA of (a) Au4f, (b) O1s, (c) Zn2p of the Au at ZnO thin film

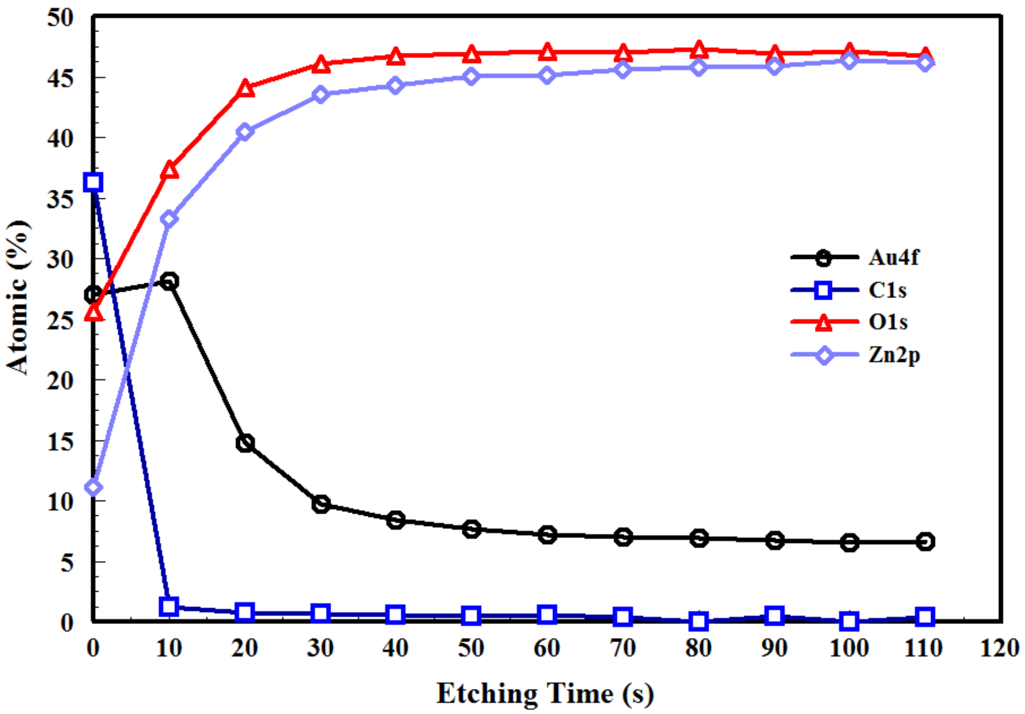

Figure 3.21. The XPS depth profile of the Au at ZnO thin film as a function of etching time

3.2.3 STRUCTURAL CHARACTERIZATION OF THE FABRICATED Au/ZnO FILMS

To investigate the structural aspects of the as-prepared ZnO and Au at ZnO thin films, heat-treated ZnO and AuNPsatZnO thin films, a systematic analysis of their XRD patterns was carried out. The results are summarized in Fig. 3.22. Similar to Ag/ZnO thin films, all the films showed strong preferential growth along c-axis (002 plane), indicating their formation and growth in the wurtzite structure of ZnO. Fujimura et al. [30] had suggested that the preferential growth of ZnO in thin films in the 002 direction is due to the lowest surface energy of the (002) plane compared with others. No diffraction peaks could be ascribed to Au in Au at ZnO and AuNPs at ZnO films which is likely due to the presence of too small amount of Au in them. The average crystallite size of ZnO was calculated using Debye-Scherrer's equation. The computed crystallite size of ZnO in various films is summarized in Table 3.3 As expected, the calculated crystallite size in the heat-treated films are higher (almost 3 times) than those in the pristine samples, which could be attributed to growth at higher temperatures due to Ostwald ripening [162]. There was also a slight shift in the position of the 002 peak towards higher angle in the heat-treated samples. This has been attributed by some [163-165] to the increased stress in thin films brought about by heat treatment. The positive values in Table 3.3 represent tensile stress while compressive stress is indicated by negative values. Consequently, the residual stress in the as-made films is compressive in nature, whereas the stress in the heat-treated films was tensile in nature. Tensile stresses is related to grain growth as a result of heat-treatment at higher temperatures, resulting in the coalescence of individually nucleated islands with respect to the substrate [153]. Moreover, the intensity of the (002) diffraction in the heated films increased sharply compared to that of the as-deposited counterparts. This could be ascribed to the improvement in crystallinity. In the case of Au decorated films, no significant change in the peak position could be discerned between the as-made and heat-treated Au decorated-ZnO films, thereby obviating the possibility of significant Au diffusion into the ZnO lattice.

Table 3.3. Structural information of ZnO, heat-treated ZnO, Au at ZnO and AuNPs at ZnO thin films

Sample	2θ (°)	FWHM (deg.)	grain size (nm)	Lattice parameter (c) (nm)	Stress (GPa)
pure ZnO	34.14	0.84	11	0.5248	-3.61
AuatZnO	34.21	0.80	12	0.5237	-2.71
Heated ZnO	34.83	0.25	37	0.5147	5.12
AuNPs at ZnO	34.90	0.25	38	0.5137	5.97

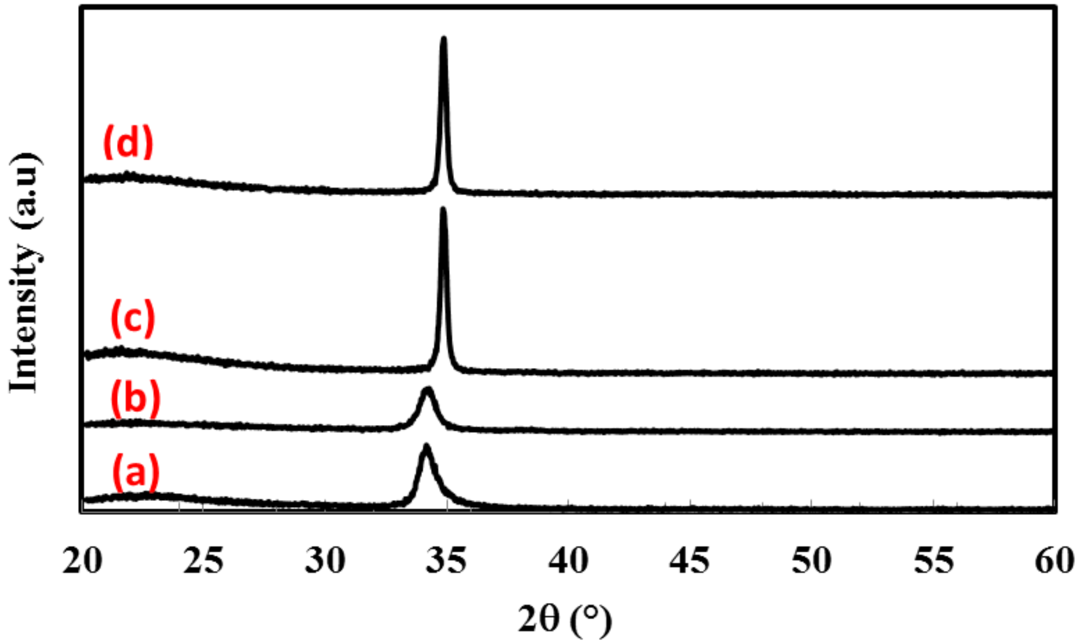

Figure 3.22. XRD patterns of: (a) as-grown ZnO, (b) Au at ZnO, heat-treated (c) ZnO and (d) AuNPs at ZnO thin films

3.2.4 MICROSTRUCTURAL CHARACTERIZATION OF THE Au/ZnO FILMS

The surface morphology and roughness of the thin films were investigated by FE-SEM and AFM, respectively. Figure 3.23 shows the FE-SEM micrographs of the as-prepared (a-b) and heat-treated (c-d) pure and Au-decorated ZnO thin films respectively. As can be seen, the as-grown thin films show dense, smooth and homogenous morphology, with grains ranging from about 15 to 35 nm in size. The surface of heat-treated ZnO film (Fig. 3.23 (c)) also possesses smooth morphology. However, isolated Au nanoparticles decorating the surface of the ZnO films were observed on the Au at ZnO thin films (Fig. 3.23 (d)), with Au nanoparticles varying in size between 20 and 90 nm.

The surface roughnesses of the Au at ZnO (as-prepared) and AuNPs at ZnO (heat-treated) films were assessed by AFM, as shown in Fig. 3.24. The 3D image of the as prepared Au at ZnO film (Fig. 3.24 (a)) revealed the presence of smooth and continuous surface with uniform columnar structure while that of the AuNPs at ZnO film (Fig. 3.24 (b)) showed the existence of rough surface texture with Au columnar spikes.

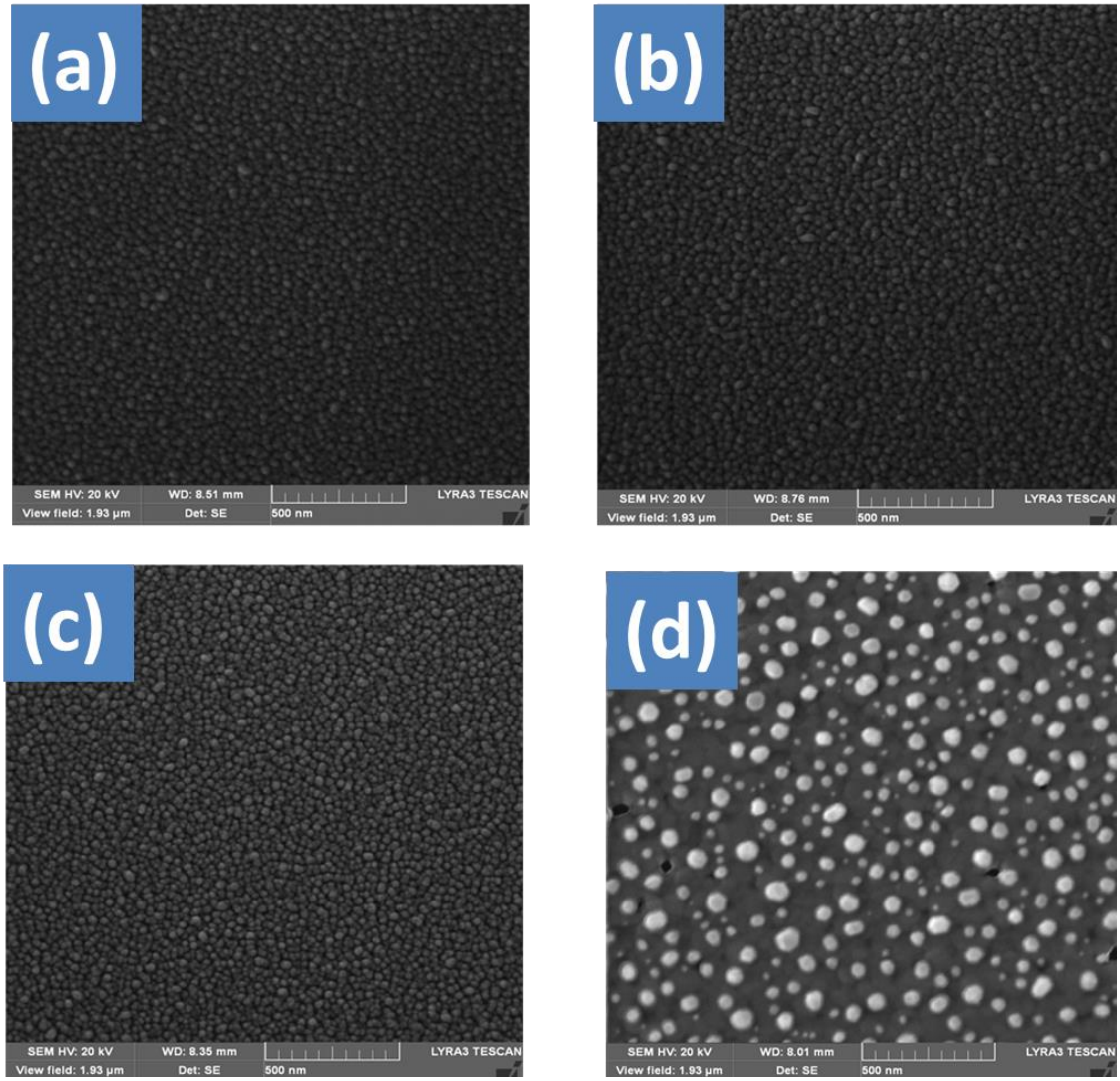

Figure 3.23. FE-SEM micrograph of (a) as-grown ZnO, (b) Au at ZnO, (c) heated ZnO and AuNPs at ZnO thin films

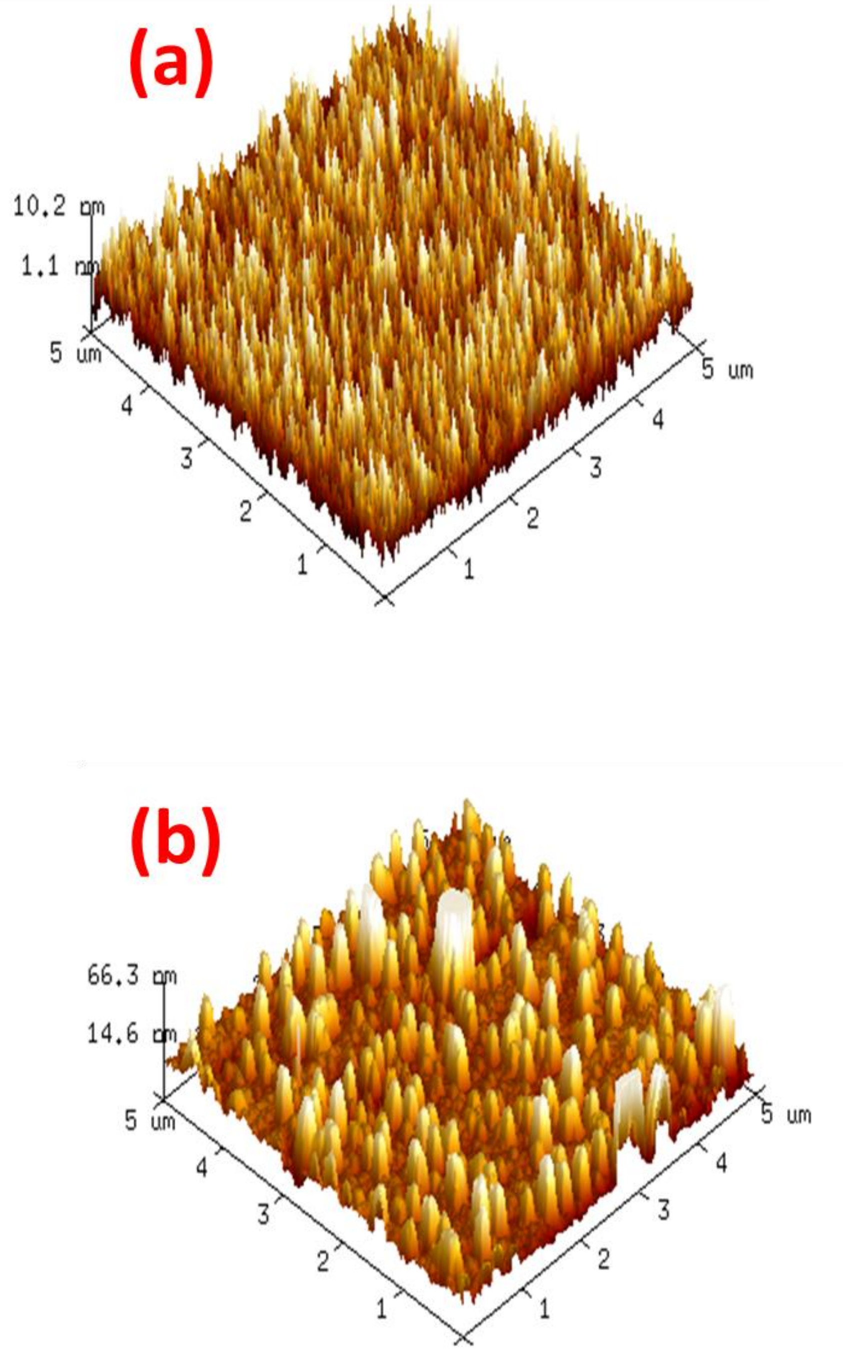

Figure 3.24. AFM 3D images of: (a) Au at ZnO, and (b) AuNPs at ZnO thin films

3.2.5 COMPOSITIONAL CHARACTERIZATION OF THE AuNPs at ZnO THIN FILM

The global XPS scan of AuNPs at ZnO film (Au at ZnO film annealed at 600 °C) shown in Fig. 3.25 (a) clearly identifies peaks due to Zn, Au, C and O. The peak signals in the deconvoluted spectrum shown in Fig. 3.25 (b) can be assigned to $Au4f_{7/2}$ (83.65 eV) and $Au4f_{5/2}$ (87.34 eV), The binding energy difference (Δ) between the two core levels was calculated to be about 3.69 eV, which is in excellent agreement with 3.63 eV reported for the spin-orbit splitting in metallic Au [166]. The Au concentration on the surface of AuNPs at ZnO film was computed to be 7.93 at.% which is about 1/4th of that on Au at ZnO film surface. This difference could be attributed to the conversion of Au films in the case of Au at ZnO to Au nanoparticles as a result of heat treatment that yielded AuNPs at ZnO as corroborated by the FE-SEM results shown earlier.

The deconvoluted O1s spectrum of AuNPs at ZnO in Fig. 3.25 (c) consists of two symmetric peaks at 530.83 and 532.63 eV, the binding energy difference (Δ) between the two core levels being 1.80 eV. These correspond to the O1s electron binding energies in various oxygen-containing layers in the sample. Thus, the peak at 530.83 eV corresponds to about 69% of the total O1s peak due to O^{2-} ions in the ZnO lattice [153]; the 532.63 eV peak is ascribed to the adsorbed oxygen or that due to OH dissociation on the film surface [176,168]. Similarly, the two peaks in the deconvoluted Zn2p spectrum (Fig. 3.25 (d)) correspond to $Zn2p3_{/2}$ (1022.17 eV) and $Zn2p_{1/2}$ (1045.23 eV), respectively. The electron binding energy difference (Δ) between the two core levels is 23.06 eV, in excellent agreement with 23.00 eV [169].

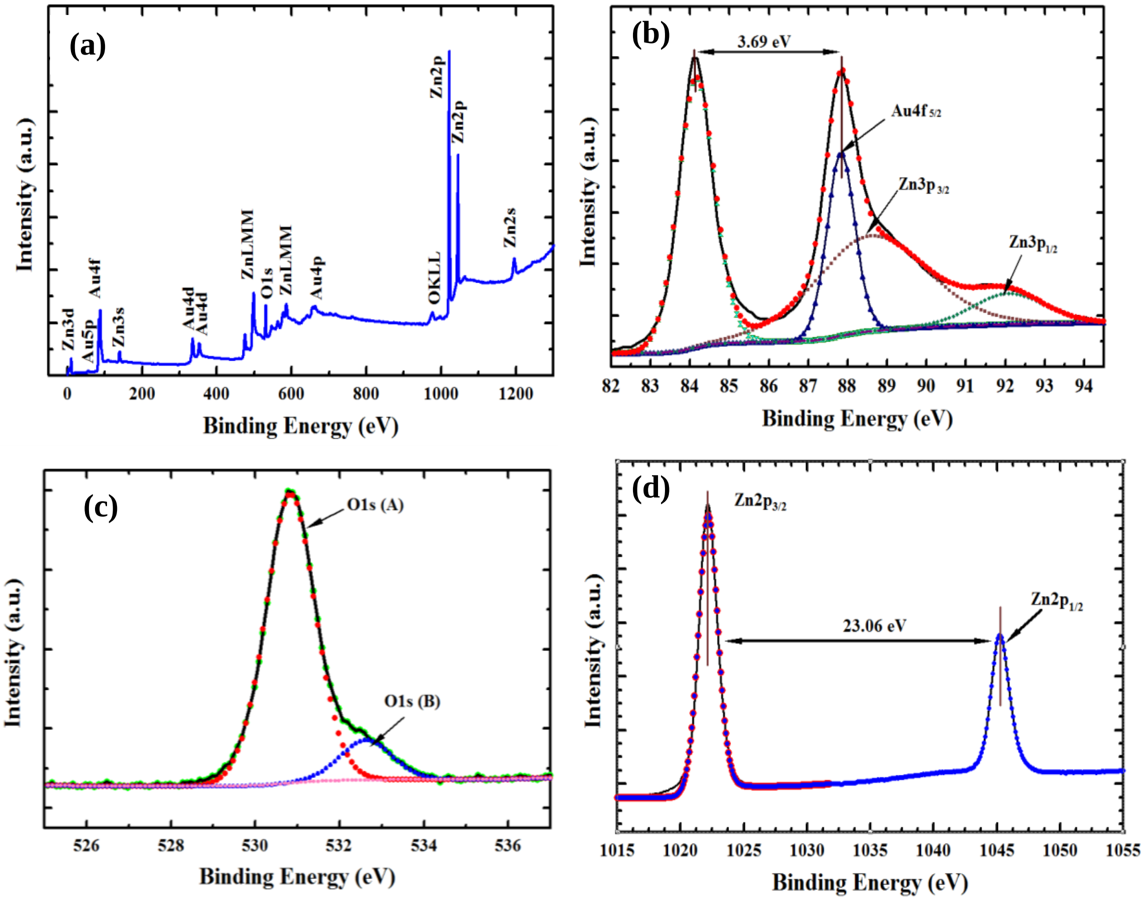

Figure 3.25. XPS spectra of AuNPs at ZnO thin film: (a) global survey, (b) Au4f, (c) O1s and (d) Zn2p

3.2.6 EFFECT OF POST ANNEALING ON THE PROPERTIES OF Au/ZnO THIN FILMS

In order to study the effect of post annealing treatment on the morphology of Au/ZnO, the as prepared thin films were annealed in a tube furnace for 4h at different temperatures: 25 ºC, 400 ºC, 600 ºC and 800 ºC. Figure 3.26 shows that the surface of as-deposited Au on ZnO is smooth and has no islands. After 4h of annealing from RT to 400 °C, agglomeration of random shape and sizes were observed. As the annealing temperature increased to 600 ºC a different sizes distribution of Au nanoparticles were observed. and 800 ºC

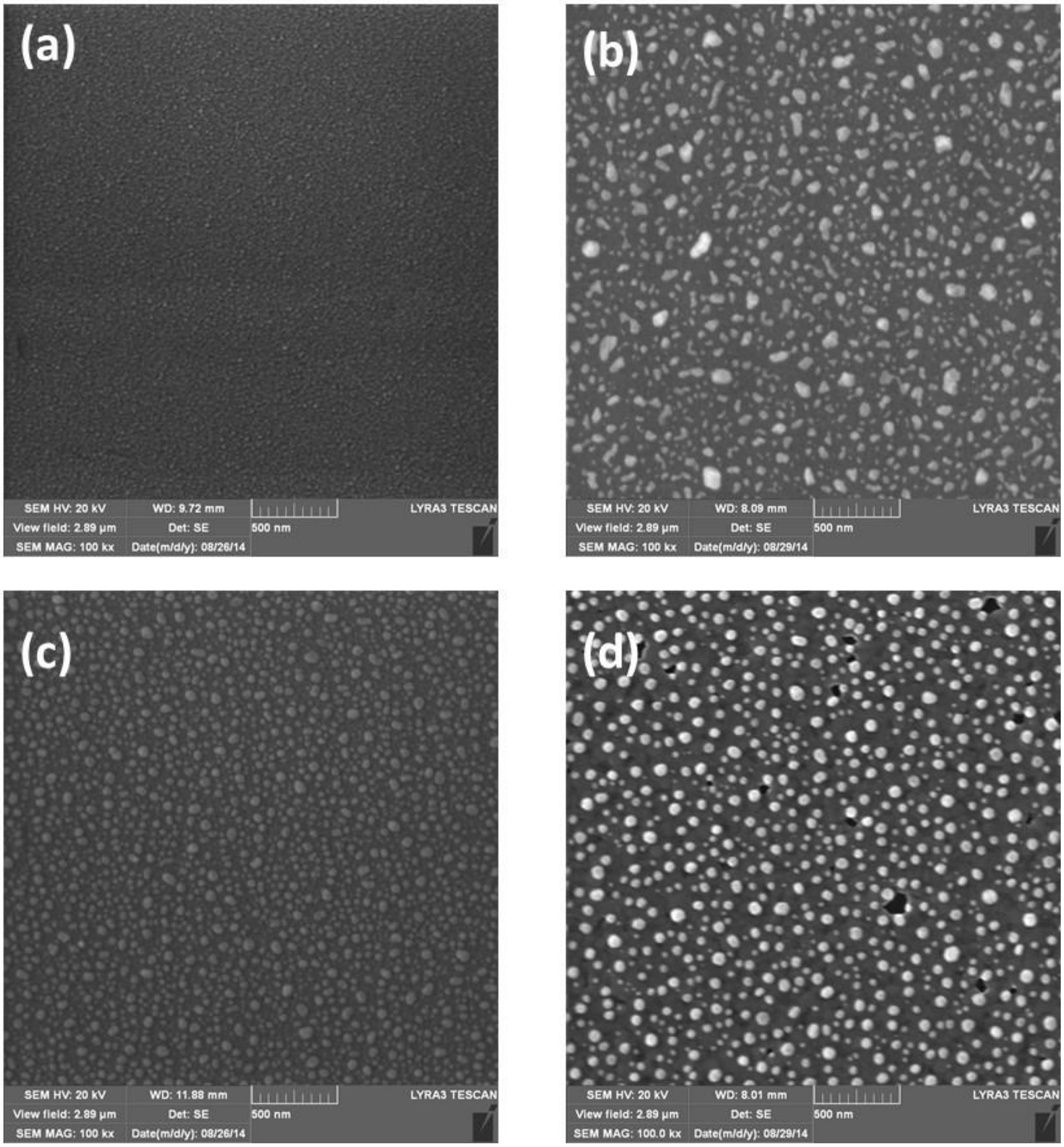

Figure 3.26. FE-SEM micrograph of (a) as-grown Au at ZnO, and AuNPs at ZnO annealed at (b) 400 °C, (c) 600 °C and 800 °C

3.3 SYNTHESIS AND CHARACTERIZATION OF Pt NANOSTRUCTURES ON ZnO THIN FILMS

Platinum (Pt) is one of the least reactive metals used in important catalytic applications including fuel cells[170-172], photo-catalysis [173-174], and catalysis for chemical reactions involving hydrogen gas or oxygen gas [175]. It has been reported in the literature that loading Pt nanoparticles on different materials such as metal oxides and carbon nanotube play an important role for the enhanced detection of many gases [176-179]. Chomkitichai et al., for example, compared between Pt-loaded TiO_2 and pure TiO_2 thin films toward the detection of H_2. They found that Pt-loaded TiO_2 thin films showed higher response and better recovery time than that of unloaded films [180]. The major problem for using Pt in gas sensing, and in other applications, is its price and the limited available quantity. Different methods have been investigated loading Pt on different materials with the aim of reducing the amount of Pt [181-183]. In the following section, we describe the experimental work used for modifying the surface of the ZnO by Pt nanostructures.

3.3.1 EXPERIMENTAL WORK

For the synthesis of Pt/ZnO thin films using sputtering technique, high purity zinc (99.999 %) and Pt (99.99%) targets from Semiconductor Wafer, Inc. were used. The base pressure in the sputtering chamber was below than 5×10^{-6} Torr and the working pressure was set to 7×10^{-3} Torr by adjusting the Ar and O_2 gas flows. The deposition of Pt-ZnO thin films was carried out in two steps. First, ZnO thin films were deposited on glass substrates for 40 minutes at 100 watt power in pure oxygen atmosphere. In the second step, Pt was sputtered using Ar plasma for 40 seconds at 30 watt. After that, the as deposited thin films were annealed in a tube furnace at different temperatures (500 ºC, 600 ºC, 800 ºC). This kind of preparing PtNPs on ZnO thin films has many advantages comparing with other chemicals methods. The main advantages of our method are:

1- Very small quantity of Pt is used because we are only sputtering atoms from the surface of the Pt.
2- The size and density of Pt nanostructures (number of particles per unit area), as we will see in the following sections, can be controlled through the treatment during nanostructures synthesis.
3- This method is ultra-pure of contamination.

3.3.2 XPS DEPTH PROFILING OF THE AS DEPOSITED PtatZnO

In order to investigate the XPS depth profiling of the as deposited Pt at ZnO, the surface was systematically etched by a low energy (~2 keV) ion gun for 10s. Figure 3.26 shows the variation of the as deposited Pt at ZnO thin films at twelve depths from the exposed film surface. The variation of the Pt4f concentration displayed that the Pt concentration declined sharply and Pt almost vanishes after 30 s etching indicating the formation of ultra-thin layer of Pt (Fig. 3.27 (a)). Zn and O concentrations in contrast increased with etching time (Fig. 3.27 (b,c)).

(a) **Pt4f Scan**

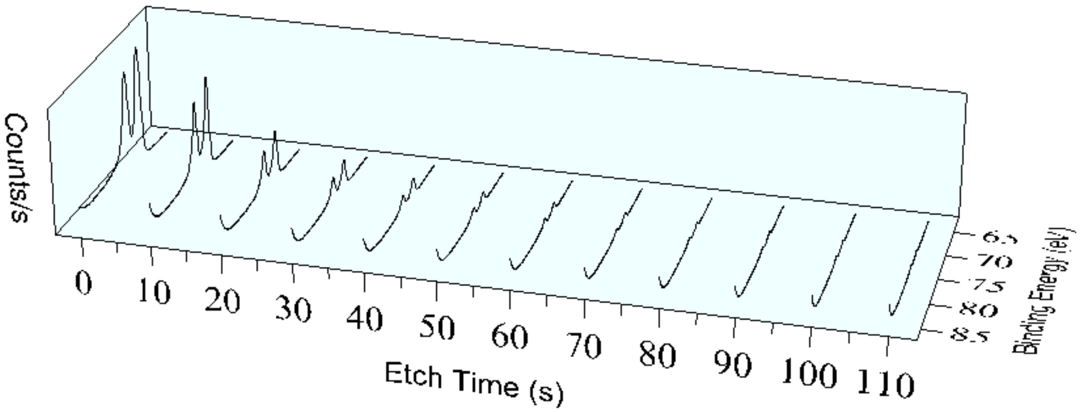

(b) **O1s Scan**

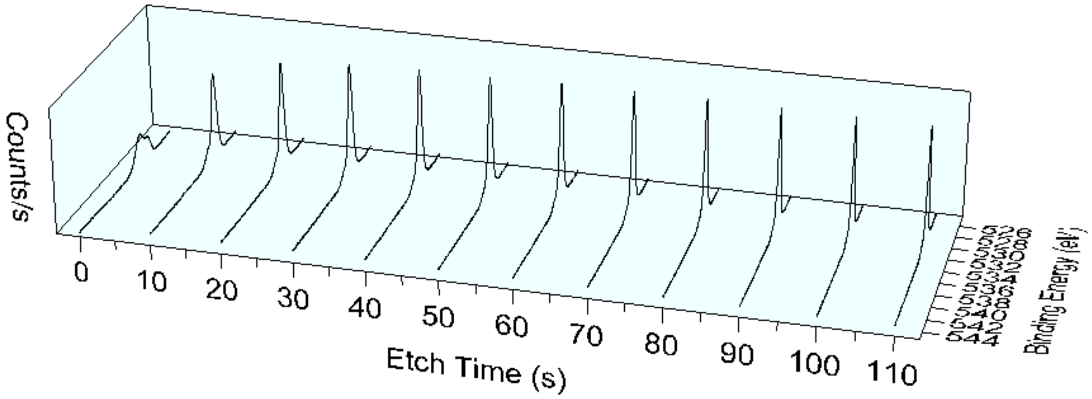

(c) **Zn2p Scan**

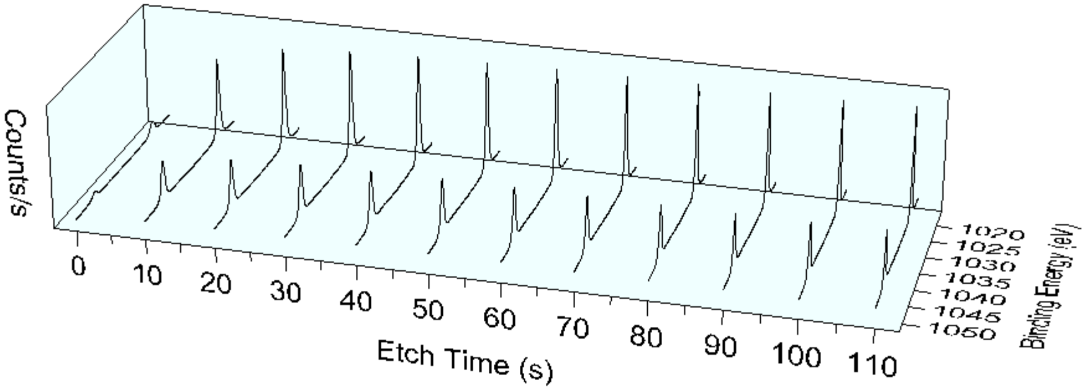

Figure 3.27. XPS depth profiling analysis of (a) Pt4f, (b) O1s, (c) Zn2p of the Pt at ZnO thin film

Figure 3.28 shows the concentration profiles (at.%) for Pt4f, C1s, O1s and Zn2p at twelve depths from the exposed film surface. As can be seen, the Pt concentration decreased from (ca. ~ 8 at. % at the surface to ~ 0.6 at. %) after 40 s of etching indicating the formation of thin layer of Pt. Due to the adsorbed oxygen at the surface, the variation of O1s and Zn2p core levels with the etching time shows more oxygen and less zinc at the surface. After cleaning the surface, the Zn concentration slightly increased after 50 s of etching while the oxygen concentration decreased. This deficiency in the oxygen in the ZnO lattice might be due to the evaporation of oxygen atoms during the sputtering. This assumption is confirmed by the XPS depth profile of the oxygen (Fig. 3.28). As can be seen, by increasing the etching time the binding energy position of O1s core level shifted to the higher binding energy. It was mentioned in section 3.1. that O1s core level in ZnO sample has three compounds. The lowest binding energy component is attributed to O^{2-} ions on the wurtzite structure of hexagonal Zn^{2+} ion array while the highest binding energy (O_C) is attributed either due to a water vapour component or adsorbed oxygen. The medium binding energy (O_B) is attributed due to the presence of partially reduced ZnO. In Fig. 3.29, one can see clearly that the low binding energy that is attributed to the presence of oxygen in the ZnO lattice is shifted to medium binding energy (oxygen in partially reduced ZnO).

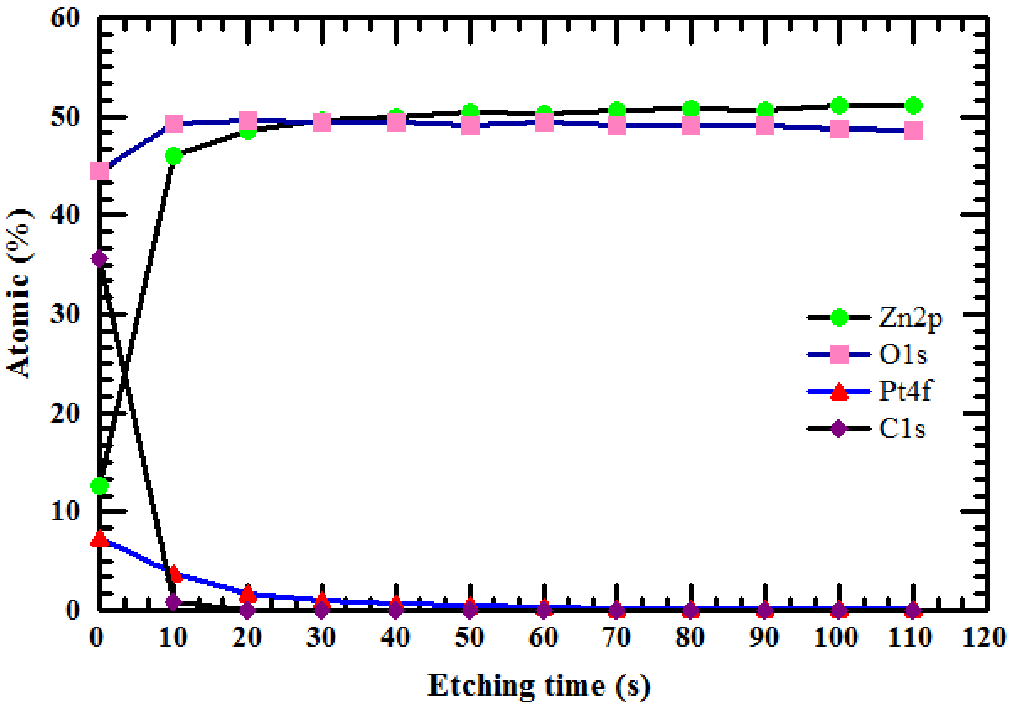

Figure 3.28. The XPS depth profile of the Pt at ZnO thin film as a function of etching time

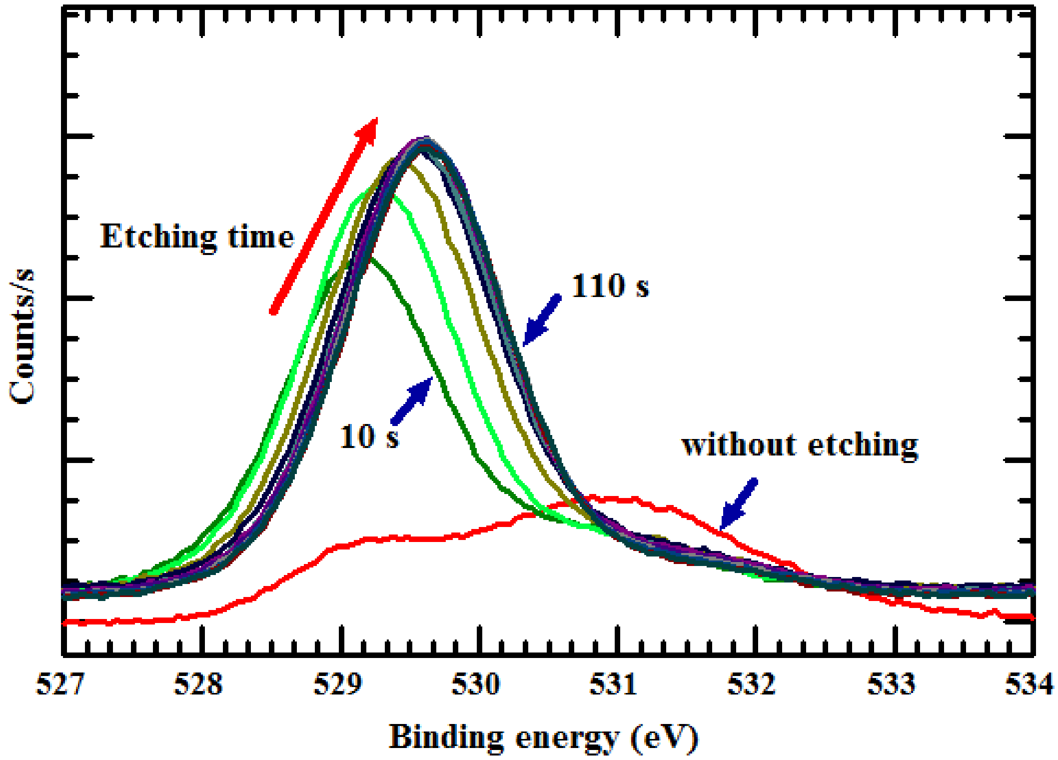

Figure 3.29. XPS O1s depth profile of the Pt at ZnO thin film

3.3.3 EFFECT OF POST ANNEALING ON THE PROPERTIES OF Pt/ZnO THIN FILMS

The effect of post annealing on the structural, morphological and optical properties of Pt/ZnO thin films was investigated. After preparing Pt at ZnO thin films, the samples were annealed at different temperatures: 500 °C, 600 °C and 800 °C for duration of 4 h. Morphological observations were carried out using FE-SEM before and after annealing. Figure 3.31 shows FE-SEM images before and after thermal treatment at T = 500, 600 and 800 ^{o}C. The surface of the as-prepared sample was smooth and uniform and showed no aggregation of platinum particles (Fig. 3.30 (a)). After 4 hours of annealing from RT to 400 ^{o}C, we found similar smoothness surface. By annealing the Pt/ZnO thin film at 500 ^{o}C we observed the beginning of agglomeration of Pt nanostructures with grain size less than 30 nm (Fig. 3.30 (b)). As the annealing temperature was increased to 600 ^{o}C a random distribution and various sizes of bright, round shape platinum nanostructures were observed. The nanostructures formed in this sample can be classified roughly in four main categories: A – particles of size less than 25 nm, B-particles of size between 25 and 100 nm, C-particles C of size between 100 nm and 200 nm, and D-particle of size between 200 and 300 nm). Fig. (3.30(d)) shows the distribution of Pt particles on the surface of the ZnO thin film after 4 hours annealing duration at 800 °C. In this sample, one can see clearly that the nanostructures of small size (A-particles and B-particles) have almost vanished. In addition, the grain sizes of Pt particles in (C and D) have increased indicating the formation the large particles at the expenses of the small ones. In addition, the shapes of the particles at high temperature (Fig. 3.30 (d)) become inhomogeneous. This variation in the shapes from rounded rectangular to spherical particles can be attributed to the difference of the time of the agglomeration process which usually happens at higher temperatures where the formation of larger particles are more energetically favored than smaller particles (e.g. two particles in the box A Fig. 3.30 (d)). As the nanostructures tries to lower its overall energy, small particles on the surface of a small (energetically unfavorable) will tend to diffuse and add to the surface of another particle (B, C and D in Fig. 3.30. Therefore, the number of smaller particles continue to shrink while larger particles continue to grow in size.

The structural and optical properties of Pt/ZnO thin films prepared via DC sputtering followed by post annealing at different temperature were investigated (not shown). Our results in this section are almost the same of that discussed in sec. 4.1.3 and since those results are comprehensively discussed there; we will avoid repeating the same discussion.

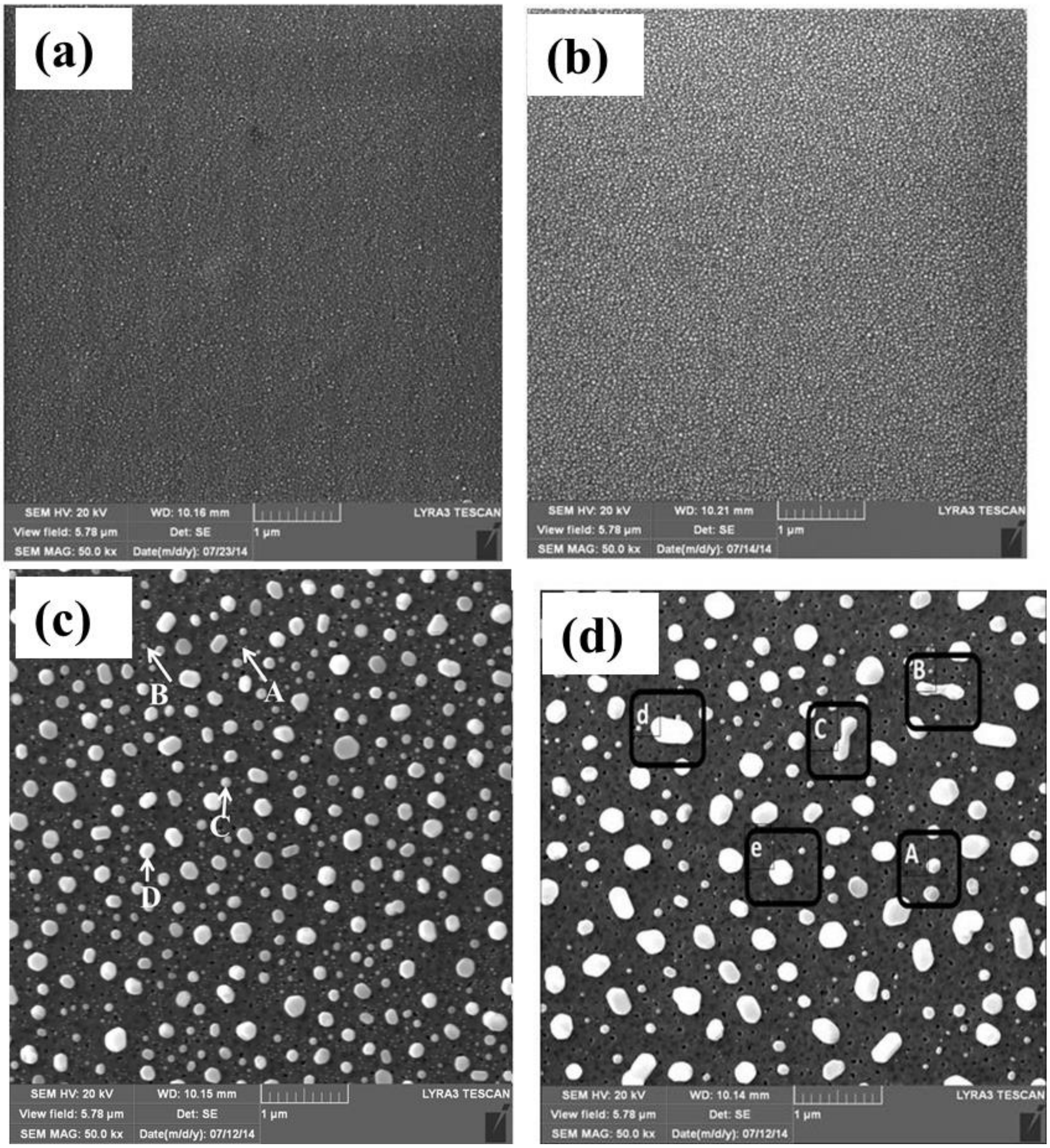

Figure 3.30. FE-SEM micrographs of Pt/ZnO thin film at (a) RT, (b) 500 ºC, (c) 600 ºC and (d) 800ºC

CHAPTER 4

MORPHOLOGICAL VARIATION OF ZnO THIN FILM BY PO_2 MODULATION

In this chapter we present the effect of the variation in the oxygen partial pressure (PO_2) on the morphological and structural properties of ZnO thin films. The ZnO films are oxidized in H_2/H_2O mixtures at different temperatures (400, 600 and 800ºC). We first calculate the theoretical values of PO_2 needed for Zn oxidation as a function of temperature based on the thermodynamics of Zn/ZnO coexistence. We then introduce a novel method to control the PO_2 by manipulating the ratio of H_2 and H_2O species. We find that the microstructural features of the surface of ZnO is affected by the variation of the oxygen partial pressure and annealing temperature.

4.1 THEORETICAL ASPECTS

At a given temperature, pressure and a well-defined oxygen partial pressure (PO_2), the below reaction will take place.

$$Zn(s)+\frac{1}{2}O_2(g)\rightarrow ZnO(s) \qquad 4.1$$

The equilibrium constant (K_1), concentrations of the products each raised to the power of its stoichiometric coefficient divided by the concentrations of the reactants each raised to the power of its stoichiometric coefficient [184], for this reaction is given by:

$$K_1 = \frac{PZnO}{PZn\, PO_2^{1/2}} \qquad 4.2$$

The standard Gibbs energy change (ΔG^0) at equilibrium is given by

$$\Delta G^0 = -RT\, ln(K_1) \qquad 4.3$$

Where R is the ideal gas constant = 1.987 cal K^{-1} mol^{-1} .

Since Zn and ZnO are pure solid, we can assume [Zn] and [ZnO] to be unity.

So equation 4.2 and 4.3 can be combined to be:

$$\Delta G^0 = -RT\, ln(PO_2)^{\frac{-1}{2}} \qquad 4.4$$

We can also write PO_2 in term of Gibbs free energy as following:

$$\left.\begin{aligned} \ln PO_2 &= \frac{2\Delta G^0}{RT} \\ PO_2 &= e^{\frac{2\Delta G^0}{RT}} \end{aligned}\right\} \qquad 4.5$$

According to the Hess's law, the standard Gibbs free energy change can be defined as the difference between sum of standard free energy energies of formation of products and standard free energy energies of formation of reactants [185].

The Gibbs free energy change for equation 4.1 can be written as:

$$\left.\begin{aligned} \Delta G^0 &= \sum \Delta G_{f\,(\text{products})} - \sum \Delta G_{f\,(\text{reactants})} \\ \Delta G^0 &= \Delta G_{f\,(ZnO)} - (\frac{1}{2}\Delta G_{f\,(O_2)} + \Delta G_{f\,(Zn)}) \end{aligned}\right\} \qquad 4.6$$

4.6

Since the standard Gibbs free energy changes for the formation of pure metals is zero, equation 4.6 become:

$$\Delta G^0 = \Delta G^0{}_{f(ZnO)}$$

However, the standard Gibbs free energy formation of ZnO is given by [186]:

$$\Delta G^0{}_{f(ZnO)} = -84{,}100 - 6.9T\log T + 44.1T$$

$$\text{Therfore, } \mathrm{PO_2} = \mathrm{e}^{(2/\mathrm{R})(84100/\mathrm{T} + 6.9\log\mathrm{T} - 44.1)} \qquad 4.7$$

Equation 4.7 gives the theoretical value of PO_2 needed for Zn/ZnO coexistence at a given temperature. The data obtained from equation 4.7 are listed in Table 4.1. From the table, it can be concluded that the amount of PO_2 required for oxidizing ZnO is very little. That is 10^{-30} atm PO_2 is enough to oxidize Zn at 600 ºC. These PO_2 values are negligible comparing with annealing in air in which PO_2 is about 0.21 atm (thirty orders of magnitude greater). Figure 4.1 displays the variation of equilibrium PO_2 as a function of temperature for Zn/ZnO pairs. By manipulating the (PO_2) across the line, one can cause Zn oxidation (below the curve) or ZnO reduction (above the curve). On the path of the curve Zn and ZnO will be coexistent.

Table 4.1. Theoretical calculations of PO_2 required for the formation of Zn and ZnO

T (K)	T (°C)	PO_2 (atm)	Log (PO_2)
523	250	6×10^{-60}	-59.2
573	300	7×10^{-54}	-53.2
673	400	1×10^{-44}	-44.0
873	600	2×10^{-32}	-31.7
1073	800	8×10^{-25}	-24.1
1273	1000	1×10^{-19}	-19.0

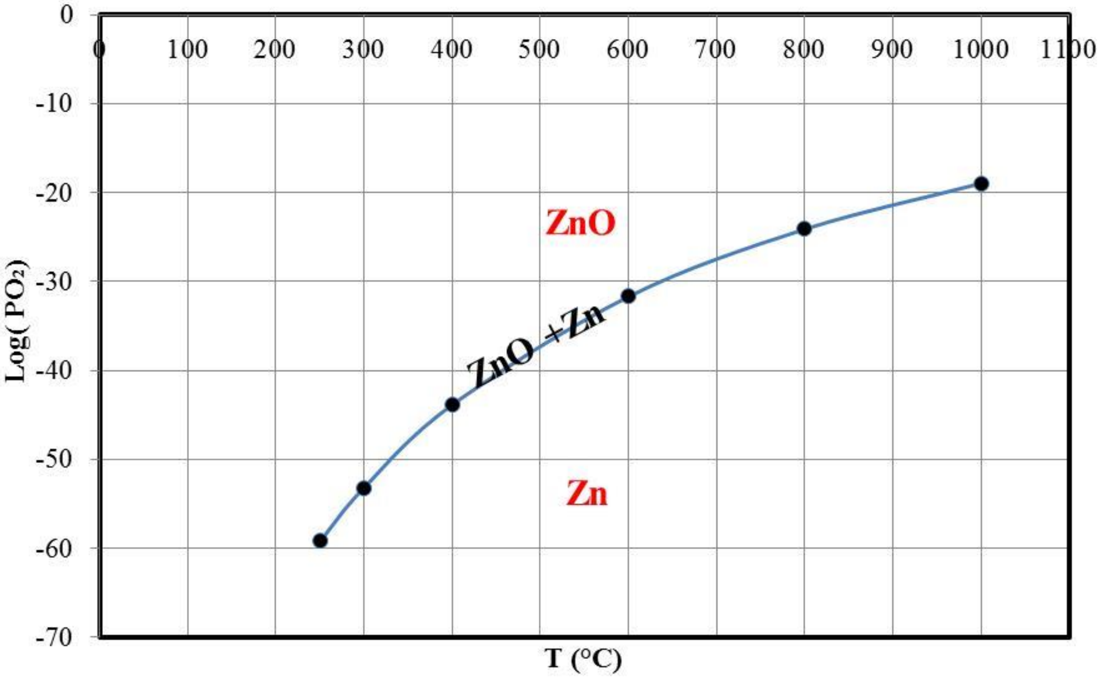

Figure 4.1. Temperature dependence of the equilibrium PO_2 for Zn/ZnO coexistence

4.2 METHOD OF CREATING THE DESIRED PO_2 USING H_2/H_2O MIXTURE

Commonly, there are two methods used to control the PO_2 [186]. One is using CO/CO_2 mixture, and the second by H_2/H_2O mixture.

According to the following reaction:

$$H_2 + \frac{1}{2}O_2 \rightarrow H_2O \qquad 4.8$$

The standard Gibbs energy change (ΔG^0) is given by

$$\Delta G^0 = -RT\, ln\, K_2$$

$$K_2 = \frac{PH_2O}{PH_2\, PO_2^{1/2}}$$

$$\Rightarrow \Delta G^0 = -RT\, ln \frac{PH_2O}{PH_2\, PO_2^{1/2}} \text{ or}$$

$$PO_2 = (\frac{PH_2O}{PH_2})^2\, e^{\frac{2\Delta G^o}{RT}} \qquad 4.9$$

The standard Gibbs free energy change for the formation of H_2O is given by [187]:

$$\Delta G_{H_2O} = \ -58900 + 13.1\ T \qquad 4.10$$

By combining equation 4.9 and equation 4.10:

$$PO_2 = (\frac{PH_2O}{PH_2})^2\, e^{\frac{2\ (-58900+13.1\,T)}{R\ T}} \qquad 4.11$$

From the last equation and by controlling the ratio of the concentration of H_2 and H_2O, one can calculate the theoretical values of PO_2. For example, if the partial pressure of water vapour and H_2 are 1000 and 999000 ppm respectively, the PO_2 at 523 K will be about 3×10^{-50} atm.

Antoine's equation is an empirical equation that describes the relation between the vapor pressure and it's temperature [188]

$$\log_{10}(P(mmHg)) = A - \frac{B}{T^*(^0C) + C} \quad 4.12$$

where A, B, and C are Antoine coefficients that vary from substance to substance. These constants for the reaction in equation 4.8 are: 8.07131, 1730.63 and 233.426 respectively [189]. T^* represent the temperature of the water. Table 4.2 shows the vapor pressure for different water temperatures. It is straight forward to put the partial pressure in ppm since we know that at 760 mmHg (1 atm.) the total concentration is 10^6 ppm.

Table 4.2. Water vapor pressure and water vapor concentration in pure water at different temperatures

T (ºC)	Log_{10} P	P (mmHg)	$H_2O \times 10^3$ (ppm)	% H_2O
0	0.66	5	6031	0.60
15	1.11	13	17013	1.70
20	1.24	18	23102	2.31
25	1.38	24	31580	3.16
30	1.50	32	41930	4.19
40	1.74	55	72901	7.29
50	1.97	93	121918	12.19
60	2.17	150	196842	19.68
70	2.37	234	307789	30.78
80	2.55	355	467408	46.74
90	2.72	525	691258	69.13
100	2.88	760	1000000	100.00

4.3 SAMPLE PREPARATION

For the synthesis of Zn thin films using DC sputtering, a high purity Zn target was used. Before sputtering, the gass substrates were ultrasonicated in acetone for 30 minutes. The Zn target was cleaned before each experiment by a pre-sputtering process for 30 s. The base pressure in the sputtering chamber was less than 3×10^{-6} Torr and the working presser was set to 7 mTorr by adjusting the Ar gas flow at 60 sccm. The deposition of Zn thin film was carried out using 100 watt power for 20 minutes.

4.4 SET-UP FOR CREATING THE DESIRED PO_2

Figure 4.2 shows the schematic of the experimental set-up used for creating the desired PO_2 of Zn films. In the beginning, the prepared Zn film was placed in a tube furnace (OTF-1200X from MTI Corp.). H_2 gas (14.7 psi (1 atm)) was introduced through calibrated flow meter to a closed flask containing deionized water and then to the tube furnace. The concentration of H_2O above the surface and the variation of the ratio between the water vapor and the hydrogen (H_2/H_2O) was achieved by heating the deionized water at different temperatures (from 20 °C to 60 °C). The Zn thin films were annealed in the tube furnace at different temperatures (from 400 ºC to 800 ºC). The concentration of water vapor, Gibbs free energy and the PO_2 are calculated and listed in Table 4.3. All experiments were carried out in the fume hood due to flammability of the gas and all samples were tested at the same environmental conditions.

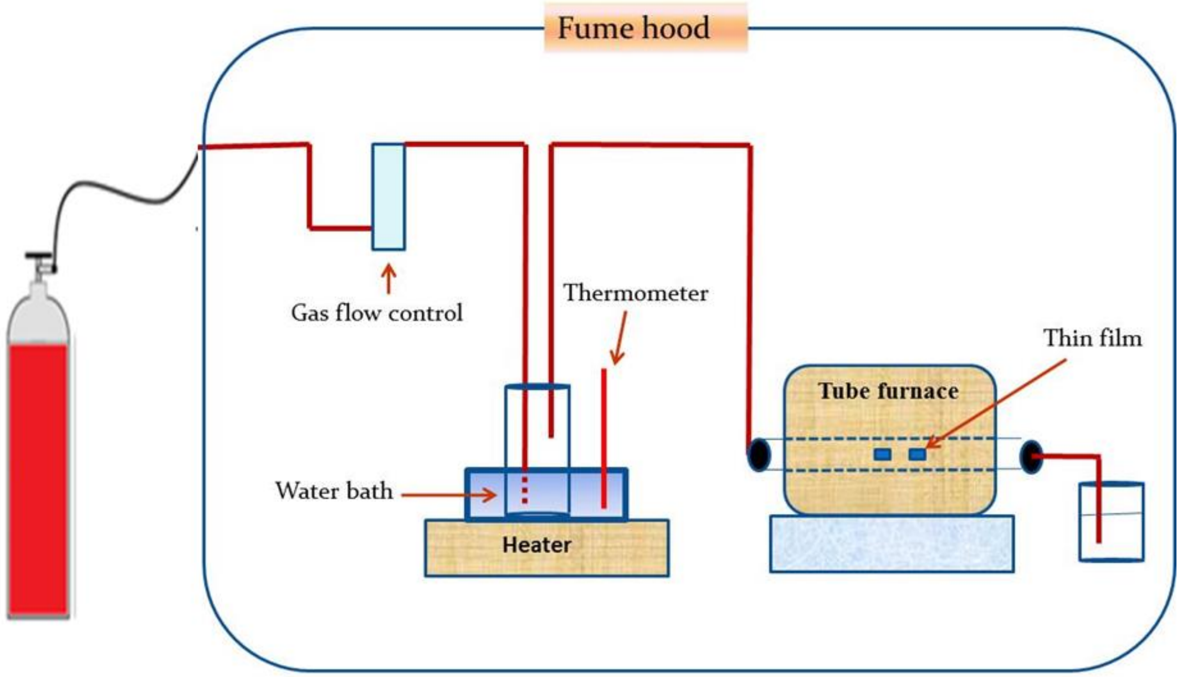

Figure 4.2. Sketch displaying the set-up used for controlling the oxidation of Zn films in H_2/H_2O mixture

Table 4.3. Variation of the PO_2 obtained by manipulating the H_2/H_2O mixture

Water Temp. (ºC) (+/- 0.5° C)	Film Temp. (ºC) (+/- 1° C)	% H_2O	ΔG (cal.) × 10^3	PH_2O/PH_2	PO_2 (atm)
20	200	2.31	-52.7	0.0236	1 E-52
20	400	2.31	-50.1	0.0236	2 E-36
20	600	2.31	-47.5	0.0236	9 E-28
20	800	2.31	-44.8	0.0236	3 E-22

4.5 MICROSTRUCTURAL EVOLUTION IN ZnO FILMS FABRICATED FROM Zn FILMS OXIDATION IN H_2/H_2O MIXTURE

Structural and microstructural examination of the as prepared Zn film and the ZnO films products after each of the oxidizing reactions was conducted by XRD and FE-SEM. Figure 4.3 shows the FE-SEM images of as deposited Zn film and ZnO films oxidized for 2 hours in H_2/H_2O mixture at 400, 600 and 800 ºC. The as deposited Zn film (4.3 (a)) shows rough morphology and a high density of nanoparticles. Figure 4.3 (b-d) represent the FE-SEM images of ZnO films oxidized at different PO_2: 2E-36 atm., 9E-28 atm. and 3E-22 atm. corresponding to annealing the samples in 2.31 % H_2O and 97.69% H_2 at 400 ºC, 600 °C and 800 ºC respectively. The FE-SEM micrograph of the ZnO sample oxidized at 400 ºC show that the films morphologies start to change. As the annealing temperature increases from 400 °C to 600 ºC, the ZnO film shows porous surface compared to as deposited Zn film and ZnO film oxidized in H_2/H_2O mixture at 400 ºC. Figure 4.3 (d) shows the FE-SEM micrograph of the ZnO film oxidized in H_2/H_2O mixture at 800 ºC, it appears that the surface of the film turned from continuous and dense to individual islands and grains.

In order to confirm that the morphology change was the result of oxidation of the Zn thin films at very low PO_2, a series of Zn samples prepared by DC sputtering at the same conditions were annealed in air (0.21 atm. O_2) at different temperatures (from 400 °C to 800 ºC). Figure 4.4 displays the FE-SEM micrographs of the ZnO film oxidized in air. As can be seen, by increasing the annealing temperature, the small ZnO grain size coalesce together to make larger grains with inhomogeneous distribution. Figure 4.5 displays a comparison in morphology between the ZnO samples annealed at 800 °C in H_2/H_2O mixture and in air. As can be seen the grain size and the density in both samples are clearly different.

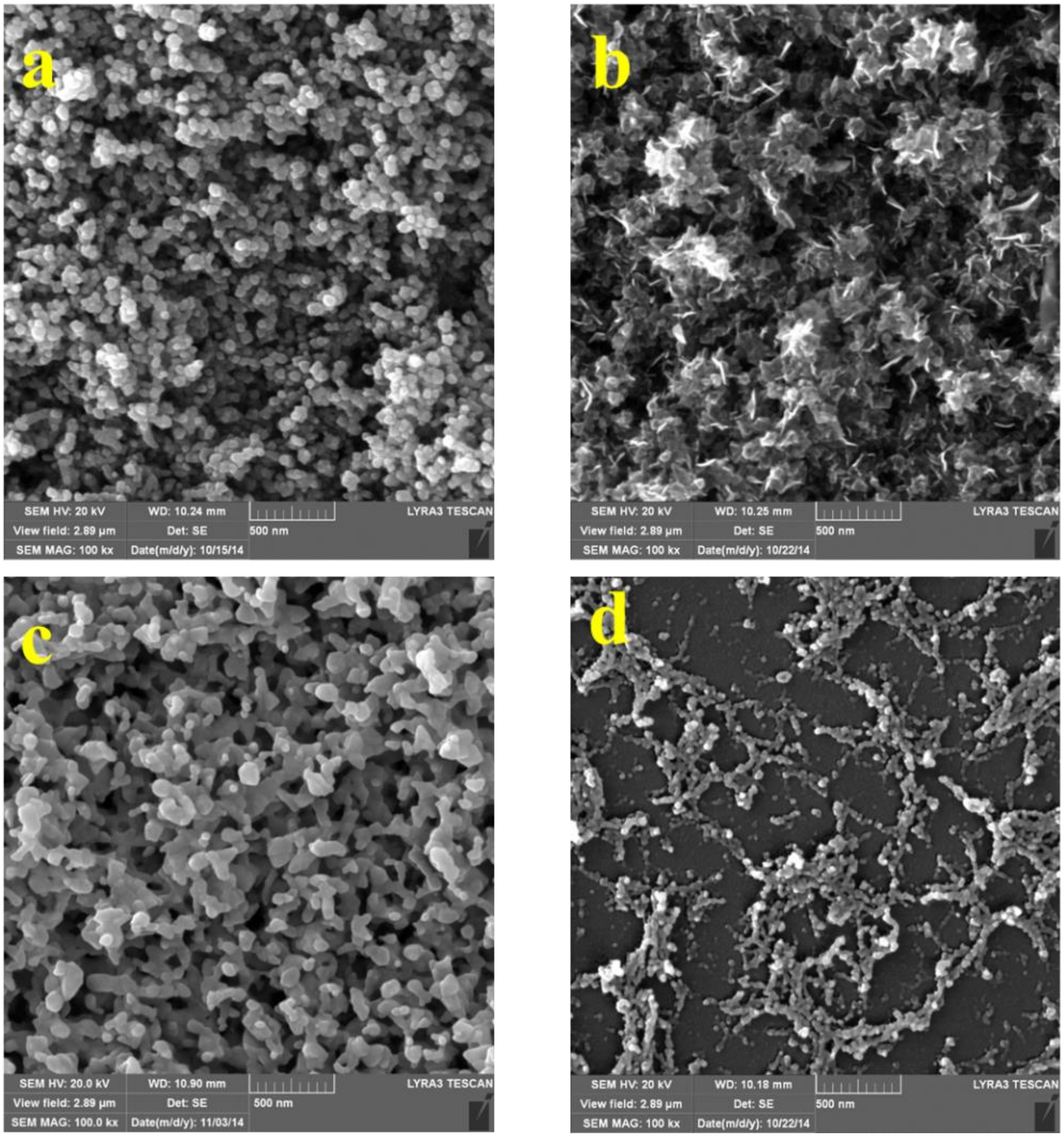

Figure 4.3. FE-SEM micrographs of (a) as prepared Zn films and ZnO films annealed for 2 hours in H_2/H_2O mixture (2.31 % H_2O) at (b) 400 (c) 600 and (d) 800 °C

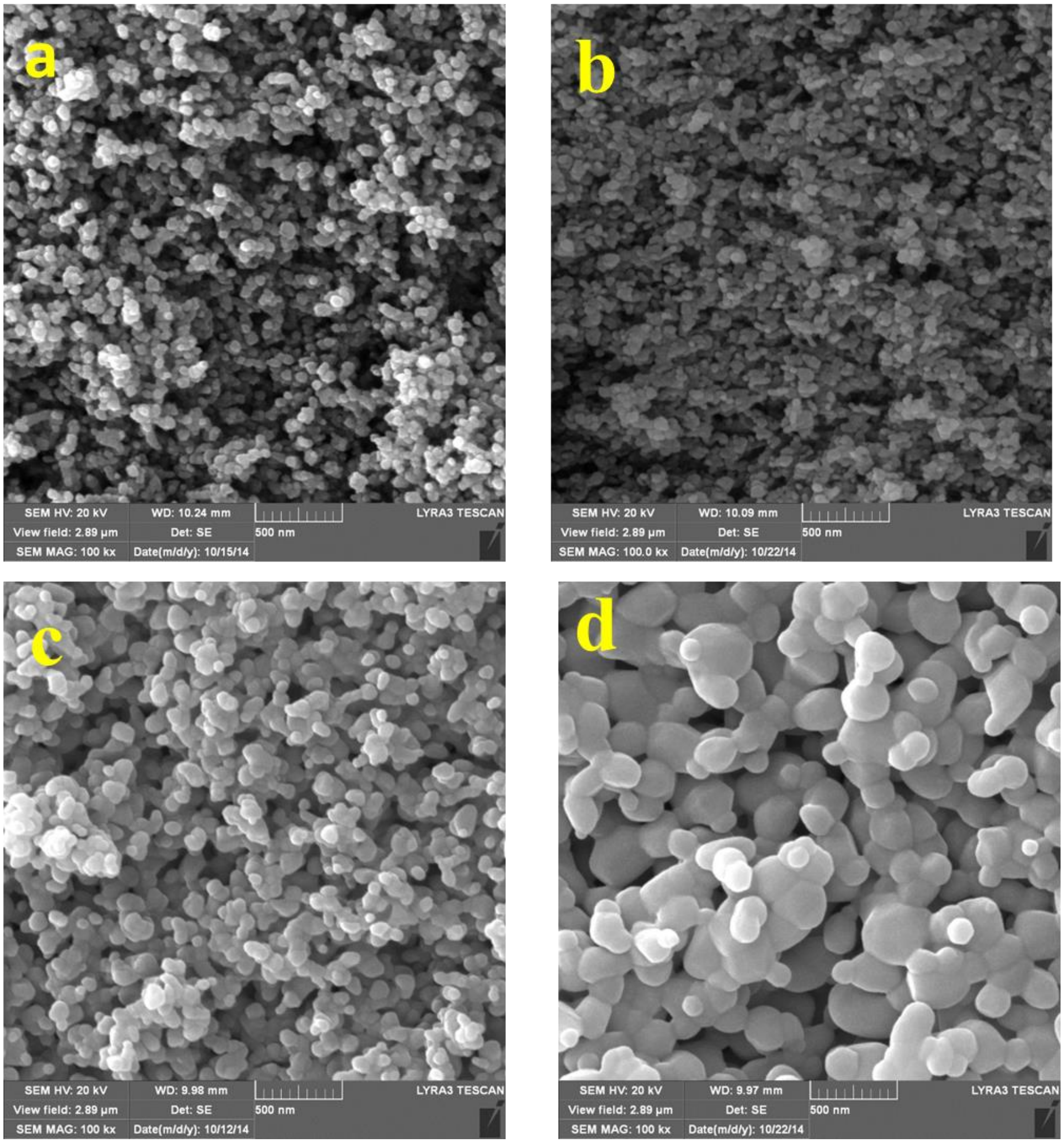

Figure 4.4. FE-SEM micrographs of (a) as prepared Zn films and ZnO thin films annealed for 2 hour in air at (b) 400 (c) 600, and (d) 800 °C

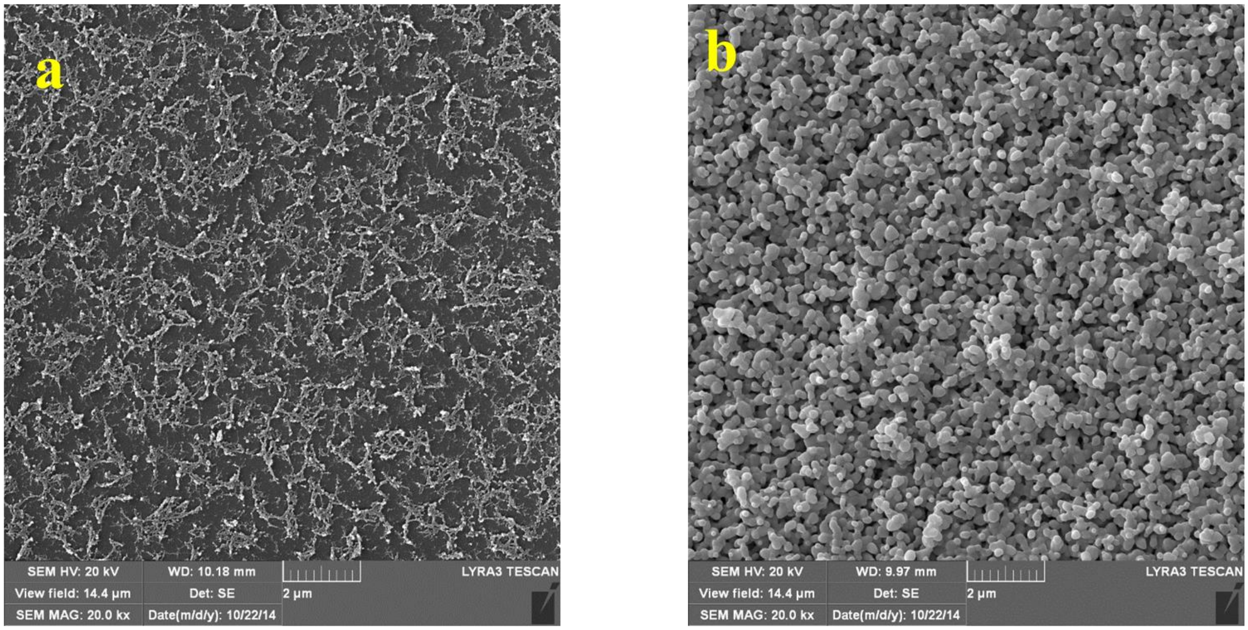

Figure 4.5. FE-SEM micrographs of ZnO thin films prepared by oxidizing metallic Zn at 800 °C (a) in H_2/H_2O mixture, and (b) in air

To investigate the structural aspects of the as-prepared Zn and ZnO thin films oxidized in air and low PO_2 systematic analysis of their XRD patterns was carried out. Figure 4.6 shows the XRD patterns of as prepared Zn film and ZnO films annealed at different temperatures (400, 600 and 800 ºC) in H_2/H_2O mixture. Figure 4.6 (a) shows that all XRD peaks of the as prepared Zn film are assigned to the typical pattern of hexagonal structure Zn. Figure 4.6 (b-c) show that all the XRD peaks correspond to wurtzite hexagonal structure ZnO. The absence of the Zn characteristic peak located at $2\theta = 42°$ in Fig. 4.6 (b-c) indicates the full transformation of Zn into ZnO. By increasing the annealing temperature to 800 ºC, we found that all XRD peaks disappeared, as seen in fig 4.6(d/), due to the melting of the film as was confirmed by FE-SEM (Fig. 4.6 (d)).

Figure 4.7 shows the XRD patterns of Zn films oxidized in air at 400, 600 C and 800 ºC. As clear from the figure, the intensity of the annealed ZnO peaks increase by increasing the annealing temperature from 400 to 800 °C. In addition, the FWHM of the characteristic XRD peak of ZnO ($2\theta = 36.2^{o}$) decrease by increasing the annealing temperature which means that the crystallite size increases.

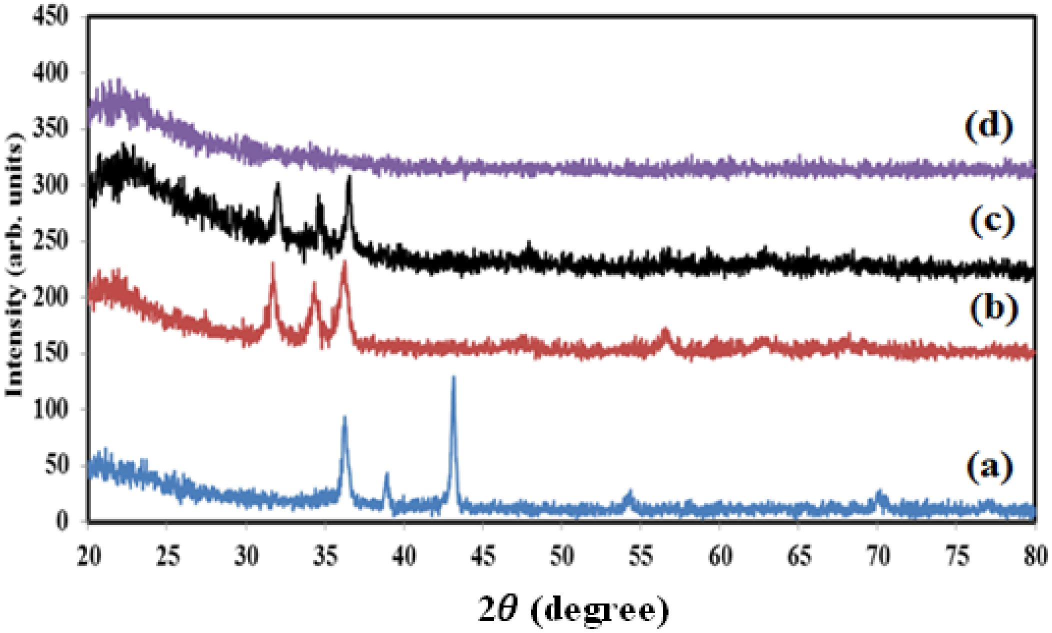

Figure 4.6. XRD patterns of (a) as prepared Zn film and ZnO films oxidized in H_2/H_2O mixture at (b) 400 °C (c) 600 ºC, and (d) 800 °C

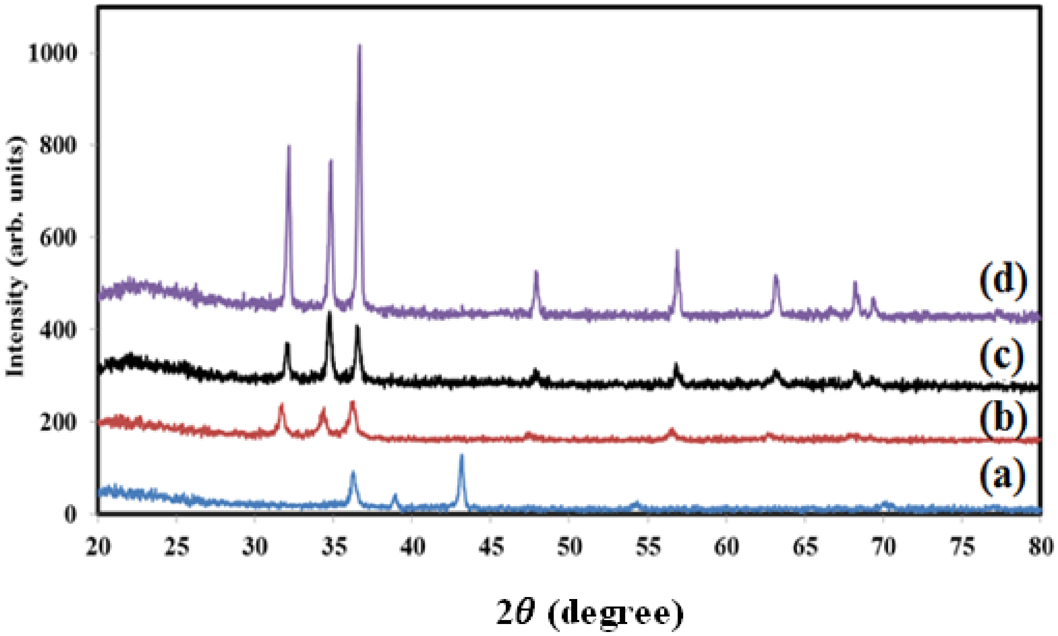

Figure 4.7. XRD patterns of (a) as prepared Zn film and ZnO films oxidized in air at (b) 400 °C (c) 600 ºC, and (d) 800 °C

CHAPTER 5

GAS SENSING BEHAVIOR OF ZnO-BASED THIN FILMS

In this chapter, the gas sensing behavior of the M/ZnO (M = Ag, Au or Pt) thin films towards hydrogen as a function of temperature at different H_2 concentrations was investigated and compared with that of pure ZnO. All the films showed promising response towards H_2 even at very low concentration (close to part per billion (ppb) level). Among them, the performance of Pt/ZnO film was the most promising with the highest response and shortest response time. The effect of the density of Pt nanostructures on the performance of gas sensing was investigated. the optimal operating temperature (in terms of higher response signal and shorter response time) of the Pt/ZnO sensors was 300ºC while in the case of Ag- and Au/ZnO films, the optimum temperature was 400ºC. A plausible mechanism for the observed enhancement in the sensing behavior of Pt/ZnO sensor towards H_2 is proposed. The response of the Pt/ZnO sensors toward NO_2 and NH_3 was also investigated.

5.1 GENERAL MECHANISM OF ZnO GAS SENSING

In order to understand the physics behind the change in the electrical resistance when metal oxide semiconductors, such as ZnO, are exposed to specific adsorption, it is useful to start with the concept of band bending in semiconductor. This was which introduced for the first time by Schottky and Mott in 1938 to explain the metal-semiconductor contacts [190]. This concept is central to explain the operation mechanism for gas sensors.

5.1.1 METAL/ ZnO CONTACT

When a metal comes into contact with ZnO, which is n-type semiconductor, free electrons will transfer between metal and ZnO based on the work function difference. If the work function of metal (ϕ_m) is greater than the work function of the ZnO (ϕ_s), the electrons will flow into metal until Fermi level in both sides become the same (left side of Fig. 5.1). These electrons will leave positive charge at the interfaces resulting in a depletion region. The term "depletion region" refers to the insulating region within the conduction band where the free electrons have been forced away to move toward the surface by an electric field [191,192]. As the electron in the ZnO experiences repulsion from the negative charge located in the metal side, the potential energy of the electron will increase and the ZnO band bends upward [192]. The surface barrier (ϕ_{SB}) created during this contact can be defined by the following formula:

$$\phi_{SB} = \phi_m - \chi_s \qquad (5.1)$$

where χ_s is the electron affinity.

On the contrary, when $\varphi_s > \varphi_m$ (right side of Fig. 5.1), electrons will move into ZnO leading to a positive charge on the metal and extra electrons accumulate at the interface resulting in an accumulation layer, and the bands of ZnO will bend downward.

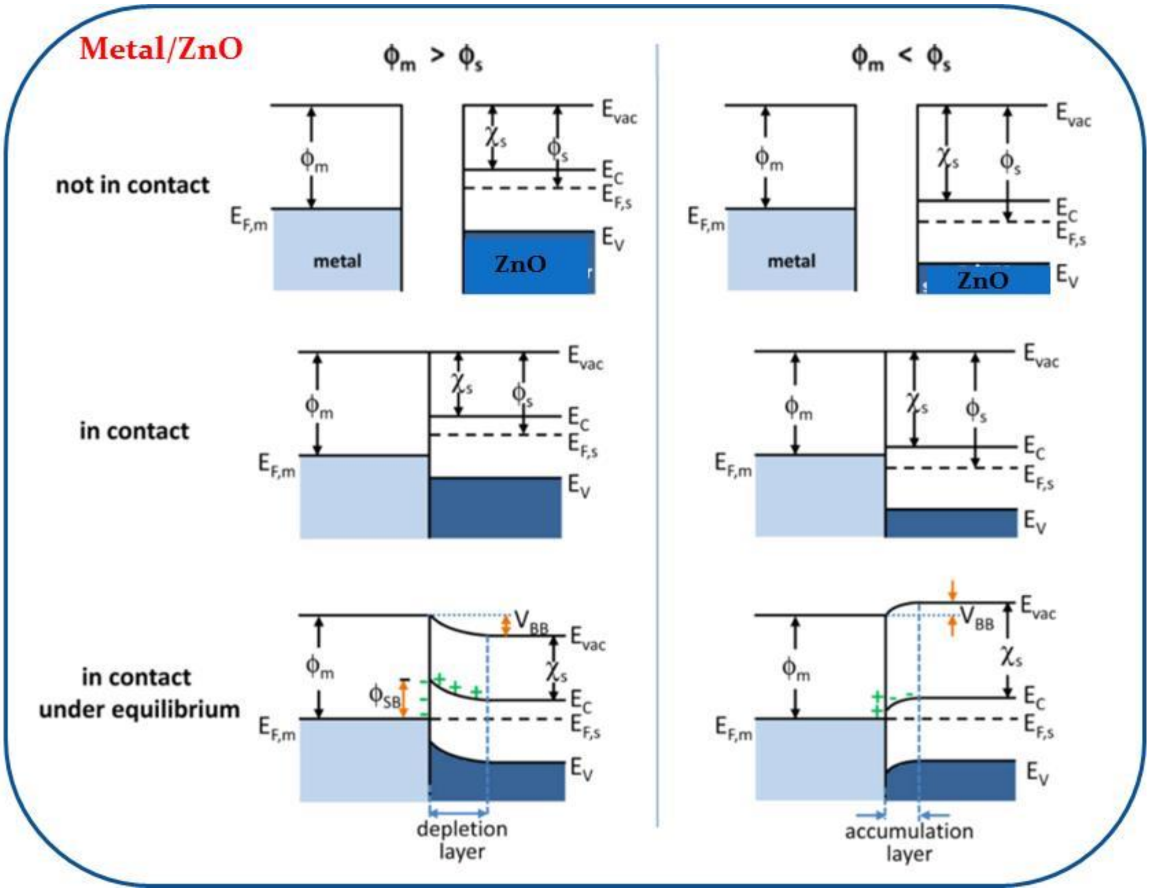

Figure 5.1. Energy band diagram of metal/ZnO contact [192]

5.1.2 GAS ADSORPTION INDUCED BAND BENDING

Similar to metal/ZnO contact, the bands of the ZnO can be bent upward or downward depending on specific adsorption of atoms. If one grain of ZnO (Fig. 5.2 (a)) is exposed to atmospheric oxygen, and due to the high electronegativity of the oxygen,electron transfers from the conduction band to the adsorbed oxygen, adsorbed O_2^-, O^-, and O^{2-} ions are formed. This leads to the depletion of electrons and creation of a space charge region near the surface of ZnO. As the electron in the ZnO experiences repulsion from the negative charge located on the surface, the potential energy of the electron will increase and the bands bend upward (fig 5.2 (b)).

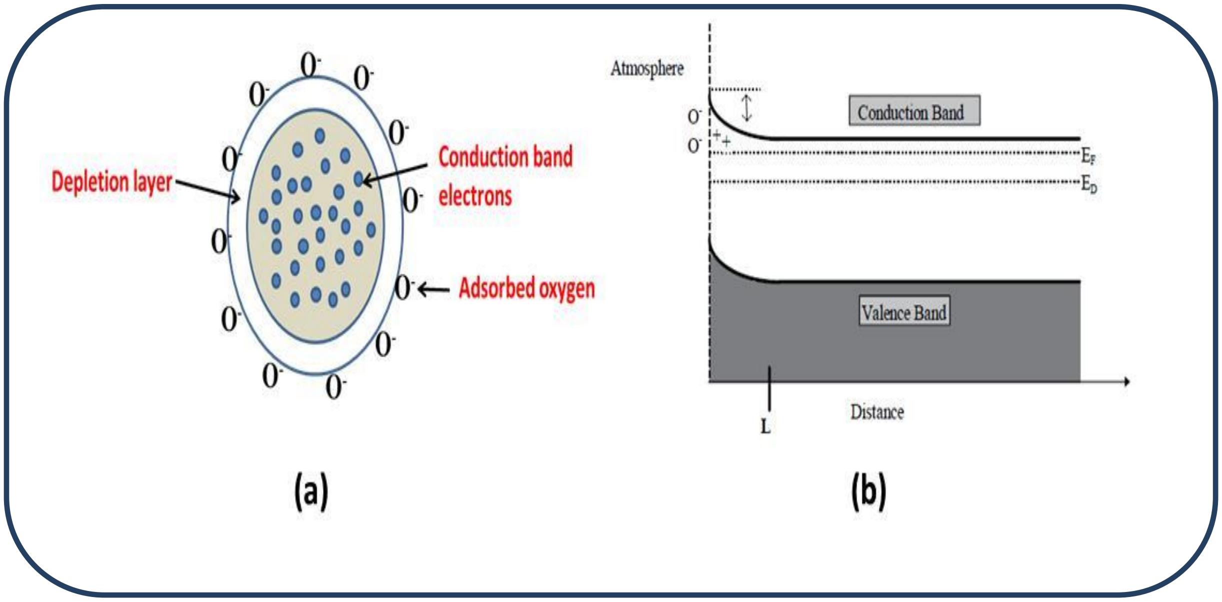

Figure 5.2. Schematic representation of (a) adsorbed oxygen on one grain of ZnO (b) the band structure in the presence of absorbed oxygen.

It has been proved experimentally that dominant oxygen species are temperature dependent as follows [193]:

1- Molecular O_2 below 150 °C

2- Atomic O^- between 150 °C and 300 °C

3- Atomic O^{2-} above 300 °C

The sequence of reactions leading to this is shown below:

$$O_{2\,(air)} + ZnO_{surface} \longrightarrow O_{2\,(ads)} \qquad (5.2)$$

$$O_{2\,(ads)} + e^- \longrightarrow O^-_{2\,(ads)} \qquad (5.3)$$

$$O^-_{2\,(ads)} + 2\,e^- \longrightarrow 2\,O^-_{2\,(ads)} \qquad (5.4)$$

When the surface of ZnO is exposed to reducing gases such as hydrogen, the reduced gas reacts with the adsorbed charged oxygen species on the surface of ZnO leading to a donation of electrons to the conduction band and the conductivity is seen to increase [194].

$$2X_{gas} + 2O^-_{(ads)} \longrightarrow 2XO_{gas} + e^- \qquad (5.5)$$

$$2X_{gas} + O^{2-}_{(ads)} \longrightarrow 2XO_{gas} + 2e^- \qquad (5.6)$$

where *X* is the reducing gas of interest.

Figure 5.3 (a) shows the schematic of two ZnO grains with high barrier high due to the presence of adsorbed oxygen, when hydrogen gas, for example, is introduced to the surface of ZnO, the barrier high is reduced (Fig.5.3 (b)) so electrons can move from one grain to another leading to the reducing of the resistivity.

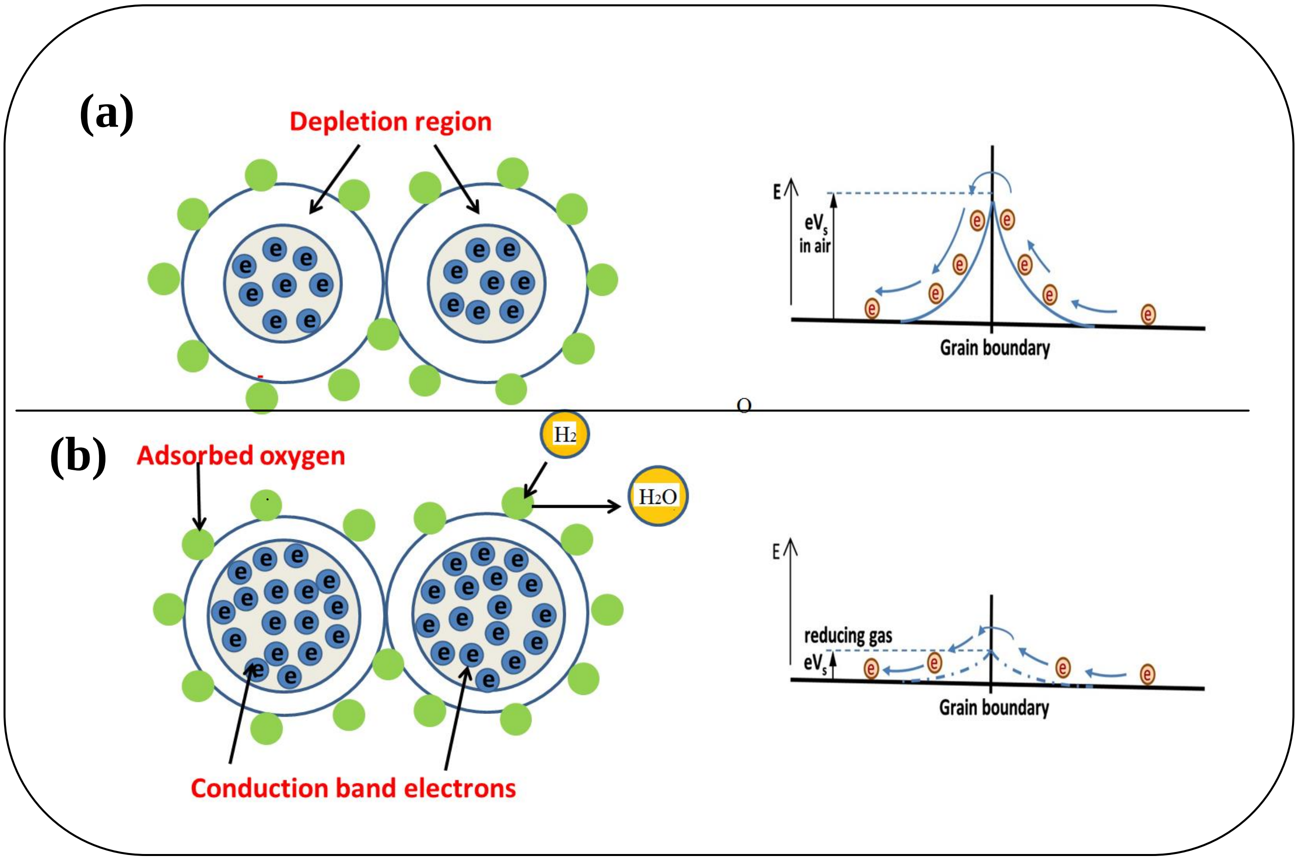

Figure 5.3. Sensing model of ZnO showing the depletion region and energy barrier (eV_S) at the intergranular contact when (a) atmospheric oxygen, and (b) reducing gases adsorbed on its surface

Since the depletion layer and barrier height are the key factors in the gas sensing mechanism, it might be useful to calculate the barrier potential (qV_s) and the voltage across the depletion region of the ZnO surface.

Poission equation, that describes the change in the potential as a function of distance through the space charge region in one dimensional, is given by [191]:

$$\frac{d^2V}{dx^2} = \frac{q\,\rho(x)}{\varepsilon\,\varepsilon_0} \tag{5.7}$$

Where V is the voltage that can be related with the electric field as

$$E = -\frac{dV}{dx} \tag{5.8}$$

$\rho(x)$ represents the net density of charges in the space charge region.

$$\rho(x) = (n - p + N_d - N_a) \tag{5.9}$$

ε is the dielectric constant of the ZnO which is around 10 [195] and ε_0 is the permittivity of free space.

To simplify equation 5.7 let us assume:

A- The minority carrier is negligible ($p = 0$).

B- The majiorty carrier in the depletion layer is negligible ($n = 0$ when $0 < x < x_0$) where x_0 is the thickness of the depletion layer.

C- At $x > x_0$, $n = N_d$

Now equation 6.7 can be rewritten after using the above boundry conditions of equestion 5.9 and by adding equation 5.8 as:

$$\left.\begin{aligned} \frac{d^2V}{dx^2} &= \frac{-q}{\varepsilon\,\varepsilon_0} N_d = -\frac{dE}{dx} && 0 \langle x \langle x_0 \\ &= 0 && x \rangle x_0 \end{aligned}\right\} \tag{5.10}$$

The first differential equation of equation 5.10 is

$$E(x) = \frac{dV}{dx} = \frac{q}{\varepsilon\,\varepsilon_0} N_d\,(x - x_0) \tag{5.11}$$

From equation 5.11, the electric field at the surface of ZnO, where ($x = 0$) will be:

$$E(x) = \frac{-q}{\varepsilon\,\varepsilon_0} N_d\,x_0 \tag{5.12}$$

Integration of equation 6.11 yields

$$V(x) = \frac{q\,N_d\,(x - x_0)^2}{2\,\varepsilon\,\varepsilon_0} \tag{5.13}$$

This equation gives the value of the voltage across the depletion layer. The barrier height (qV_s at x = 0) will be

$$qV_s = \frac{q^2\,N_d\,{x_0}^2}{2\,\varepsilon\,\varepsilon_0} \tag{5.14}$$

5.2 GAS SENSING SET-UP

Figure 5.4 shows the schematic of the experimental setup used for assessing the gas sensing attributes of the films made in this work. A small-volume test-stage, fully equipped with sample pad and gold-tipped tungsten contacts, procured from Linkam Scientific instruments (Model HFS-600E-PB4, UK) was used as the test chamber (Fig. 5.5). The unit could be used for temperatures as high as 600 °C and cooled very quickly. Commercial grade dry air was used as the background/reference gas. The film resistance and change in resistance in the presence of various concentrations of hydrogen were measured relative to those in the background air. A gas tank (1%H_2 - balance N_2) was used as the test gas source; the concentration of hydrogen in the test chamber was varied by mixing with air via digital mass flow controllers (MFCs, Horiba, USA), controlled through an external X PH-100 power supply. The signal in the form of film resistance was measured as a function of time (i.e., H_2 concentrations, at different temperatures) using an Agilent B1500A Semiconductor Device Analyzer (SDA) (Fig. 5.6).

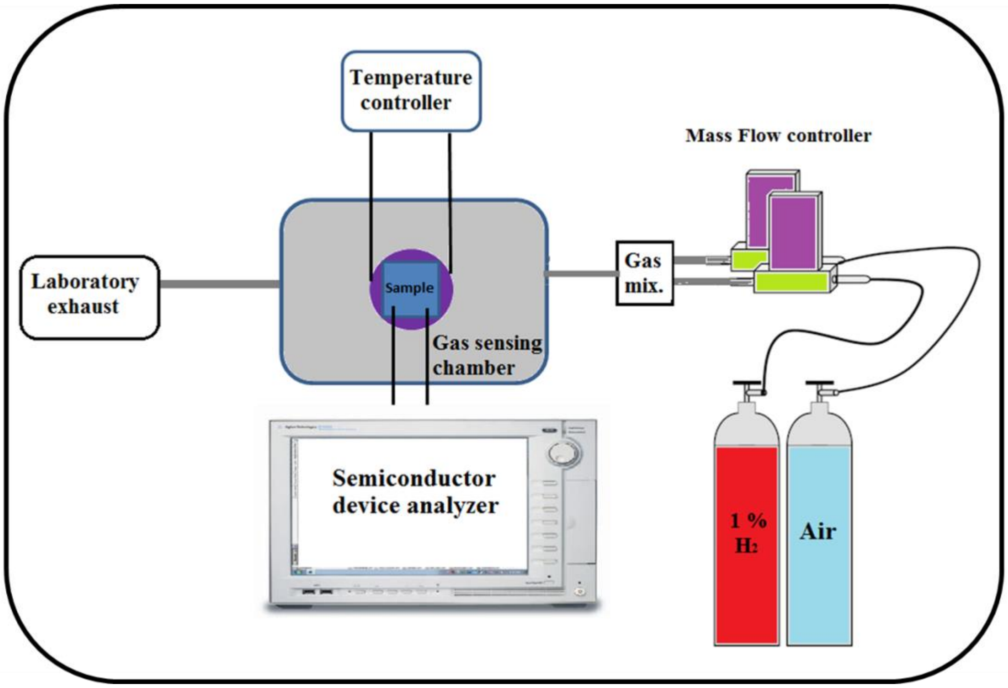

Figure 5.4. Schematic of the sensor testing facility

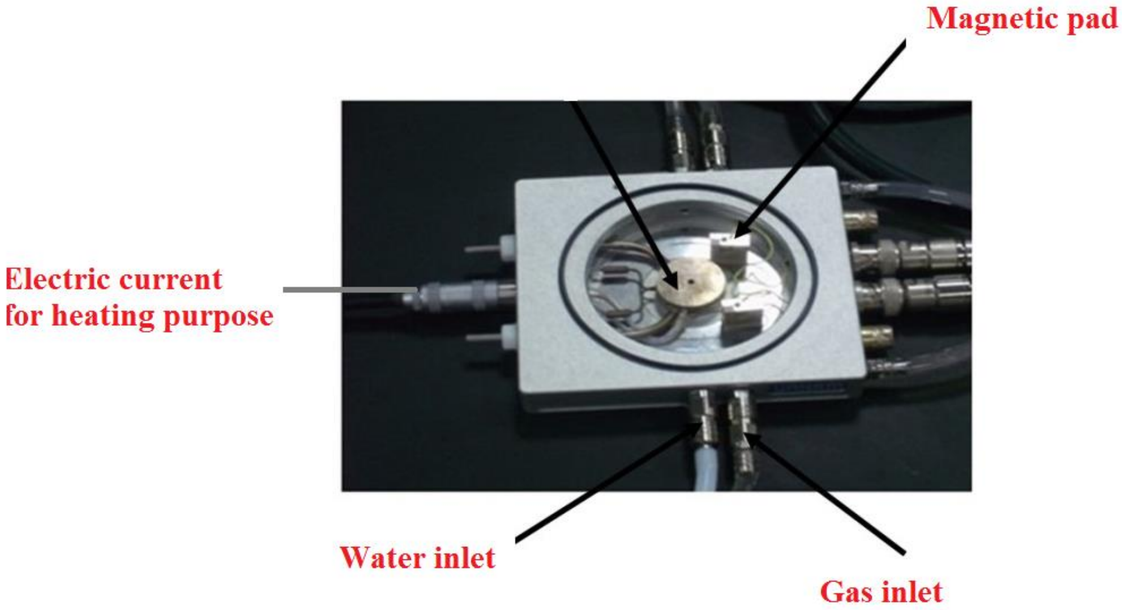

Figure 5.5. Photograph of the gas chamber used for gas sensing applications

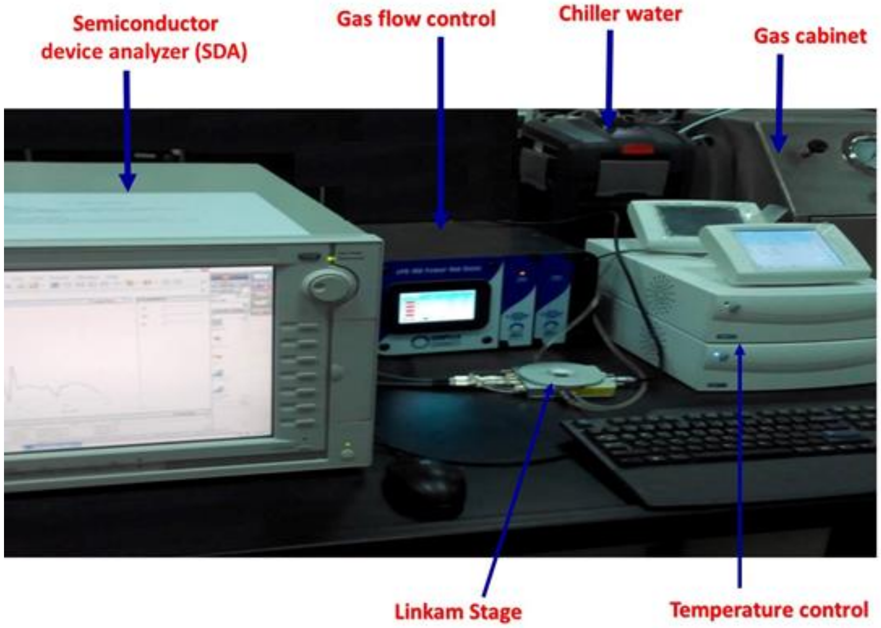

Figure 5.6. Gas sensing apparatus at CENT, KFUPM

5.3 SENSOR FABRICATION

In order to fabricate ZnO-based thin film sensor, different ZnO-based thin film were fabricated by DC reactive sputtering of metallic zinc at 100 W in oxygen for 40 min. on Al_2O_3 substrates with pre-interdigitated Au electrodes (IDE) (240 nm thick with 250 μm interspace distance) supplied by the Electronic Design Center at Case Western Reserve University, Cleveland, USA. Figure 5.7 shows the FE-SEM of an IDE on Al_2O_3 substrate.

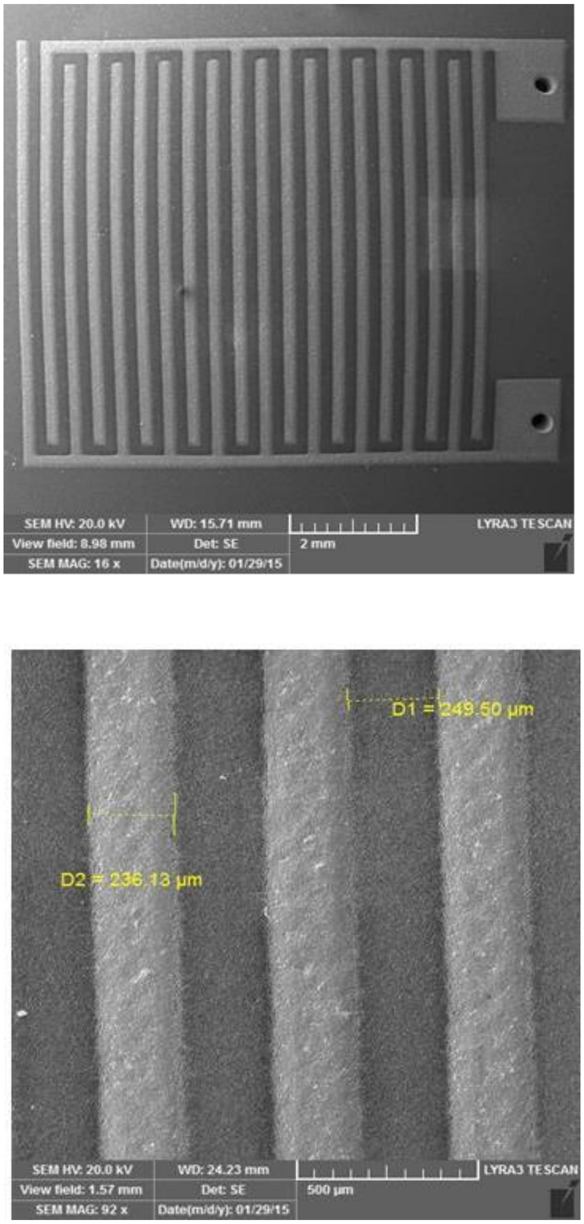

Figure 5.7. Interdigitated electrodes after applying the sensing material

As explained in chapters 3 and 4, two different methods were developed to modify the surface of ZnO thin films. In the first method, the surface of ZnO thin films was modified by incorporating nanostructures of Pt, Au, Ag. In the second method, ZnO thin films were prepared by oxidizing of Zn in H_2/H_2O mixture. In case of the first method, four ZnO thin films prepared by DC reactive sputtering technique were prepared. After that, one of ZnO thin films was kept as a reference while the rest were Ag, Pt and Au deposited followed by subsequent annealing at 600 °C for 3 hours. A description of the parameters used for preparing pure ZnO (reference sample), Ag/ZnO, Au/ZnO and Pt/ZnO thin films is listed in Table 5.1. It is important to mention that the parameters used for depositing metal layers on ZnO thin film are normalized based on the results of chapter 3 to have almost the same density of nanostructures on the surface of ZnO thin film. In the second method, Zn thin films were prepared by DC sputtering with the following parameters: (a) power: 40 watt (b) time: 20 s (c) working pressure: 4 mTorr. After that, the thin film was annealed at 600 ºC in H_2/H_2O mixture while the temperature of the deionized water was 40 ºC.

Table 5.1 Sputtering parameters used for preparing pure ZnO, Ag/ZnO, Au/ZnO and Pt/ZnO sensors

	Target	Base pressure (μTorr)	Working pressure (mTorr)	Deposition power (watt)	Deposition time	Target substrate distance(cm)	Sample
1	Zn	9	4	100	40 min.	10	ZnO
2	Ag + Zn	9	4	100 (ZnO) 20 (Ag)	25 s	10	Ag/ZnO
3	Au + Zn	9	4	100 (ZnO) 30 (Au)	30 s	10	Au/ZnO
4	Pt+Zn	9	4	100 (ZnO) 30 (Pt)	30 s	10	Pt/ZnO

5.4 HYDROGEN GAS SENSING MEASUREMENTS

Prior to introducing hydrogen, the chamber was purged with dry air for 1h at a flow rate of 40 sccm to attain steady-state baseline film resistance, at all temperatures of measurements. The main purpose of using air is to use as a reference gas. The concentration of hydrogen is presented in ppm (parts per million) units, indicating the number of hydrogen molecules per total number of molecules in the mixture. The concentration of hydrogen (C_{H_2}) was varied according to this formula:

$$C_{H_2}\,(ppm) = C_{cy.}\left(\frac{F_{H_2}}{F_{H_2} + F_{air}}\right)$$

where C_{cy} is the concentration of hydrogen inside the cylinder which is 10,000 ppm, F_{H_2} and F_{air} are the flow rate of hydrogen gas and the air gas respectively.

5.5 ACTIVE SENSING MATERIAL SYSTEMS

ZnO is one of the metal oxides that are commonly used for gas sensor applications. Due to its unique properties such as low fabrication cost, high electron mobility, nontoxicity and good thermal stability, it has been used to detect many gases. However, the response of ZnO toward some gases is still low and cannot satisfy current requirements for fast and trace detection. In the following sections, we study the effect of modifying the surface of ZnO thin film by Ag, Au and Pt on gas sensing performance.

5.5.1 Ag/ZnO SYSTEM

In order to study the gas sensing performance of Ag/ZnO sensor, the two Source Measureurment Units (SMU) channels of the SDA system were connected to the two end points of the interdigitated electrodes (IDEs) of the sensor. The voltage of the SMU was 5V. Figure 5.8 shows the resistance of the Ag/ZnO at 300 °C in air background. As can be seen, the resistance of the sensor was constant for 2 hours. Any change in the resistance after introducing the hydrogen should be due to the interaction between the hydrogen and the surface of the Ag/ZnO sensor.

Different levels of H_2 (75, 150, 300, 600, 1,200) ppm in the temperature range 200-400 ºC were introduced to the gas chamber to measure the change of the resistivity of the Ag/ZnOwith the introduction of H_2. The response of the Ag/ZnO sensor operated at 400 ºC at the above concentrations is presented in Fig. 5.9. Three are a few points to note. First, the resistance at all concentrations decreased in the presence of H_2. Second, the higher the concentration, the greater the response as expected for sensors. Finally, the resistance of the sensor does not return to the initial baseline. Upon shutting off the H_2 source, the resistance of the sensor does not return back to the initial baseline resistance. This can be attributed to the presence of residual H_2 over the surface of the sensor. Figure 5.10 shows good repeatability of the gas sensor by showing multiple exposures to a 600 ppm of hydrogen at 400 °C. The average of the sensor response toward 600 ppm at 600 °C is about 25.8 % with the standard deviation less than 1.5%.

In order to study how the sensor acts when the concentration of hydrogen is increased or decreased with no purge in between, the hydrogen concentration was varied as 125 ppm, 250 ppm, 500 ppm, 750 ppm, 1000 ppm followed by going back to 125 ppm. Figure 5.11 shows that the resistance decreased in the presence of hydrogen and recover backed to the initial resistance (which indicates that the sensor is stable.

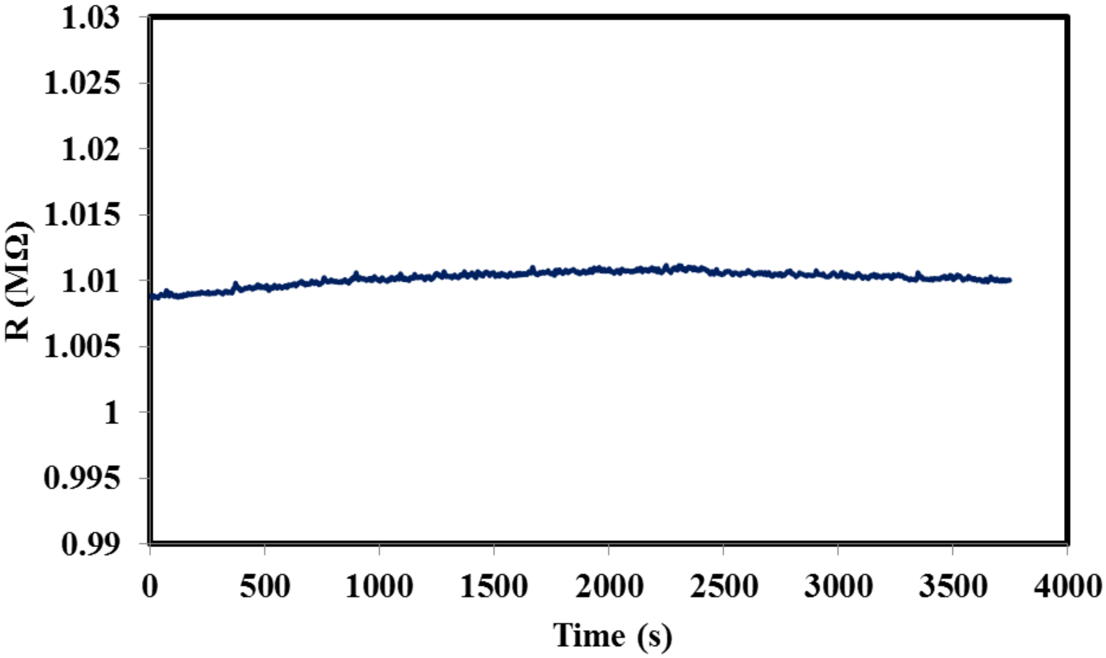

Figure 5.8. Stability of the Ag/ZnO thin film resistivity in air at 300 °C

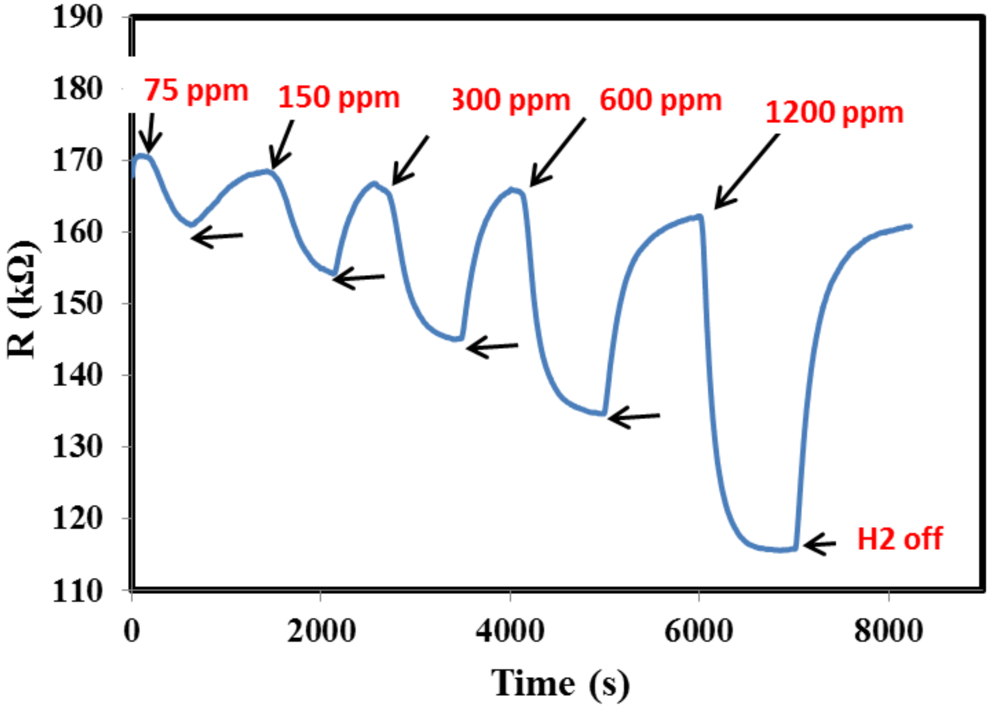

Figure 5.9. Ag/ZnO thin film response at different H_2 concentration at 400 °C

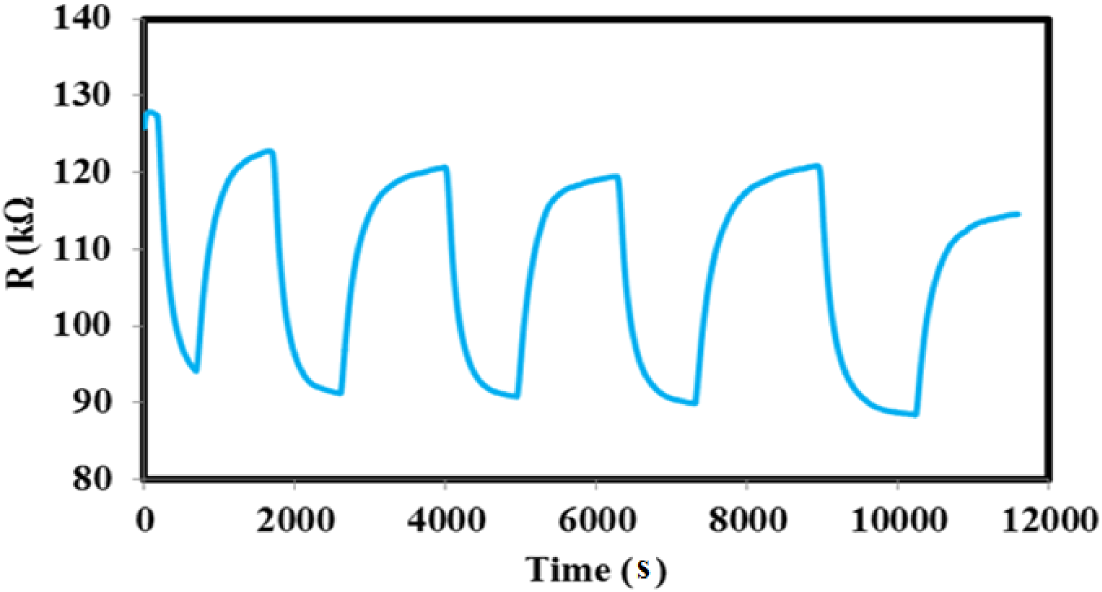

Figure 5.10. Response of Ag/ZnO thin film to 600 ppm H_2 at 400 °C

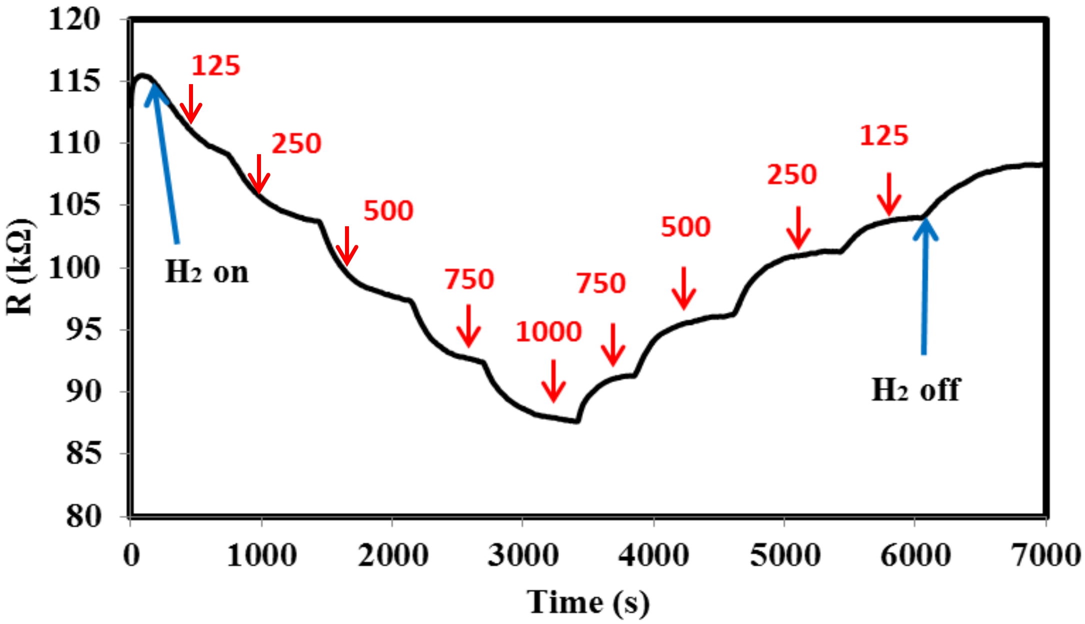

Figure 5.11. Ag/ZnO thin film repetitive response time for different concentration of H_2 at 400 °C

The sensing behavior of the Ag/ZnO films towards H_2 at different temperatures (25-400ºC) was also investigated in order to identify the optimal temperature window of operation. As expected, the performance of the Ag/ZnO films at room temperature was very poor at all levels of hydrogen (75 to 1200 ppm); this can ascribed to the rather high film resistance and slow kinetics of interaction between the oncoming hydrogen and the adsorbed oxygen species at the surface.

On the other hand, temperatures above 200 ºC had a significant effect on the response of the sensor. As shown in Fig. 5.12, the response increased as the operating temperature increased, reaching a maximum value (~ 29%) to 1,200 ppm H_2 at 400 ^{o}C. We also found that the baseline resistance of Ag/ZnO device decreased with increasing opertion temperature of the sensor from 200 ºC to 400 ºC. This decrease in the resistance of the Ag/ZnO sensor is attributed to the increase in number of electrons that escape from the valance band to the conduction band with temperature. The electrons transport between neighboring grains which increases with the conductivity according to the following formula [196]:

$$R = R_0 \, e^{\frac{-qV_s}{k_B T}} \qquad (5.15)$$

Where R_0 is the resistance at V_s (potential energy barrier height) = 0 and kB is the Boltzmann constant.

Figure 5.13 shows that the response time of the Ag/ZnO sensor toward hydrogen is temperature and concentration dependent.

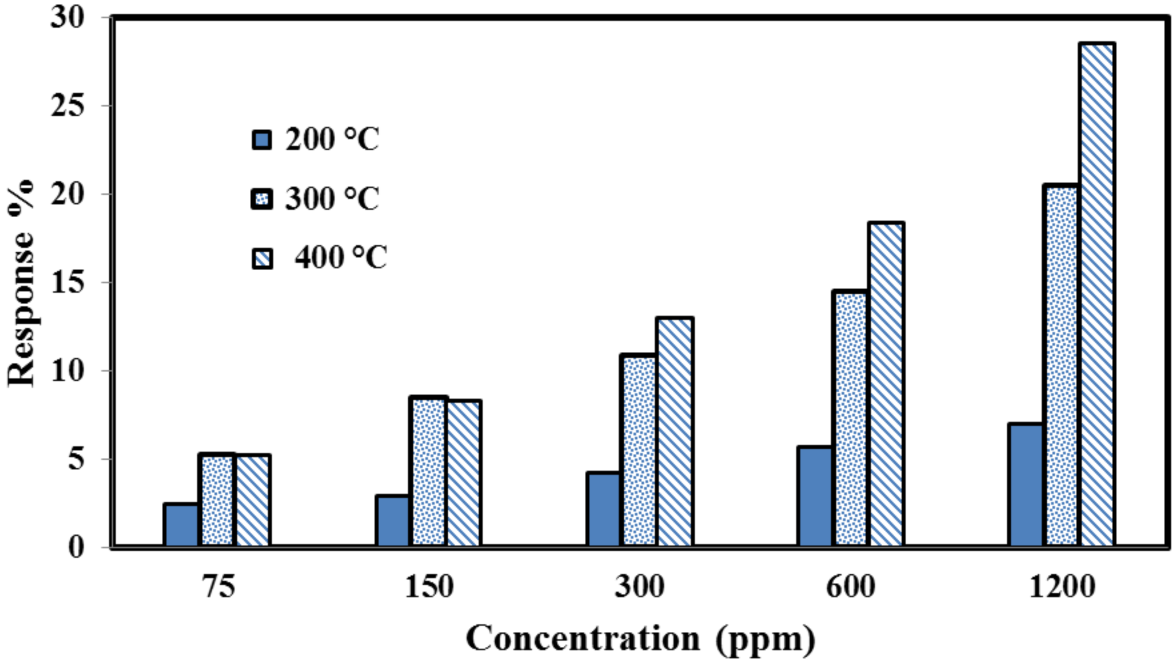

Figure 5.12. Effect of temperature on gas response of Ag/ZnO thin film at different concentration of H_2 (75, 150, 300, 600, 1200) ppm

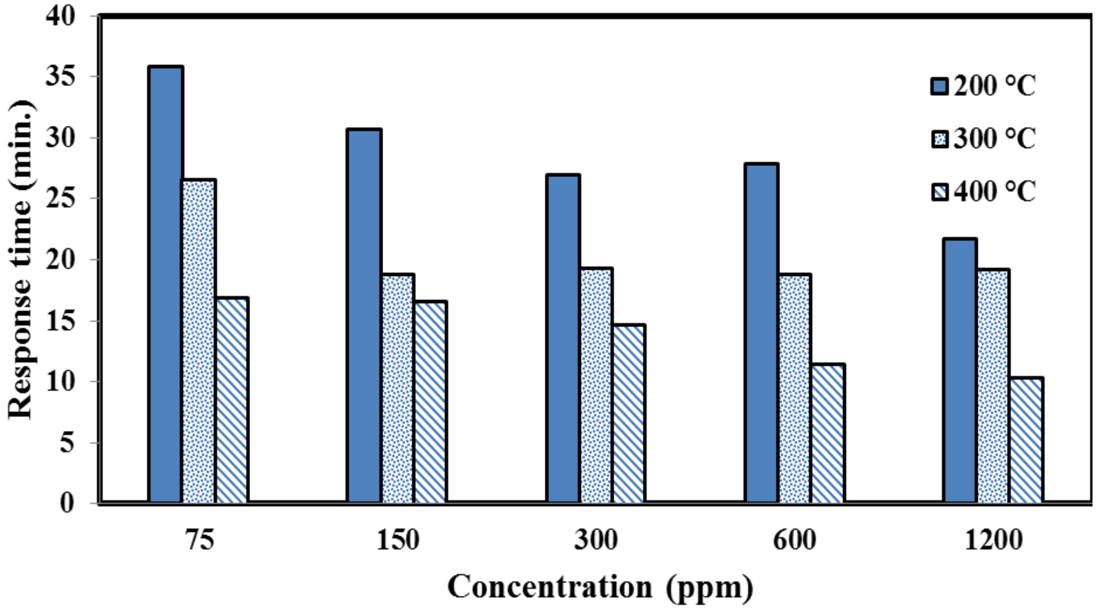

Figure 5.13. Effect of temperature on gas response (T_{90}) of Ag/ZnO sensor at different concentrations

5.5.2 Au/ZnO SYSTEM

The combination of gold nanoparticles with different morphologies of ZnO to detect different gases has been reported in recent years. Fengshou at el. [197] studied the influence of Au nanoparticles functionalized flower-like ZnO structure on the response of various gases: acetone, ethanol, benzene, methanol and hydrogen. Their results revealed that the response of Au at flower-like ZnO was much higher than pure ZnO. In addition, they found that the response of Au nanoparticles functionalized flower-like ZnO toward acetone is higher than other gases. Guo et al. [198] found that ZnO nanowires decorated with Au nanoparticles displayed enhanced resistivity and, response/recovery time towards ethanol. Mun et al. [199] investigated the performance of porous ZnO nanosheets functionalized with Au nanoparticles for NO_2 detection under UV illumination, and showed that the response was higher than that of pure ZnO.

In our work, the gas sensing performance of the Au/ZnO films was qualified and quantified in terms of relative resistance change when exposed to hydrogen-containing mixtures at a given temperature. Figure 5.14 shows the response of the sensor exposed to hydrogen over a wide range of concentrations (75-1200 ppm) at 400ºC. Clearly, the film responded to hydrogen rather quickly; the recovery upon removal of hydrogen was also swift and complete. The change of resistance even for the lowest H_2 concentration in air (75 ppm; limitation of experimental set-up flow meters) is about 21%, indicating that the film could detect even lower H_2 concentrations.

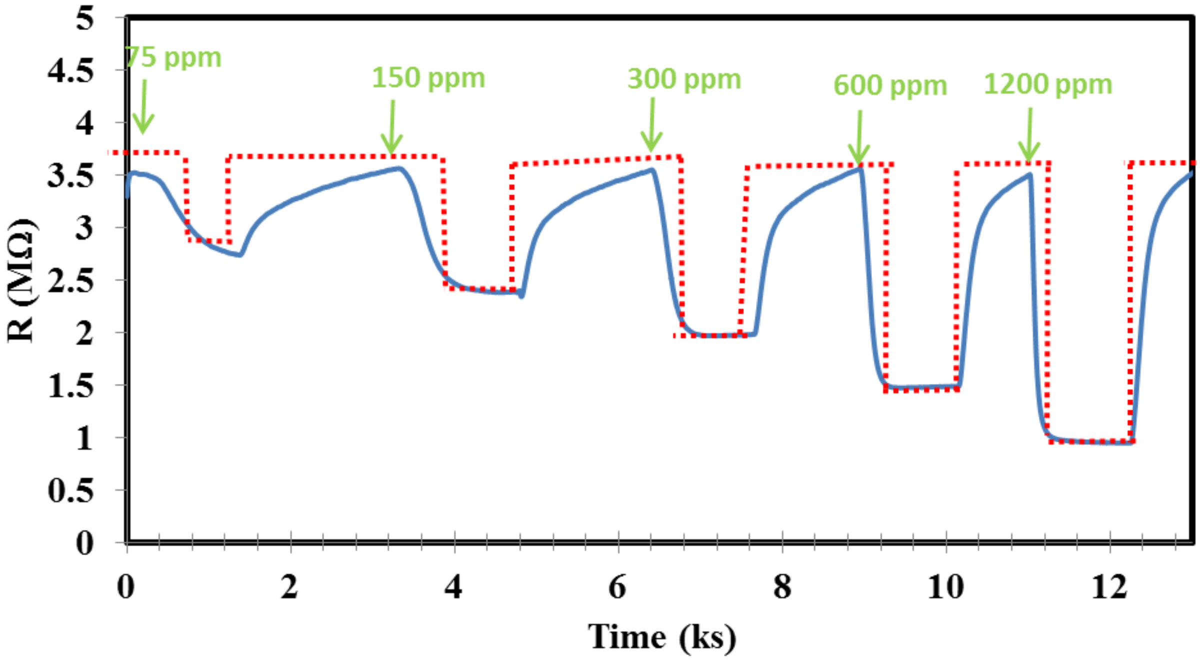

Figure 5.14. The dynamic response of Au/ZnO film to various concentrations of H_2 at 400 °C

Reproducibility of response over a large number of cycles is an important aspect when evaluating the suitability of a sensor device. Figure 5.15 shows the highly repeatable response of the Au/ZnO film over four cycles of exposure to 600 ppm H_2 at 400°C. The sensor was capable of complete recovery upon removal of hydrogen from the stream. The average of the sensor response toward 600 ppm at 600 °C is about 66.4 % with the standard deviation less than 0.5%.

The sensing behavior of the Au/ZnO films towards H_2 at different temperatures (25-400ºC) was also investigated in order to identify the optimal temperature window of operation. As expected, the performance of the Au/ZnO films at room temperature was very poor at all levels of hydrogen concentration; this could be ascribed to rather high film resistance and slow kinetics of interaction between the oncoming hydrogen and the adsorbed oxygen species at the surface. The film became responsive above 200ºC and the response increased with increasing temperature as shown in Fig. 5.16. This could be attributed to the contribution of the higher thermal energy at higher temperatures, towards overcoming the activation energy barrier of the interaction at the surface with the adsorbed hydrogen. Figure 5.17 shows that the response time of the Au/ZnO sensor toward hydrogen is temperature and concentration dependent. From the figure, one can conclude that the response time decreased with increasing the hydrogen concentration.

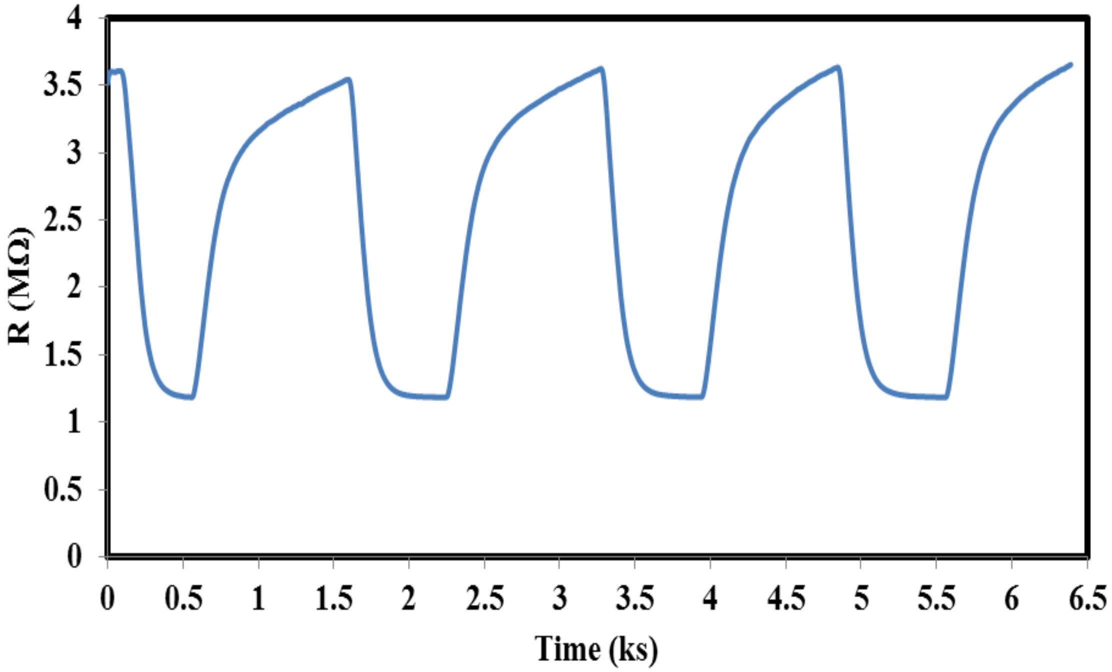

Figure 5.15. Response of Au/ZnO sensor to 600 ppm H_2 at 400 ° C.

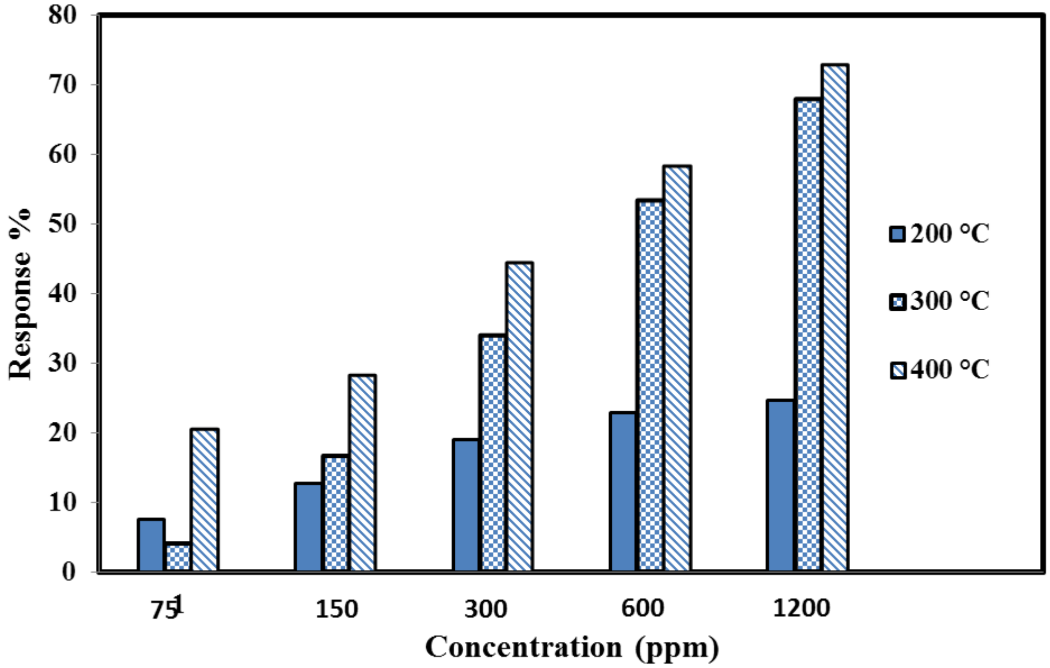

Figure 5.16. Effect of temperature on gas response of Au/ZnO thin film at different concentrations of H_2 (75, 150, 300, 600, 1200) ppm

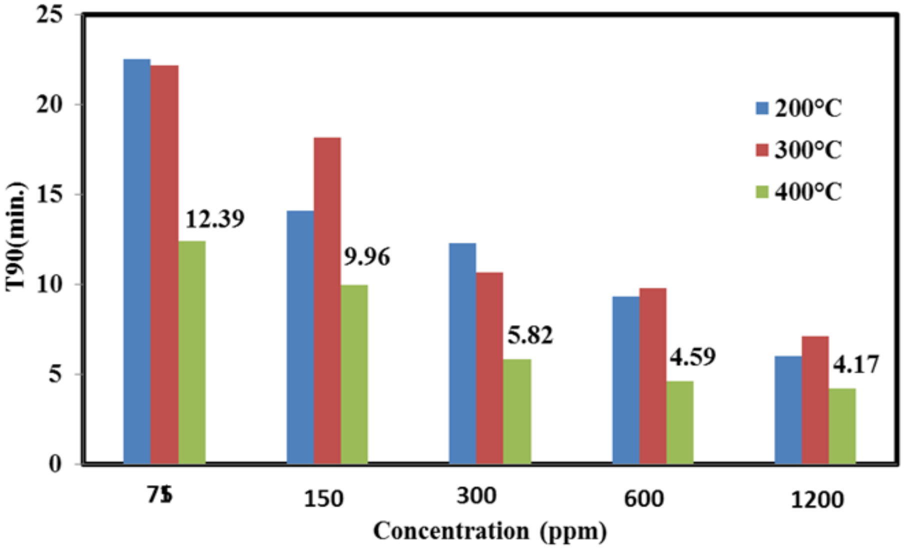

Figure 5.17. Effect of temperature on response time of Au/ZnO thin film at different concentrations

In order to study how the sensor response with increasing and decreasing H_2 concentration with no purge in between, the hydrogen concentration was increased from 75 ppm to 1200 ppm followed by decreasing the H_2 flow from 1200 ppm to 75 ppm. Figure 5.18 shows a rather excellent reversibility aspect (the so-called staircase behavior) of the sensor film in the ascending and descending mode of hydrogen level at 400°C. This behviour indicates that the sensor is in stable mode and responds dependably at different concentrations.

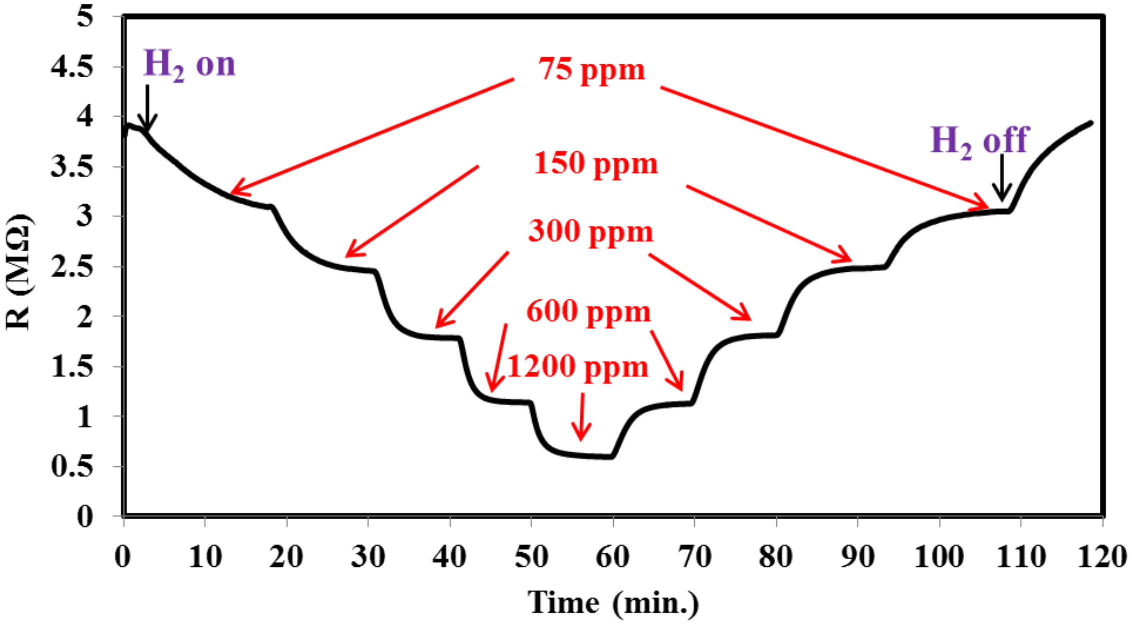

Figure 5.18. Response of Au/ZnO sensor with increasing and decreasing the H_2 concentration with no purge of air in between.

5.5.3 Pt/ZnO SYSTEM

Platinum is one of the metals that combined with metal oxides for detecting different gases such as H_2, NO_2, CO. The combination of Pt with ZnO thin film has been studied by different research groups [200-203]. However, most of the research in the literature focused on doping ZnO by different concentration of Pt. There are only few studies which focused on the functionalization of the surface of nanostructured ZnO by Pt nanoparticles [204-206]. In chapter 4, we introduced a novel method to modify the surface of ZnO thin films by Pt nanoparticles. In this section, the gas sensing performance of Pt/ZnO sensor toward H_2 is investigated.

Figure 5.19 shows the response of Pt/ZnO sensor for different concentration of H_2 (75, 150, 300, 600, 1200) ppm at 400 ºC. It is clear from the figure that the sensor is able to detect 75 ppm of H_2 with response reach to 60 % .This means that the sensor is promising for detection down to ppb level. Unfortunately, due to the limitation of our system (MFC) we were unable to test the ability of the sensor for detecting the H_2 in the ppb level. For comparison, the response of Ag/ZnO, Au/ZnO and Pt/ZnO sensors for 75 ppm of H_2 at 400 ºC is 6, 21 and 60 % respectively.

From Fig. 5.19 we can also observe that as the H_2 concentration was increased above150 ppm, the response of the sensor seemed saturate. In addition, we found that the resistance of the sensor at low concentration (75 ppm and 150 ppm) does not fully come to the back to the initial baseline resistance. This can be explained due to the presence of some hydrogen residue left on the surface of the sensor. It is not clear why this reduction in the resistance appears mostly at low concentrations, and not at higher concentrations. Figure 5.20 demonstrates the sensor's repeatability by showing multiple exposures to a 600 ppm concentration of H_2 at 400 ºC. The average of the Pt/ZnO sensor toward hydrogen at 400 °C is about 91.97% and the standard deviation is less than 0.8%.

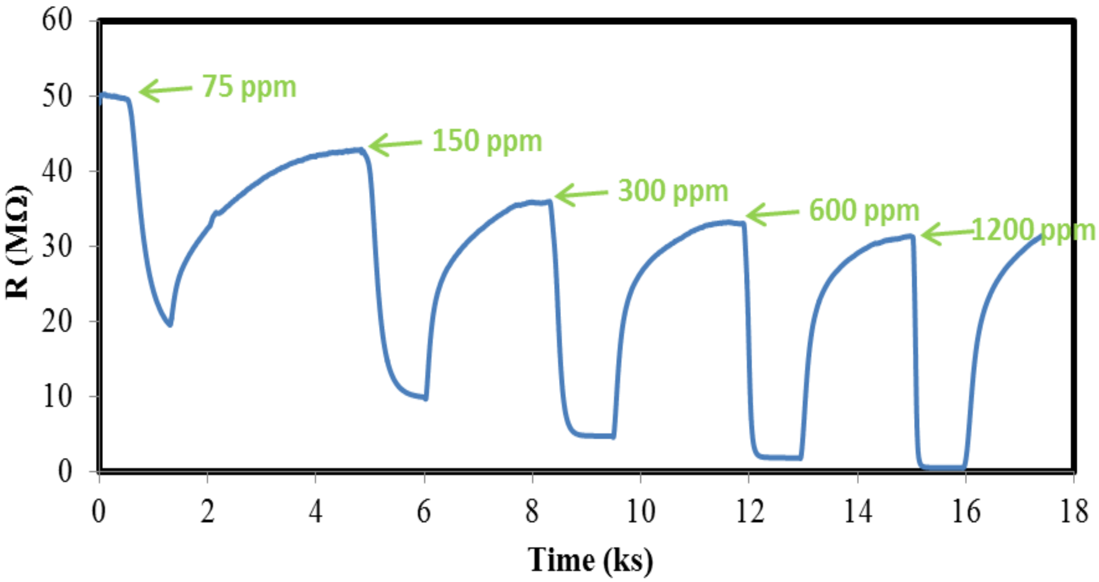

Figure 5.19. Pt/ZnO thin film response at different H_2 concentration at 400 °C

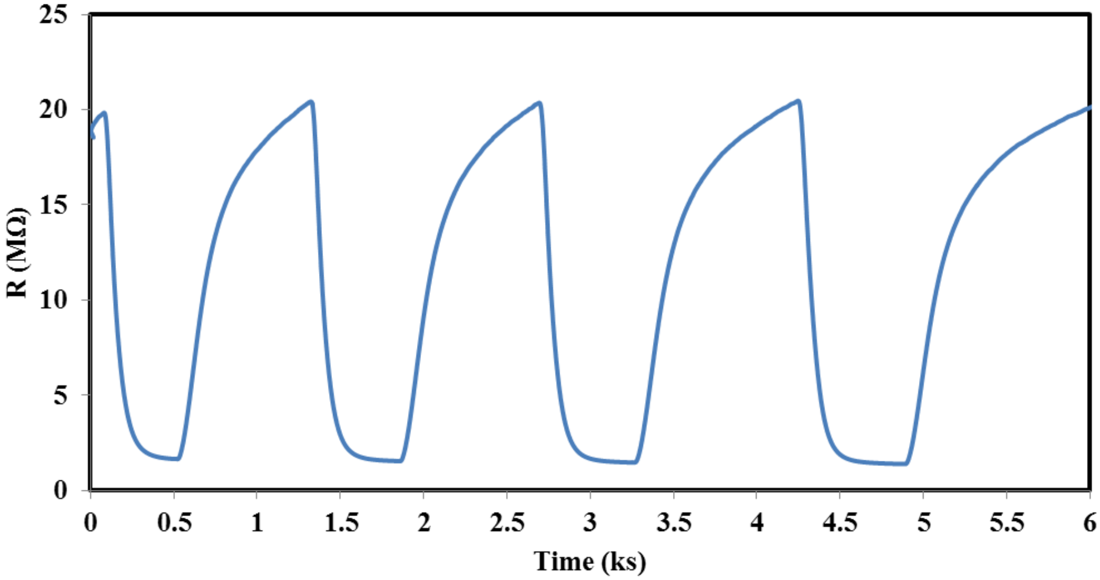

Figure 5.20. Response of Pt/ZnO thin film to 600 ppm H_2 at 400 °C

The influence of the operation temperature on the Pt/ZnO sensor performance toward H_2 was studied. Figure 5.21 shows the effect of operation temperature on the performance of Pt/ZnO toward H_2 sensing. Three important points can be noticed in Fig. 5.21. First, the optimum operating temperature at low concentration (75, 150, 300) ppm is 300 ºC while it was 400 ºC in case of Ag/ZnO and Au/ZnO sensors. At high concentration (600 ppm, 1200 ppm) the response are almost the same for the three temperatures (200, 300, 400 °C) °C. This means that Pt/ZnO sensor has not only enhanced the response, but it also reduced optimal operating temperature. Figure 5.22 shows that the response time of the Pt/ZnO sensor toward hydrogen is temperature and concentration dependent. From the figure, one can conclude that the lowest response time was recorded at 300 °C at all levels of hydrogen.

In order to study how the sensor responds with increasing and decreasing the concentration of H_2, with no purge in between, the hydrogen concentration was increased from 75 ppm to 1200 ppm. Figure 5.23 shows that the resistance decreases with increasing the concentration of hydrogen and recovers back to the initial resistance when the hydrogen flow is stopped. This indicates that the sensor is stable and the response properly designates concentrations.

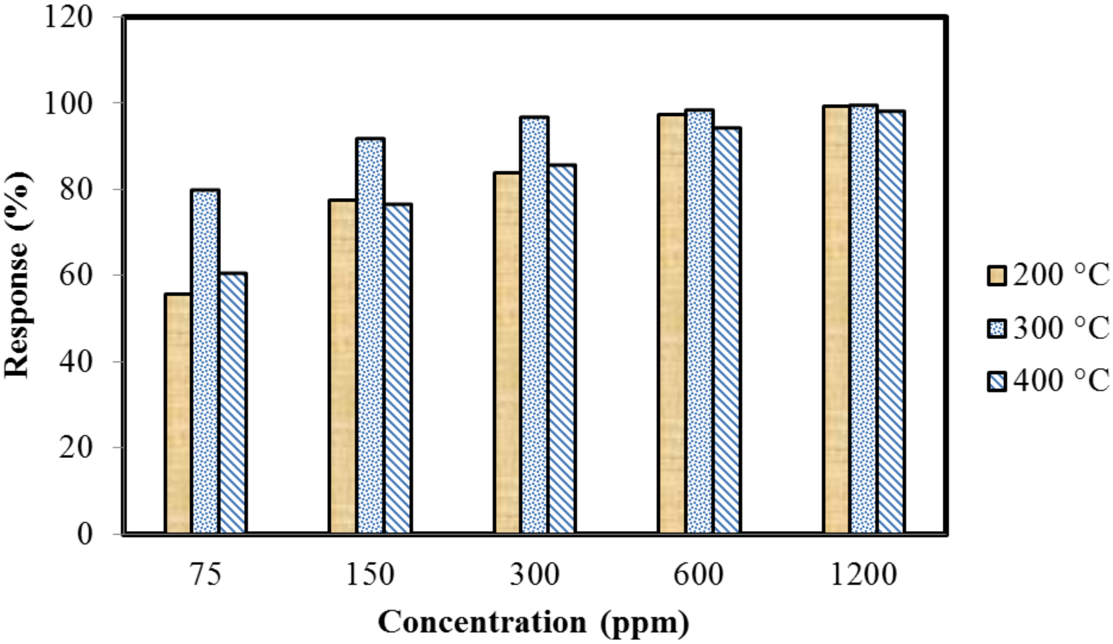

Figure 5.21. Effect of temperature on gas response of Pt/ZnO thin film at different concentration of H_2 (75, 150, 300, 600, and 1200 ppm)

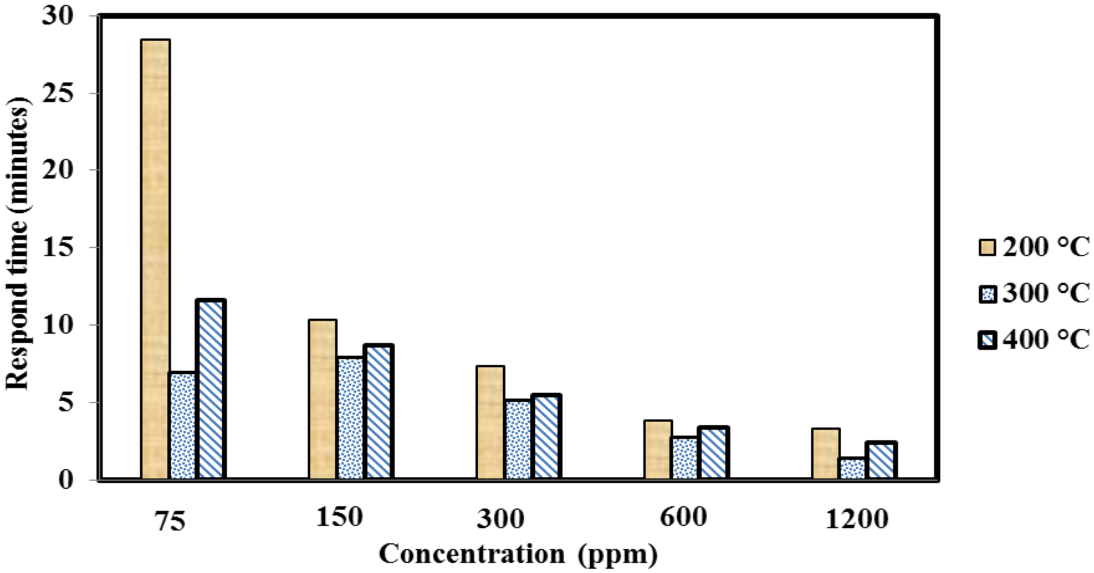

Figure 5.22. Effect of temperature on gas respond time of Pt/ZnO thin film at different concentration of H_2

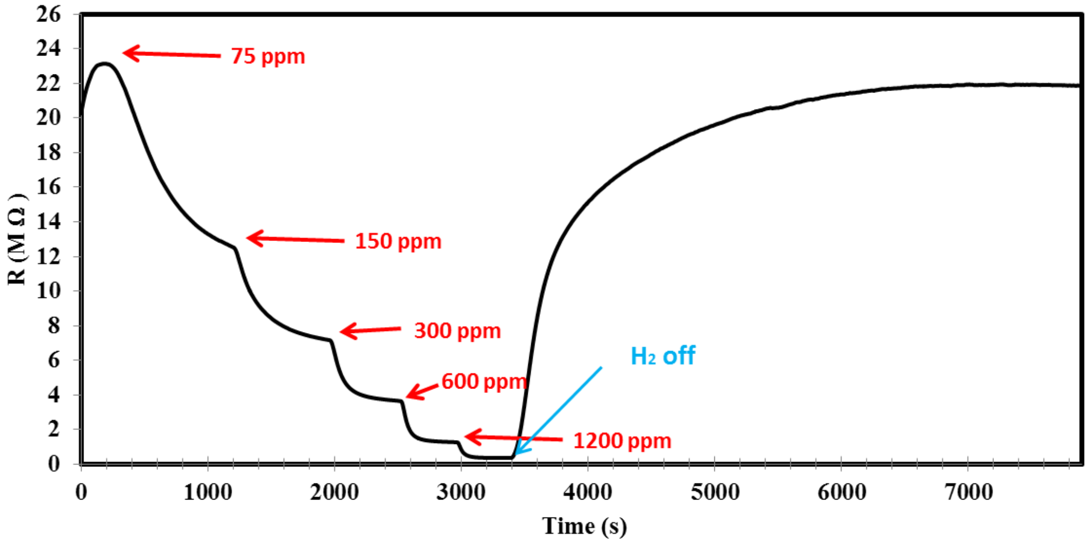

Figure 5.23. Pt/ZnO thin film repetitive response for 75, 150, 300, 600 and 1200 ppm H_2 at 400 °C

5.5.4 COMARTIVE STUDY OF THE ROLE OF NOBLE METALS TOWARD HYDROGEN SENSING

Figures 5.24 and 5.25 provide a comparison of the response and response time of different sensors (pure ZnO, Pt/ZnO, Au/ZnO, Ag/ZnO) to 300 ppm, 600 ppm and 1200 ppm of H_2 at 400 ºC. As can be seen, the response of the Pt/ZnO is the greatest followed by Au/ZnO sensor while Ag/ZnO sensor does not show significant improvement over pure ZnO. In addition, the Pt/ZnO sensor shows the fastest response followed by Au/ZnO sensor.

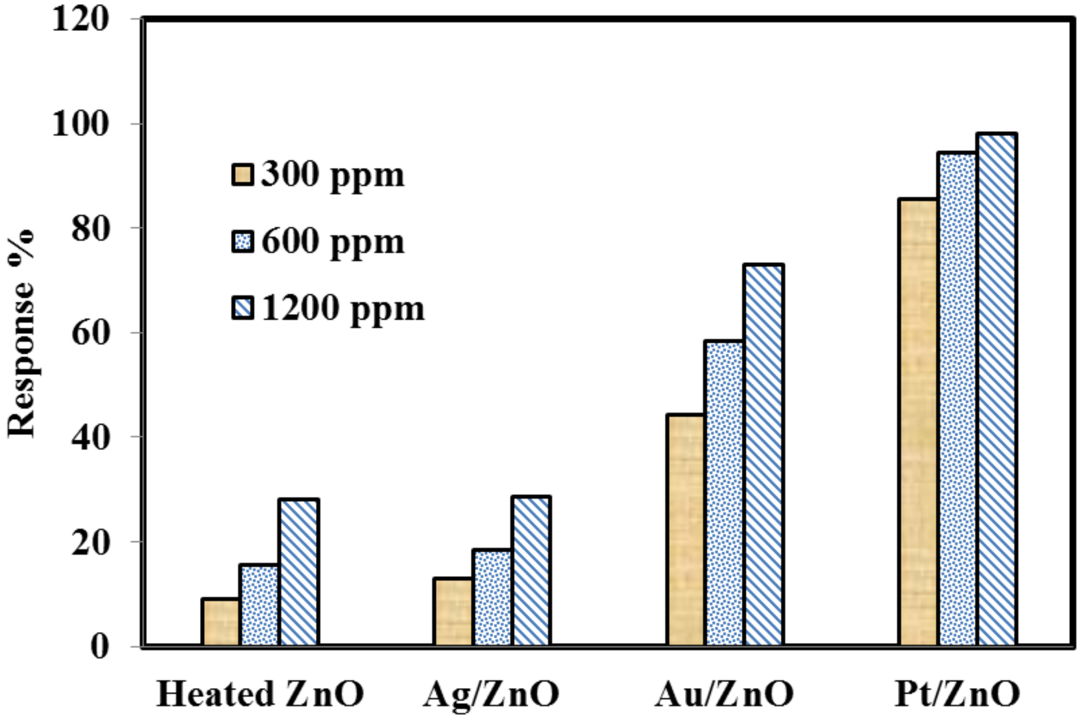

Figure 5.24. Comparison of the response of different sensors (ZnO, Ag/ZnO, Au/ZnO, Pt/ZnO) to (300, 600, and 1200 ppm) of H_2 at 400 °C

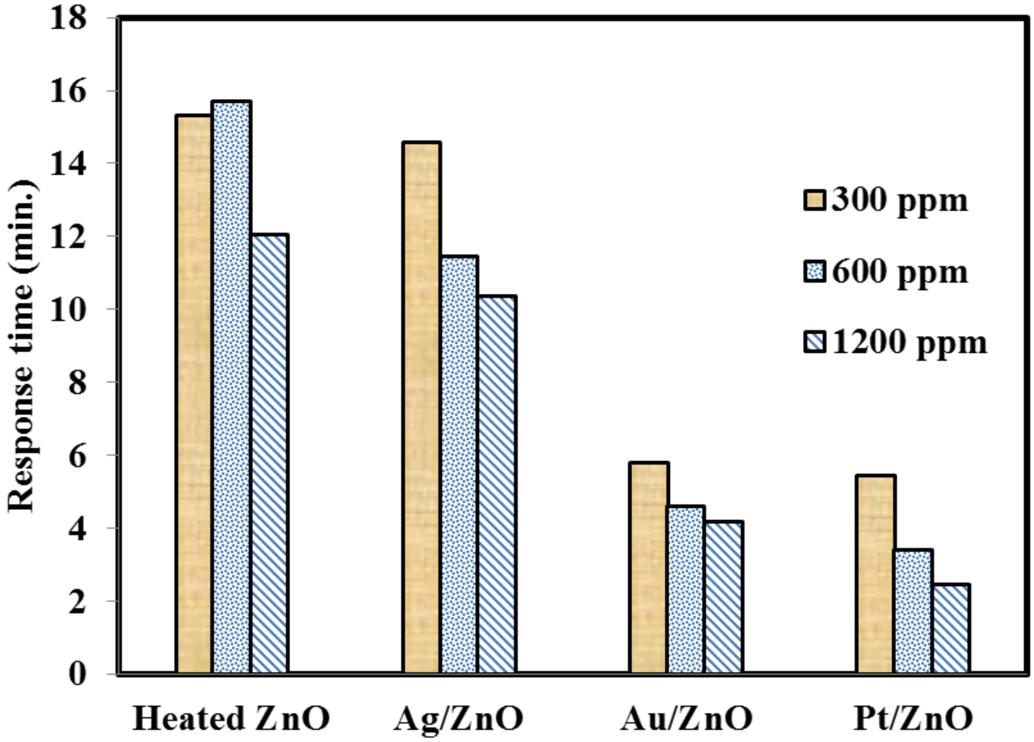

Figure 5.25. Comparison of the response time of different sensors (ZnO, Ag/ZnO, Au/ZnO, Pt/ZnO) to (300, 600, and 1200 ppm) of H_2 at 400 °C

There are two possible mechanisms that might explain the improvement of the response and the response time of M/ZnO comparing with pure ZnO. One is the spill-over mechanism and the second is the Fermi energy control. Spillover refers to the process in which metals such as (Pt, Au, Ag) dissociate the gas molecule to atoms, then the atom can spillover onto the surface of the semiconductor sensor [207]. Spillover of H_2 and O_2 on the noble metals has been reported by different researchers [208-210].

In order to understand the role of noble metals in the dissociation of gas molecules, one may assume that the metal is Pt and the gas is H_2. It has been reported that the bonding energy of the hydrogen atoms to each other is similar to the bonding energy of hydrogen-platinum atoms [211]. This means that little energy is required for freeing the H_2 atoms and forming Pt-H bond. However, the Pt-H bond is relatively unstable and adding electrons to the platinum from the ZnO surface should therefore weaken this bond [211]. Weakening the platinum hydrogen bond should lead to a lower activation energy and increase the probability of a reaction [211]. After the hydrogen atoms dissociate, they diffuse to the ZnO surface to react with reactive surface oxygen species (especially O_2^{--}). For the above process to be possible, the spilled over species are able to transfer from the surface of the metal to the grain boundaries or the inter-granular contact of ZnO grains (Fig. 5.26). As a consequence, for a metal to be effective, there must be good dispersion of the metal on the surface of ZnO thin film.

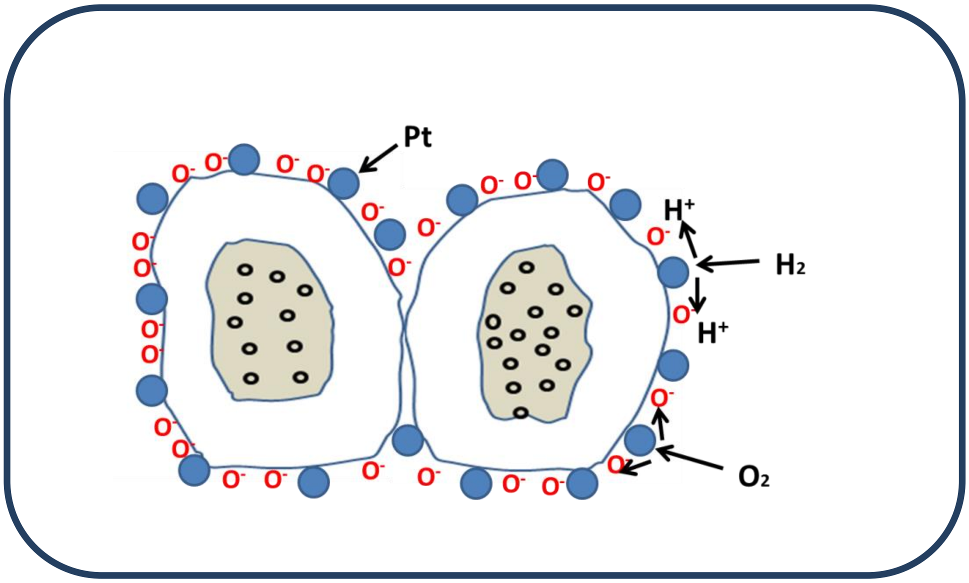

Figure 5.26. Gas sensing mechanisms based on spillover effect of Pt nanostructures dispersed on ZnO grains

The second possible mechanism that noble metals might enhance the gas sensing performance of pure ZnO is by Fermi energy control. As mention in section 5.1.1, at metal/ZnO contacts, due to the work function difference between the metal and ZnO, the free electrons can transfer between ZnO and the metal. Since the work function of the metal that we used (Pt, Au, Ag) are higher than the work function of the ZnO (Table 5.2), the electrons will transfer from the ZnO to the metal. When oxygen molecules or atoms are adsorbed on the surface of the additives, they easily remove electrons from the metals which will remove electrons from the ZnO conduction band leading to increasing of the resistivity. In contrast when H_2 atoms are adsorbed on the surface of the additives, electrons will get injected to the surface of ZnO, decreasing the resistivity of the M/ZnO film. Figure 5.27 shows schematically the above two mechanisms.

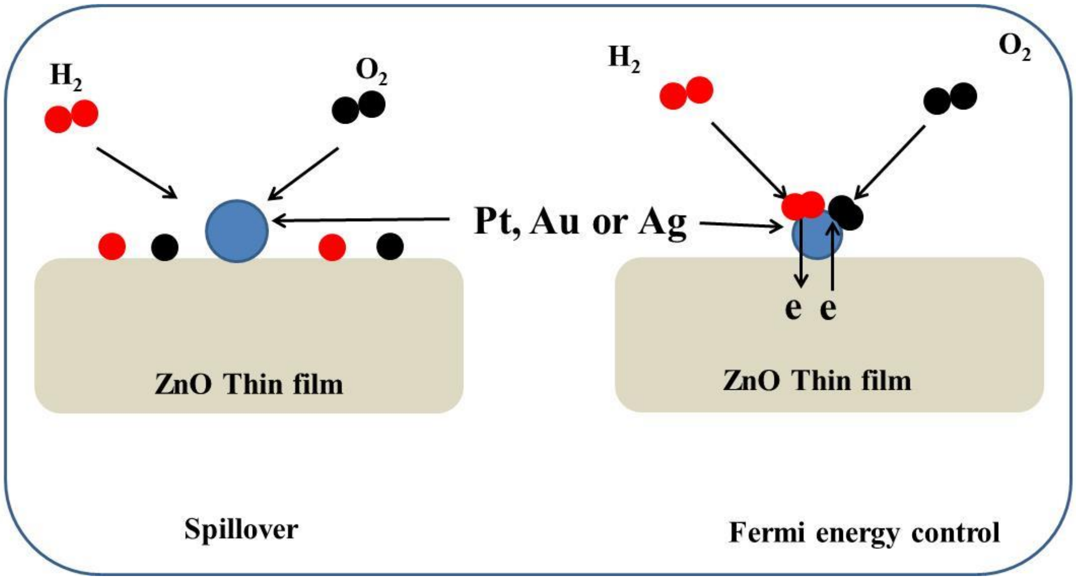

Figure 5.27. Spill-over and Fermi energy control mechanisms

Now, we are ready to answer the question why Pt/ZnO sensors show the highest response and lowest response time among the different prepared sensors. According to the equation 5.14, the degree of the band bending and the depletion layer is propositional to the square root of the barrier potential. Figure 5.28 illustrates the energy band diagram of the (Ag-Au-Pt)-ZnO systems before and after contact. In the case of Ag/ZnO sensor and since the electron affinity of ZnO (4.09 eV) is close to the work function of silver (4.26 eV), few electrons will transfer from the ZnO to the silver and the barrier height (Schottky barrier) between the ZnO and the silver will be small. However, in the case of Pt/ZnO sensor, due to the greater value of the work function of Pt (6.35 eV) [212], the degree of band bending will be higher resulting in high resistance. When the prepared sensors are exposed to hydrogen, the change in the Schottky barrier in case of Pt/ZnO will be greater than of the other sensors. This means the change in the resistance (ΔR) resembling response is higher for Pt, as experimentally observed in this work.

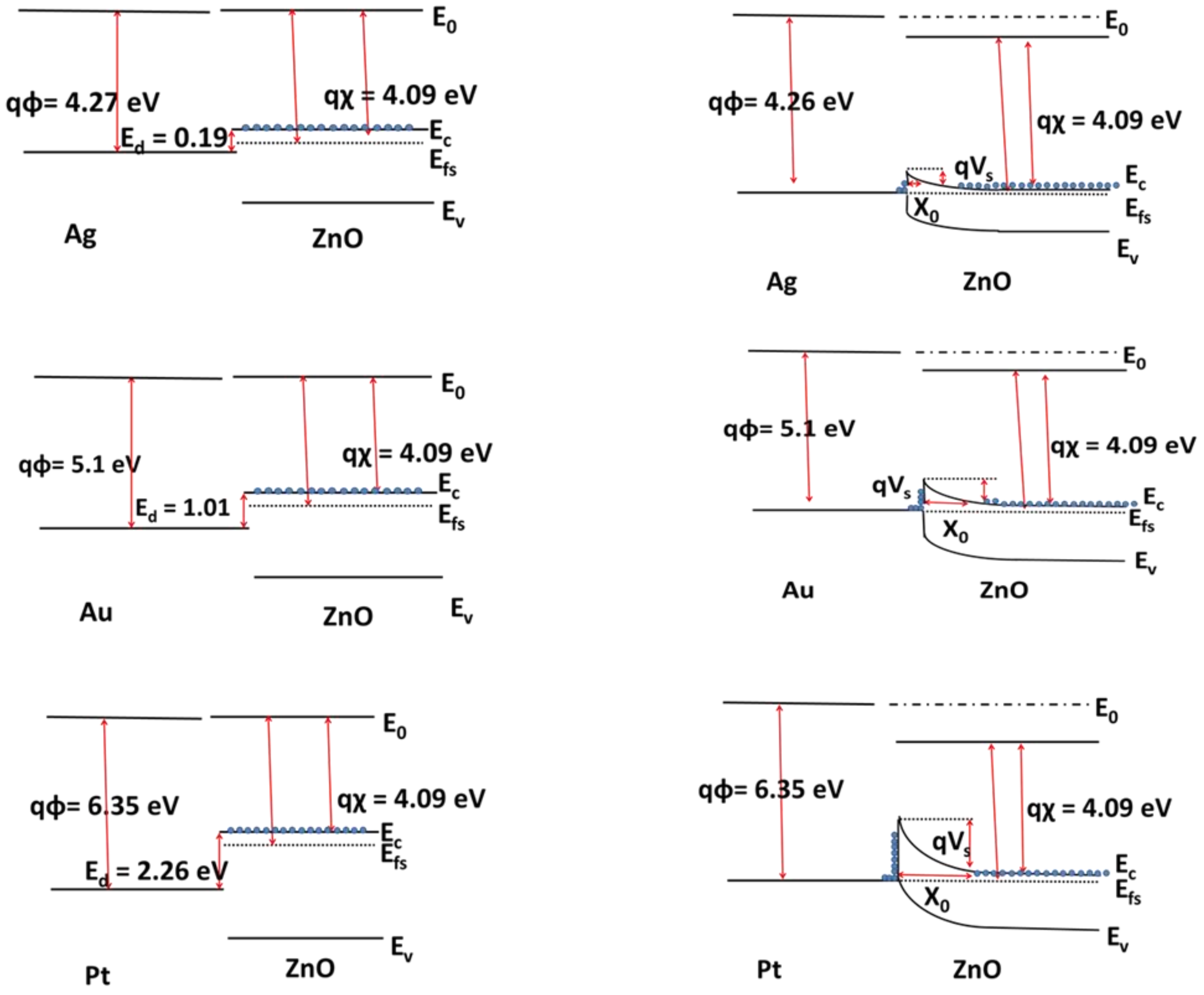

Figure 5.28. Energy band diagram showing the effect of the work function on the depletion region and hence the response of the metal/ZnO sensor

Table 5.2 Work function of elements, in units of electron volt (eV) [213]

Element	Work function (eV)
Ag	4.26
Au	5.10
Fe	4.50
Pt	6.35
Nb	4.30
Ir	5.27
Cu	4.56
Pd	5.12

5.6 EFFECT OF THICKNESS OF THE Pt THIN FILM ON THE RESPONSE OF Pt/ZnO SENSOR

The dependence of the response of Pt/ZnO sensor on the density of the Pt on the surface of ZnO thin films was also investigated. In order to control the thickness of Pt films, the deposition time varying from 5 s to 50 s (5 s, 10s, 30s, 50s) while other deposition parameters were left constant for preparing Pt/ZnO sensor described in section 5.3. After preparing Pt/ZnO thin films, the samples were annealed at 600 ºC for 4 hours. Figure 5.29 gives the response of the prepared sensors versus H_2 concentration at 400 ºC. From the figure., it can be seen that the response of the prepared sensors slightly increased with decreased sputtering deposition time of Pt nanostructures especially at low hydrogen concentrations. According to the model described in section previous section, it was expected that the response of the prepared sensor increase by increasing the Pt deposition time since the depletion layer, the barrier height (qV_s) and the initial resistance increase by increasing the thickness of Pt. However, it seems that if the thickness of the Pt increases beyond a critical limit of thickness, the relative change in the resistance and hence the response of the sensor, decrease (Fig. 5.30 (d)). The possible reasons behind the reduction of the response of the Pt/ZnO sensor with increasing the density of the Pt nanostructures could be electron tunneling between the Pt nanostructures. Due to this tunneling, electrons could be lost between Pt grains rather than contribute to the conductivity of ZnO.

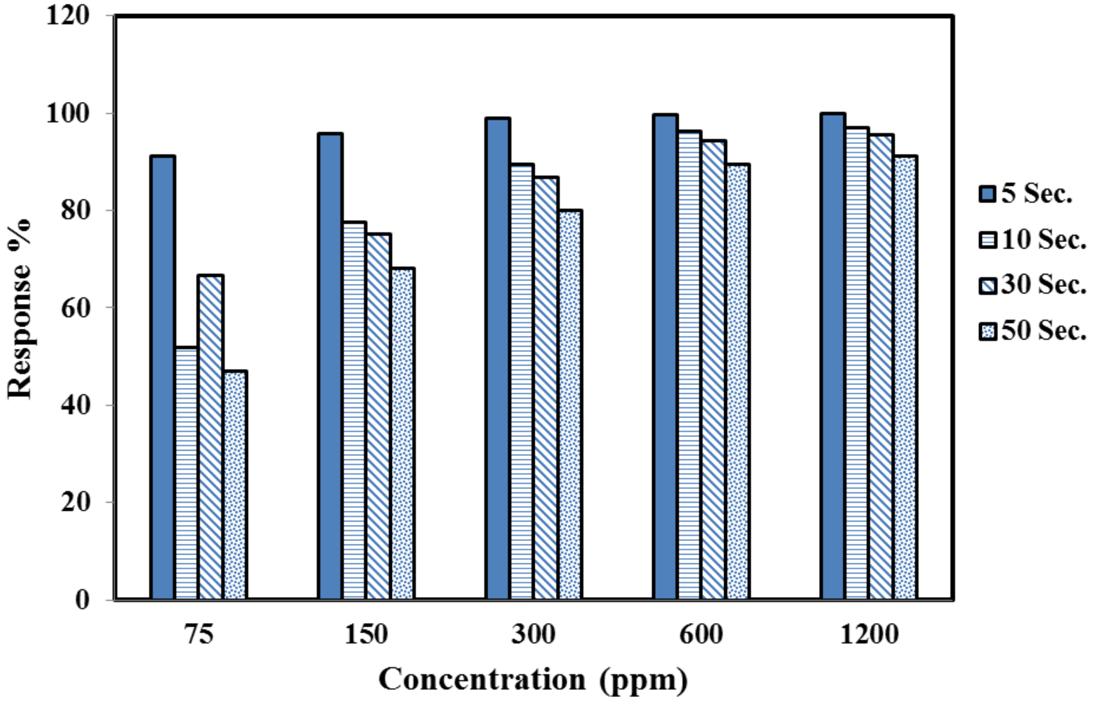

Figure 5.29. Effect of the deposition time of Pt on the response of Pt/ZnO sensors at (75, 150, 300, 600, and 1200 ppm) of H_2 at 400 ºC

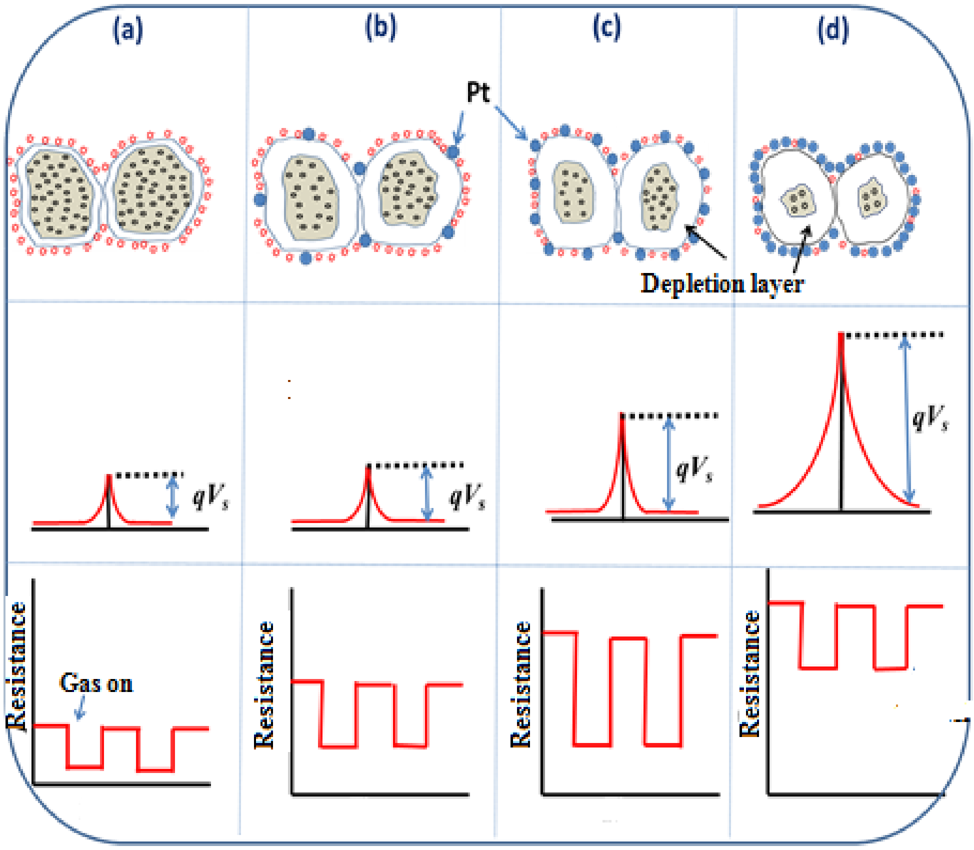

Figure 5.30. Mechanism of the change of the response of Pt/ZnO sensors due to the change of the deposition time of Pt (a) without Pt (b) low

5.7 REPRODUCIBILITY ASPECTS OF SENSORS

In order to test the stability of the response and the response time of the Pt/ZnO sensor, the response and the response time were tested at different concentrations on three different days at the same conditions. Figures 5.31 and 5.32 give the response and the response time of the Pt/ZnO sensor measured at five different concentrations (75, 150, 300, 600, 1200) ppm at 300 ºC on three different days. The results show that the response and the response time within three days are not significantly changed.

In order to evaluate the reproducibility of the sensing materials, two Pt/ZnO sensors were prepared at the same condition. Figure 5.33 and 5.34 show the response and the response time measured at five different concentrations (75, 150, 300, 600, 1200) ppm at 300 ºC. The results show that the response and the response time of both samples are consistently close to each other.

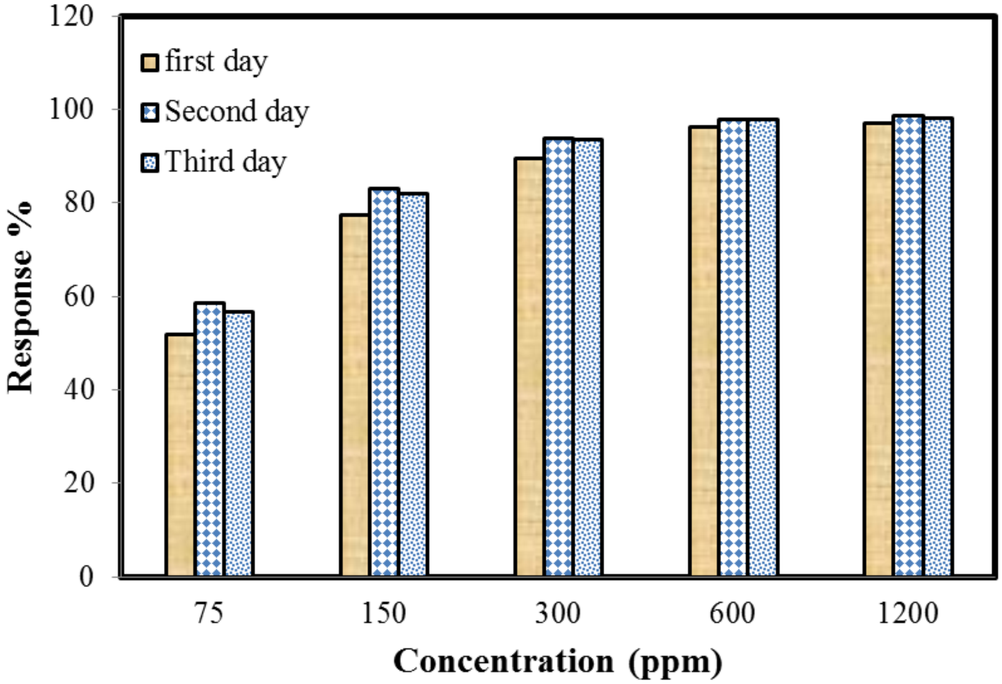

Figure 5.31. Response of Pt/ZnO sample versus concentration measured at three different days

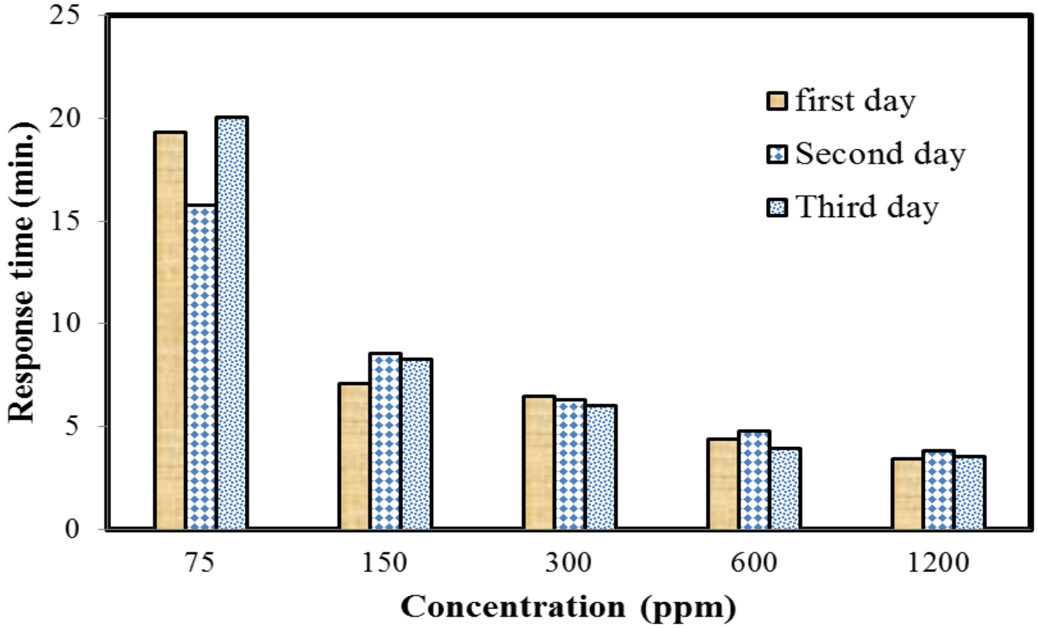

Figure 5.32. Response time of Pt/ZnO sensor versus concentration measured at three different days

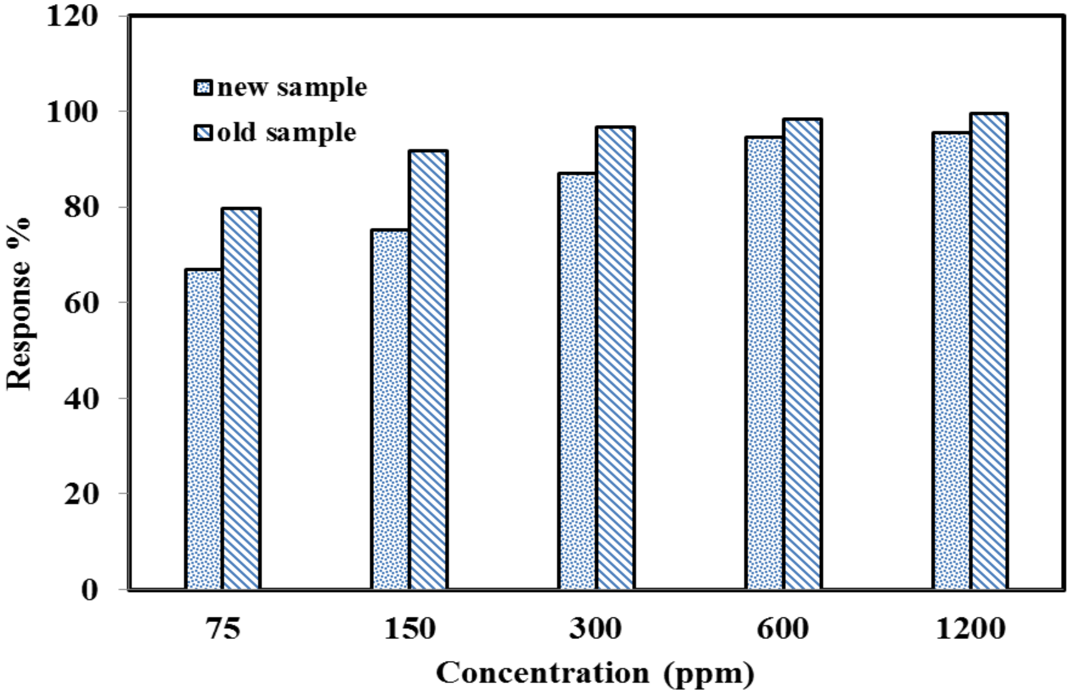

Figure 5.33. Response versus various concentrations of H_2 of two Pt/ZnO sensors prepared at the same conditions

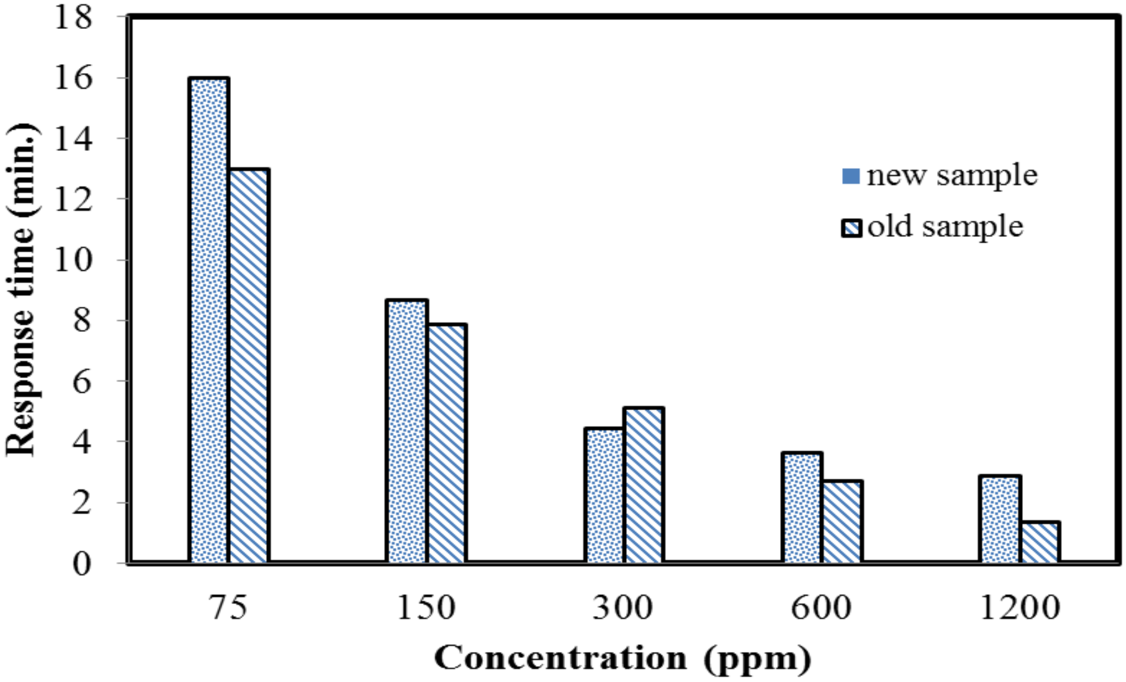

Figure 5.34. Response time versus various concentrations of hydrogen of two Pt/ZnO sensors prepared at the same conditions

5.8 SELECTIVITY ATTRIBUTE

Selectivity points to the ability of a gas sensor to identify a specific gas amongst a mixture of gases. It is one of the important characteristics of gas sensors. Selectivity is considering as one of the major challenges in metal oxide sensors. According to the literature, there are four main methods used to improve the selectivity of metal oxide gas sensors: introducing additives in the sensing material by means of doping [214], surface functionalization [215], using filters [216], and modulation of temperature [217]. In our work, in order to test the selectivity of the Pt/ZnO sensor, the response of reducing gas (ammonia (NH_3)) and oxidizing gas (nitrogen dioxide (NO_2)) gas are measured and compared with H_2.

5.8.1 SELECTIVITY TOWARD REDUCING GAS (NH_3)

In order to test the response of Pt/ZnO sensor toward NH_3 (reducing gas), the change of the resistivity as a function of time of the Pt/ZnO sensor at different levels of NH_3 (50, 150, 200, 300, 400) ppm at 400 ºC were recorded (Fig. 5.35). From the figure, it can be seen that the resistance of the sensor decreases when the NH_3 introduced to the gas chamber.

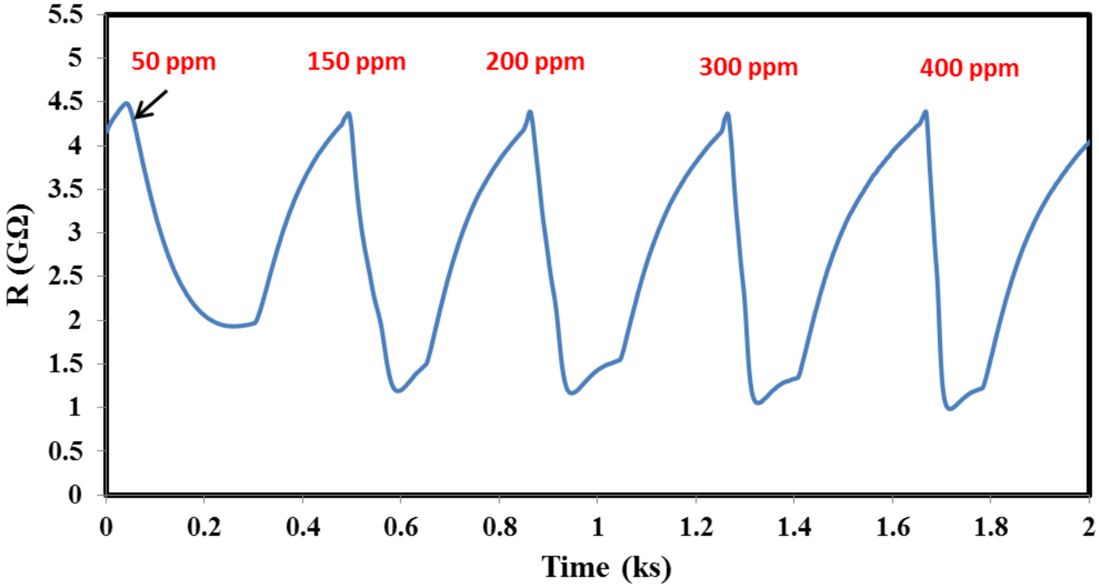

Figure 5.35. Pt/ZnO sensor responses at different NH_3 concentration at 400 °C

The possible mechanism for decreasing the resistance of the Pt/ZnO sensor can be attributed to the following steps [218]:

1- First, O_2 and NH_3 are adsorbed on the ZnO surface as showing in the below two equations:

$$\left.\begin{array}{l} ½\, O_2(g) + e^- \rightarrow O^-_{(ads)} \\ NH_3(gas) \rightarrow NH_{3(ads)} \end{array}\right\}$$

2- Second, the two adjacent adsorbed species $O^-_{(ads)}$ and $NH_{3(ads)}$ interact via hydrogen bonding to form the $[NH_2.H\text{---}O]^-$ complex.

$$NH_{3\,(ads)} + O^-_{(ads)} \rightarrow [NH_2.H\text{---}O]^-_{(ads)}$$

3- Third, the $[NH_2.H\text{---}O]-$ complex further reacts with an additional adsorbed oxide ion leading to release the electrons of the oxygen ions back into the conduction band of the ZnO resulting in the decreasing of the resistance of the Pt/ZnO sensor film.

$$O^-_{(ads)} + 2\,[NH_2.H\text{---}O]^-_{(ads)} \rightarrow N_2\ (g) + 3H_2O + 3e^-$$

The comparison between the response of the Pt/ZnO sensor toward $H_2$and NH_3 was investigated. As seen in the comparison graph, Fig. 5.36, the responses of Pt/ZnO sensor toward H_2 and NH_3 are close to each other. This, unfortunately, means that the selectivity of the Pt/ZnO sensor toward reducing gases is poor. However, Fig. 5.37 shows that the response time of the sensor toward NH_3 is faster comparing with H_2.

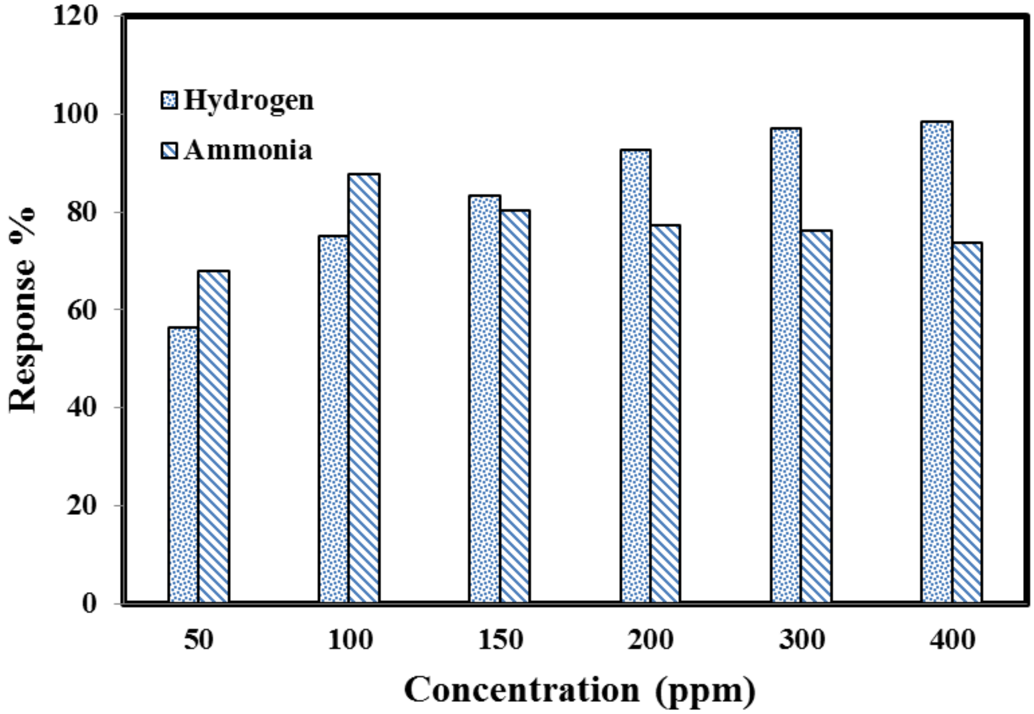

Figure 5.36. Comparison of the response of Pt/ZnO sensor toward H_2 and NH_3 at 500 °C

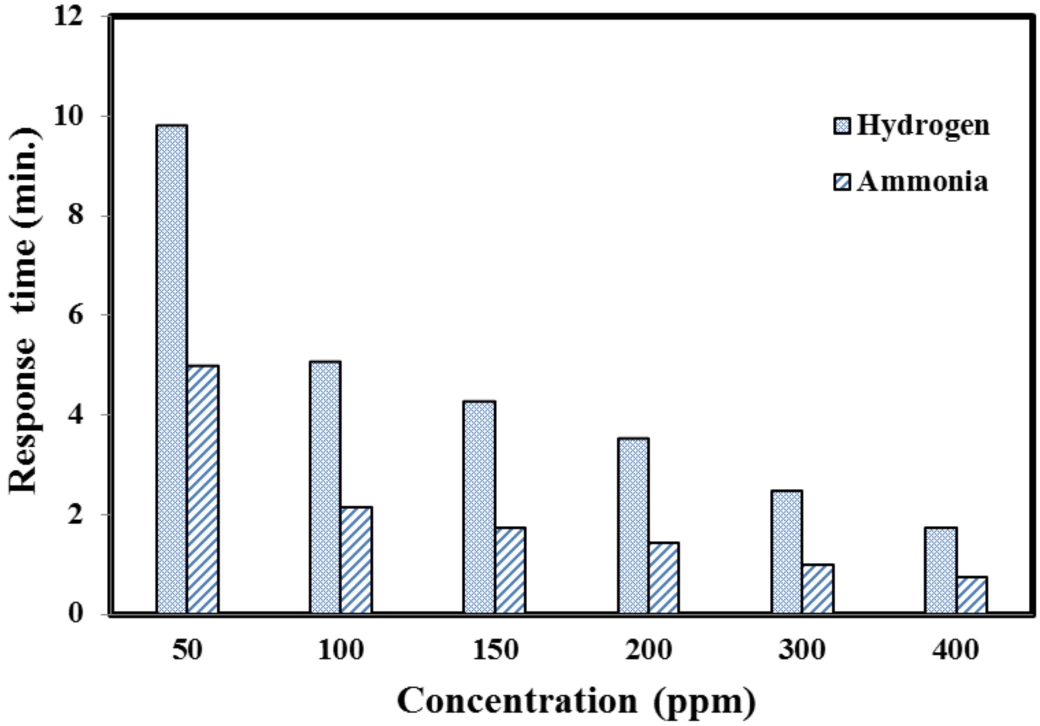

Figure 5.37. Comparison of the response time of Pt/ZnO sensor toward H_2 and NH_3 at 500 ºC

5.8.2 SELECTIVITY TOWARD OXIDIZING GAS (NO_2)

The response of the Pt/ZnO sensor toward oxidizing gas (NO_2) was also investigated and compared with the response to H_2 at same concentration and temperature. Figure 5.38 shows the resistance versus time for Pt/ZnO sensor exposed to (50, 100, 200) ppm NO_2 at 400 °C. The resistance of the sensor increases by increasing the NO_2 concentration.

The sensing mechanism for NO_2 can be summarized in two steps. First, oxygen molecules adsorbed on the surface of ZnO capture electrons from conduction band of the ZnO and produce ionic species, forming an electron inversion layer and causing upward band bending resulting in increased resistance. Second, $NO_2^-(ads)$ react with the O^- species resulting in further decreasing of the resistance. These two processes can be described by the following reactions [219]:

$$NO_2(g) + e^- \rightarrow NO_2^-(ads)$$

$$NO_2^-(ads) + 2O^-(ads) \rightarrow 2O^{2-}(ads) + NO_2(g)$$

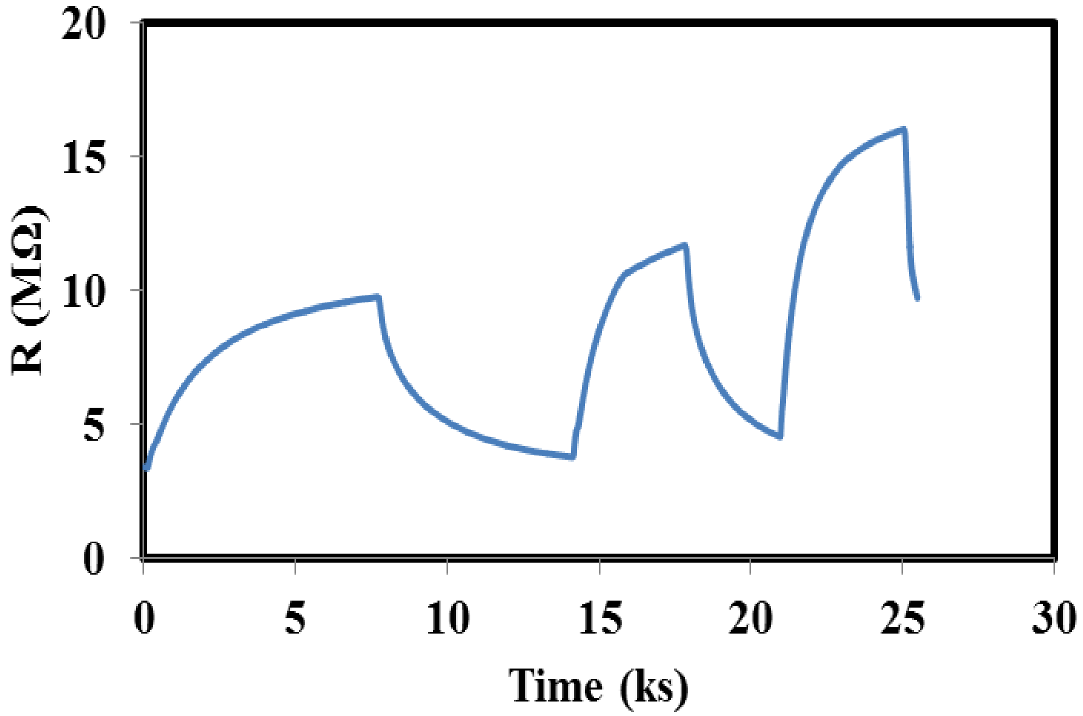

Figure 5.38. Response-recovery time of Pt/ZnO sensor at three different concentrations of NO_2 at 400 ºC

By comparing the response time of the Pt/ZnO toward H_2 and NO_2 at 400 ºC, one can see that the response time in case of NO_2 is very long. This means that the Pt/ZnO sensor at 400 ºC cannot be used as NO_2 sensor while it can be used as a hydrogen sensor. At higher temperature (500 ºC) as seen in figures 5.39 and 5.40, the response of the Pt/ZnO sensor toward NO_2 is much better as seen in Fig. 5.41. This means that the optimum working temperature of Pt/ZnO toward NO_2 is 500 ºC while the optimum working temperature toward H_2 is 300 ºC. This is potential for selectivity. Basically, in chemical gas sensing, if the difference between two operating temperatures of two different target gases is large, a single sensor could be designed to detect both gases species by modulating the temperature.

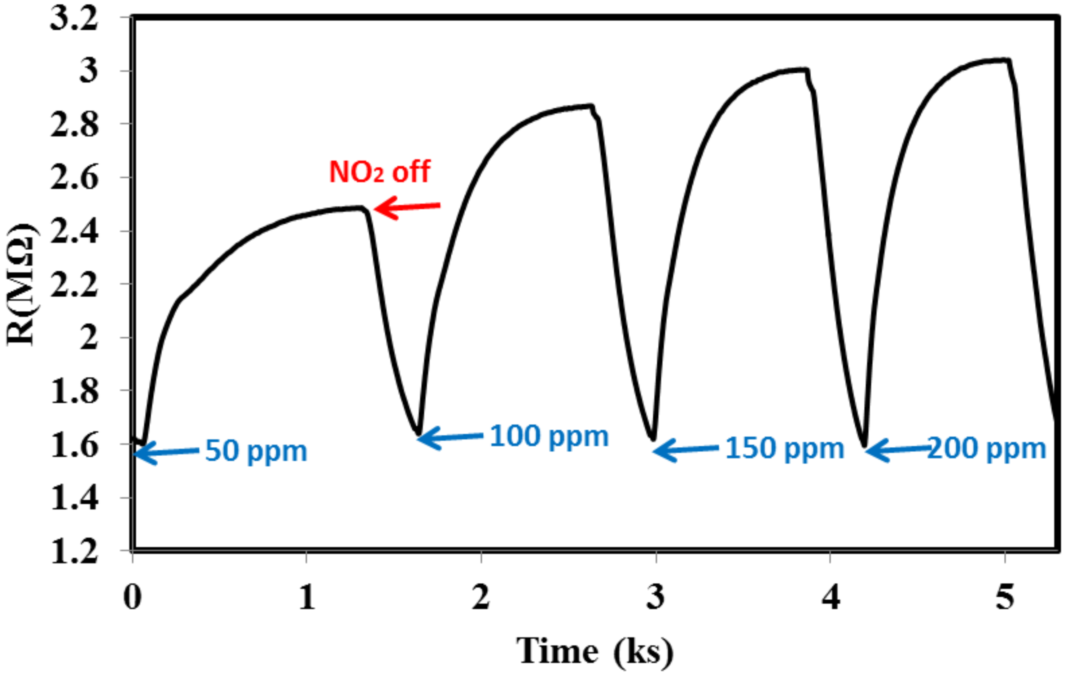

Figure 5.39. Response-recovery time of Pt/ZnO sensor at four different concentrations of NO_2 at 500 ºC

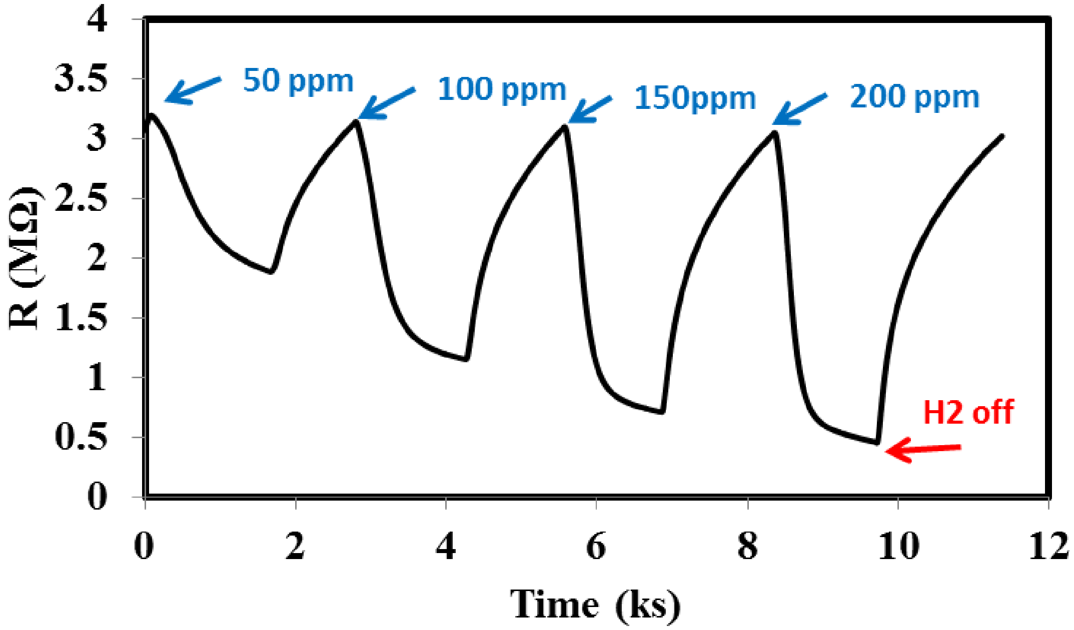

Figure 5.40. Response-recovery time of Pt/ZnO sensor at four different concentrations of H_2 at 500 °C

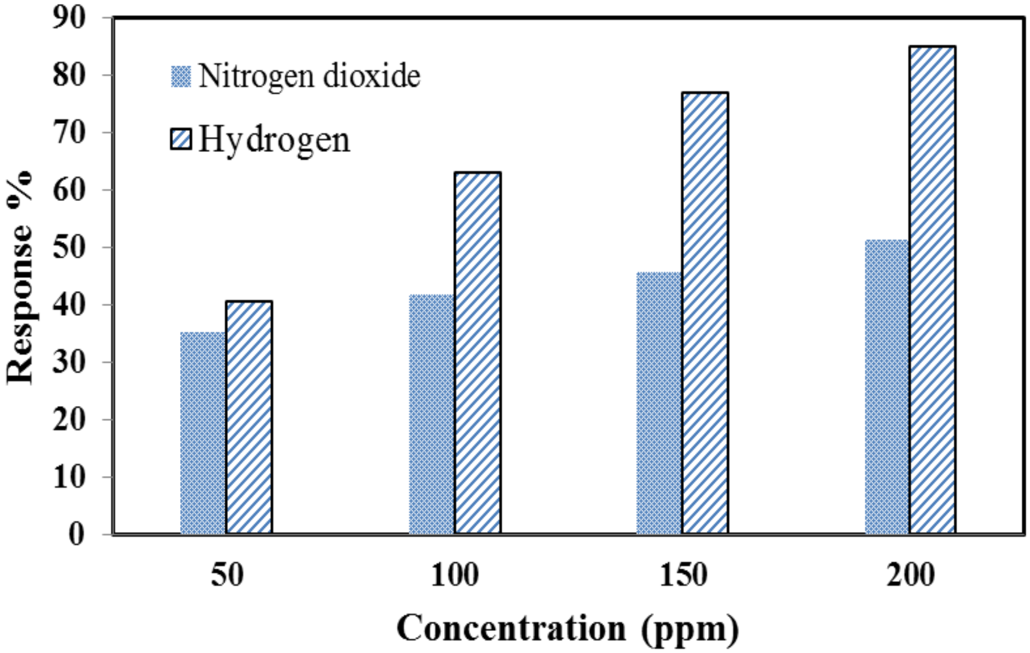

Figure 5.41. A comparison of response of Pt/ZnO sensor to H_2 and NO_2 gases at 500 ºC

5.9 ZnO SENSOR PREPARED BY OXIDIZING Zn IN H_2/H_2O MIXTURES

In the previous sections, we studied the effect of decoration of the surface of the sputtered ZnO thin films by metals on gas sensing parameters. In this section, we investigate the gas sensing properties of ZnO thin film prepared by oxidation of metallic zinc in H_2/H_2O mixture. The details for preparing the Zn thin film and the conditions of the oxidation process were described in chapter 4.3 and 5.3.

The gas sensing performance of the ZnO film oxidized in H_2/H_2O mixture was qualified and quantified in terms of resistance change when exposed to hydrogen-containing air mixtures at specific operating temperatures. Figure 5.42 shows the response of the film exposed to hydrogen over a wide range of concentrations (75-1200 ppm) at 400ºC. Clearly the film responded to hydrogen rather quickly; the recovery upon removal of hydrogen was also swift and complete.

Reproducibility of data over a large number of cycles is an important aspect in evaluating the suitability of a sensor device. Figure 5.43 shows the highly repeatable response of the prepared film over four cycles of exposure to 600 ppm H_2 at 400°C. For the effect of operating temperature, it can be seen that the maximum response and the lowest response time are recorded at 400 ºC (Fig. 5. 44 and Fig. 5.45) which means that the optimum temperature for this sensor is 400 ºC.

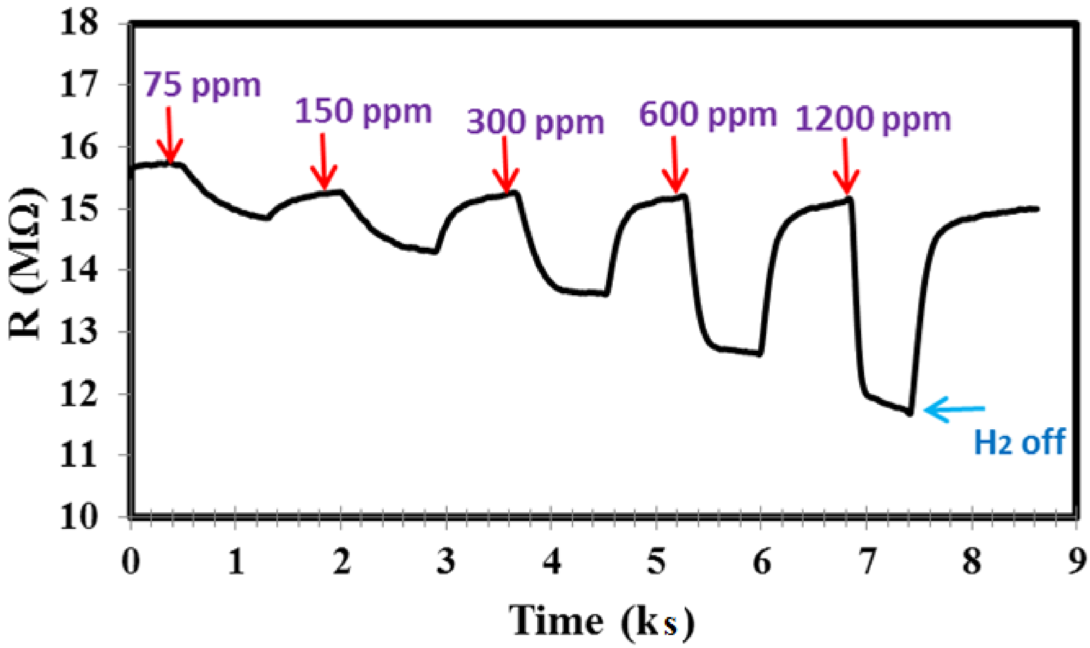

Figure 5.42. Response of pure ZnO sensor to various concentration of H_2 at 400 ºC

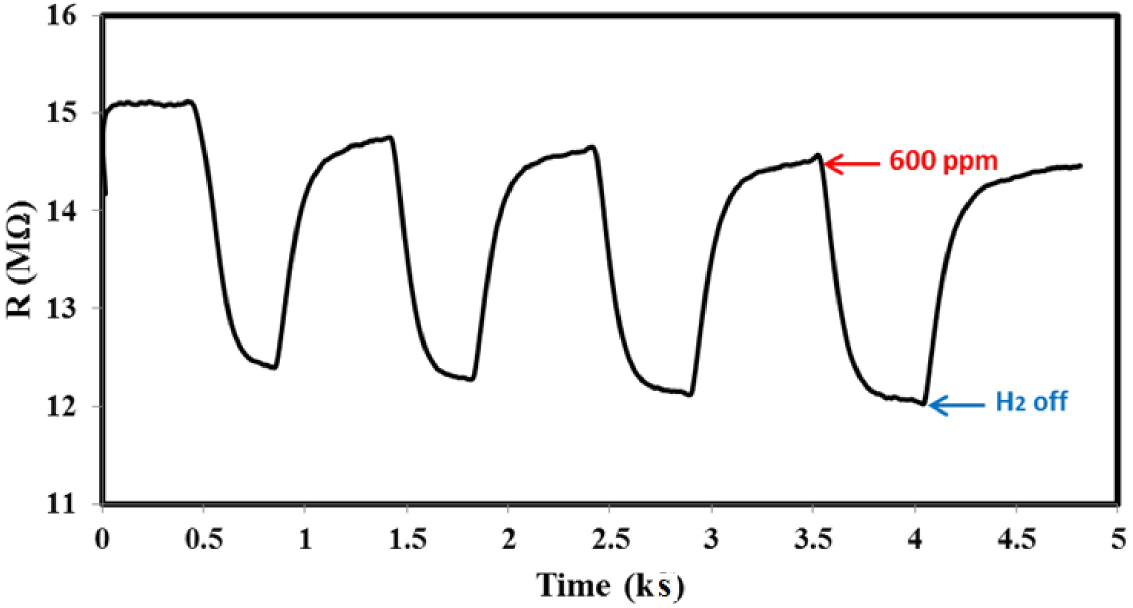

Figure 5.43. Response-recovery time of pure ZnO sensor toward 600 ppm H_2 at 400 ºC

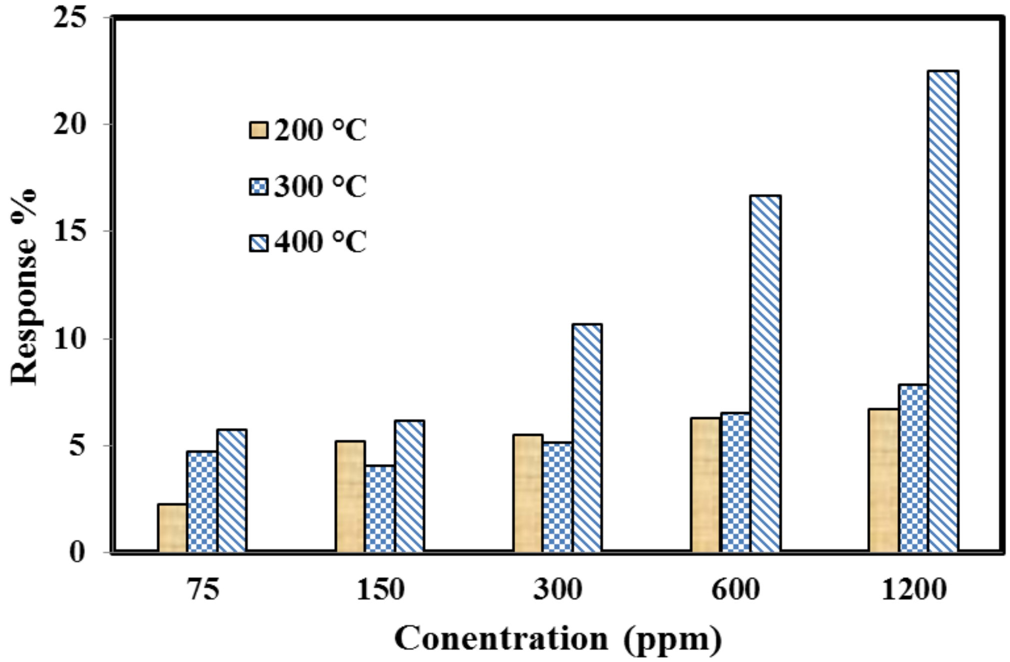

Figure 5.44. Effect of the temperature on the response of pure ZnO sensor fabricated via oxidizing of Zn in H_2/H_2O mixture.

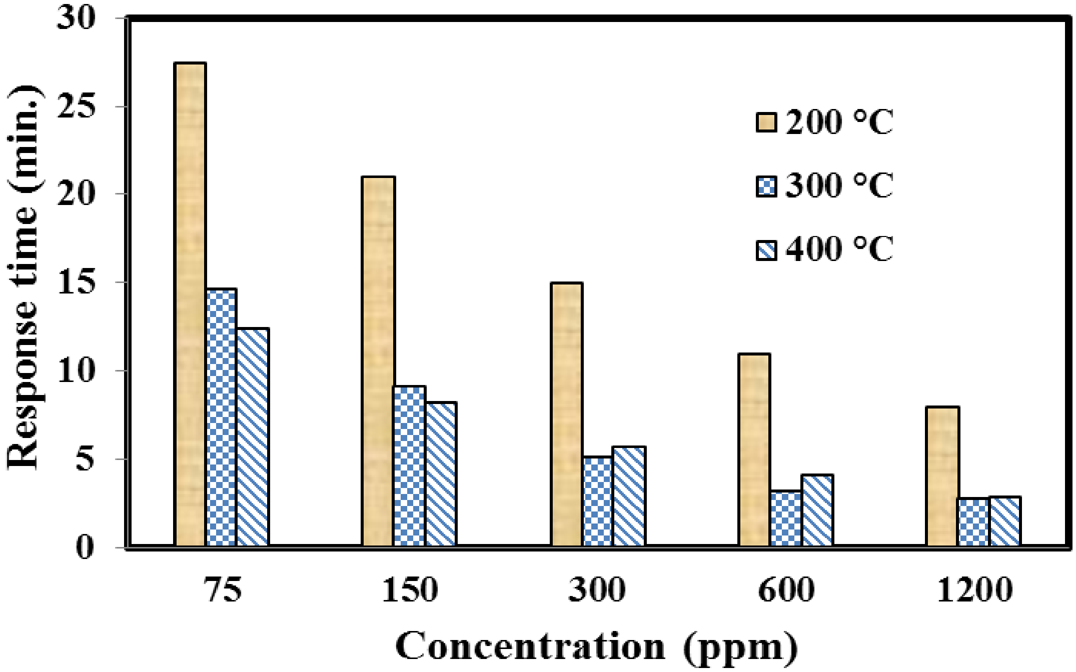

Figure 5.45. Effect of the temperature pure ZnO thin films on the response time of the sensor

We now compare the response and the response time of the sputtered ZnO thin film and the ZnO thin film prepared by oxidizing the metallic zinc in H_2/H_2O mixture. Figure 5.46 shows the response (a) and the response time (b) of both sensors toward different concentration of H_2 (300, 600, 1200) ppm. We observe two features. First, the responses in both sensors are similar. Second, the response time of the ZnO thin film prepared by oxidizing the metallic zinc in H_2/H_2O mixture is considerable smaller than ZnO thin film prepared by DC reactive sputtering. The difference in the response time between the two sensors can be explained based on the morphology. Fig. 5.46 (c) shows that the surface of the ZnO thin film oxidized in H_2/H_2O mixture is rough with high porosity that might help in gas sensing allowing larger interaction with the target gas. On the other hand, the surface of pure ZnO thin film prepared by DC reactive sputtering is relatively smooth with grain sizes less than 30 nm.

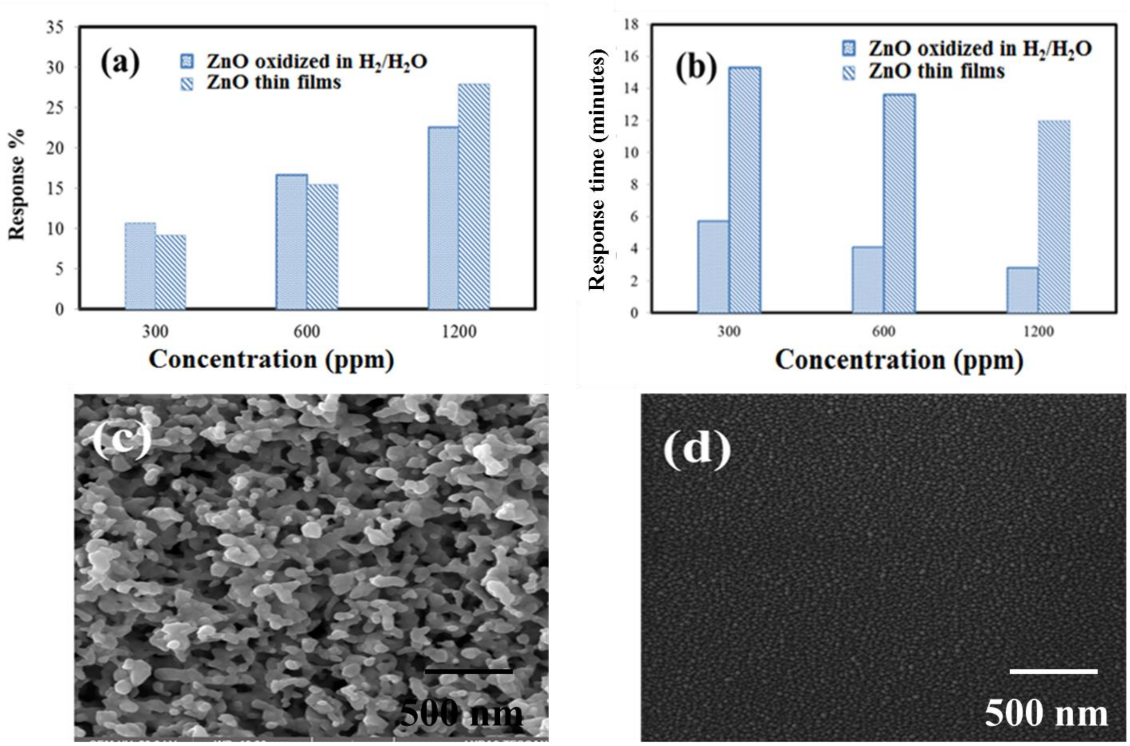

Figure 5.46. A comparison of (a) the response and (b) response time of the pure ZnO prepared by DC reactive sputtering and pure ZnO prepared by oxidizing of Zn in H_2/H_2O mixture. FE-SEM micrographs of (c) pure ZnO prepared by oxidizing of Zn in H_2/H_2O mixture, and (d) pure ZnO prepared by DC reactive sputtering

CHAPTER 6

CONCLUSION

The work in this dissertation concentrated on modifying the surface of ZnO-based thin films for gas sensing applications. In one method, the surface of sputtered ZnO thin films was modified by incorporating metal nanostructures; namely Ag, Au or Pt. The synthesis of metal on the surface of ZnO thin films (metal/ZnO) was carried out in three steps. In the first step, ZnO thin films were prepared by DC reactive sputtering. In the second step, ultra-thin layer of metal was deposited on the surface of ZnO thin films. In the last step, the ultra-thin layer of metal was converted to nanoparticles by annealing the M/ZnO thin films at different temperature under different atmospheric conditions.

The growth of continues thin layers of metal on the surface of as synthesized ZnO thin films was confirmed by FE-SEM images and XPS depth profile measurements. The XRD patterns of as prepared and post annealed ZnO thin films confirmed a preferential orientation along the c axis (002) and a peak-shift to higher diffraction angle after treatment. The crystal sizes of the metal/ZnO thin films calculated using Sherrer equation increased by increasing annealing temperature. FE-SEM images of metal/ZnO thin films show that the size and density of the metal nanoparticles (number of particles per unit area) on the surface of the ZnO thin films can be controlled by means of deposition time and post annealing treatment.

The optical properties of the films were studied by UV–Vis spectrophotometry. A reduction in optical band gap was observed after the heat treatment with a slight increase in transmittance. In addition to prepared metal/ZnO thin films, we succeeded to prepare Ag nanorings on the surface of ZnO thin films by annealing Ag/ZnO thin films in a tube furnace at 600 ºC in N_2 atmosphere for 4 hours. FE-SEM showed that the rings have an inner and outer diameter of about 600 nm and one µm respectievly.

ZnO thin films were prepared by another method. The surfaces of the sputtered Zn films were modified by varing the oxygen partial pressure (PO_2). In this regard, we first calculated the theoretical values of PO_2 needed for oxidation of ZnO as a function of temperature based on the thermodynamics of Zn/ZnO coexistence. We then controlled the PO_2 of Zn films by manipulating the ratio of H_2 and H_2O species. We found that the microstructural feature of the surface of ZnO changed by the variation of the oxygen partial pressure and annealing temperature.

The gas sensing performance of the prepared sensors toward H_2, NH_3 and NO_2 was tested. Our results showed that all the metal/ZnO thin films exhibited excellent response towards H_2 even at very low concentration (close to ppb level). We found that the performance of Pt/ZnO film was the most promising with the highest response and shortest response time. It was also found that the gas response of the Pt/ZnO films was inversely proportional with the deposition time of the precious metal. The optimum temperature of operation of the Pt/ZnO sensor was 300ºC while in the case of Ag and Au/ZnO films it was 400ºC.

In order to test the selectivity of Pt/ZnO sensor, the response and response time toward NO_2 (oxidizing gas) and NH_3 (reducing gas) were investigated. Our results showed that at temperature lower than 400 ºC the response time of Pt/ZnO sensor toward NO_2 is too long. By comparing the response and the response time of the as prepared ZnO thin film and ZnO film oxidized in H_2/H_2O toward H_2, we found that the response time of the latter sensor was shorter.

RECOMMENDATION FOR FUTURE WORK

Based on our results and observations in this work, the following issues are recommended for future investigation:

- Study of the gas sensing mechanism for quantitative/qualitative description of chemical sensing behavior for different gases.
- Test the response of other oxidizing gases to further verify the proposed sensing mechanism.
- Numerically model the proposed sensing to explain the role of noble metals in gas sensing.
- Develop a model to study the transient response behavior with flow rate and film thickness.
- Investigating the depth profile of the deposits films as a function of XPS ion sputtering time.
- Study the thickness of the deposits films through cross-section measurements of the films.
- Investigate the porosity of the thin films with annealing and the possible correlation as sensing sensitivity.
- Study the synthesis of silver nanorings on the ZnO films, and model its nucleation and formation process.

- Explain why the ZnO film becomes brittle when annealed @ 800 ºC in H_2/H_2O mixture.
- Investigate the reason(s) behind the difference between morphological features of ZnO films annealed, at different temperature, in air and H_2/H_2O mixture.

REFERENCES

1- Y. Sing, and S. Agnihotri, Semiconductor devices, I.K. International Publishing House Pvt. Ltd. (2009).

2- S. M. Sze, Semiconductor Devices: Physics and technology, Wiley (2001).

3- D. A Neamen, Semiconductor physics and devices basic principles, R. D Irwin Inc. (1992).

4- Y. P. Varshni, Temperature dependence of the energy gap in semiconductors, Physica 34 (1967) 149-154.

5- S. Kim, H. Park, G. Nam, and H. Yoon, Temperature-dependent photoluminescence of boron-doped ZnO nanorods, Korean Chem. Soc. 34 (2013) 3335-3339.

6- S. Singh, P. Thiyagarajan, K.M. Kant, D. Anita, S. Thirupathiah, N. Rama, B. Tiwari, M. Kottaisamy and M.S.R. Rao, Structure, microstructure and physical properties of ZnO based materials in various forms: bulk, thin film and nano, J. Phys. D: Appl. Phys. 40 (2007) 6312- 6327.

7- M.A. Gondal, Q.A. Drmosh, Z.H. Yamani, and T.A. Saleh, Synthesis of ZnO_2 nanoparticles by laser ablation in liquid and their annealing transformation into ZnO nanoparticles, Applied Surface Science 256 (2009) 298-304.

8- S.J. Pearton, D.P. Norton, K. Ip, Y.W. Heo and T. Steiner, Recent progress in processing and properties of ZnO, Prog. Mater. Sci. 50 (2005) 293-340.

9- H.E. Brown, Zinc oxide properties and applications, International Leads Zinc Research Organization Inc. (1976).

10- K. Vanheusden, W. L. Warren, C. H. Seager, D. R. Tallant, J. A. Voigt, and B. E. Gnade, Mechanisms behind green photoluminescence in ZnO phosphor powders, J. Appl. Phys. 79 (1996) 7983-7990.

11- B.J. Jin, S. Im, and S.Y. Lee, Violet and UV luminescence emitted from ZnO thin films grown on sapphire by pulsed laser deposition, Thin Solid Films 366 (2000)107-110.

12- K. Sowri Babu, A. Ramachandra Reddy, Ch. Sujatha, K.V.G. Reddy, and A.N. Mallika, Annealing effects on photoluminescence of ZnO nanoparticles, Materials Letters 110 (2013) 10–12.

13- K. L. Chopra, and I. Kaur, Thin film device applications, Plenum Press (1983).

14- Q. A. Drmosh, S. G. Rao, Z. H. Yamani, and M. A. Gondal, Crystalline nanostructured Cu doped ZnO thin films grown at room temperature by pulsed laser deposition technique and their characterization, Applied Surface Science 270 (2013) 104-108.

15- S.D. Singh, R.S. Ajimsha, C. Mukherjee, Ravi Kumar, and L.M. Kukreja, Realization of epitaxial ZnO layers on GaP (111) substrates by pulsed laser deposition, Journal of Alloys and Compounds 617 (2014) 921–924.

16- Z.G. Zhang, F. Zhou, X.Q. Wei, M. Liu, G. Sun, C.S. Chen, C.S. Xueb, H.Z. Zhuang, and B.Y. Man, Effects of oxygen pressures on pulsed laser deposition of ZnO films, Physica E 39 (2007) 253–257.

17- R. Serhane, S. Abdelli-Messaci, S. Lafane, H. Khales, W. Aouimeur, A. Hassein-Bey, and T. Boutkedjirt, Pulsed laser deposition of piezoelectric ZnO thin films for bulk acoustic wave devices, Applied Surface Science 288 (2014) 572–578.

18- Z. Li, Z. Hua, L. Jiang, H. Huang, F. Liu, X. Zhang, Y. Wang, P. Yin, and L. Guo, Synthesis and optical properties of three-dimensional nanowall ZnO film prepared by atmospheric pressure chemical vapor deposition, Applied Surface Science 258 (2012) 10175–10179.

19- G.Z. Wang, Y. Wang, M.Y. Yau, C.Y. To, C.J. Deng, Dickon, and H.L. Ng, Synthesis of ZnO hexagonal columnar pins by chemical vapor deposition, Materials Letters 59 (2005) 3870–3875.

20- K. Kim, and H. W. Kim, Synthesis of ZnO nanorod on bare Si substrate using metal organic chemical vapor deposition, Physica B 328 (2003) 368–371.

21- X. Cai, F. Wangn, D. Yan, Z. Zhu, and X. Gu, Luminescence characteristics and growth mechanism of awl-like ZnO Nanostructures fabricated on Ni-coated silicon substrate via chemical vapor deposition method, Ceramics International 40 (2014) 12293–12298.

22- I. Saf, Recent aspects concerning DC reactive magnetron sputtering of thin films: a review, Surface and Coatings Technology 127 (2000) 203-219.

23- V. S. enay, S. Pat, S. Korkmaz, T. Aydogmus, S. Elmas, S. Özenb, N. Ekemb, and M. Z. Balbag, ZnO thin film synthesis by reactive radio frequency magnetron sputtering, Applied Surface Science 318 (2014) 2–5.

24- M. Shirazi, M.T. Hosseinnejad, A. Zendehnam, M. Ghoranneviss, and G. R. Etaati, Synthesis and characterization of nanostructured ZnO multilayer grown by DC magnetron sputtering, Journal of Alloys and Compounds 602 (2014) 108–116.

25-R. Siddheswaran, M. Netrvalová, J. Savková, P. Novák, J. Očenášek, J. Kováč, and R. Jayavel, Reactive magnetron sputtering of Ni doped ZnO thin film: Investigation of optical, structural, mechanical and magnetic properties, Journal of Alloys and Compounds 636 (2015) 85-92.

26- O. Cuchillo, U. Pala, and C. Vazquez-Lopez, Synthesis of Cu/ZnO nanocomposites by r.f. co-sputtering technique, Solar Energy Materials & Solar Cells 70 (2001) 369–377.

27- J.R.R. Bortoleto, M. Chaves, A.M. Rosa, E.P. da Silva, S.F. Durrant, L.D. Trino, P.N. and Lisboa-Filho, Growth evolution of self-textured ZnO films deposited by magnetron sputtering at low temperatures, Applied Surface Science 334 (2015) 210–215.

28- S. Rahmane, M. S. Aida, M. A. Djouadi, and N. Barreau, Effects of thickness variation on properties of ZnO:Al thin films grown by RF magnetron sputtering deposition, Superlattices and Microstructures 79 (2015) 148–155.

29- J. Rashid, M.A. Barakat, N. Salah, and S. S. Habib, ZnO-nanoparticles thin films synthesized by RF sputtering for photocatalytic degradation of 2-chlorophenol in synthetic wastewater, Journal of Industrial and Engineering Chemistry 23 (2015) 134–139.

30- S.H. Seo, and H.C. Kang, Self-assembled ZnO hexagonal nano-disks grown by radio-frequency magnetron sputtering, Materials Letters 94 (2013) 34–37.

31- C. Chang, Y. Lee, C. Dai, C. Hsiao, S. Chen, N. P. D. Nurmalasari, Jyh-C. Chen, Y. Cheng g, W. Shih, and P. Chang, A large area bimaterial sheet of piezoelectric nanogenerators for energy harvesting: Effect of RF sputtering on ZnO nanorod, Microelectronic Engineering 88 (2011) 2236–2241.

32- H. Woo Kim, M. A. Kebede, H. S. Kim, M. H. Kong, and C. Lee, Effects of annealing on the structure and photoluminescence of ZnO-sputtered coaxial nanowires, Journal of Luminescence 129 (2009) 1619–1624.

33- N. Ouldhamadouche, A. Achour, I. Musa, K. Ait Aissa, F. Massuyeau, P.Y. Jouan, M. Kechouane, L. Le Brizoual, E. Faulques, N. Barreau, and M.A. Djouadi, Structural and photoluminescence characterization of vertically aligned multiwalled carbon nanotubes coated with ZnO by magnetron sputtering, Thin Solid Films 520 (2012) 4816–4819.

34- V. Tvarozek, I. Novotny, P. Sutta b, S. Flickyngerova, K. Schtereva, and E. Vavrinsky, Influence of sputtering parameters on crystalline structure of ZnO thin films, Thin Solid Films 515 (2007) 8756–8760.

35- R. Vyas, S. Sharma, P. Gupta, Y.K. Vijay, A. K. Prasad, A.K. Tyagi, K. Sachdev, and S.K. Sharma, Enhanced NO_2 sensing using ZnO–TiO_2 nanocomposite thin films, Journal of Alloys and Compounds 554 (2013) 59–63.

36- J. George, Preparation of Thin Films, Marcel Dekker Inc (1992).

37- M.J. Madou and S.R. Morrison, Chemical Sensing with Solid State Devices, Academic Press (1989).

38- S. C. Lee, S. Y. Kim, W. S. Lee, S. Y. Jung, B. W. Hwang, D. Ragupathy, D. D. Lee, S. Y. Lee, and J. C. Kim, Effects of textural properties on the response of a SnO_2-based gas sensor for the detection of chemical warfare agents, Sensors 11 (2011) 6893–6904.

39- M. Ahsan, M.Z. Ahmad, T. Tesfamichael, J. Bell, W. Wlodarski, and N. Motta, Low temperature response of nanostructured tungsten oxide thin films toward hydrogen and ethanol, Sensors and Actuators B 173 (2012) 789– 796.

40- T. Seiyama, A. Kato, K. Fujisishi, and M. Nagatoni. A new detector for gaseous components using semiconductive thin films, Anal Chem 34 (1962)1052-1053.

41- K. Vijayalakshmi, K. Karthick, and D. Gopalakrishna, Influence of annealing on the structural, optical and photoluminescence properties of ZnO thin films for enhanced H2 sensing application, Ceramics International 39 (2013) 4749–4756.

42- J. Zhang, E. Guo, L. Wang, H. Yue, G.Cao, and L. Song, Effect of annealing treatment on morphologies and gas sensing properties of ZnO nanorods, Trans. Nonferrous Met. Soc. China 24 (2014) 736−742.

43- K. Vijayalakshmi, and A. Renitta, Enhanced H_2 sensing performance presented by Mg doped ZnO films fabricated with a novel ITO seed layer, J Mater Sci: Mater Electron 26 (2015) 3458–3465.

44- M. Kashifa, M.E. Ali, Syed M. U. Ali, and U. Hashim, Sol–gel synthesis of Pd doped ZnO nanorods for room temperature hydrogen sensing applications, Ceramics International 39 (2013) 6461–6466.

45- M. R. Kumar, K. Rajesh, G.L. Sharma, S.P.Pavunny, and R. S. Katiyar, Lithium doped ZnO thin film for hydrogen gas sensor at reduced operating temperature, Sensor Letters 12 (2014)1769-1775.

46- B. Mondal, B. Basumatari, J. Das, C. Roychaudhury, H. Saha, and N. Mukherjee, ZnO-SnO_2 based composite type gas sensor for selective hydrogen sensing, Sensors and Actuators B: Chemical 194 (2014) 389-396.

47- K. Anand, O. Singh, M. Singh, J. Kaur, and R. Singh, Hydrogen sensor based on graphene/ZnO nanocomposite, Sensors and Actuators B 195 (2014) 409–415.

48- F. Tian, Y. Liu, and K. Guo, Au nanoparticle modified flower-like ZnO structures with their enhanced properties for gas sensing, Materials science in semiconductor processing 21 (2014) 140–145.

49- J. Guo, J. Zhang, M. Zhu, D. Ju, H. Xu, and B. Cao, High-performance gas sensor based on ZnO nanowires functionalized by Au nanoparticles, Sensors and Actuators B 199 (2014) 339–345.

50- Y. Mun , S. Park, S. An, C. Leea, and H. W. Kim, NO_2 gas sensing properties of Au-functionalized porous ZnO nanosheets enhanced by UV irradiation, Ceramics International 39 (2013) 8615–8622.

51- C. Wagner, The mechanism of the decomposition of nitrous oxide on zinc oxide as catalyst, Journal of Chemical Physics 18 (1950) 69–71.

52- Y Yamaguchi, S Imamura, S. Ito, K. Nishio, and K. Fujimoto, Influence of oxygen gas concentration on hydrogen sensing of Pt/WO_3 thin film prepared by sol–gel process, Sensors and Actuators B: Chemical 216 (2015) 394–401.

53- A. Boudiba, C. Zhang, P. Umek, C. Bittencourt, R. Snyders, M. Olivier, and M. Debliquy, Sensitive and rapid hydrogen sensors based on $PdeWO_3$ thick films with different morphologies, International journal of hydrogen energy 38 (2013) 2565-2577.

54- S. Majumdar, P. Nag, and P. S. Devi, Enhanced performance of CNT/SnO2 thick film gas sensors towards hydrogen, Materials Chemistry and Physics 147 (2014) 79-85.

55- S. Das, and V. Jayaraman, SnO_2: A comprehensive review on structures and gas sensors, Progress in Materials Science 66 (2014) 112–255.

56- A. I. Ayesh, S. T. Mahmoud, S. J. Ahmad, and Y. Haik, Novel hydrogen gas sensor based on Pd and SnO_2 nanoclusters, Materials Letters 128 (2014) 354–357.

57- I. Kocemba, and J. Rynkowski, The influence of catalytic activity on the response of Pt/SnO_2 gas sensors to carbon monoxide and hydrogen, Sensors and Actuators B 155 (2011) 659–666.

58- S. Dhall, and N. Jaggi, Room temperature hydrogen gas sensing properties of Pt sputtered F-MWCNTs/SnO_2 network, Sensors and Actuators B 210 (2015) 742–747.

59- F. Berger, J. Sanchez, and O. Heintz, Detection of hydrogen fluoride using SnO_2-based gas sensors: Understanding of the reaction mechanism, Sensors and Actuators B 143 (2009) 152–157.

60- L. Yang, C. Yin, Z. Zhang, and B. Zhu, A study of hydrogen sensing properties and microstructure for highly dispersed Pd SnO_2 thin films with high response magnitude, Applied Surface Science 311 (2014) 74–82.

61- M. Shafiei, J. Yub, G. Chen, P.T. Lai, N. Motta, W. Wlodarski, and K. Kalantar-zadeh, Improving the hydrogen gas sensing performance of Pt/MoO_3 nanoplatelets using a nano thick layer of La_2O_3, Sensors and Actuators B 187 (2013) 267–273.

62- M.B. Rahmani, S.H. Keshmiri, J. Yua, A.Z. Sadek, L. Al-Mashat, A. Moafic, K. Latham, Y.X. Li, W. Wlodarski, and K. Kalantar-zadeh, Gas sensing properties of thermally evaporated lamellar MoO_3, Sensors and Actuators B 145 (2010) 13–19.

63- R. Abdul Rani, A. S. Zoolfakar, J. Z. Oua, M. R. Fieldb, M. Austina, and K. Kalantar-zadeh, Nanoporous Nb_2O_5 hydrogen gas sensor, Sensors and Actuators B 176 (2013) 149–156.

64- Z. Wang, Y. Hu, W. Wang, X. Zhang, B. Wang, H. Tian, Y. Wang, J. Guan, and H. Gu, Fast and highly-sensitive hydrogen sensing of Nb_2O_5 nanowires at room temperature, international journal of hydrogen energy 37 (2012) 4526 -4532.

65- K. M. Garadkar, B. S. Shirke,Y. B. Patil and D. R. Patil, Nanostructured ZrO_2 Thick Film Resistors as H_2-Gas Sensors Operable at Room Temperature, Sensors & Transducers Journal 110 (2009) 17-25.

66- Hafeezullah, Z. H. Yamani, J. Iqbal, A. Qurashi, and A. Hakeem, Rapid sonochemical synthesis of In_2O_3 nanoparticles their doping optical, electrical and hydrogen gas sensing properties, Journal of Alloys and Compounds 616 (2014) 76–80.

67- Y. Wang, B. Liu, D. Cai, H. Li, Y. Liu, D. Wang, L. Wang, Q. Li, and T. Wan, Room-temperature hydrogen sensor based on grain-boundary controlled Pt decorated In_2O_3 nanocubes, Sensors and Actuators B 201 (2014) 351–359.

68- A. Hazra, S. Das, J. Kanungo, C.K. Sarkar, and S. Basu, Studies on a resistive gas sensor based on sol–gel grown nanocrystalline p-TiO_2 thin film for fast hydrogen detection, Sensors and Actuators B 183 (2013) 87–95.

69- J. Lee, D. Hong Kim, S. Hong, and J. Y. Jho, A hydrogen gas sensor employing vertically aligned TiO_2 nanotube arrays prepared by template-assisted method, Sensors and Actuators B 160 (2011) 1494–1498.

70- K. Sirok, J. Jireovfi, and L. Hudec, Iron oxide thin film gas sensor, Thin Solid Films, 245 (1994) 211-214.

71- M. Kandyla, C. C. Moustakas, M. Guziewicz, and M. Kompitsas, Nanocomposite NiO:Pd hydrogen sensors with sub-ppm detection limit and low operating temperature, Materials Letters 119 (2014) 51–55.

72- P. Chou, H. Chen, I. Liu, C. Chen, J. Liou, Kai-Siang Hsu, and W. Liu, Hydrogen sensing performance of a nickel oxide (NiO) thin film-based device, International journal of hydrogen energy 40 (2015) 729-734.

73- V.G. Ponomareva, G.V Lavrova, and E.F Hairetdinov, Hydrogen sensor based on antimonium pentoxide-phosphoric acid solid electrolyte, Sensors and Actuators, B: Chemical 40 (1997) 95-98.

74- N. Tamaekong, C. Liewhiran, A. Wisitsoraat and S. Phanichphant, Sensing characteristics of flame-spray-made Pt/ZnO thick films as H_2 gas sensor, Sensors 9 (2009) 6652-6669.

75- H. S. Al-Salmana, M. J. Abdullah, N. Al-Hardan, ZnO thin film nanostructures for hydrogen gas sensing applications, Ceramics International 39 (2013) S447–S450.

76- N. S. Ramgir, P. K. Sharma, N. Datta, M. Kaur, A. K. Debnath, D. K. Aswal, and S. K. Gupta, Room temperature H2S sensor based on Au modified ZnO nanowires, Sensors and Actuators B 186 (2013) 718–726.

77- S. An, S. Park, H. Ko, C. Jin, W. Lee, and C. Lee, Enhanced gas sensing properties of branched ZnO nanowires, Thin Solid Films 547 (2013) 241–245.

78- P. K. Guha, S. Santra, J. A. Covington, F. Udre, and J. W. Gardner, Zinc oxide nanowire based hydrogen sensor on SOI CMOS platform, Procedia Engineering 25 (2011) 1473 – 1476.

79- Z.A. Ali, W.A. Ismail, and R. Puteh, Synthesis of ZnO nanowires for hydrogen sensor application using simple heating technique, Advanced Materials Research 652 (2013) 272-27.

80- A. Qurashi, N.Tabet, M. Faiz, and T. Yamzaki, Ultra-fast microwave synthesis of ZnO nanowires and their dynamic response toward hydrogen gas, Nanoscale Research Letters 81 (2009) 948-954.

81- A. Qurashi, M. Faiz, N. Tabet, and M. Alam, Low temperature synthesis of hexagonal ZnO nanorods and their hydrogen sensing properties, Superlattices and Microstructures 50 (2011) 173–180.

82- Y. T. Lim , J. Y. Son, and J.-S. Rhee, Vertical ZnO nanorod array as an effective hydrogen gas sensor, Ceramics International 39 (2013) 887–890.

83- J. J. Hassan, M.A. Mahdi, C. W. Chin, H. Abu-Hassan, and Z. Hassan, Room-temperature hydrogen gas sensor with ZnO nanorod arrays grown on a quartz substrate, Physica E 46 (2012) 254–258.

84- T. Rashid, D. Phan, and G. Chung, A flexible hydrogen sensor based on Pd nanoparticles decorated ZnO nanorods grown on polyimide tape, Sensors and Actuators B 185 (2013) 777–784.

85- M. Kashif, M.E. Ali, Syed M. Usman Ali, and U. Hashim, Sol–gel synthesis of Pd doped ZnO nanorods for room temperature hydrogen sensing applications, Ceramics International 39 (2013) 6461–6466.

86- B. Huang, and J. Lin, Core–shell structure of zinc oxide/indium oxide nanorod based hydrogen sensors, Sensors and Actuators B 174 (2012) 389–393.

87- Y.T. Lim, J.Y. Sonb, and J.-S. Rhee, Vertical ZnO nanorod array as an effective hydrogen gas sensor, Ceramics International 39 (2013) 887–890.

88- B. Huang, and J. Lin, A facile synthesis of ZnO nanotubes and their hydrogen sensing properties, Applied Surface Science 280 (2013) 945–949.

89- F. Wang, J. Liu, X. Wang, J. Kong, S. Qiu, G. Lu, and C. He, Alpha-Fe2O3atZnO heterostructured nanotubes for gas sensing, Materials Letters 76 (2012) 159–161.

90- V. E. Galstyan, V. M. Aroutiounian, V. M. Arakelyan, and G. E. Shahnazaryan, Investigation of hydrogen sensor made Of ZnO <Al> thin film, Armenian Journal of Physics 1 (2008) 242-246.

91- K. Vijayalashmi and A. Renitta, Growth of high quality ZnO:Mg films on ITO coated glass substrates for enhanced H_2 sensing, Ceramics International 40 (2014) 6171–6177.

92- Y. Liu, T. Hang, Y. Xie, Z. Bao, J. Song, H. Zhang, and E. Xie, Effect of Mg doping on the hydrogen-sensing characteristics of ZnO thin films, Sensors and Actuators B 160 (2011) 266– 270.

93- K. Vijayalakshmi, K. Karthick, and D. Gopalakrishna, Influence of annealing on the structural, optical and photoluminescence properties of ZnO thin films for enhanced H_2 sensing application, Ceramics International 39 (2013) 4749-4756.

94- S. Öztürk, N. Kılınç, İ. Torun, A. Kösemen, Y. Şahin, and Z. Z. Öztürk, Hydrogen sensing properties of ZnO nanorods: Effects of annealing, temperature and electrode structure, International Journal of Hydrogen Energy 39 (2014) 5194–5201.

95- B. Mondal, B. B. A. Vitae, J. Das, V. C. Roychaudhury, V. H. Saha, and V. N. Mukherjee, ZnO–SnO2 based composite type gas sensor for selective hydrogen sensing, Sensors and Actuators B: Chemical 194 (2014) 389–396.

96- H. S. Al-Salman, and M.J. Abdullah, Hydrogen gas sensor based on ZnO nanstructure prepared by RF- sputtering on quarts and PET substrates, Sensors and Actuators B: Chemical 181 (2013) 259-266.

97- J. Eriksson, V. Khranovskyy, F. Söderlind, P. O. Käll, R. Yakimova, and A. L. Spetz, ZnO nanoparticles or ZnO films: A comparison of the gas sensing capabilities, Sensors and Actuators B: Chemical 137 (2013) 94-102.

98- P. Mitra, A.P. Chatterjee, and H.S. Maiti, ZnO thin film sensor, Materials Letters 35 (1998) 33–38.

99- B. E. Warren, X-ray diffraction, Addison-Wesley, MA (1969).

100- S.K. Chatterjee, X-Ray diffraction: its theory and applications, Prentice Hall New Delhi (1999).

101- V. Mote, Y. Purushotham and B. Dole, Williamson-Hall analysis in estimation of lattice strain in nanometer-sized ZnO particles, Journal of Theoretical and Applied Physics 6 (2012) 1-8.

102- A. Khorsand Zak, W.H. Abd. Majid, M.E. Abrishami, and R. Yousefi, X-ray analysis of ZnO nanoparticles by Williamson-Hall and size strain plot, Solid State Sciences 13 (2011) 251-256.

103- Y. Leng, materials characterization introduction to microscopic and spectroscopic methods, John Wiley & Sons Asia Pte Ltd. (2008).

104- M. Hezam, N. Tabet, and A. Mekki, Synthesis and characterization of DC magnetron sputtered ZnO thin films under high working pressures, Thin Solid Films 518 (2010) 161–164.

105- A.A. Ogwu, E. Bouquerel, O. Ademosu, S. Moh, E. Crossan, and F. Placido, The influence of RF power and oxygen flow rate during deposition on the optical transmittance of copper oxide thin films prepared by reactive magnetron sputtering, J. Phys. D. Appl. Phys. 38 (2005) 266–271.

106- S. Ilican, M. Caglar, and Y. Caglar, Sn doping effects on the electro-optical properties of sol gel derived transparent ZnO films, Appl. Surf. Sci. 256 (2010) 7204–7210.

107- W.T. Yen, Y.C. Lin, P.C. Yao, J.H. Ke, and Y.L. Chen, Effect of post-annealing on the optoelectronic properties of ZnO: Ga films prepared by pulsed direct current magnetron sputtering, Thin Solid Films 518 (2010) 3882–3885.

108- B. David. C. Williams and C. Barry, Transmission electron microscopy: a textbook for materials science, Plenum Publishing Corporation New York (1996).

109- M. D. Graef, Introduction to conventional transmission electron microscopy, Cambridge University presses UK (2003).

110- L.W. Wang, F.Wu, D.X. Tian, W.J. Li, L. Fang, C.Y. Kong, and M. Zhou, Effects of Na content on structural and optical properties of Na-doped ZnO thin films prepared by sol–gel method, Journal of Alloys and Compounds 623 (2015) 367–373.

111- B. Cappella, and G. Dietler, Force-distance curves by atomic force microscopy, Surface Science Reports 34 (1999) 1–104.

112- B. P. Carlo, and D. Ricci, Atomic Force Microscopy: Biomedical Methods and Applications, Springer Science & Business Media (2004).

113- W. Jin, S. Yan, W. Chen, S. Yang, C. Zhao, and Y. Dai, Enhanced ethanol sensing characteristics by decorating dispersed Pd nanoparticles on vanadium oxide nanotubes, Materials Letters (2014) 362-365.

114- H.A.E. Dole, L.F. Safady, S. Ntais, M. Couillard, and E.A. Baranova, Electrochemically enhanced metal-support interaction of highly dispersed Ru nanoparticles with a CeO_2 support, Journal of Catalysis 318 (2014) 85-94.

115- X. Li, W. Zheng, H. Pan, Y. Yu, L. Chen, and P. Wu, Pt nanoparticles supported on highly dispersed TiO_2 coated on SBA-15 as an efficient and recyclable catalyst for liquid-phase hydrogenation, Journal of Catalysis 300 (2013) 9-19.

116- G. Korotcenkov, V. Brinzari, L.B. Gulina, and B.K. Cho, The influence of gold nanoparticles on the conductivity response of SnO_2-based thin film gas sensors, Applied Surface Science 353 (2015) 793-803.

117- G. L. Hornyak, H.F. Tibbals, J. Dutta and J. J. Moore, Introduction to Nanoscience and Nanotechnology, CRC Press Taylor and Francis Group, Boca Raton, London, New York (2009).

118- A. H. Alshehri, M. Jakubowska, A. Mlozniak, M. Horaczek, D. Rudka, C. Free and J. D. Carey, Enhanced electrical conductivity of silver nanoparticles for high frequency electronic applications, Appl. Mater. Interfaces 4 (2012) 7007-7010.

119- C-W. Chou, S-H. Hsu, H. Chang, S-M. Tseng and H-R. Lin, Enhanced thermal and mechanical properties and biostability of polyurethane containing silver nanoparticles, Poly. Deg. and Stab. 91 (2006) 1017-1024.

120- M. K. Hossain, Surface-enhanced Raman scattering: A technique of choice for molecular detection, Mat. Sci. Forum 754 (2013) 143-169.

121- M. K. Hossain, G. R. Willmott, P. G. Etchegoin, R. J. Blaikie and J. L. Tallon, Tunable SERS using gold nano-aggregates on an elastomeric substrate Nano Scale 5 (2013) 8945-8950.

122- J. Turkevich, P. C. Stevenson and J. Hillier, A study of the nucleation and growth processes in the synthesis of colloidal gold, Discuss. Faraday. Soc. 11 (1951) 55-75.

123- J. Kimling, M. Maier, B. Okenve, V. Kotaidis, H. Ballot and A. Plech, Turkevich method for gold nanoparticle synthesis revisited, J. Phys. Chem. B 110 (2006) 15700-15707.

124- M. Brust, M. Walker, D. Bethell, D. J. Schiffrin and R. Whyman, Synthesis of thiol-derivatized gold nanoparticles in a 2-phase liquid-liquid system, Chem. Commun. 7 (1994) 801-802.

125- A. Manna, P. Chen, H. Akiyama, T. Wei, K. Tamada and W. Knoll, Optimized photoisomerization on gold nanoparticles capped by unsymmetrical azobenzene disulfides, Chem. Mater. 15 (2003) 20-28.

126- S. D. Perrault and W. C. W. Chan, Synthesis and surface modification of highly monodispersed, spherical gold nanoparticles of 50-200 nm, J. Am. Chem. Soc. 131 (2009) 17042-17043.

127- A. J. Christy and M. Umadevi, Synthesis and characterization of monodispersed silver nanoparticles, Advances in Natural Sciences: Nanoscience and Nanotechnology 3 (2012) 035013-035016.

128- S. K. Ghosh, S. Kundu, M. Mandal, S. Nath and T. Pal, Studies on the evolution of silver nanoparticles in micelle by UV-photoactivation, Journal of Nanoparticle Research (2003) 577–587.

129- J. Siegel, O. Kvıtek, P. Ulbrich, Z. Kolska, P. Slepicka and V. Svorcık, Progressive approach for metal nanoparticle synthesis, Mater. Lett. 89 (2012) 47-50.

130- V. Vaithianathan, S. Hishita, J. Park, and S. Kim, Photoluminescence in phosphorous-implanted ZnO films, J. Appl. Phys. 102 (2007) 086107-086110.

131- M.N. Kamalasanan, Subhas Chandra, Sol-gel synthesis of ZnO thin films, Thin Solid Films 288 (1996) 112-115.

132- V. Gupta, A. Mansingh, Influence of post-deposition annealing on the structural and optical properties of sputtered Zinc oxide Film, J. Appl. Phys. 80 (1996) 1063-1073.

133- J.C. Gawlak, and P.C. Aita, The dependence of aluminum nitride film crystallography on sputtering plasma composition, J. Vac. Sci. Technol. A 1 (1983) 403-408.

134- Z. B. Fang, Z.J.Yan, S. Y. Tan, Q. X. Liu and Y.Y. Wang, Influence of post-annealing treatment on the structure properties of ZnO films. Applied Surface Science 241 (2005) 303-308.

135- M. Wang, J. Wang, W. Chen, Y. Cui, and L. Wang, Effect of preheating and annealing temperatures on quality characteristics of ZnO thin film prepared by sol–gel method Mater. Chem. Phys. 97 (2006) 219-225.

136- H.W. Lee, S.P. Lau, Y.G. Wang, B.K. Tay, and H.H. Hng, Internal stress and surface morphology of zinc oxide thin films deposited by filtered cathodic vacuum arc technique, Thin Solid Films 458 (2004) 15-19.

137- C. Y. Lee, Y. S. Hu, W. Water, K. K. Tiong, C.Z. Feng, T.Y. Chen, C. J. Huang, W.J. Lee, C.C. Huang, L. J. Shen, and M.H. Cheng, Rapid thermal annealing effects on the structural and optical properties of ZnO films deposited on Si substrates, Journal of Luminescence 129 (2009)148-152.

138- V. Gupta, and A. Mansingh, Influence of postdeposition annealing on the structural and optical properties of sputtered zinc oxide film, Journal of Applied Physics 80 (1996) 1063-1070.

139- B. Z. Fang, J. Z. Yan, S.Y. Tan, Q. X. Liu and Y. Y. Wang, Influence of post-annealing treatment on the structure properties of ZnO films, Applied Surface Science 241 (2005) 303-308.

140- F. Spaepen, Interfaces and stresses in thin films, Acta mater 48 (2000) 31-42.

141- K.S. Kim, W.H. Kim, and M.C. Lee, Effect of growth temperature on ZnO thin film deposited on SiO_2 substrate, Materials Science and Engineering: B 98 (2003)135-139.

142- B.R. Strohmeier, and D.M. Hercules, Surface spectroscopic characterization of the interaction between zinc ions and γ-alumina, Journal of Catalysis. 86 (1984) 266-279.

143- NIST X ray Photoelectron Spectroscopy Database, version 4.1 (2000), http://srdata.nist.gov/xps/

144- M.N. Islam, T.B. Ghosh, K.L. Chopra and H.N. Acharya, XPS and X-ray diffraction studies of aluminum-doped zinc oxide transparent conducting films, Thin Solid Films 280 (1996) 20-25.

145- N.L. Tarwal, A.V. Rajgure, A.I. Inamdar, R.S. Devan, I.Y. Kim, and S.S. Suryavanshi, Growth of multifunctional ZnO thin films by spray pyrolysis technique, Sensors and Actuators A: Phys.199 (2013) 67–73.

146- M. Chen, X. Wang, Y.H. Yu, Z.L. Pei, X.D. Bai, C. Sun, R.F. Huang, and L.S. Wen, X-ray photoelectron spectroscopy and auger electron spectroscopy studies of Al-doped ZnO films, Applied Surface Science 158 (2000) 134-140.

147- L. Jing, Z. Xu,. J. Sun, and W. Cai, The surface properties and photocatalytic activities of ZnO ultrafine particles, Applied Surface Science 180 (2001) 308-314.

148- O. Lupan, T. Pauporte´, L. Chow, B. Viana e, F. Pelle´, L.K. Ono, and B. Roldan Cuenya, H. Heinrich, Effects of annealing on properties of ZnO thin films prepared by electrochemical deposition in chloride medium, Applied Surface Science 256 (2010) 1895–1907.

149- Ranjan K. Sahu, K. Ganguly, T. Mishra, M. Mishra, R.S. Ningthoujam, S.K. Roy, and L.C. Pathak a, Stabilization of intrinsic defects at high temperatures in ZnO nanoparticles by Ag modification, Journal of Colloid and Interface Science 366 (2012) 8–15.

150- NIST X ray Photoelectron Spectroscopy Database, version 4.1 (2000), http://srdata.nist.gov/xps/

151- A. de Rooij, The oxidation of silver by Atomic Oxygen, ESA J. 13 (1989) 363.

152- L. Meng, P Carlos, D Moreira, and M.P. Santos, Study of the structural properties of ZnO thin films by x-ray photoelectron spectroscopy, Applied Surface Science 78(1994) 57-61.

153- Q. A. Drmosh, M. K. Hossain, F. H. Alharbi, and N. Tabet, Morphological, structural and optical properties of silver treated zinc oxide thin film, Journal of Materials Science: Materials in Electronics DOI 10.1007/s10854-014-2375-3.

154- P. Georgiev, N. Kaneva, A. Bojinova, K. Papazova, K. Mircheva, and K. Balashev, Effect of gold nanoparticles on the photocatalytic efficiencyof ZnO films, Colloids and Surfaces A: Physicochemical and Engineering Aspects Colloids and Surfaces A: Physicochem. Eng. Aspects 460 (2014) 240–247.

155- E. Gaspera, M. Guglielmi, A. Martucci, L. Giancaterini, and C. Cantalini, Enhanced optical and electrical gas sensing response of sol–gel based NiO–Au and ZnO–Au nanostructured thin films, Sensors and Actuators B: Chemical 164 (2012) 54-63.

156- T. Okuno, G. Kawamura, H. Muto, and A. Matsuda, Fabrication of Shape-Controlled Au Nanoparticles in a TiO_2-Containing Mesoporous Template Using UV Irradiation and Their Shape-Dependent Photocatalysis, Journal of Materials Science & Technology 30 (2014) 8-12.

157- W. Yue, Y. Yang, Z. Wang, L. Chen, and X. Wang, Surface-enhanced Raman scattering on gold nanorod pairs with interconnection bars of different widths. Sensors and Actuators B: Chemical171 (2012) 734-738.

158- P. Rai, Y. S. Kim, H. M. Song, M. K. Song, and Y. T. Yu, The role of gold catalyst on the sensing behavior of ZnO nanorods for CO and NO_2 gases, Sensors and Actuators B 165 (2012) 133– 142.

159- C. Worsch, M. Kracker, W. Wisniewski, and C. Rüssel, Optical properties of self-assembled oriented island evolution of ultra-thin gold layers, Thin Solid Films 520 (2012) 4941–4946.

160- S. Reymond-Laruinaz, L. Saviot, V. Potin, C. Lopes, F. Vaz, and M.C. Lucas, Growth and size distribution of Au nanoparticles in annealed Au/TiO_2 thin films, Thin Solid Films 553 (2014) 138–143.

161- M. Kracker, C. Worsch, C. Bocker, and C. Rüssel, Optical properties of de-wetted thin silver/gold multilayer films on glass substrates, Thin Solid Films 539 (2013) 47–54.

162- A. Imre, D.L. Beke, E. Gontier-Moya, I.A. Szab, and E. Gillet, Surface Ostwald ripening of Pd nanoparticles on the MgO (100) surface, Applied Physics A 71 (2000) 19–22.

163- S. Ozen, and M. A. Gulgun, Residual stress relaxation and microstructure in ZnO thin films, Advances in Science and Technology 45 (2006)1316-1321.

164- S. B. Yahia, L. Znaidi, A. Kanaev, and J. P. Petitet, Raman study of oriented ZnO thin films deposited by sol–gel method, Spectrochimica Acta 71 (2008) 1234–1238.

165- A.G. Rolo, J. Ayres de Campos, T. Viseu, T. de Lacerda-Arôso and M.F. Cerqueira, The annealing effect on structural and optical properties of ZnO thin films produced by rf sputtering, Superlattices and Microstructures 42 (2007) 265-269.

166- S.R. Laruinaz, L. Saviot, V. Potin, C. Lopes, F. Vaz, M.C. Marco de Lucas, Growth and size distribution of Au nanoparticles in annealed Au/TiO_2 thin films, Thin Solid Films 553 (2014) 138–143.

167- T. Prasada Rao and M.C. Santhosh Kumar, Resistivity stability of Ga doped ZnO thin films with heat treatment in air and oxygen atmospheres, Journal of Crystallization Process and Technology 2 (2012) 72-79.

168- H.T. Cao, Z.L. Pei, J. Gong, C. Sun, R.F. Huang, and L.S. Wen, Preparation and characterization of Al and Mn doped ZnO (ZnO: (Al, Mn)) transparent conducting oxide films, Journal of Solid State Chemistry 177 (2004) 1480–1487.

169- A. Lebugle, U. Axelsson, R. Nyholm, N. Mårtensson, Experimental L and M. core, level binding energies for the metals ^{22}Ti to ^{30}Zn, Physica Scripta 23 (1980) 825-828.

170- S.H. Jeong, B.N. Park, S.B. Lee and J. H. Boo, Structural and optical properties of silver-doped zinc oxide sputtered films, Surface and Coatings Technology 193 (2005) 340-343.

171- I. Kim, E. Jeong, D. Kim, M. Kumar and S. Choi, Investigation of p-type behavior in Ag-doped ZnO thin films by E-beam evaporation, Applied Surface Science 255 (2009) 4011-4014.

172- M.A. Raso, I. Carrillo, E. Mora, E. Navarro, M.A. Garcia, and T.J. Leo, Electrochemical study of platinum deposited by electron beam evaporation for application as fuel cell electrodes, International Journal of Hydrogen Energy 39 (2014) 5301-5308.

173- S. Ji, I. Chang, G. Y. Cho, Y. H. Lee, J. H. Shim, and S. W. Cha, Application of dense nano-thin platinum films for low-temperature solid oxide fuel cells by atomic layer deposition, International Journal of Hydrogen Energy 39 (2014) 12402-12408.

174- S.S. Pethaiah, G.P. Kalaignan, G. Sasikumar, and M. Ulaganathan, Evaluation of platinum catalyzed MEAs for PEM fuel cell applications, Solid State Ionics 190 (2011) 88-92.

175- A. Ekaterina. P Tatyana. A. M. Nasalevich, A.V. Vorontsov, A.V. Miller, and V.V. Kaichev, Influence of the method of platinum deposition on activity and stability of Pt/TiO_2 photocatalysts in the photocatalytic oxidation of dimethyl methylphosphonate, Catalysis Communications 12 (2011) 597-601.

176- S. Zhao, G. Ramakrishnan, P. Shen, D. Su, and A. Orlov, The first experimental demonstration of beneficial effects of sub-nanometer platinum particles for photocatalysis, Chemical Engineering Journal 217 (2013) 266-272.

177- L. Dapeng, and Q. Jiuhui, The progress of catalytic technologies in water purification: A review, Journal of Environmental Sciences 6 (2009) 713-719.

178- P. Sun, Y. Yu, J. Xu, Y. Sun, J. Ma, and G. Lu, One-step synthesis and gas sensing characteristics of hierarchical SnO_2 nanorods modified by Pd loading, Sensors and Actuators B: Chemical 160 (2011) 244-250.

179- M. Penza, R. Rossi, M. Alvisi, D. Suriano, and E. Serra, Pt-modified carbon nanotube networked layers for enhanced gas microsensors, Thin Solid Films 520 (2011) 959-965.

180- D. Haridas, A. Chowdhuri, K. Sreenivas, and V. Gupta, Effect of thickness of platinum catalyst clusters on response of SnO_2 thin film sensor for LPG, Sensors and Actuators B: Chemical 153 (2011) 89-95.

181- N. Van Duy, N. Hoa, and N. Hieu, Effective hydrogen gas nanosensor based on bead-like nanowires of platinum-decorated tin oxide, Sensors and Actuators B: Chemical 173 (2012) 211-217.

182- W. Chomkitichai, H. Ninsonthi, C. Liewhiran, A. Wisitsoraat, S. Sriwichai, and S. Phanichphant , Flame-Made Pt-Loaded TiO_2 Thin Films and Their Application as H2 Gas Sensors, Journal of Nanomaterials 2013 (2013) ID 497318.

183- D. Gruber, N. Ponath, J. Müller, and F. Lindstaedt, Sputter-deposited ultra-low catalyst loadings for PEM fuel cells, Journal of Power Sources 150 (2005) 67–72.

184- R. Chang, Physical Chemistry for the Biosciences University Science Books (2005).

185- N. K. Verma. S. K. Khanna, and B. Kapila, Comprehensive chemistry XII, Laxmi publications (2015).

186- W. Ahmed, and M. J. Jackson, Gas Phase Nanofication: Emerging Nanotechnologies for Manufacturing, William Andrew (2009).

187- O. Kubaschewski, and C. B. Alcock, Metallurgical Thermochemistry 4th edition (1967).

188- D. Mackay and R. S. Boethling, Handbook of Property Estimation Methods for Chemicals: Environmental Health Sciences, CRC Press (2000).

189- A. Dimian, Integrated Design and Simulation of Chemical Processes, Elsevier Science (2003).

190- W. Schottky, H. Dr-Sperrschicht, Semiconductor theory of the barrier layer, Naturwissenschaften, 26 (1938) 843-844.

191- Marc J. Madou and S. Roy Morrison, Chemical Sensing with Solid State Devices, Academic Press (1989).

192- Z. Zhang, and J. Yates, Band bending in semiconductors: chemical and physical consequences at surfaces and interfaces, Chemical Review 112 (2012) 5520-5551.

193- P. V. Bakharev , V. V. Dobrokhotov and D. N. McIlroy, A method for integrating ZnO coated nanosprings into a low cost redox-based chemical sensor and catalytic tool for determining gas phase reaction kinetics, Chemosensors 2 (2014) 56-68.

194- H. Okamoto, H. Obayashi and T. Kudo, Carbon monoxide gas sensor made of stabilized zirconia, Solid State Ionics 1 (1980) 319-326.

195- N. H. Langton and D. Matthews, The dielectric constant of zinc oxide over a range of frequencies, Journal of Applied Physics 453 (1958) doi:10.1088/0508-3443/9/11/308.

196- V. Lantto, P. Romppainen, and S. Leppavuori, A study of the temperature dependence of the barrier energy in porous tin dioxide, Sensors and Actuators 14 (1988) 149–163.

197- F. Tian, Y. Liu, and K. Guo, Au nanoparticle modified flower-like ZnO structures with their enhanced properties for gas sensing, Materials science in semiconductor processing 21 (2014) 140–145.

198- J. Guo, J. Zhang, M. Zhu, D. Ju, H. Xu, and B. Cao, High-performance gas sensor based on ZnO nanowires functionalized by Au nanoparticles, Sensors and Actuators B 199 (2014) 339–345.

199- Y. Mun , S. Park, S. An, C. Leea, and H. W. Kim, NO_2 gas sensing properties of Au-functionalized porous ZnO nanosheets enhanced by UV irradiation, Ceramics International 39 (2013) 8615–8622.

200- N. Tamaekong, C. Liewhiran, A. Wisitsoraat, and S. Phanichphant, Sensing characteristics of flame-spray-made Pt/ZnO thick films as H_2 gas sensor, Sensors 9 (2009) 6652-6669.

201- Rout, C.S. Raju, A.R. Govindaraj, and A. Rao, C.N.R. Hydrogen sensors based on ZnO nanoparticles, Solid State Communcation 138 (2006)136–138.

202- Rout, C.S. Krishna, S.H. Vivekchand, S.R.C. Govindaraj, and A. Rao, Hydrogen and ethanol sensors based on ZnO nanorods, nanowires and nanotubes. Chemical Physics Letters 418 (2006) 586–590.

203- S. Kim, B.S Kang, Ren, F. Ip, K. Heo, Y.W. Norton, and D.P. Peartona, Sensitivity of Pt/ZnO Schottky diode characteristics to hydrogen. Applied Physics Letter 84 (2004)1698–1700.

204- S. Ozturk, N. Kilinc, and Z.Z. Ozturk, The effects of annealing on gas sensing properties of ZnO nanorod sensors coated with Pd and Pt, Procedia Engineering 47 (2012) 434-437.

205- L.C. Tien, P.W. Sadik, D.P. Norton, L.F. Voss, S.J. Pearton, H.T. Wang, B.S. Kang, F. Ren, J. Jun, and J. Lin, Hydrogen sensing at room temperature with Pt-coated ZnO thin films and Nanorodse. Applied Physics Letter 87 (2005) 222106:1–3.

206- C. Jin, S. Park, H. Kim, S. An, and C. Lee, CO gas-sensor based on Pt-functionalized Mg-doped ZnO nanowires, Bulletin of the Korean Chemical Society 33 (2012) 1993-1997.

207- S.M. Kanan, O.M. El-Kadri, I.A. Abu-Yousef, and M.C. Kanan, Semiconducting metal oxide based sensors for selective gas pollutant, Sensors 9 (2009) 8158-8196.

208- A.C.C. Tseung, and K.Y. Chen, Hydrogen spill-over effect on Pt/WO_3 anode catalysts, Catalysis Today 38 (1997) 439-443.

209- H. Lin, The study of oxygen spillover and back spillover on Pt/TiO_2 by a potential dynamic sweep method, Journal of Molecular Catalysis A: Chemical 144 (1999) 189–197.

210- S. Basu and P. K. Basu, Nanocrystalline Metal Oxides for Methane Sensors: Role of Noble Metals, Journal of Sensors 2009 (2009) ID 861968.

211- S.R. Morrison, Selectivity in semiconductor gas sensors, Sensors and Actuators 12 (1987) 425–440.

212- D. Haridas, A. Chowdhuri, K. Sreenivas, and V. Gupta, Effect of thickness of platinum catalyst clusters on response of SnO_2 thin film sensor for LPG, Sensors and Actuators B: Chemical 153 (2011) 89–95.

213- H. Ibah, and H. Luth, Solid-State Physics an introduction to principle of materials science, Springer (2009).

214- A Salehi, Selectivity enhancement of indium-doped SnO_2 gas sensors, Thin Solid Films 416 (2002) 260–263.

215- S. Park, S. Kim, S. Park,1 W. Lee, and C. Lee, Effects of functionalization of TiO_2 nanotube array sensors with Pd nanoparticles on their selectivity, Sensors (Basel) 14 (2014) 15849–15860.

216- J.P. Viricelle, A. Pauly, L. Mazet, J. Brunet, M. Bouvet, C. Varenne, and C. Pijolat, Selectivity improvement of semi-conducting gas sensors by selective filter for atmospheric pollutants detection, Materials Science and Engineering: C 26 (2006) 186–195.

217- A. Fort, M. Gregorkiewitz, N. Machetti, S. Rocchi, B. Serrano, L. Tondi, N. Ulivieri, V. Vignoli, G. Faglia, and E. Comini, Selectivity enhancement of SnO_2

sensors by means of operating temperature modulation, Thin Solid Films 418 (2002) 2-8.

218- I. Haq, and A. Azad, Experimental artifacts for morphological tweaking of chemical sensor materials: studies on ZnO, Sensors 12 (2012) 8259-8277.

219- W. Yan, M. Hu, P. Zeng, S. Ma, and M. Li, Room temperature NO_2-sensing properties of WO_3 nanoparticles/porous silicon, Applied Surface Science 292 (2014) 551-555.

VITA

Full Name: Qasem Ahmed Qasem Drmosh.

Place & date of Birth: Ibb- Yemen: 19-4-1977.

Nationality: Yemeni.

Present address: King Fahd University of Petroleum & Minerals (KFUPM) P.O. Box: 771, Dhahran 31261, Saudi Arabia.

Permanent address: Taiz street, Ibb, Yemen.

Email: qdrmosh@yahoo.com

PUBLICATIONS AND CONFERENCES

1. Patents

1. M.A. Gondal, **Q.A. Drmosh**, Z.H.Yamnai and T.A. Saleh " Method for detection of Cyanide in water, USPTO Pat US20130203178 A1(2013).
2. M.A. Gondal, **Q.A. Drmosh**, Z.H.Yamnai and T.A. Saleh "Method for detection of Cyanide in water-02, USPTO Pat. US9034169B2 (2015).
3. **Q.A. Drmosh,** M. K. Hossain, and Nouar Tabet "Method of preparing silver nanoparticles and silver nanorings", USPTO application number 14/632316 Feb. 26- 2015.
4. **Q.A. Drmosh,** M. K. Hossain "Silver nanoparticles on conducting electrode: a simple two-step process for realizing plasmonic solar cell design" USPTO Pat application number 62/164403 May 28 2015 (2015).

2. Papers

5. **Q. A. Drmosh,** Z.H. Yamani, Synthesis, characterization, and hydrogen gas sensing properties of AuNPs-catalyzed ZnO sputtered thin films, Applied Surface Science In Press available online 2 March 2016.
6. **Q. A. Drmosh,** Z.H. Yamani, Hydrogen sensing properties of sputtered ZnO films decorated with platinum nanoparticles, Ceramics International, under revision.
7. **Q. A. Drmosh,** M. K. Hossain, F. H. Alharbi & N. Tabet M. K. Hossain, Morphological, structural and optical properties of silver treated zinc oxide thin film, *Journal of Materials Science: Materials in Electronics 26(2015) pp. 139-148.*
8. Mohammad Qamar, **Qasem Drmosh**, Muhammad I Ahmed, Muhammad Qamaruddin and Zain H Yamani, Enhanced photoelectrochemical and photocatalytic activity of WO_3-surface modified TiO_2 thin film, *Nanoscale Research Letters DOI 10.1186/s11671-015-0745-2 (2015) 1-6.*
9. Mohammad Kamal Hossain, **Qasem Ahmed Drmosh,** Fahhad Al Harabi and Nouar Tabet, Silver Nanoparticles on Zinc Oxide: An Approach to Plasmonic PV solar cell, *Advanced Materials Research 938 (2014) pp. 280-285.*
10. **Q. A. Drmosh**, A. M. Wajeh and H. M. Bahaidarah “Silver nanoparticles on conducting electrode: A simple two-steps process for realizing plasmonic solar cell design” *Appl. Phys. A, DOI 10.1007 (2014) pp 459-465.*
11. M. K. Hossain, **Q. A. Drmosh,** Z. H. Yamani, Silver nanoparticles on Zinc Oxide thin film: An insight in fabrication and characterization, *IOP Conf. Series:*

Materials Science and Engineering 64 doi:10.1088/1757-899X/64/1/012018 (2014) 012018.

12. **Qasem A. Drmosh**, Saleem G. Rao, Zain H. Yamani, Mohammed A. Gondal, Crystalline nanostructured Cu doped ZnO thin films grown at room temperature by pulsed laser deposition technique and their characterization, *Applied Surface Science 270 (2013) pp. 104-108.*
13. Fahhad Al Harabi, **Qasem Ahmed Drmosh,** Mohammad Kamal Hossain, and Nouar Tabet Metallic quantum dots as sensitizers for solar cells, Photovoltaic Specialists Conference (PVSC) IEEE 39th DOI: 10.1109/ PVSC. 2013 6744308 (2013) 0993- 0996
14. M. A. Gondal**, Q. A. Drmosh**, and T.A. Saleh **“**Optical Properties of Bismuth Oxide Nanoparticles Synthesized by Pulsed Laser Ablation in Liquids, *Science of Advanced Materials 4(2012*) *pp. 1–4.*
15. T .A. Saleh, M.A. Gondal,, **Q.A. Drmosh** and Z. H. Yamani, Enhancement in Photocatalytic Activity for Acetaldehyde Removal by Embedding ZnO nano particles on Multi Wall Carbon Nanotubes *Chemical Engineering Journal, 166(2011) pp. 407-412.* (Top cited paper for 2011-2012)
16. M. A. Gondal, **Q. A. Drmosh,** and T.A. Saleh, Synthesis of Nickel oxide nanoparticles using pulsed laser ablation in liquids and their optical characterization, *Applied Surface Science 258 (2012) pp. 6982-6986.*
17. M. A. Gondal, **Q. A. Drmosh**, Growth of metal oxide nanoparticles using pulsed laser ablation technique, *Proc. SPIE 7940,794013(2011) doi:10.1117/ 12.878596.*

18. T.A. Saleh, M.A. Gondal,, **Q.A. Drmosh**, Preparation of a MWCNT/ZnO nanocomposite and its photocatalytic activity for the removal of cyanide from water using a laser, *Nanotechnology 21 (2010) 495705 (8 pp).*
19. M. A. Gondal, **Q. A. Drmosh,** and T.A. Saleh, Effect of post-annealing temperature on structural and optical properties of nano -ZnO synthesized from ZnO_2 by Laser Ablation Method, *International Journal of Nano Particles 3 (2010) pp.257-266.*
20. M.A, Gondal. **Q.A. Drmosh** and Z. H. Yamani, Synthesis of ZnO_2 nanoparticles by laser ablation in liquid and their annealing transformation into ZnO nanoparticles, *Applied Surface Science 256 (2009)pp. 298–304* (listed as Top 25 Hot Papers by Science Direct).
21. **Q.A. Drmosh**. M.A. Gondal. T.A. Saleh, Spectroscopic characterization approach to study surfactants effect on ZnO_2 nanoparticles synthesis by laser ablation process, *Applied Surface Science 256 (2010) pp. 4661-4666.*
22. **Q.A. Drmosh**, M.A. Gondal, T.A. Saleh, Preparation and Characterization of SnO_2 Nanoparticles Using High Power Pulsed Laser ablation Technique, *Applied Surface Science 256 (2010) pp. 4661-4666.*
23. M.A. Gondal. **Q.A. Drmosh**, Z. H. Yamani and M. Rashid, Synthesis of Nanostructure ZnO and ZnO_2 by Laser Ablation Process Using Third Harmonic of Nd:YAG Laser, *Int.J. Nanoparticles 2 (2009) pp.142–149.*

Conferences

24. **Q. A. Drmosh,** M. K. Hossain, Z. H. Yamani and N. Tabet,' Silver Nanoparticles on Zinc Oxide Thin Film: An insight in Fabrication and Characterization, Nanostruc 2014, Madrid, Spin (20-22 May 2014).

25. M.K. Hossain, **Q. A. Drmosh**, F. A. Harbi, N. Tabet, "Fabrication of Silver Nanoparticles on Zinc Oxide: An Approach to Plasmonic PV solar cell", International Conference on Nano Materials: Science, Technology And Applications (ICNM' 13), Chennai, India (5-7 Dec. 2013).

26. **Q.A. Drmosh,** M.A. Gondal, T.A. Saleh and Z. H. Yamani, Growth of oxide nanoparticles using pulsed laser ablation technique, , Oxide-based Materials and Devices II *the Moscone Center, San Francisco, California United States (*22 - 27 January 2011).

27. **Q.A. Drmosh,** M.A. Gondal, T.A. Saleh and Z. H. Yamani, synthesis and characterization of nanoparticles using optical techaniques, *Fourth Saudi Conference, Tibah University, Saudi Arabia,* (21-24 March, 2010).

28. **Q.A. Drmosh** and T.A. Saleh" Synthesis of Catalytic Nano-Metal Oxides and Peroxides using laser ablation technique and Their Applications for Pollutants Removal from Water" *1st Annual International Conference (Environmental Science & Technology), Ibb University, Yemen (1-3 Aug. 2010).*

29. **Q.A. Drmosh,** M.A. Gondal, T.A. Saleh and Z. H. Yamani Synthesis of Nano-ZnO2 Using Pulsed Laser Ablation Technique and its Application in Cyanide Sensing, Fifth Saudi Physical Society, , *Saudi Arabia*, (25-27,October 2010).

30. M.A. Gondal. **Q.A. Drmosh**, Z.H. Yamani, Study of Surfactants and Post Annealing Temperature On Size of Synthesized Nano Structure ZnO Using High Power Pulsed Laser Ablation Technique, *The International Conference For Nanotechnology Industries The Leading Technology of 21st Century Riyadh, Saudi Arabia*, (5-7 April, 2009).
31. M.A. Gondal. **Q.A. Drmosh**, Z.H. Yamani, Surfactants Effect On The Morphology Of Nanoparticles Synthesized By Novel Laser Ablation Method at 355 nm, *International Conference of Nanotechnology and Advanced Materials (ICNAM), Bahrain, (* 4-7 May, 2009).
32. M.A. Gondal, Z.H. Yamani**, Q. A. Drmosh** and M. Rashid , Synthesis of Nanostructured ZnO and ZnO_2 by Laser Ablation Process Using Third Harmonic of Nd:YAG Laser, *International Conference on Nanotechnology (ICON008), Jeddah, Saudi Arabia* (17-19 June, 2008).